Alma Mater Studiorum – Università di Bologna

DOTTORATO DI RICERCA IN

CHIMICA

Ciclo XXXVI

Settore Concorsuale: 03/B1-FONDAMENTI DELLE SCIENZE CHIMICHE E SISTEMI INORGANICI

Settore Scientifico Disciplinare: CHIM/03

DEVELOPMENT OF MECHANICALLY REINFORCED POROUS CERAMICS FOR BONE REGENERATION

Presentata da: ZAHID ABBAS

Coordinatore Dottorato

Prof. Luca Prodi

Supervisore

Prof. Giuseppe Falini

Co-Supervisore

Dr. Simone Sprio
Dr. Massimiliano Dapporto

Esame finale Anno 2024

ACKNOWLEDGMENTS

I feel the great pleasure and honor to express my heartiest gratitude to my kind co-supervisors**, Dr. Simone Sprio** and **Dr. Massimiliano Dapporto,** National Research Council of Italy-Institute of Science, Technology and Sustainability for Ceramics (CNR-ISSMC), Italy for their dynamic supervision, inspiring gaudiness, keen interest and valuable suggestion throughout the PhD research and write up of this manuscript.

Heartiest thanks are extended to my supervisor **Prof. Giuseppe Falini,** Department of Chemistry, University of Bologna, Italy and **Dr. Anna Tampieri**, National Research Council of Italy-Institute of Science, Technology and Sustainability for Ceramics (CNR-ISSMC), Italy for providing valuable help in the completion of PhD thesis.

No acknowledgments could ever adequately express my obligations to my affectionate and adoring **parents and my family**, who always raised their hands in prayers for me. They always acted as a lighthouse for me in the dark ocean of life. No words can really express the feelings that I have for my beloved parents. I must extend deep emotions of appreciation to my colleagues for their most cooperative attitude. I offer my profound obligations to **Marta Tavoni, Federico Pupilli and Hina Inam** for their much loving caring and cooperative attitude during my stay in CNR-ISSMC, Faenza, Italy.

Zahid Abbas

SUMMARY

Calcium phosphates, particularly hydroxyapatite (HA) have been widely considered as elective materials for the development of bone scaffolds, as their good mimicry with the chemical composition of the mineral bone provides excellent biocompatibility and osteogenic ability. Furthermore, the development of scaffolds with wide open and interconnected porosity is a major factor ensuring the complete integration with the surrounding bone and the achievement of effective mechanical stability.

Despite such a great potential, a main drawback associated to calcium phosphates and generally to all ceramics, refers to their intrinsic brittleness, i.e. incapacity to withstand plastic deformation under loading which is a major problem causing possible sudden failure of the scaffold structure under physiological mechanical loading. This is a major reason making the regeneration of load-bearing bone defects such as maxillofacial regions and spine region, a still unmet clinical need of great socio-economic relevance.

In this respect, my Ph.D. project is focused on the development of new processes to achieve calcium phosphate-based scaffolds featuring enhanced bioactivity and mechanical properties. The research was carried out at the Institute of Science, Technology and Sustainability for Ceramics, belonging to the National Research Council of Italy (CNR-ISSMC) under the supervision of Dr. Simone Sprio and Dr. Massimiliano Dapporto.

The first part of my PhD thesis involves the development of mechanically reinforced porous apatitic ceramics scaffolds. The design of porous bioactive scaffolds based on hydroxyapatite basically involves the preparation of powders, then manipulated by the preparation of slurries, that are ternary systems involving aqueous dispersions of particles and dispersants. For this reason, the preparation of stable, homogeneous and manageable dispersions of powders in water is required to prevent final structural defects. The stability of calcium phosphate slurries is associated with various processing parameters including the powder content, the specific surface area of powder and the dispersant amount. Several processing techniques have been described in literature to prepare porous bone scaffolds with complex shapes and morphology including replica method, sacrificial template and direct foaming method. Moreover, 3D printing has been assessed and reported as an effective method for the preparation of scaffolds with controlled morphology and porosity. Therefore, the rheological characterization of hydroxyapatite-based slurries becomes a mandatory task to understand the effect of the processing factors on the colloidal stability of slurries. On this basis, a significant contribution of my research activity was focused on the development and rheological characterization of apatite-based slurries. However, scaffolds obtained by such slurries generally exhibit a brittle mechanical behavior. In this context, I investigated novel approaches for the mechanical reinforcement of hydroxyapatite scaffolds by the addition of carbon or alumina fibers to the slurries, with the purpose to achieve a toughening effect.

The second part of my PhD activity involves the development of porous apatitic bone cements mechanically reinforced with fibers. The apatite cements (CPC) are obtained by mixing a precursor powder with a liquid phase thus obtaining a self-hardening paste that can be extruded or molded before complete setting. Among inorganic precursors for apatitic CPCs, α-tricalcium phosphate (α-TCP) is especially interesting as a cement precursor essentially due to its hydraulic reactivity upon contact with water and its ability to set at body temperature, while transforming into nanocrystalline calcium deficient apatite (CDHA). Considering that highly crystalline precursors can compromise hydraulic and biological reactivity, I further explore the synthesis of α-TCP at significantly lower temperatures.

Numerous studies have attempted to introduce bioactive ions naturally found in bone tissue into the structure of inorganic precursor of CPC to improve some features of the apatitic bone cement, such as osteointegration and mechanical properties. Particularly, Mg and Sr are trace elements naturally found in human bones and play an important role in modulating cell behavior and natural bone turnover. Sr-doped CPCs gained increasing interest due to potential anti-osteoporotic character, while Mg is one of the most important elements for living organisms, as an essential regulatory factor for the pH and free calcium in cells. The morphological features of CPCs also make them good candidates for functionalization with bioactive molecules, towards the generation of multifunctional devices with enhanced therapeutic ability.

This second part includes three sub-chapters dealing with: i) apatitic cements obtained from inorganic precursors synthesized by low and high-temperature treatments, ii) magnesium-doped apatitic cements with intrinsic antibacterial properties and iii) reinforcement of magnesium and strontium-doped apatitic cements with carbon fibers.

- The objectives of the first sub-chapter were to compare the structural, physicochemical and hydraulic reactivity of α-TCP obtained through two different routes: solid-state reaction at 1400°C (High Temperature, HT-αTCP) and conversion from amorphous calcium phosphate at 650°C (Low Temperature, LT-αTCP). Moreover, the addition of carbon fibers in both cements was investigated to improve the mechanical performance.
- The second sub-chapter is focused on the development of magnesium doped apatitic cements, exhibiting antibacterial properties. Moreover, the antibacterial character of cements was also modulated by introducing tetracycline, a common broad-spectrum antibiotic.
- The third sub-chapter explores the design and development of carbon fiber-reinforced calcium phosphate cements by mixing αTCP and Sr-αTCP with MgHA nanoparticles as inorganic precursors. Carbon fiber (CF) exhibits superior mechanical properties and biocompatibility, making it a promising choice for bone scaffold reinforcement.

Table of Contents

List of Figures

List of Tables

CHAPTER 1: INTRODUCTION

1.1. The Skeleton

The human skeleton serves as the body's framework, composed of 270 bones at birth that eventually fuse (grow together) to form 206 bones by adulthood (Figure 1.1). However, some adults may have 213 bones, which is caused by variations in the number of bones in their fingers, toes, vertebrae and ribs.

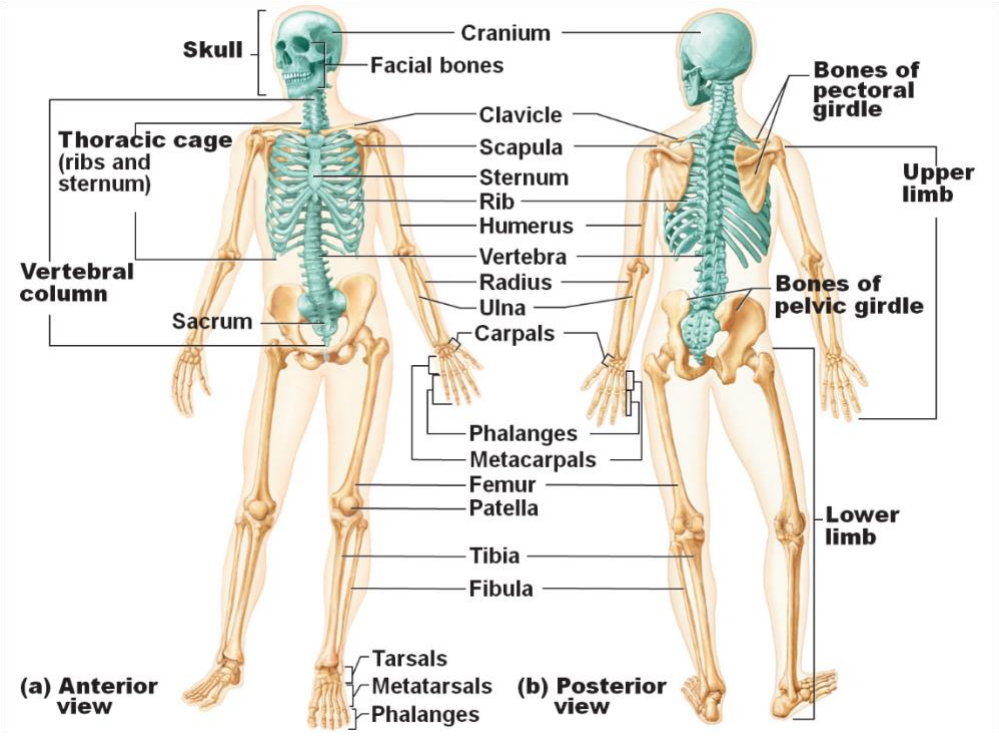

Figure 1-1: The human skeleton [1, 2]

The skeleton is crucial to human existence since it enables essential daily activities such as sitting, standing, walking and breathing by providing a rigid framework [3].

The skeletal system is comprised of bones, cartilage and ligaments in the body. It provides structural support for the entire body, protects vital organs including the brain, enables movement and locomotion by serving as levers for muscles, helps to maintain mineral homeostasis and acid-base balance, stores fat and is responsible for producing blood cells, serves as a reservoir for growth factors and cytokines and provides the environment for haematopoiesis in the marrow spaces [4]. Bones serve as attachment points for muscles, which allow us to move our limbs and perform complex actions such as running, jumping and lifting. The various joints in the skeleton allow for a wide range of movements, from simple hinge-like movements in the knee and elbow to complex rotational movements in the hip and shoulder [5].

The skeleton is divided into two principal parts based on origins and features: the axial and appendicular components8. The axial skeleton consists of the skull, vertebral column and thoracic cage formed by 12 pairs of ribs and sternum, or breastbone. The ribs attach to the vertebrae at the back of the spine and wrap around to attach to the sternum at the front of the chest. The rib cage serves to protect the heart and lungs. The appendicular skeleton includes all bones of the upper and lower limbs (arms and legs), as well as the bones that connect each limb to the axial skeleton [6]. The arms are made of three bones: humerus, radius and ulna. The humerus is the long bone that runs from the shoulder to the elbow, while the radius and ulna are the bones of the forearm. The hands are composed of 27 individual bones, including eight carpal bones, five metacarpal bones and 14 phalanges. The legs are composed of four bones: the femur, or thighbone, the patella, or kneecap and the tibia and fibula, which are the bones of the lower leg. The foot is composed of 26 individual bones, including seven tarsal bones, five metatarsal bones and 14 phalanges. The pelvis is composed of three bones, the ilium, ischium and pubis, which are fused together to form a basin-like structure that supports the weight of the upper body [7].

The bones of the skeleton are classified into five types based on their shape: long, short, flat, irregular and sesamoid. Long bones include the bones in the lower limbs (femur, tibia, fibula, metatarsals, phalanges) and the upper limbs (radius, humerus, ulna, metacarpals, phalanges) which support the weight of the body and facilitate movement. Short bones include the carpals in the wrist (hamate, pisiform, scaphoid, triquetral, lunate, capitate, trapezoid, trapezium) and the tarsals in the ankle (cuboid, calcaneus, navicular, talus, lateral cuneiform, intermediate cuneiform, medial cuneiform) provide the stability to the joints. The skull, thoracic cage and pelvis are flat bones that protect internal organs. Irregular bones include the vertebrae (protect the spinal cord), sacrum, coccyx, hyoid bone and patella also called sesamoid bone [8].

1.2. General Aspects on Bone Structure and Bone Tissue

The macrostructure of long bones comprises of two peripheral epiphysis and a central shaft referred to as diaphysis (Figure 1.2). The diaphysis consists of dense compact bone whereas the epiphysis is composed of trabecular meshwork bone bordered by a relatively thin shell of dense compact bone [9].

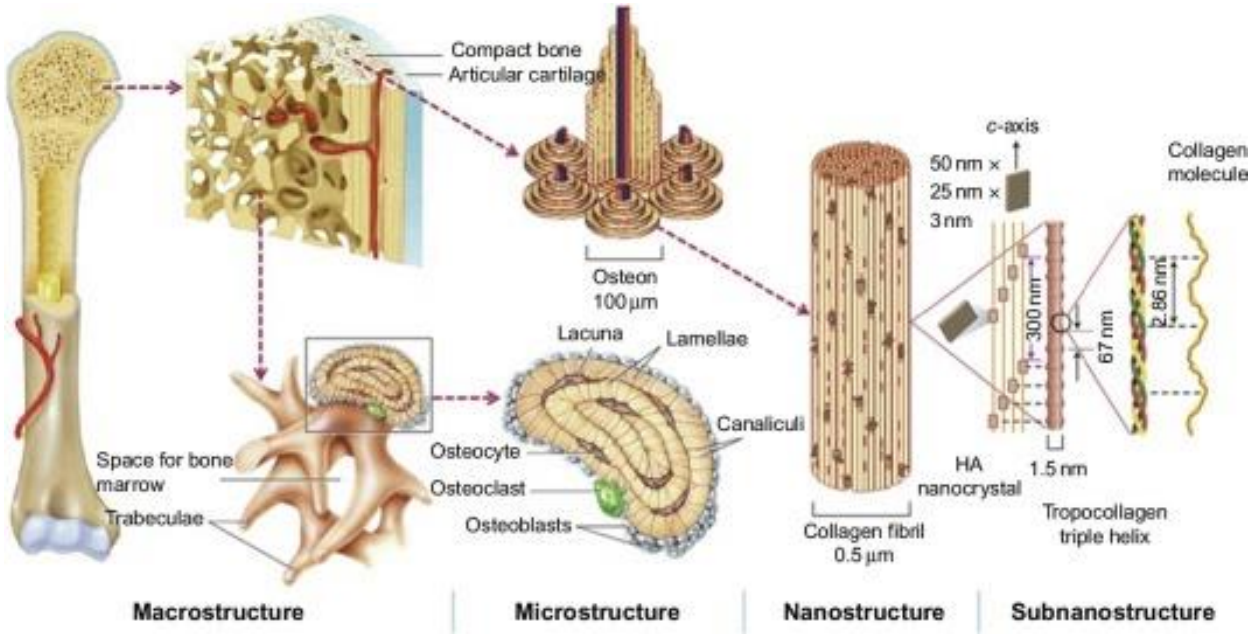

Figure 1-2: Macro to micro-structure of a long bone [10]

The adult human skeleton is normally composed of 80% cortical bone and 20% trabecular bone. Nevertheless, the ratio of cortical to trabecular bone can vary from bone to bone; for instance, the femoral heads, vertebrae and femoral diaphysis are composed of cortical to trabecular ratio of 50:50, 25:75 and 95:5 approximately [11].

Each bone contains two main types of bone based on the arrangement of their structure: cortical (compact) bone and trabecular (spongy or cancellous) bone. Cortical bone tissues form a dense and hard outer layer of bone, while the trabecular bone is composed of a honeycomb-like structure containing trabeculae plates and bars of bone adjacent to small, irregular cavities that contain red bone marrow. The cortical bone tissue consists of closely packed osteons. The cylindrical osteon structures contain concentric rings (lamellae), lacunae and osteocytes arranged around a central canal [10].

The bone tissue is classified as a calcified connective tissue comprised of the extracellular bone matrix, bone marrow as well as bone cells (Figure 1.2). An extracellular matrix is composed of a tough organic matrix which greatly strengthens by deposits of inorganic minerals containing mainly ion-doped calcium phosphate salts, particularly in the form of needle-like or thin plates of hydroxyapatite crystals ($Ca_{10}(PO_4)_6(OH)_2$). However, bone is composed of an average of 10% water, 30% organic components (Collagen Type I, non-collagenous proteins, cells, proteoglycans) and 60% inorganic components. The organic bone matrix contains 90-95% type 1 collagen and the remaining part is ground substance. Type

I collagen is the most abundant form of intrinsic collagen found in bone, while the ground substance is an amorphous gel-like material, which fills the space between fibers and cells. It is primarily composed of water and large organic molecules, such as glycosaminoglycans (GAGs), proteoglycans and glycoproteins [12].

Type-I collagen fibers consist of collagen fibrils which are composed of type-I collagen molecules (average 200nm long and 1.5nm diameter) and hydroxyapatite nanocrystals (average 10 nm long and 2nm thick) spread along the collagen fibrils. A collagen molecule is made of three polypeptide chains termed pro-α1 and pro-α2 procollagen chains are coiled together into a triple-helix of approximately 1000 amino acids, 3000 in each chain (Figure 1.2). The bone structures form from type I collagen and ground substance is tough and lightweight, adaptive, self-healing and multifunctional. Bone develops its resistance to fracture by multitude of deformation and toughening mechanisms that act at various size scales, from the macroscale physiological scale to the nanoscale structure of its protein molecules[13].

Additionally, bone tissue also contains exogenously derived proteins that can circulate in the blood and become trapped in the bone matrix. These include cytokines such as interleukin, tumour necrosis and colony-stimulating and growth factors such as transforming, platelet, fibroblast and insulin produced by bone-associated cells, which are crucial for bone cell activity. These proteins remain inactive in the bone and become mobilized when osteoclasts reabsorbed the bone [14].

1.2.1. Bone Cells

There are five different types of bone cells: osteoprogenitor cells, bone lining cells, osteocytes, osteoblasts and osteoclasts cells. Bone lining cells, osteoblasts and osteoclasts are observed on the surface of bone and osteoprogenitor cells are presented in the central canal of the bone, originate from embryonic mesenchymal cells called progenitor cells. While osteocytes are produced by fusing of mononuclear blood-borne precursor cells and are observed entrapped into the bone matrix [15].

1.2.1.1.Osteoprogenitor cells

The osteoprogenitor cells, also known as osteogenic cells, are stem cells that play a vital role in bone growth and repair. These cells work as a precursor of osteoblasts and osteocytes. They originate from infant mesenchymal cells and turn into spindle cells at the matured bone surface. In growing bone, these cells trigger the multifunctional stages to remodel the bone tissue. With the aging fact, the body loses the ability to produce and utilize the osteoprogenitor cells [16].

1.2.1.1. Bone Lining Cells

Bone lining cells are post-mitotic flattened and elongated osteoblast cells lining on the surface of the bone. When the bone surface is neither in formative nor resorptive phases and are found effective to bone remodeling. These cells protect from osteoclast resorption by covering the bone surface and stimulating bone formation by reactivating bone-lining cells to become active osteoblasts. These cells serve as an ion barrier separating fluids percolating through the osteocytes and lacunar canalicular system from the interstitial fluids [2].

1.2.1.2.Osteocytes

Osteocyte cells are the most abundant cells, are entrapped within the bone matrix and are actively involved in bone turnover. The cellular network of these cells in bone matrix provides contact with bone surface involved in ion exchange and signaling. It is reported that mechanical stress can be sensed by osteocytes and they secrete paracrine factors such as insulin-like growth factor-I (IGF-I) and express c-fos in response to mechanical stress. These can play a major role in the formation of bone by solubilizing both mineral and organic components of the bone matrix. Osteocytes also remain in communication with osteoblasts at the bone surface [17].

1.2.1.3.Osteoblasts

Osteoblasts are unpolarized cells that are primarily responsible for the synthesis and mineralization of bone, during the formation of bone. Osteoblasts are present on the surface of the bone in form of continuous sheet, extending the cellular processes through the developing bone. These cells originate from the differentiation of osteogenic cells in the periosteum, on the surface of bone tissue and in endosteum of bone marrow. These cells are surrounded by the growing bone matrix and eventually, trapped in the calcified matrix and differentiate into less active osteocytes. Many cell products are produced by osteoblasts such as growth factors, enzymes alkaline phosphatase and collagenase, hormones, collagen and unmineralized organic component of bone called osteoid. They serve as seeding sites for hydroxyapatite formation through the mineralized enzymatic accumulation of calcium and phosphate [18].

1.2.1.4.Osteoclasts

Osteoclasts are large, polarized and multinucleated resorbing cells that differentiate from the monocyte-macrophage lineage cell. They are involved in bone matrix resorption by solubilization of both the mineral and organic components of the bone matrix. These cells migrate from the bone marrow to sites

of resorption on the surface of the bone. Osteoclasts selectively recognize their fusion partners followed by cell-to-cell fusion and maturation. These cells express the enzyme tartrate-resistant acid phosphatase (TRAP), vacuolar proton ATPase, calcitonin receptors and vitronectin receptors [19].

1.3. Bone growth and bone remodeling

The process of bone tissue's development and growth is called osteogenesis or ossification. The internal structure of bone undergoes continual changes in response to functional demands, that occur by the activity of osteoclasts and osteoblasts. After the formation of osteoblastic lines, progenitor cells undergo three stages of cell differentiation development, including proliferation, maturation of matrix and mineralization. There are two different types of ossification processes occur in bone growth, based on their embryological origin: first is the intramembranous ossification, which involves the direct differentiation of mesenchymal cells, found in primitive connective tissue, into osteoblasts within the ossification center. This process occurs without prior cartilage formation and is observed in various cranial bones, such as the mandible, maxilla and skull bones. The second is the endochondral ossification, which involves the initial formation of cartilage, followed by the mineralization of bone tissue. Bone formation occurs directly during intramembranous ossification, mesenchymal cells proliferate into sites with high vascularization in embryonic connective tissue during the development of cell condensation or primary ossification center. Mesenchymal cells continue to differentiate into osteoblasts, located in the periphery, which synthesize new bone matrix. After that, mature lamellar bone will reshape and replace the bone. The primary ossification center will be formed by endochondral ossification and the cartilage will expand further by chondrocyte proliferation and cartilage matrix deposition. Chondrocytes in the center of the cartilage start to mature into hypertrophic chondrocytes after this stage of development. After the formation of the primary ossification center, the marrow cavity starts to expand towards the epiphysis. The subsequent endochondral ossification phases will later occur in different regions of the bone [20].

Bone growth is influenced by several genetic and environmental factors, including hormone influences, dietary factors and mechanical stimuli. The growth rate is not necessarily similar throughout all regions, because the internal pattern of the spongiosum depends on the direction of bone pressure. For example, the proximal end of the humerus grows more quickly than the distal end. The direction of bone growth within the epiphysis plane is dependent on the direction and arrangement of the pressure line. The deposition of new bone in the form of circumferential lamellae under the periosteum is responsible for

the increase of bone thickness or width. As the bone formation continues, the lamella will get embedded inside the newly formed bone surface and subsequently replaced by the haversian canal system [20, 21].

The bone is a dynamic connective tissue that is continuously regenerated by longitudinal and radial growth, modeling and remodeling, reaching complete bone tissue renewal every 10 years and it persists throughout the life shown in Figure 1.3. Both bone modeling and remodeling occurs during early childhood. Bone modeling is a prominent process throughout the childhood, whereas bone remodeling predominates in adulthood. Bone growth occurs in the bones longitudinally and radially during childhood and adolescence, while it occurs longitudinally in the growth plates, where cartilage proliferates before undergoing mineralization to primary new bone formation [22].

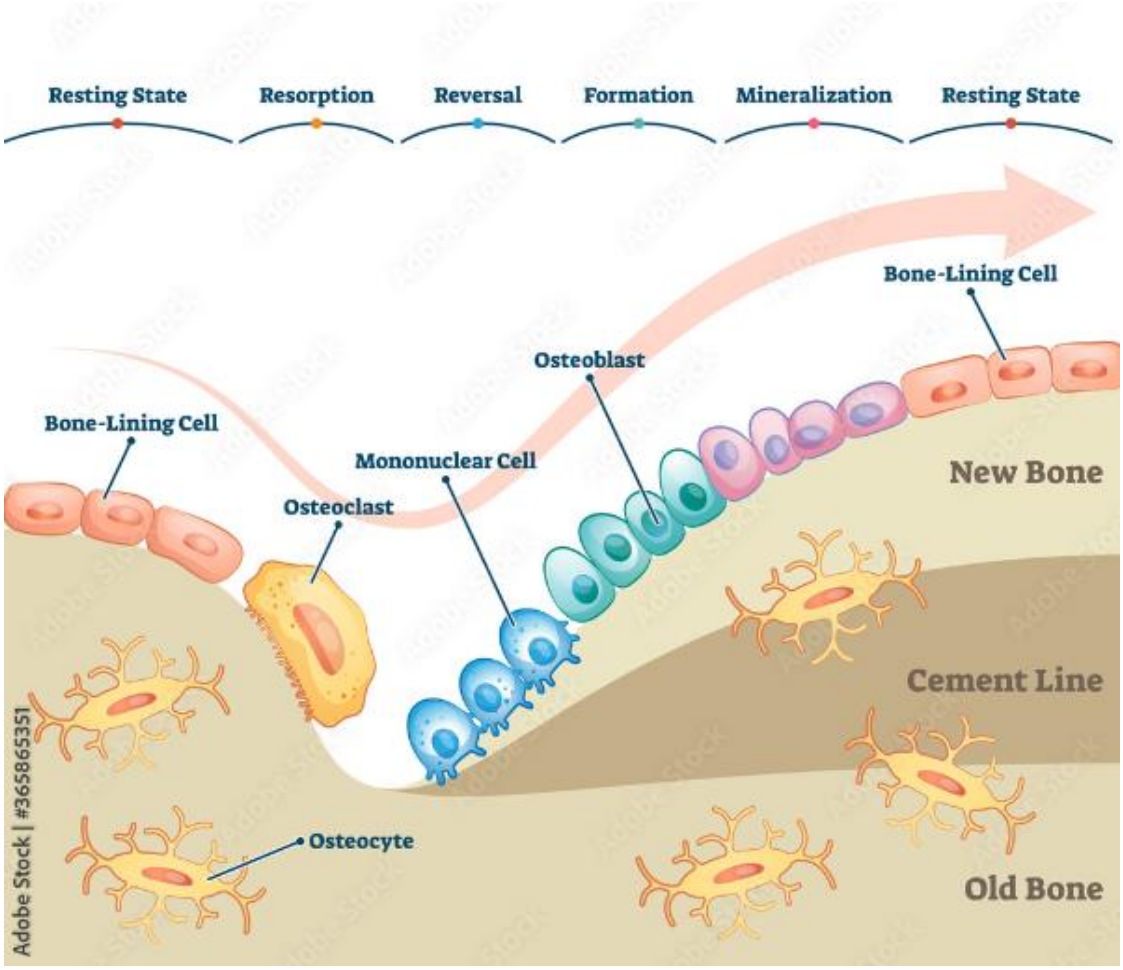

Figure 1-3: Bone remodeling process [23]

Bone modeling describes as either bone formation by osteoblasts or bone resorption by osteoclasts on the surface of bone. The primary function of bone modeling is skeleton development and growth and primarily serves to reshape the bone in response to physiologic influences or mechanical forces and their movement through space. Despite the formation and resorption modeling are locally independent, they are not globally independent because both processes occur at same time throughout the skeleton development and must be coordinated to bone shape. Local tissue strain serves as principal signal for bone modeling. The formation modeling process stimulates to add new bone matrix if local tissue strain exceeded a certain threshold, whereas resorption modeling process is started if strain is low [24].

Bone remodeling involves sequential osteoclast-mediated bone resorption and osteoblast-mediated bone formation at the same surface of bone. The term "bone remodeling" refers to a complex biochemical process involving the degradation and formation of the mineralized bone via bone cells to maintain the bone strength and homeostasis. Bone remodeling process involves continuous replacement of discrete packets of old bone with new synthesized proteinaceous matrix through the coupled activity of osteoblasts and osteoclasts, to prevent accumulation of bone microdamage. Bone remodeling process is more frequent than modeling in adults. The remodeling process begins before birth and continues until death. The process of remodeling often referred as remodeling cycle consists of five sequential phases: activation, resorption, reversal, formation and quiescence. The entire remodeling cycle normally takes average 4-6 months in heathy humans and can be highly altered by bone disease. The activation stage involves recruitment and activation of monocyte-macrophages osteoclast precursors to the bone surface followed by their differentiation and fusion to form multinucleated preosteoclasts. The resorption stage involves the osteoclasts resorb bone and the in-reversal stage, osteoclast undergoes apoptosis and osteoclast are recruited. During the bone formation stage osteoblasts lay down into new unmineralized organic bone matrix [15]. The process of bone-repairing through different stages are shown in Table 1-I.

Table 1-I: The bone-healing process and its stages [25].

Early inflammatory stage	Hematoma development: Hematomas develop within hours of an injury, when blood flows into the wound.
	Granulation tissue formation: Macrophages, monocytes, lymphocytes and polymorphonuclear cells are just some of the inflammatory cells that enter the site of injury via the circulation. Prostaglandin facilitates the infiltration of fibroblasts into bone. The mixture of these components produces granulation tissue.
	Ingrowth of vascular tissue: Granulation tissue is formed by inflammation cells, which also promote vasculogenesis.
	Migration of mesenchymal cells: Inflammatory cells that are present in the wound are responsible for stimulating final process.
Repair stage	Stroma formation to support vasculature: Fibroblasts produce stroma at the initial stage of the healing process. The goal is to promote the development of vasculature.
	Vascular ingrowth progress: The formation of the stroma allows for the subsequent growth of vascular tissue, which then supplies nutrients to the wound.
	Mineralization of the osteoid: Osteoblasts are responsible for the deposition of the collagen matrix, which is subsequently followed by mineralization.
	Soft callus formation: The mineralization of the osteoid tissue results in the development of a callus, which is a soft tissue that surrounds the wound. The soft callus is an extremely weak structure that will eventually harden into the ossified callus. During this period, any movement between bones can cause macrotrauma, which can hinder the healing process.
	Woven bone formation: Both of the extremities of the bone are joined by a woven bone structure as the callus ossifies.
Remodeling stage	Bone returns to original structure: Bone regeneration is the final and longest step of the healing process, take at least three months and continue for the rest of the bone's natural lifespan. Adequate mechanical loading is one factor that influences the time required for bone remodeling. This enables organic matrix mineralization where it is needed and for bone to be resorbed where it is not.

1.4. Clinical needs: reconstruction of critical and load-bearing bone regions.

Natural bone has the ability to repair itself through a very well-studied healing cascade in response to injury, as well as during skeletal development and growth throughout adult life. The process of bone regeneration involves a well-orchestrated sequence of biological events, including bone induction and conduction. This process involves various types of cells and molecular signalling pathways within the cells and external environment, with a definable temporal and spatial sequence to enhance bones repair and restore skeletal function. In the clinical context, the fracture repair is most common form of bone regeneration, in which the pathway of normal foetal skeletogenesis is replicated, including both intramembranous and endochondral ossification pathways. Unlike to other types of tissues, the bone

healing process often does not include the formation of scar tissue and regenerated with many of its pre-existing qualities restored and finally becomes indistinguishable to the adjacent healthy bone. However, bone formation may be impeded in certain situations of fracture healing; for example, up to 13% of tibial fractures are linked to delayed union or fracture non-union. Furthermore, there are other conditions in the field of orthopaedic surgery and oral and maxillofacial surgery that require an extensive level of bone regeneration, exceed the intrinsic self-healing ability of bone and consequently bone repair is delayed and impaired, referred as critical bone defects. Calculating the volume of a critical bone defect, especially a cranio-maxillofacial bone defect, is a challenging task since the criticality of a defect depends on a number of criteria, including its location, size, depth, surrounding tissue vascularity, and patient-specific characteristics. Several studies have claimed that the diameter of defect ≧4 mm in the mandibular sites is a critical size to evaluate bone repair in the guided bone regeneration (GBR) therapy paradigm [26].

Such situations require skeletal reconstruction to address critical bone defects in which the regenerative process is hindered due to avascular necrosis and osteoporosis [27].

However, the reconstruction of critical and load-bearing bone defects caused by trauma or disease is still a major challenge for orthopaedic surgeons. Table 1-II, summarizes the most common causes of critical bone defects and lists the risks associated with leaving these defects untreated. Such type of defects requires extra treatment with porous bone substitutes (scaffolds) able to fill the bone gap and function as a physical bridge permitting colonization by bone and vascular cells and regrowth of bone tissue with pre-existing functions.

Table 1-II: Different causes and consequences of untreated critical bone defects *[28]*

Trauma injuries	Blast injuries: These kinds of injuries are quite prevalent among armed military personnel. The injury caused by the explosion of a weapon or explosive device is of a serious nature, as it not only affects the skeleton structure, but also the muscles, circulation of blood and neurological system.
	Fractures and sport injuries: These kinds of bone fractures are frequently segmental and are distinguished by broken and shattered fragments of bone. The gap between the two extremities develops after the removal of the fractured part by surgery.
Degenerative diseases	Conditions like bone cancer (which requires tumour resection and reconstruction), osteoporosis, osteoarthritis, common infections, correcting genetic deformities and pathological degenerative bone destruction all fall into this category. The bone in these conditions is either abnormally weak and required to be eliminated to avoid disease transmission. Therefore, large segments of bone are missing or medically removed and must be restored.

Critical bone defects are emerging as a significant concern across diverse anatomical regions, as a result of extensive trauma, tumour excisions and congenital disorders that can cause serious damage resulting in noticeable dysfunctions and deformities. These defects are commonly addressed through bone grafting with substitutes such as autogenous, allogeneic or xenogenic bones. However, despite the many advantages of these grafting technique, there are some drawbacks such as the risk of infections, donor-site morbidity, multiple surgeries, limited availability, blood loss, long stays in hospitals, post-operative complications and immune rejection. In addition, existing grafts pose certain limitations in simultaneously achieving both morphological and functional repair of three-dimensional bony parts, particularly when load-bearing bones such as craniomaxillofacial or spinal bone or the limbs are involved [29]. Thus, the development of synthetic bone scaffolds is considered as a highly desired solution since decades [30-32]. Nevertheless, in spite a variety of scaffolds have been developed and some of them are clinically used [33], extensive bone regeneration is still a clinical challenge.

The mechanical properties of scaffolds play a crucial role in tissue engineering applications, particularly in craniomaxillofacial and spine bone repair, where scaffold qualities have utmost significance. The bone exhibits many significant mechanical characteristics, including Young's modulus, toughness, shear modulus, tensile strength, fatigue strength and compressive strength. Mimicking the mechanical characteristics of bone at a macroscopic level is crucial for a bone scaffold during the implantation period, as well as for maintaining these qualities to support the regeneration of new tissue [34-36].

The desired scaffold should meet the following criteria: deliver and/or recruit native stem cells into the defect site, allow vascularization and new bone tissue formation, facilitate exchange of nutrient and oxygen in vivo, incorporate growth factors into biomaterial scaffolds, stand a high structural load-bearing capacity; and ability to support and balance new bone tissue formation and scaffold degradation. These requirements appear to be critical for effective regeneration of load-bearing bones [37].

1.4.1. Reconstruction of craniomaxillofacial and spinal bone defects

The maxillofacial and spinal bone are the most exposed region of the body and is highly vulnerable to trauma and disease. Particularly, the reconstruction of maxillofacial defects is still a big challenge for surgeons due to the need to comply with strict mechanic, aesthetic and functional requirements, which are made hard to achieve, also due to the complex and intricate bone structure and geometry in such anatomical areas, involving different curvature planes and different thicknesses [38]. Indeed, facial muscles are among the strongest ones in human body, and they are responsible for a wide range of

actions, including talking, chewing and facial expressions. The mechanical aspect of craniomaxillofacial bone repair refers to the ability of the implant to withstand the forces exerted by the facial muscles. Hence, a bone implant must be strong enough to prevent deformation and displacement, but a key requirement is also its biocompatibility and bioactivity relevant for bone regeneration [39].

Mechanical failures may be caused by issues arising from excessive load and functional stress, leading to structural failure in both the implants and the supporting prosthetic systems. Therefore, the mechanical characteristics of these materials play a crucial role in determining their in vivo performance. It is crucial to carefully plan the position and number of implants to ensure the long-term preservation of prosthesis. The establishment of a direct connection between the implant and bone, known as osseointegration, results in increased functional stress on both the prosthetic parts of the implants and the antagonistic components that interact with the implant prosthetics. The efficacy of implants is dependent upon several factors, including the recipient's overall health status, the potential interactions between drugs and osseointegration and the oral tissue condition [40].

The mechanical properties of scaffolds have to be designed to be close to the native tissues being repaired. After production, characterizing the mechanical properties of the scaffolds is essential prior to implantation to ensure good performance and the success of subsequent repair procedures [41].

Spinal bone defects are a major clinical problem, affecting millions of people worldwide. Spinal bone defects can lead to a number of serious complications, including pain, instability and nerve damage. There is a growing need for new and improved treatments for spinal bone defects. One of the main challenges in treating spinal bone defects is that the spine is a complex and delicate structure and reconstructing a spinal defect without affecting the function of the spine is difficult. The location of the defect, the size of the defect, the condition of the surrounding tissues and the patient's health can all affect the difficulty of reconstruction. Any surgical intervention carries the risk of damaging nerves or spinal cord. Additionally, the spine is constantly under load, which can make it difficult for bone grafts to heal properly.

There have been significant advances in spinal reconstruction in recent years such as computer-assisted surgery (CAS) and minimally invasive surgery (MIS), making possible to reconstruct even complex spinal defects with a high degree of success [42]. The crucial challenges for successful biomaterial scaffold improvement lies in the achievement of multilayer controlled local drug release and in-vivo degradation. To address these problems, materials which exhibits tunable biodegradation, heterogeneous

regulatory facilities, simultaneous guided bone tissue regeneration and comparable mechanical properties of bone tissue are in great demand for vertebroplasty [43].

1.4.2. Craniomaxillofacial Anatomy, Defects and Surgery.

The human skull is a brain protective cavity, composed of four different types of bone such as cranial bones, ear ossicles, facial bones and hyoid bone (Figure 1.4). The function of skull is protection of brain, support the face and fix the position of the eyes and ears in order to enable stereoscopic vision and sound localization [44]. Like other skeleton bones, it's also composed of compact and spongy bone and divided into two parts; neurocranium, which refers to the bone surrounding the brain and viscerocranium, referring to the bone surrounding the face. The adult skull is normally composed of 22 bones, joined with each other by sutures except the mandible [45].

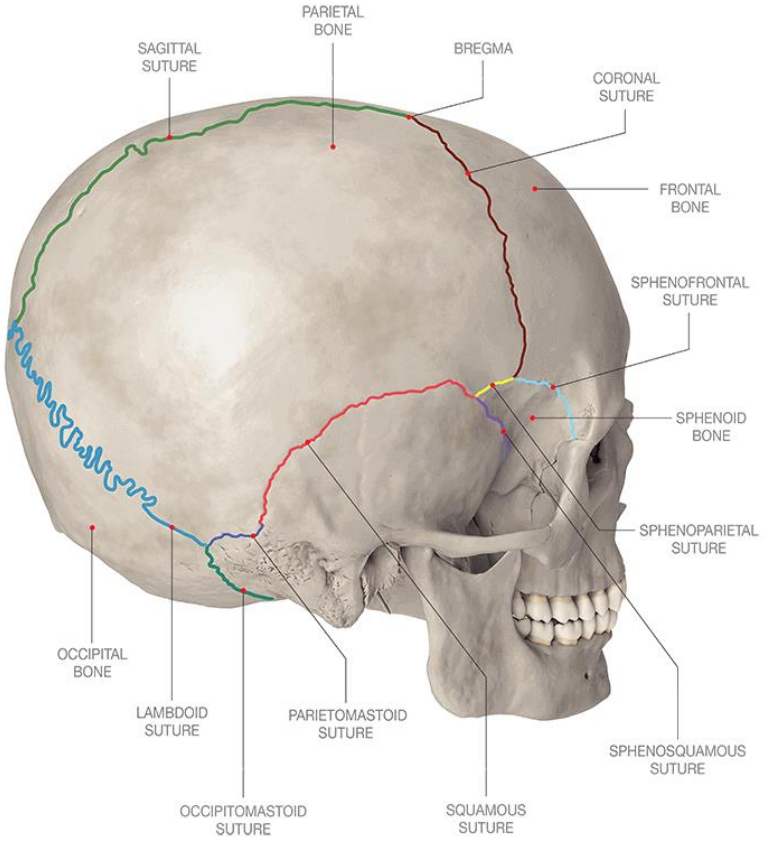

Figure 1-4: The sutures of human skull

The craniomaxillofacial region is composed of skull and jaw. Commonly, cranial and maxillofacial defects occur due to trauma, congenital abnormalities, tumours, deformities, sports injuries, surgical defects and periodontal diseases, affecting both function and aesthetics. The most common critical bone

defects in craniomaxillofacial are generally described as skull fractures and jawbone fractures that can impair the person's ability to breathe, speak, chew and listen as well as prolonged psychological difficulties, permanent disability and death. The common craniomaxillofacial surgeries are cranial surgery, mid-face surgery, mandibular surgery, orbital floor reconstruction surgery. It is reported that road accidents are linked with 50% of mortality. Cranial injury is higher in adults' people, of age 15-24 years due to accidents. Cranial surgery is described as the surgical repair of skull bone defects after a serious injury (Figure 1.5) [46].

The history of CMF surgery is very old, the first recorded attempt for craniomaxillofacial surgery is from ancient Egypt, where trephination or creating holes in the skull was used to treat fractures and injuries of the skull and face. The first time craniofacial surgery by bone grafting procedure was reported in a book by Job Janszoo van Meekeren, a surgeon in Amsterdam [47]. In 1967, the first time Paul Tessier presented the idea of craniomaxillofacial surgery at a meeting in Rome, Italy, emphasizing the challenges of the biology and anatomy between the cranium and the face. Over the past couple of centuries, many technologies and materials for maxillofacial surgery have been developed [48]. The reconstruction of cranial and maxillofacial defects is very important for human survival since the brain needs permanent protection and the segmental jaw requires mechanical integrity, temporomandibular joint function and intermaxillary dental occlusion. Nowadays, CMF devices in market with their advantages and disadvantages are listed in Table 1-III.

Table 1-III: The main cranio-maxillofacial devices available in the market.

Device	Description	Indications	Pros	Cons	
Plate and Screw Fixators	Inflexible metallic implants used to hold bones in place after surgery or trauma	Craniofacial reconstruction, orthognathic surgery, fracture fixation	Customizable, highly stable and efficient, versatile	Associated to potential issues such as infection, malunion, failure to heal, and may need the removal of implants.	[49]
Distraction Systems	Devices that progressively lengthen bones, usually with the purpose of repairing abnormalities	Diverse facial irregularities, including lip and palate malformations and jaw joint dysfunctions	Offers controlled bone lengthening, treats a variety of deformities, and produces good cosmetic and	Compared to plate and screw fixation, it is more intricate to utilise and may necessitate regular modifications.	[50]

	or enhancing functionality.		functional results.		
Temporomandibular Joint (TMJ) Prostheses	Implants used to replace or restore the TMJ, the joint connecting the jawbone to the skull.	TMJ reconstruction, TMJ disorders	Relieve pain, reconstruct TMJ after trauma or surgery, improve jaw function	Expensive, may not be reimbursed by insurance, need extra placement/removal procedures	[51]
Bone Grafts	Pieces of bone transferred from one place of the body to another to treat bone defects.	Promote bone healing and regeneration	Can promote bone healing and regeneration, fill in large defects	Requires extra surgery to harvest the graft, may not be accessible in all cases	[52]
Patient-Specific Implants (PSIs)	Custom-made implants developed by using 3D imaging technology.	Maxillofacial defects, TMJ reconstruction, bone augmentation	Precisely suit the patient's anatomy and function, may decrease need for bone transplants and dissection	Custom-made implants are pricier than pre-made ones and may require a longer fabrication time.	[53]
Biomaterials	Materials such as polymers, ceramic, used to replace or augment bone tissue.	Cranio-maxillofacial defects	Biocompatible, resorbable, can restore bone structure	May exhibit poor strength and durability compared to natural bone, perhaps necessitating supplementary removal or replacement treatments.	[54]

From a wide range of treatments, bone grafting is considered as a gold standard for treatments of skull and maxillofacial critical defects [55]. Bone grafting is a surgical procedure that is used to implant material into bony defects. The reconstruction of bone healing occurs through different mechanisms such as osteoinduction, osteoconduction and osteogenesis [47].

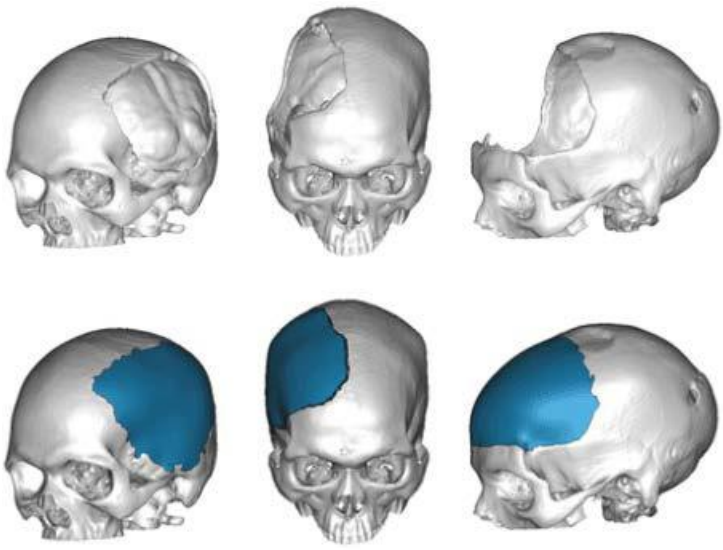

Figure 1-5: Craniomaxillofacial defects with customized scaffolds

Biomaterial approaches allow for patient-tailorable options as well as these typically being easier to modify, enabling changes in bioactivity, mechanics and drug-loading to improve regeneration and anti-bacterial properties [56-59].

The most common synthetic craniomaxillofacial devices in the market are customized/patient-specific implants and standard implants made from a range of materials such as metals, polymers, bioabsorbable materials and ceramics [60]. For example, the Midface 1.5mm/2.0mm Titanium system for CMF by ZIMMER BIOMET, USA, the Midface Titanium system offers versatile plating options including generic meshes and preformed orbital plates that can be used in multiple maxillofacial procedures (Figure 1.6a). Titanium 3D-printed plates & implants by DEPUY SYNTHES, USA, are manufactured by Selected Laser Melting (SLM) of commercially pure grade 2 titanium powder (CPG2Ti), layer by layer, using a high-power laser (Figure 1.6b). Osteoplug™ by Osteopore, UK, is a bioresorbable cranial implant that is used for covering trephination burr holes in neurosurgery. Its interconnecting porous matrix architecture allows it to be rapidly saturated with marrow, blood and nutrients for bone growth and remodeling (Figure 1.6c). LithaBone HA 480 was developed by Lithoz GmbH, Wien, Austria. The slurry, designed and produced by Lithoz, comprises hydroxyapatite powder and a photocurable binder matrix containing solvent, reactive monomers based on acrylates and methacrylates and photoinitiator (Figure 1.6d). Mybone by Cerhum, Belgium (Figure 1.6e) and Custom-Bone by Finceramica, S.p.A, Faenza, Italy (Figure 1.6f) are the most common implants devices in the market for craniomaxillofacial bone regeneration applications (Figure 1.6).

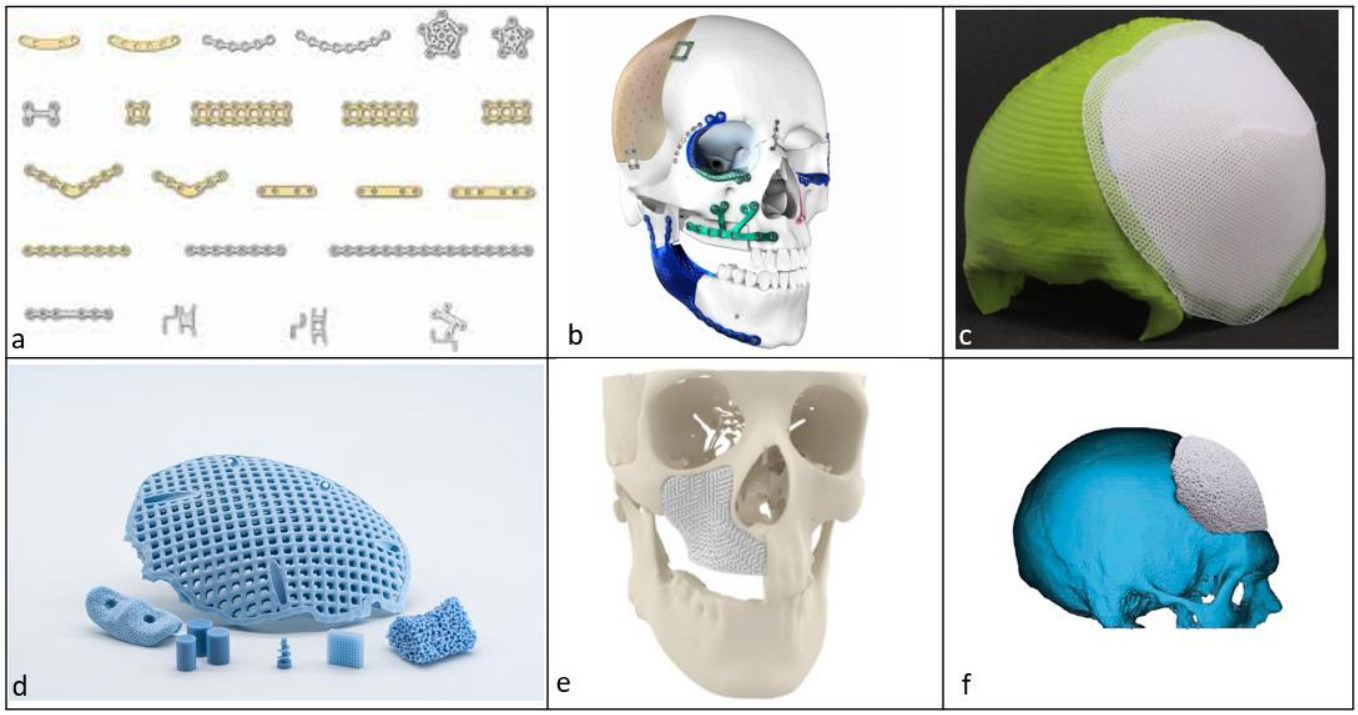

Figure 1-6: Different commercial craniomaxillofacial bone.

The Custom-Bone for regenerative cranial bone defects is made of porous HA, a biocompatible and osteoconductive calcium-phosphate material. In particular, manufacturing process of custom-made implants (Finceramica) starts with the acquisition of raw digital data through a CT scan. The data is then extensively processed to generate a 3D computer reproduction of the patient's skull, which is essential for constructing a 3D synthetic model using stereolithography. The initial prototype of the implant is created from this model and a thorough review is conducted with the surgeon to allow for potential modifications that may lead to better patient outcomes and surgical feasibility. Upon approval by the surgeon, the final implant is produced via the Replica method, undergoes rigorous refinement, quality control and sterilization before being shipped to the hospital for implantation. This method ensures the production of a custom-made implant that meets both the aesthetic requirements of the patient and the technical needs of the surgical procedure.

1.4.3. Spine anatomy, defects and surgery

The vertebral column of a human, also known as spine or backbone is a bony structure that houses the spinal cord and connect the head to pelvis are shown in Figure 1.7. The most crucial role of vertebral column is to protect the spinal cord which serves as the entire body’s nerve supply, originating in brain. Together with this primary function, it also supports the body mass and enables mobility and flexibility

while protecting against outer impact. The vertebral column is connected to the ligaments and muscles of trunk for postural control and backbone stability. The vertebral column can be divided into five sections such as cervical, thoracic, lumbar, sacrum and coccyx. All these sections are made of 33 bones stacked on each other to form the spinal canal [61].

The cervical section of vertebral column composed of 7 vertebrae from C1 to C7 and 6 intervertebral discs that connect head to the top of trunk where ribs start. The main function of the cervical part is to support the head and neck load, allow to rotate and protect the spinal cord extended from brain. The thoracic section of vertebral column is composed of 12 vertebrae from T1 to T12 and 12 intervertebral discs that connect cervical bottom to the top of lumbar. The primary functions of the thoracic part include protection of the spinal cord and heavy load bearing, supporting posture and stability of the trunk and connecting the rib cage that protects and houses vital organs, such as the lungs, liver and heart. The lumbar is composed of 5 vertebrate and 5 intervertebral that connect the thoracic bottom to sacrum biggening. The important functions of lumbar include the spinal cord protection during locomotion and trunk bending/torsion, providing maximum stability while maintaining crucial mobility of the trunk about the hips/pelvis. The sacrum section is composed of 5 fused vertebrae that connect the trunk to the lower body and serve as a bridge between the spine and hips. The coccyx section is composed of 4 fused vertebrate that is connected with sacrum bottom. Th coccyx provides attachment sites for ligaments, pelvic tendons and muscles which support body while sitting position [62].

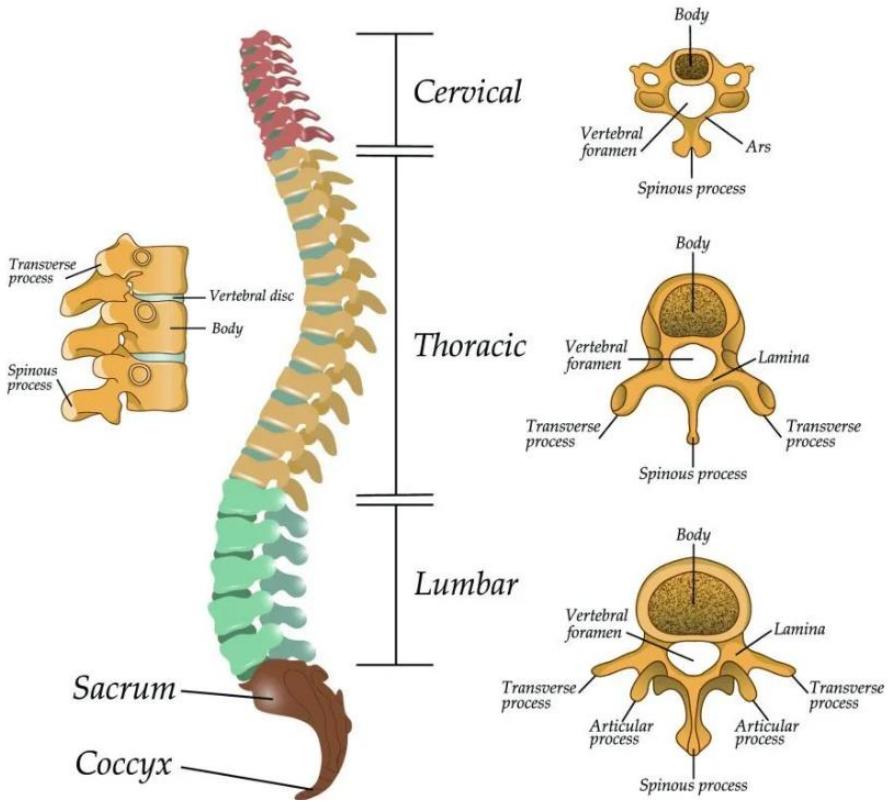

Figure 1-7: The structure of segments of the spine [63].

The spine protects our nervous system, provides flexibility for daily activities and supports the weight of the body. It is subjected to various physical loads including bending and twisting moments, compression and tension. Spine disorder leads to back pain, neurological problems and movement challenges. It occurs due to inflammation infections, tumours and degenerative wear and tear that comes with the natural aging process. Low back pain is the most common problem reported in various studies [64, 65]. It is reported that the human population up to 80% have low back pain experienced during daily activities and overall low back pain burden of 21.8 million disability-adjusted life years because of work ergonomic exposures. The most common causes for low back pain are degenerative diseases such as disc herniation, osteoporosis and stenosis, which need conservative treatment (non-surgical interventions) or non-conservative treatment (surgical interventions). The surgical intervention treatments are broadly categorized into two surgeries fusion and non-fusion. The fusion treatment is considered as a gold standard in which various prostheses such as plates, pedicles screws, cages and rods are used to fuse the concerned spine segments [66]. Various studies have been reported for various surgical approaches and prosthesis designs on the clinical needs of spine surgeries are shown in Table 1-IV [42, 67].

Table 1-IV: Various surgical approaches and prosthesis designs for the clinical needs of spine surgeries [68].

Approaches	Description	Pros	Cons
Posterior spinal fusion	A surgical treatment that combines many vertebrae into one, usually with the use of bone transplants and metal implants	Useful in stabilizing the spine and halting the progression of deformities; applicable to the treatment of scoliosis, kyphosis, and lordosis, among others.	- Possible extensive surgery requiring a lengthy period of recuperation. - Extra operations, such removing implants or doing bone grafting, may be necessary.
Interspinous process devices (IPSDs)	Intervertebral implants are surgically placed between the spinous processes of many vertebrae to enhance stability and alleviate discomfort.	- Minimally invasive compared to surgical procedures. - Can effectively address a range of spine conditions, such as spondylosis, facet arthritis, and spinal stenosis.	- May lack efficacy for some categories of spinal abnormalities. - May be necessary to undergo many operations in order to get the desired result.
Anterior spinal fusion	A surgical treatment that involves fusing two or more vertebrae together from the front of the spine, generally utilizing bone grafts and screws.	- May exhibit a lower degree of invasiveness compared to posterior spinal fusion. - Could potentially be a more favorable alternative for people presenting certain sorts of spinal abnormalities.	Posterior spinal fusion may be more successful than this method for stabilizing the spine. - This method may need a longer period of rehabilitation.
Kyphoplasty	A non-invasive technique that raises and realigns a collapsed vertebra by injecting it with bone cement	- Minimally invasive compared to surgical procedures. - Can be used for the treatment of spinal compression fractures	.- May lack efficacy for some categories of spinal defects. - May require multiple procedures to achieve the desired outcome.
Vertebral augmentation	A minimally invasive procedure in which a bone substitute material is injected into a fractured or compromised vertebra in order to enhance its strength and stability.	- Minimally invasive compared to surgical procedures. - Can effectively address a range of spinal abnormalities, such as vertebral compression fractures and osteoporotic spondylosis.	- May lack efficacy for some categories of spinal abnormalities. - It may be necessary to undergo many operations in order to acquire the desired result.

The non-fusion surgery is a useful approach that can eliminate the pain while preserving the motion of spine segments but high rate of failures of existing devices is a matter of concern. So, minimally invasive spine surgery is possible an alternative solution that involve the injection of a biomimetic bone cements into defected sites to provide the relief from back pain and mechanical support [69, 70]. Minimal invasive surgery reduces the incision size as well as decreases the length of patient stay in hospital, lead to less

blood loss, less pain and less tissue trauma, while simultaneously allowing for better postoperative immune function [71]. Infuse Bone Graft by Medtronic, USA are the commercial implant used for spine repair [72].

1.5. Key materials for bone scaffolding

It is imperative to say that the properties of a scaffold are determined by the synthesis approach and materials used for its development. The prerequisites for the selection of material to fabricate scaffolds for bone regeneration applications are specifically centred around their structure and form, molecular weight, surface energy, material chemistry, solubility, lubricity, hydrophilicity, hydrophobicity, erosion and water absorption capacity, degradation mechanism and intended application. Metals, glasses, alloys, polymers, ceramics and their composites are some of these materials that have gained a lot of attention recently owing to their distinctive features (Table 1-V) [73].

Table 1-V: Materials that are now under investigation for bone tissue regeneration [74].

Material Type	Description	Key Properties	Potential Drawbacks
Calcium Phosphate	A broad class of bioceramics including HA, TCP, and BCP, A natural bioceramic mimicking bone mineral structure	Biocompatible, osteoconductive, good mechanical properties, controllable degradation rate, extensive clinical experience	Brittleness
Polymers	Synthetic or natural polymers, such as PLA, PGA, and chitosan	Biodegradable, customizable, tunable properties, low cost	May exhibit lower biocompatibility than ceramics
Natural Materials	Biomaterials derived from nature, like collagen, silk, and alginate	Biocompatible, biodegradable, highly porous for cell infiltration, often possess good mechanical properties	Less consistent and reproducible than synthetic polymers
Hybrid Materials	Combinations of different materials, such as HA with polymers or natural materials	Combine advantages of multiple materials, enhance mechanical properties, biocompatibility, and degradation rate	More complex fabrication and characterization
Engineered Nanomaterials	Nanoscale materials with specific structures and properties, like nano-HA and carbon nanotubes	High surface area for cell attachment and growth, improved mechanical properties and drug delivery	Difficult to control, potential long-term effects unknown

Advances in materials science have led to the development of bioceramics, such as hydroxyapatite and tricalcium phosphate, which are more compatible with bone tissue because mineral phase of bone are mainly composed of hydroxyapatite but may have limited mechanical strength. Bioactive glasses and

composites incorporating polymers or natural materials have also been explored, offering a compromise between bioactivity and strength.

1.5.1. Calcium phosphates

Calcium phosphates are known as the major inorganic part (~60%) of the natural human bones. Therefore, calcium phosphates have been considered a potential candidate for bone regeneration applications, due to their osteoconductive and osteo-inductive properties [75]. There are different types of calcium phosphate-based on composition and physio-chemical properties, are currently being investigated for orthopaedic applications are shown in Table 1-VI.

Table 1-VI: Various calcium phosphates with their respective Ca/P ratios [76]

Name	Formula	Acronym	Ca/P
Hydroxyapatite	$Ca_{10}O(PO_4)_6(OH)_2$	HA	1,67
Amorphous calcium phosphate	$Ca_{10-x}H_{2x}(PO_4)_6(OH)_2$	ACP	
Dicalcium phosphate	$CaHPO_4$	DCPA	1,0
Dicalcium phosphate dihydrate	$CaHPO_4 \cdot 2H_2O$	DCPD	1,0
Tetracalcium phosphate	$Ca_4O(PO_4)_2$	TetCP	2,0
Tricalcium phosphate (α,β,γ)	$Ca_3(PO_4)_2$	TCP	1,50
Octacalcium phosphate	$Ca_8H_2(PO_4)_6 \cdot 5H_2O$	OCP	1,33
Calcium pyrophosphate (α,β,γ)	$Ca_2P_2O_7$	CPP	1,0
Calcium pyrophosphate dihydrate	$Ca_2P_2O_7 \cdot 2H_2O$	CPPD	1,0
Tetracalcium dihydrogen phosphate	$Ca_4H_2P_6O_{20}$	TDHP	0,67
Calcium metaphosphate (α,β,γ)	$Ca(PO_3)_2$	CMP	0,5
Heptacalcium phosphate	$Ca_7(P_5O_{16})_2$	HCP	0,7
Monocalcium phosphate monohydrate	$Ca(H_2PO_4)_2 \cdot H_2O$	MCPM	0,5

Among various types of calcium phosphates, hydroxyapatite (HA) with a chemical formula ($Ca_{10}(PO_4)_6(OH)_2$), is the most used bioceramic for bone regeneration due to its excellent

biocompatibility, osteoinductivity and biodegradability, since its composition is very close to the mineral component of bone. For this reason, bone scaffolds prepared with HA have the ability to stimulate new bone formation by promoting cell attachment, proliferation and differentiation with very low degradation rate. Beta-tricalcium phosphate (β-TCP) is the second most widely used bioceramics for orthopaedic applications. β-TCP degrades much faster than HA, also stimulating osteogenic differentiation of stem cells and new bone formation. To control the degradation rate of bioceramics, scaffolds prepared by the mixture of HA and β-TCP are widely considered as promising candidates for bone regeneration applications [77].

Despite the numerous advantages associated with calcium phosphates, it is important to acknowledge certain significant drawbacks including mechanical instability, challenges in shaping and molding them into desired structures and geometries, as well as limited bioactivity and a slow degradation rate. One of the main limitations associated with hydroxyapatite refers to its unsuitability for load-bearing bone applications because of their inherent brittleness, which results in failure without plastic deformation, as well as its poor mechanical properties and exhibits a significantly low degradation rate.

It is well known that sintering process increases the strength of hydroxyapatite ceramics but reduces the bioactivity of scaffolds due to an increase in crystallinity and crystal size. To enhance the bioactivity of HA ceramics, different bioactive ions such as Mg^{2+}, Sr^{2+}, Zn^{2+}, Mn^{2+}, Fe^{2+}, Ag^{2+} and CO_3^{2-} can be doped into HA to mimic the chemical compositions of natural HA. In addition, there are many challenges to process the hydroxyapatite ceramics slurries and produce porous scaffold. Moreover, since it's a challenge to shape sintered scaffold because of their brittleness, researcher have to make an incision in the bone defect sites to fit the scaffold when utilizing hydroxyapatite scaffolds, resulting in additional bone loss, trauma and surgical time.

In this context, the possibility to introduce additional inorganic phases in bioceramics opened a wider choice of materials for their use as implants. Some of these materials include ceramic/ceramic, ceramic/metal and ceramic/polymer composites. However, ceramic/polymer composites have been observed to release toxic components in the surrounding tissues, while metals undergo corrosion-related issues as the ceramic coating on the metallic implant degrades over time. Ceramic/ceramic composites are thought to have a better performance because they resemble bone minerals and exhibit high biocompatibility. Nevertheless, the biological activity of bioceramic composites has to be defined, especially considering the specific implantation site. Bioceramic composites have exceptional

biocompatibility and are non-toxic and some additional features of bioceramics composites include their hydrophilicity and antibacterial properties [78].

1.5.2. Hydroxyapatite

Hydroxyapatite (HA) has been extensively investigated for the regeneration of bone defects, due to its excellent biocompatibility, osteoconductivity and osteoinductivity. The chemical formula of stoichiometric HA is $Ca_{10}(PO_4)_6(OH)_2$ with a Ca/P ratio of 1.67 and its elemental composition is similar to that of bones and teeth, making it advantageous for dental and orthopaedic applications. The most frequently encountered form of HA is hexagonal shape (space group $P6_3/m$) with the lattice parameters of a = 9.432 Å, c = 6.881 Å and β = 120°, with two binding sites on its surface: the negatively charged phosphate site and the positively charged calcium site [79]. The crystalline network of HA is formed by compactly assembled tetrahedral PO_4 groups, where P^{5+} ions are located at the center of the tetrahedron and four O atoms occupy the top. Each PO_4 tetrahedron share a column and delimit two types of unconnected channels. The first type of channel has a diameter of 2.5 Å and is surrounded by four Ca^{2+} ions in each unit cell (Figure 1.8B). The Ca(I) ion is surrounded by three oxygen triangles, with two located above and below the Ca(I) ion and the third, larger triangle situated at nearly the same height along the c axis as the Ca(I) ion (Figure 1.8C). The second type of channel (diameter: 3–4.5 Å) is surrounded by six Ca(II) ions located at the periphery of the channel (Figure 1.8A). These Ca(II) ions are positioned in two dimensions at 1/4 and ¾, create alternating equilateral triangles around the helicoidal senary axis of the HA lattice (Figure 1.8D). In addition, the Ca(II) ions are coordinated with 7 oxygen (O) atoms, six of them belonging to the PO4 tetrahedra and the remaining one comes from OH^-. These OH^- ions are positioned perpendicularly to the unit cell face and present at the column's center in the second type of channel. The O atom of the OH- ion is situated 0.4 Å outside the plane of Ca(II), while its H atom is approximately 1Å away, nearly on the triangle plane of Ca(II). The OH^- ions are aligned along the c axis of the column to balance the positive charge of the HA crystal. Due to the dimensions of the two channels, Ca^{2+}, PO_4^{3-} and OH^- can exit their lattice sites and move along the tunnel in the direction of the OZ axis (Figure 1.8C). Meanwhile, the remaining vacancies can be substituted by various ions or ion clusters without changing the crystallographic structure of HA. Hence, HA is a highly non-stoichiometric compound and its Ca/P molar ratio can range from 1.50 to 1.67. The formula for non-stoichiometric HA can be expressed as $M_{10}(XO_4)_6(Y)_2$, where M, X and Y may vary [80].

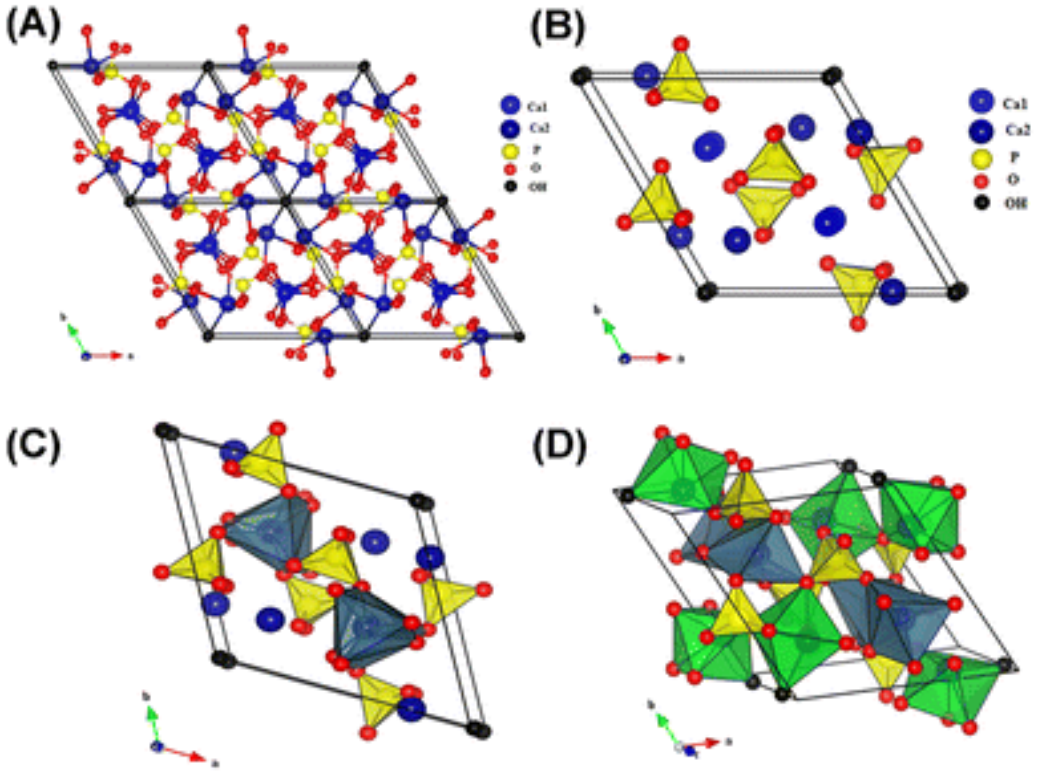

Figure 1-8: Projection of (A) unit cell of HA; (B) arrangement of [Ca(1)O_6] (C) sequence of [Ca(1)O_6] and [PO_4]; (D) sequence of [Ca(1)O_6] and [Ca(2)O_6] and also [PO_4] in the HA [81].

Besides, M ions can also include monovalent cations such as Na^+ and K^+ or trivalent cations like Eu^{3+}, while PO_4^{3-} can be replaced by CO_3^{2-} and HPO_4^{2-} and OH^- can be substituted by O^{2-}, S^{2-} and CO_3^{2-}. Numerous types of HA have been reported, but those with varying morphologies, such as plates, nanofibers, nanorods and nanotubes, are the most frequently studied. However, several synthesis factors such as pH, temperature, templates used, etc., could influence the properties of HA. For intense, HA with different morphology, size and phase composition was investigated by adjusting the pH, temperature and duration of hydrothermal treatment are shown in Figure 1.9.

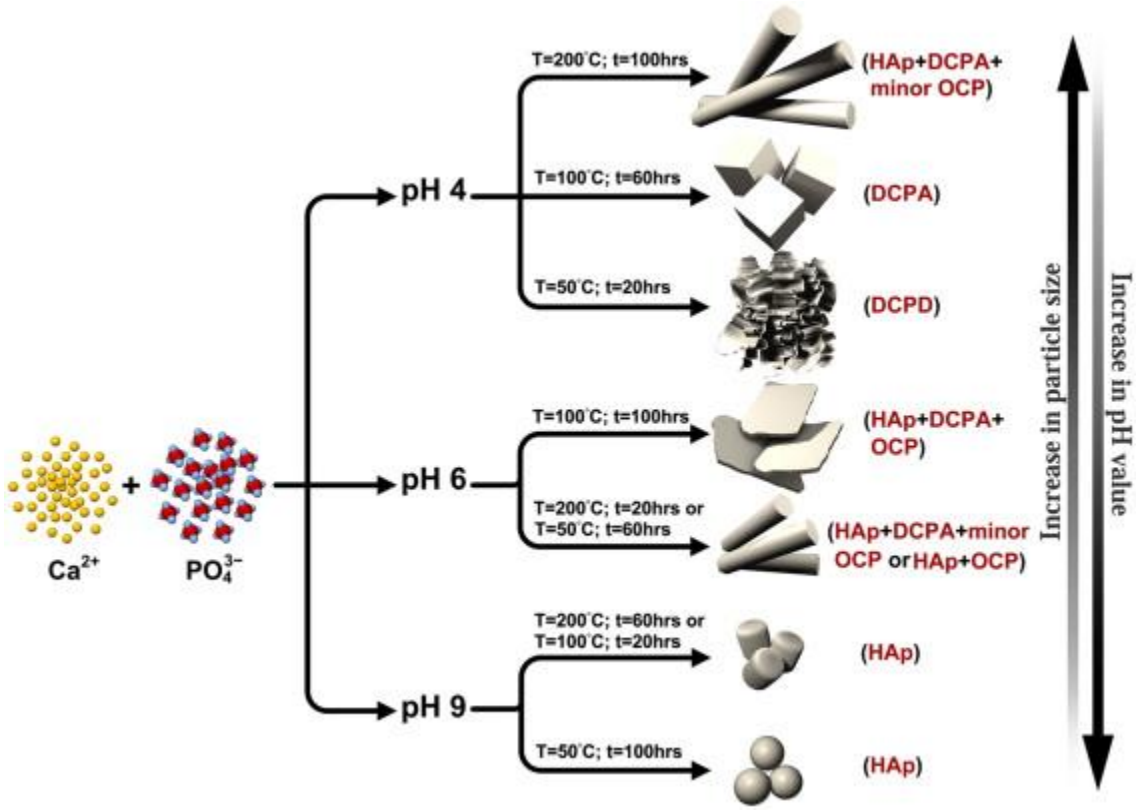

Figure 1-9: Effect of pH, temperature and duration of hydrothermal treatment on the phase, morphology and particle size of the HAP powder [82].

The stoichiometric HA is a white powder, while naturally occurring HA may have a brown, yellow, or green coloration similar to that of dental fluorosis stains. The mechanical properties of HA are influenced by various factors such as porosity, density, crystal size, sinterability and phase composition. The bending, compressive and tensile strength values of HA ceramics range from 38 to 250 MPa, 120 to 150 MPa and 38 to 300 MPa, respectively. The young's modulus of dense HA ceramics varies from 35 to 120 GPa, depending on residual porosity and impurities, while Weibull's modulus ranges from 5 to 18, reflecting the brittleness of the material. The Vickers hardness of dense HA ceramics is typically in the range of 3 to 7 GPa. The mechanical properties of HA bioceramics are strongly influenced by the microstructure and sintering ability, with densely sintered bodies having finer grains being tougher and stronger than porous ones with larger grains [83].

Hydroxyapatite (HA) has been successfully used as bone scaffolds due to its favorable biological properties such as biocompatibility, bioactivity, osteo-conduction, bioaffinity, osteointegration and osteo-induction (in certain conditions). As HA contains mainly calcium and phosphate ions, no adverse local or systemic toxicity has been observed in any study. Following implantation, newly formed bone

adheres directly to HA through a carbonated calcium-deficient apatite layer at the bone implant interface. The HA surface also supports the adhesion, growth and differentiation of osteoblastic cells and new bone is deposited through the creeping substitution from the adjacent living bone. Additionally, HA scaffolds can serve as delivery vehicles for cytokines that have the ability to bind and concentrate bone morphogenetic proteins (BMPs) in vivo [84].

The interaction between apatite and biological tissues is crucial for successful tissue regeneration. HA has demonstrated the ability to directly bond with bone and exhibits osteoinductivity. The specific mechanism behind bone induction by synthetic materials remains unclear, although factors such as microporosity, surface area, geometry and topography have been identified as important, with microporosity having a positive effect on ectopic bone formation. The biodegradation of HA occurs when the surrounding biofluids undergo changes and biomolecules are adsorbed onto the surface of the material. The physicochemical dissolution process is influenced by factors such as the surface area to volume ratio, fluid convection, acidity and temperature. The rate of dissolution is usually inversely proportional to the Ca/P ratio, purity, crystal size and surface area of the HA [85].

The degree of porosity plays a significant role in determining the bioactivity of bone scaffolds, which in turn influences the rate of bone regeneration, local environment and equilibrium of new bone at the site of repair. The pore interconnectivity, geometry, topography and porosity influence osteogenesis, which synergistically enhances the osteoconductivity and inductivity potential of bone graft. Several studies have been conducted in recent years to understand the potential of HA to induce bone growth [86].

The biological apatite is characterized by their nano-sized plate-like crystals, which are typically a few nanometers thick and a few tens of nanometers long are shown in Figure 1.10. Nano-sized HA has been widely recognized as a promising strategy to address the limitations of conventional forms, owing to their large surface area to volume ratio and unusual chemical/electronic synergistic effects. It is anticipated that nanocrystalline HA exhibits enhanced bioactivity and dissolution rates as compared to its coarser crystals. Furthermore, nanostructured biomaterials have been demonstrated to promote osteoblast adhesion and proliferation, osseointegration and deposition of calcium-containing minerals on their surface [87].

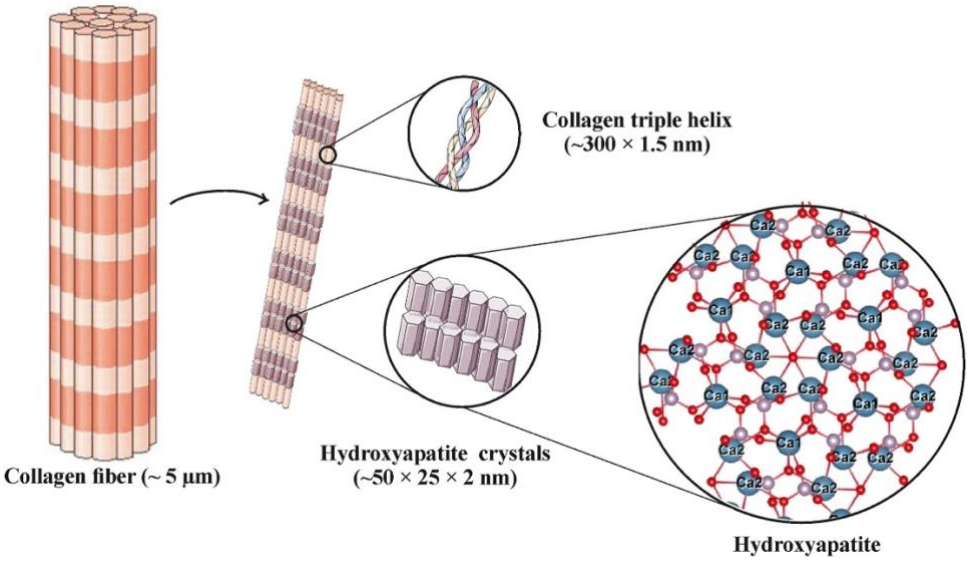

Figure 1-10: The hierarchical structure of collagen and hydroxyapatite as main constituents of bone tissue.

Furthermore, biological HA is significantly different from synthetic HA in terms of chemical composition, due to multiple ion exchanges within the local microenvironment, e.g., Mg^{2+}, Zn^{2+}, K^{+}, Sr^{2+}, Fe^{2+}, Mn^{2+}, Mo^{3+}, Cu^{2+}, Ni^{2+} and CO_3^{2-} (Figure 1.11). This doping significantly affects a lot of powder features including particle size, morphology, crystallinity, thermal stability, solubility and degradation rate. Therefore, ionic substitution during the synthesis was proposed as a valuable approach to modulate some features of HA, possibly enhancing the degradation rate and the densification by sintering to improve the mechanical properties [88].

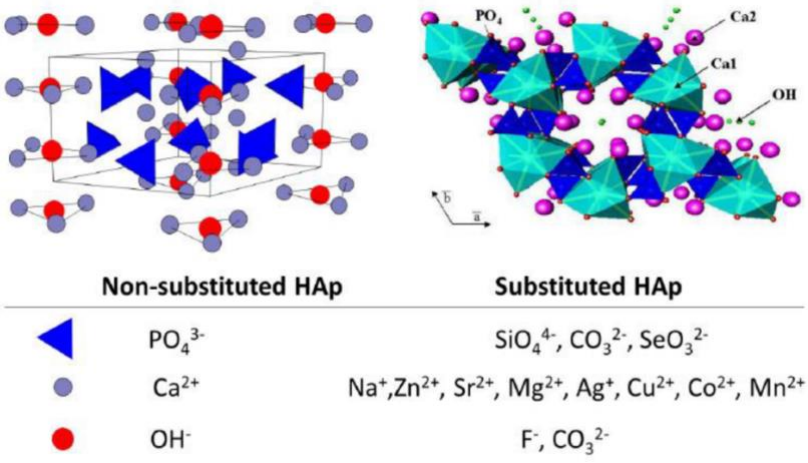

Figure 1-11: The doping of hydroxyapatite with many other ions.

1.5.2.1. Ion-Doping

To mimic the chemical composition of biological HA containing trace ions, different ions such as Mg^{2+}, Sr^{2+}, Zn^{2+}, Mn^{2+}, Fe^{2+}, Ag^{2+} and CO_3^{2-} can be engaged into synthetic HA lattice (Table 1-VII). These ions are capable to influence the crystallinity, grain size, morphology and surface characteristics of HA powders which alter the bioactivity, mechanical and solubility of HA scaffolds. Moreover, the thermal treatment of ion-doped HA frequently generates bi-phasic materials mainly composed of HA and β-tricalcium phosphate (β-TCP), inside of which foreign ions partially replace calcium ions. Overall, the presence of β-TCP in HA scaffolds enhance the degradation rate due to its higher solubility, which could accelerate bone formation and osseointegration and superior mechanical properties upon implantation compared to pure HA [89].

In particular, the Mg^{2+} and Sr^{2+} substitution into HA structure has been extensively studied due to their important role in the human body, since Mg^{2+} and Sr^{2+} ions are considered as particularly essential trace elements that are naturally found in human bones and play an important role in stimulating osteoblast differentiation and inhibiting the formation of osteoclasts [90-94].

Table 1-VII: Most common ions substitution and their influence on HA structure and biological properties of hydroxyapatite.

Ions	Role in HA Structure	Effect on Biological Interaction
Mg	Replace Ca^{2+} in lattice of HA, increased crystallinity, stabilizes the structure.	Improves bone cell adhesion, proliferation, and differentiation.
Zn	Serves as an antioxidant and guards against harm to cells.	Promotes osteoblast activity and enhance bone formation.
Sr	Replace Ca^{2+} in lattice of HA, increases solubility.	Increases bone growth and reduces resorption.
F	Substitute OH^- ions in the HA lattice and increases hardness.	Inhibits bone resorption, reduce mineralization defects, and promotes bone formation.
Si	Replace Ca^{2+} in lattice of HA, Enhances the crystalline structure of HA, reduces degradation, and enhances the mechanical characteristics.	Facilitates the process of bone mineralization and stimulates bone growth.
Fe	Plays a role in oxygen transport and electron transfer.	Enhances bone formation and wound healing.
Cu	Enables collagen formation and bone remodeling.	Facilitate bone mineralization and improve bone strength.
Mn	Participates in enzyme activation and free radical scavenging.	Stimulates osteoblast activity and bone formation.

Magnesium is recognized as the primary ion capable of replacing calcium in biological apatite at a level of approximately 1% by weight. The role of Mg^{2+} ions in bone metabolism extends beyond bone

formation, encompassing participation in biochemical reactions and regulation of bone growth and metabolism. Magnesium phosphates exhibit a higher dissolution rate compared to calcium phosphates. Mg has been demonstrated to impede the formation of crystalline minerals, such as hydroxyapatite, whereas more soluble phases, such as brushite, exhibit minimal susceptibility to Mg influence. In particular, Mg substitution with Ca in excess of 10% inhibits the precipitation of hydroxyapatite in alkaline solutions and amorphous calcium phosphate or whitlockite, the Mg polymorph of β-tricalcium phosphate, forms instead. The incorporation of magnesium into HA results in enhanced protein adsorption and cell adhesion on their surface. Moreover, Mg-HA exhibits intrinsic antibacterial activity [95, 96]. Several synthesis approaches can be implemented to obtain Mg-doped hydroxyapatite such as such as wet chemical synthesis [97], hydrothermal [98], sol-gel [99] and microwave method [100].

Strontium (Sr^{2+}) is a natural constituent of bones and teeth and have affinity with Ca^{2+} ions, thereby functioning as a calcium-mimetic entity with cells, influencing similar biochemical and cellular pathways. At low concentrations, strontium inhibits osteoclast activity, reduces bone resorption, stimulates osteoblast proliferation and enhances bone formation. Consequently, incorporating strontium into HA shows potential for locally treating bone conditions resulting from metabolic diseases, such as osteoporosis. A variety of techniques, such as the introduction of strontium salts in wet synthesis processes or using Sr-doped inorganic reactants in solid-state reactions at high temperatures, can be used to produce Sr-doped bioceramics. Replacing Ca^{2+} ions with Sr^{2+} ions in the crystal lattice of calcium phosphates typically induces lattice distortions due to the larger ionic radius of Sr^{2+} compared to Ca^{2+}. This affects the physicochemical properties of calcium phosphates; for example, Sr^{2+} ions stabilize the β-tricalcium phosphate polymorph during thermal synthesis reactions. Additionally, previous studies have suggested that strontium doping leads to mechanical reinforcement, possibly due to the increased strength of interatomic bonds within the CaPs crystal lattice compared to calcium [29].

1.5.3. HA Synthesis Methods

Recent research has focused on development of synthesis processes to control the structure, size, morphology and crystallinity of HA nanoparticles, in order to address issues such as low surface area, low mechanical strength and reduced biocompatibility and bioactivity that can impede their use in various applications. The synthesis methods of HA nanoparticles were classified as follows (Figure 1.12):

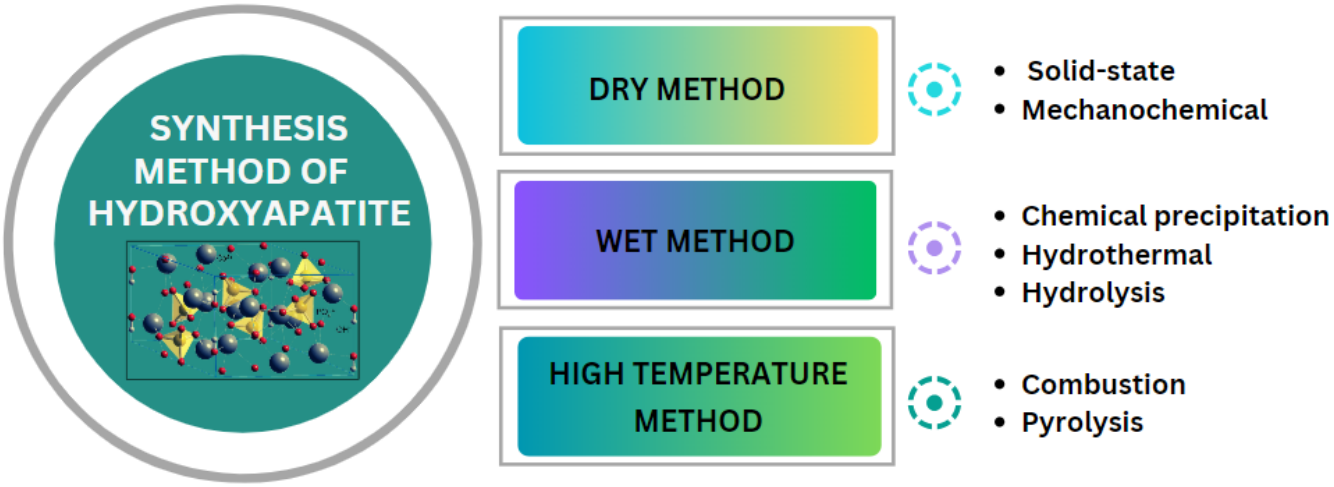

Figure 1-12: Different synthesis methods of HA nanoparticles

Wet Synthesis

Aqueous solutions of different chemicals containing phosphate and calcium ions are used to synthesize hydroxyapatite (HA) crystals via precipitation. Wet chemical processes can be performed using several technical approaches, including conventional chemical precipitation, hydrolysis, sol-gel, hydrothermal, emulsion and sonochemical methods. Wet chemical methods offer precise control over particle size and morphology and are considered the most promising techniques for producing nanoscale HA particles based on statistical analysis. Nevertheless, certain wet procedures are unsuitable for large-scale HA production due to difficulties in controlling the crystallinity and phase purity of nanoparticles, as well as the technical complexity and time-consuming details involved [101].

Dry synthesis

Dry methods, which do not involve the use of solvents, can be classified into two main categories: solid-state synthesis and mechanochemical processes. These techniques offer the advantage of producing highly crystalline HA using relatively inexpensive raw materials. However, solid-state synthesis is associated with the production of large particle sizes, while the mechanochemical process yields HA with low phase purity. Recently, the progress in the preparation of HA via dry methods, particularly solid-state synthesis, has been relatively slow [102].

Synthesis from natural sources

Over the last decade, HA has been extracted from range of natural materials, including bone waste, eggshells, exoskeletons of marine organisms, naturally derived biomolecules and bio membranes. Biogenic sources are becoming increasingly popular due to the superior physicochemical properties of

the resulting HA. However, certain materials are limited to producing HA blocks or large-sized particles, highlighting the need for additional research in this area. The field of biogenic HA production is expected to receive greater attention in the coming years [103].

High-temperature synthesis

These methods, which have the advantage of preventing the formation of unwanted CaP phases, are utilized to generate HA with excellent chemical homogeneity and high crystallinity. There are two potential approaches for high-temperature HA synthesis: the combustion method and the pyrolysis process. The combustion method has received more attention than the pyrolysis process. However, the primary drawbacks of these methods are the limited control over processing variables and the generation of secondary aggregates, particularly during pyrolysis [104].

Combination synthesis

Hybrid methods, which combine two or more distinct procedures, have emerged as new strategies for synthesizing HA nanoparticles. Combinations such as hydrothermal–mechanochemical, hydrothermal–hydrolysis and hydrothermal–microemulsion have gained attention, along with hybrids employing microwave methods. While these combination procedures have opened up exciting possibilities for improving the characteristics of HA nanoparticles, many current methods have limitations in terms of economics, performance and biological interactions. Complicated and expensive processes, diverse materials required for synthesis, aggregation and agglomeration, wide particle size distribution and various phase impurities in the crystal structure are common issues. Little effort has been made to scale up these methods or evaluate the biological interactions of the prepared nanoparticles. To address these issues, future studies should establish practical synthesis routes for use in the biomaterials industry, consider all aspects of an effective and feasible synthetic route and examine the biological characteristics of the prepared powder. Innovative and practical combinations, such as mechanochemical–solvothermal or microwave–assisted sol–gel processes, may be developed. Additionally, the synthesis of nanoparticles with new characteristics, such as novel 3D morphologies, presents an interesting challenge for future research [80, 105].

1.5.4. α-tricalcium phosphate (α-TCP)

Recently, there is a growing interest on α-tricalcium phosphate (α-TCP, α-$Ca_3(PO_4)_2$) as a potential material for various applications such as injectable hydraulic bone cements, biodegradable bioceramics and composites used in bone healing. The phase equilibrium diagram of the $CaO–P_2O_5$ system exhibits three polymorphs, namely β-TCP, α-TCP and α′-TCP, which correspond to the composition $Ca_3(PO_4)_2$. α-TCP can be synthesized by the process of heating the low-temperature polymorph β-TCP or by

thermally crystallizing amorphous precursors with appropriate composition above the transition temperature [106]. The α-tricalcium phosphate (α-TCP) phase has the potential to remain in a metastable condition at ambient temperature, with its stability range being significantly impacted by ionic substitutions. α-TCP has comparable biocompatibility to β-tricalcium phosphate (β-TCP), although has higher solubility. Moreover, α-TCP undergoes fast hydrolysis, resulting in the formation of calcium-deficient hydroxyapatite. This characteristic renders α-TCP a valuable component in the formulation of self-setting osteotransductive bone cements, as well as biodegradable bioceramics and composites used in bone healing applications [107].

The crystalline structure of α-TCP was initially recognized as being analogous to that of the mineral glaserite ($K_3Na\ (SO_4)_2$) by Dickens and Brown in 1972. Mathew et al. further investigated this relationship in 1977 and more recent studies by Yashima and Sakai have provided more insights into this subject [108]. The crystal structure of α-TCP is classified as monoclinic and it belongs to the space group P21/a. Table 1-VIII and Figure 1.13 present the cell parameters (a, b, c, α, β and γ), cell volume (V), number of formula units per cell (Z), volume per formula unit (V0), theoretical density (D_{th}) and the projections of the unit cells along the [0 0 1] direction for α-TCP and its polymorphs β-TCP and α′-TCP.

Table 1-VIII: Structural information regarding α-TCP and its various polymorphs [107].

Property	**$Ca_3(PO_4)_2$ polymorph**		
	α′-$Ca_3(PO_4)_2$	β-$Ca_3(PO_4)_2$	α-$Ca_3(PO_4)_2$
Symmetry	Hexagonal	Rhombohedral	Monoclinic
Space group	*P*6$_3$/*mmc*	*R*3*C*	*P*2$_1$/*a*
***a* (nm)**	0.53507(8)	1.04352(2)	1.2859(2)
***b* (nm)**	0.53507(8)	1.04352(2)	2.7354(2)
***c* (nm)**	0.7684(1)	3.74029(5)	1.5222(3)
α (°)	90	90	90
β (°)	90	90	126.35(1)
γ (°)	120	120	90
Z	1	21	24
***V* (nm^3)**	0.19052(8)	3.5272(2)	4.31(6)
***V*$_0$ (nm^3)**	0.19052(8)	0.1680(2)	0.180(6)
***D*$_{th}$ (g cm^{-3})**	2.702	3.066	2.866

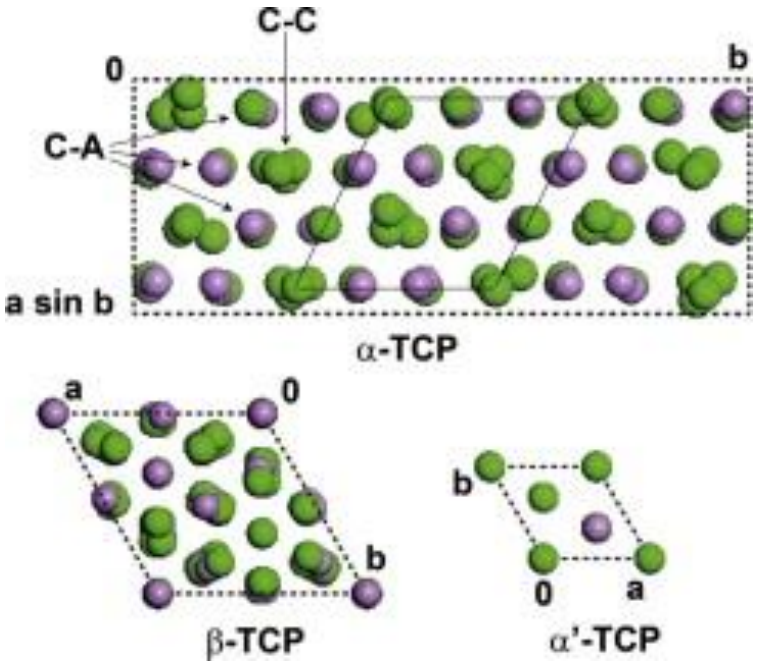

Figure 1-13: A schematic representation of the projections of the α-TCP, β-TCP and α′-TCP unit cells along the [0 0 1] direction *[107]*.

In Figure 1.14, Ca^{2+} is represented as green, whereas P^{5+} is represented as magenta. For the sake of clarity, the representation of O^{2-} has been omitted. The abbreviations C-C and C-A refer to the cation-cation column and cation-anion column, respectively. The unit cell of α-TCP has a rhombus that is inscribed with a thin solid line. This rhombus outlines a cell that is linked to the cell of hydroxyapatite. The unit cells of α-TCP and its polymorphs include Ca and PO4 ions that are arranged in columns along the [0 0 1] direction. There are two different types of columns present in α-TCP, first type referred to as C-C, exclusively consists of calcium cations. The second type, known as C-A, includes both calcium cations and phosphate anions (PO_4). Each C-C column is surrounded by six C-A columns. Additionally, a total of six C-A columns surround each C-A column, with the pattern alternating between C-C and C-A columns.

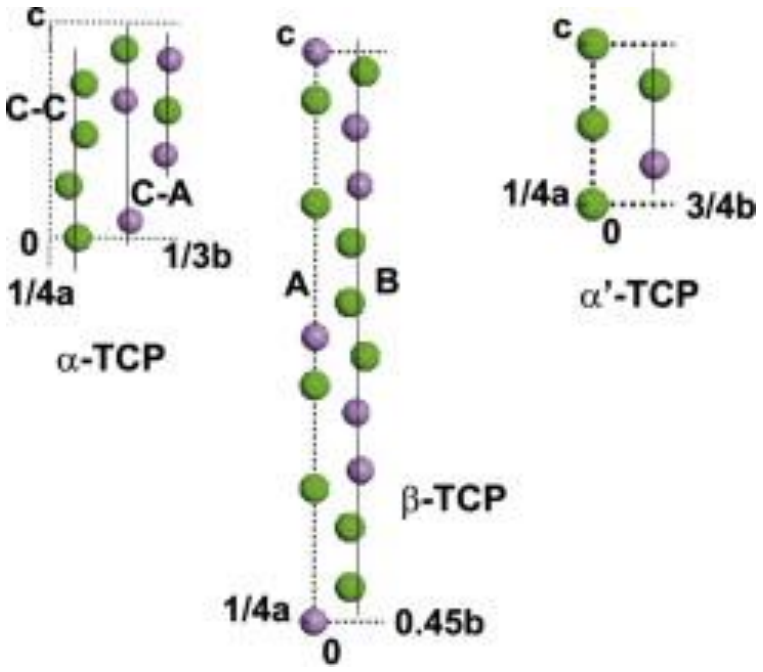

Figure 1-14: Representation of fractional projections of the α-TCP, β-TCP and α′-TCP unit cells on the bc plane, demonstrating the arrangement of component atoms in columns coordinated along the [0 0 1] direction *[107]*.

The unit cell of α-TCP, shown in Figure 1.14, has a rhombus that is inscribed with a thin solid line. This rhombus represents a cell that is closely linked with the structure of hydroxyapatite and OH columns have the potential to replace the C-C columns located at the corners of the cell. Comparatively, the Ca-PO_4 columns identified in hydroxyapatite may be regarded as highly distorted C-A "columns". Each of these columns is surrounded by three C-A columns, like α-TCP, as well as two C-C columns and one OH column [27].

The main difference in the structural composition of α-TCP and β-TCP is due to the absence of C-C columns in the latter. In β-TCP, there are two distinct categories of C-A columns. A column containing the sequence ...–P–Ca–Ca– P–... and B columns with the order ...–P–Ca–Ca–Ca–P–P–..., in this arrangement, each A column is surrounded by six B columns and each B column is surrounded by two A and four B columns. In contrast, α'-TCP is composed of alternating C-C and C-A columns, similar to the arrangement observed in α-TCP (Figure 1.14).

The α-TCP crystal structure exhibits are less densely packed as compared to β-TCP, while being more densely packed than α′-TCP. This difference is evident from the volumes per formula unit (V0) and the calculated theoretical density values shown in Table 2 for these three substances. The noted differences in packing densities across the three polymorphs may be linked to both thermodynamic factors and their

respective temperature stability ranges. Furthermore, it should be expected that, in a physiological setting, the process of dissolution and degradation of the "looser" alpha-tricalcium phosphate (α-TCP) structure occurs at more quickly compared to beta-tricalcium phosphate (β-TCP), as has been experimentally proved [109].

1.5.5. α-TCP synthesis methods

Several routes have been reported for the preparation of α-TCP [110, 111], It is usually synthesized by the thermal conversion of a precursor with a molar ratio of Ca/P approximately equal to 1.5. These precursors can be either calcium-deficient hydroxyapatite (CDHA), amorphous calcium phosphate (ACP), β-TCP or mixture of Ca and PO_4 containing reagents. The conversion process can be carried out by either using a previously obtained precursor or by a solid-state reaction of a mixture of solid precursors at elevated temperatures. In addition, self-propagating high-temperature synthesis and combustion synthesis have also been used [112].

Solid-state reaction between solid precursors is the most effective and common synthesis approach for the synthesis of α-TCP. Standard rules for solid-state reactions are followed, such as the milling of solid precursors to decrease particle size, increase contact area and mix them well. Wet milling is often the preferred method. After the milling process, a mixture of powders may be subjected to direct heating above the transformation temperature or alternatively, it can be pre-pressed to enhance the particles interaction. The suggested reaction temperatures indicated a range of 1250 to 1500°C, while the dwell period varied from 2 to 48 hours. Many studies propose the use of quenching as a preventive step against the reversion of the α-phase, despite the commonly known reconstructive nature of the first order $\alpha \rightarrow \beta$ transition and the significant observed value of the apparent activation energy for the $\beta \leftrightarrow \alpha$ transformation, which is 1.0467 MJ mol−1. On the other hand, the α-TCP synthesised often exhibited small amounts of other crystalline phases, primarily β-TCP or HA [113].

1.6. Bone Scaffolds

Scaffolds are three-dimensional structures that are designed to support and guide the growth of new tissue or organs in regenerative medicine. They provide a framework for cells to adhere, proliferate and differentiate, ultimately leading to tissue formation. Scaffolds act as temporary templates, allowing cells to repopulate damaged or missing tissue and then gradually degrade as the new tissue develops. They are essential tools in tissue engineering and regenerative medicine, offering the potential to restore function and heal various injuries or diseases [114].

Bone scaffolds are porous 3D biomaterials designed to mimic the structure and function of natural bone. Such a mimicry, in terms of chemical composition, porous structure and mechanics, should promote and facilitate the physiological processes related to new bone formation and vascularization. Therefore, bone scaffolds can play a crucial role in orthopaedic surgery by providing a bioactive framework for new bone formation, promoting tissue ingrowth and facilitating the regeneration of damaged or missing bone. It ensures a favourable environment for cell attachment, proliferation, differentiation and do not elicit adverse immune responses or toxicity when implanted in the body. Bone scaffolds should have suitable mechanical properties to withstand physiological loads during the healing process. It should provide structural support, especially in load-bearing applications, allowing for proper tissue integration and functional recovery. It should also exhibit bioactivity, which refers to its ability to stimulate and promote the attachment and growth of bone-forming cells, such as osteoblasts. Bioactive scaffolds can enhance the recruitment of osteogenic cells, trigger osteogenesis and facilitate the deposition of new bone. In addition to these essential characteristics, the scaffold's architecture and porosity are crucial considerations. The scaffold should have an interconnected pore network that allows for nutrient diffusion, oxygen supply and waste removal. The pore size and distribution should be tailored to facilitate cell infiltration and vascularization, supporting the formation of new blood vessels and promoting efficient tissue regeneration [115].

Before to figure out, what the ideal bone scaffolds requirements are, it is compulsory to understand the material and biological properties in this context. Tables 1-IX and 1-X, describe the basic material, mechanical and biological requirements that a bone scaffold must possess.

Table 1-IX: Bone scaffold requirements [116].

Biological properties	Osteogenicity: capacity of a bone scaffold to stimulate the secretion and mineralization of Extracellular matrix by bone cells and the transformation of uncommitted mesenchymal cells into pre-osteoblast lineage.
	Osteoconductivity: property of a bone scaffold characterized by a surface that is bioactive and encourages the attachment and migration of cells, in addition to their ability to penetrate the construct.
	Osteoinductivity: capability of a bone scaffold to not only maintain bone development, but to stimulate bone growth through the production of growth factors or hormones.
	Biocompatibility: the capacity of a bone scaffold to interact with the body without triggering an immunological response or rejection.
	Vasculogenic ability: the capacity of a bone scaffold to allow and/or support vasculogenesis to occur within the construct.

Material properties	Mechanical Stability: the ability of a bone scaffold to retain an appropriate structure while still possessing a final compression strength that is comparable to that of bone.
	Biodegradability: the capacity of a bone scaffold to be resorbed organically without producing harmful byproducts. In order to prevent any potential gaps in regeneration, the rate of bone degradation need to be equal to the rate of bone formation.
	Architecture: the ability of a bone scaffold to have a very open permeable structure that is linked throughout its construct. This facilitates increased cell density, nutrient/growth factor delivery within the scaffold and adhesion surface area.
	Pore size/porosity: the quality of a bone scaffold should consist of pores of a particular size and porosity percentage that are comparable to previously established guidelines. The ideal particle size is between 300 and 900 um and the total permeability is between 60 and 99%.

Table 1-X: Importance of mechanical stability in critical bone defects.

Mechanical properties	The ultimate strength of cortical bone can range nearly from 100 to 230 MPa. In order to prevent the implant from being crushed or failing, surgical fixation is necessary for any scaffold that does not meet that strength. An ideal scaffold would require compressive strength ranging from 50 to 100 MPa, tensile strength between 5 and 20 MPa, and shear strength between 2 to 10 MPa, which is comparable to that of natural bone tissue. The stiffness of the material ought to mimic that of natural bone, which generally ranges from 0.1 to 10 GPa, in order to ensure compatibility with the underlying bone and promote cell development. The degradation rate, which should be compatible with bone regeneration, ought to be 1 to 3 mm each month. Due to mechanosensory properties of bone, it is believed that a cyclically loaded scaffold will promote faster healing.
Surgical fixation	To avoid movement between the fractured ends of the bone, current bone tissue-engineered structures require surgery fixation of the extremities. This promotes the development of a callus and subsequent ossification. Screws, hardware and intramedullary nail anchors are examples of surgical fixation devices. Most of the time, metals like titanium or titanium compounds are used to make them.
Stress shielding	A condition that results from the introduction of surgical fixing devices in load-bearing bones. Metals can sustain almost all of the weight because they have a greater elasticity and compression strength than other materials. Consequently, the fractured bone is unable to detect a substantial change in mechanical activity, which results in a gradual decrease in bone density over a period.

The development of biomimetic scaffolds, bioactive molecules and stem cell delivery methods have been encouraged. Currently, there is a significant prerequisite for bone regeneration to repair the structure and functional properties of the craniomaxillofacial and spinal bone defects. There are three crucial factors such as scaffolds, cell and signalling molecules for the development of bone scaffold, need to be taken into consideration shown in Figure 1.15. The ideal bone scaffolds for bone regeneration applications must have excellent biocompatibility, as well as adequate mechanical properties and interconnected porosity help in cell growth and metabolism [117]. The usage of synthetic bone scaffolds in bone regeneration is a promising approach for craniomaxillofacial and spinal bone defects since it serves as a framework and play an important role in regeneration of defected sites by promoting biocompatibility, osteoinductivity and osteoconductivity. Various biodegradable and non-biodegradable bone scaffolds have been developed for specific craniomaxillofacial and spine defects to facilitate an appropriate biological environment [118].

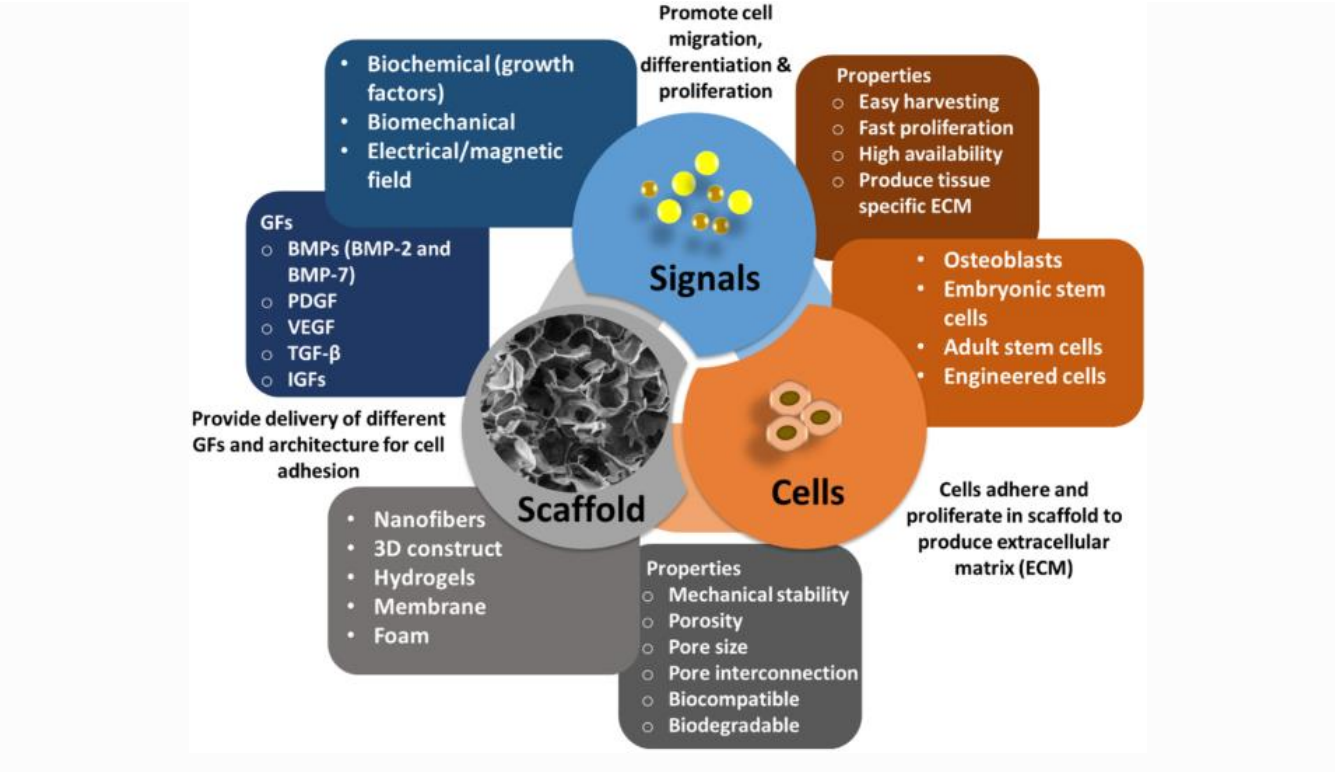

Figure 1-15: Ideal bone scaffolds requirements [31]

Bone scaffolds can be fabricated from various materials, including natural or synthetic polymers, ceramics, cements, metals, or a combination of these materials. The choice of scaffold material depends on factors such as the desired mechanical properties, biocompatibility, degradation rate and the specific application in tissue regeneration. In particular, bioceramic and bone cement with their biocompatibility

and biodegradability, offer potential advantages for these applications. They can be developed as 3D porous matrices that provide a favourable environment for bone regeneration, facilitate osseointegration and provide mechanical support until the restoration of form and function in the affected areas [119, 120] [121]. Bioceramic are mainly preferred to repair or replace damaged bone in the craniomaxillofacial (CMF) defects and bone cement is often utilized for spinal defects due to their unique properties such as self-setting ability, good injectability, moldability and increased reactivity. These cements can be injected directly into the defect site of any shape and size without any surgery and have the ability to self-harden in situ when injected, providing mechanical strength sufficient for supporting the normal physiological activities of the bone. Injectable bone-healing cements has gained significant attention due to their minimally invasive techniques [122].

1.6.1. Bioceramic scaffolds

In the last decade, bioceramics have been considered an ideal candidate for bone substitution because they exhibit excellent mechanical properties and biocompatibility, making them ideal for scaffold applications to replace dental and orthopaedic defects. Bioceramics have some extra features such as porosity, structure, composition, low thermal conductance and temperature resistance, making them suitable for medical applications [123].

One major classification of bioceramics relies on the biochemical reactions occurring between the implanted scaffold and the surrounding tissue, particularly on the increasing capacity to be resorbed upon implantation in vivo. Bioceramics can be classified as bioinert, bioactive or bioresorbable materials based on their chemical composition and their interaction with bone tissue and cells as well as biodegradability. Bioinert ceramics such as zirconia, alumina and silicon nitride are not able to interact with bone tissue or cells and thus it remains as a foreign body in biological environment. Inert bioceramics have minimal adverse reactions on bone tissue or in body after coming into contact with biological environment region. These bioceramics have low reactivity as compared to other scaffolds made by other material such as polymer, metallic and resorable ceramics. So, the biocompatibility of bioinert ceramics can be modified by surface modification, ion-doping and coating [124].

In contrast, bioactive ceramics have the ability to interact with surrounding bone tissues and cells. Among all the bioactive ceramics, bioglass, calcium phosphate and calcium silicate are considered an attractive candidate for bone regeneration applications due to their excellent bioactivity. Calcium phosphate and bio glasses are the most commonly used bioceramics for orthopedic applications due to their

osteoconductivity and osteo-stimulation properties. Bioactive glasses are composed of silicon-based material, are known to promote bioactivity. Calcium phosphate particularly hydroxyapatite are being increasingly used for orthopedic applications, due to its similar composition to human bone [123].

Bioresorbable bioceramics represent a further improvement in their long-term interaction with surrounding tissues, because in addition to their chemical similarity to the mineral component of bone, they are able to be gradually resorbed and replaced by new bone tissue over time. The in vivo behaviour of ceramic bone substitutes includes three main steps, solubility: if the compound is soluble in physiological conditions, dissolution and removal can occur; the dissolution kinetics, related to the speed at which the particular ceramic is removed from the body; and conversion into another compound via a dissolution–precipitation mechanism. Bioresorbable bioceramics are represented by calcium sulphates (Plaster of Paris) and calcium phosphates, especially with different ions doping such as Sr, Mg, Si and Zn, which can improve their biological activity [125]. However, there are some drawbacks of calcium phosphates, such as their poor mechanical strength, differences between the bone regeneration and degradation rate, inflammatory reaction of synthetic bioceramics and limited in growth due to pore size [123]. There are different types of bioceramics that are being investigated are shown in Table 1-XI.

Table 1-XI: Significant physical properties of the most common bioceramics [126].

Material	**Density (g/cm^3)**	**Tensile strength (MPa)**	**Compressive strength (MPa)**	**Modulus (GPa)**	**Fracture toughness ($MPa\ m^{1/2}$)**	**Hardness (Knoop)**
Tricalcium phosphate	3.14	40-120	450-650	90-120	1.2	N/A
Hydroxyapatite	3.1	40-300	300-900	80-120	0.6-1.0	400-4500
Bioglasses	1.8-2.9	20-350	800-1200	40-140	~2	4000-5000
SiO_2 glass	2.2	70-120	N/A	~70	0.7-0.8	7000-7500
Wollastonite glass ceramic	3.07	215	1080	118	2	N/A
Zirconia ceramics	5.6-5.89	500-650	1850	195-210	5-8	~17000
Al_2O_3	3.85-3.99	270-500	3000-5000	380-410	3-6	15000-20000
Si_3N_4	3.18	600-850	500-2500	300-320	3.5-8.0	~22000
Silicon carbide	3.10-3.21	250-600	~650	350-450	3-6	~27000

Carbon fiber	1.5-1.8	400-5000	330-360	200-700	N/A	N/A
Graphite	1.5-2.25	5.6-25	35-80	3.5-12	1.9-3.5	N/A
Glassy carbon	1.4-1.6	150-250	~690	25-40	N/A	8200

The mechanical properties of bioceramics, including compressive strength, stiffness, fracture toughness and fatigue resistance, represent the key factors for effective bone regeneration. These criteria include "static" mechanical properties (e.g., stiffness, hardness, strength), as well as "dynamic" mechanical properties (e.g., fatigue cycle resistance, crack propagation stability and fracture toughness). A major concept in defining mechanical properties of ceramics is the difference between strength and toughness. They are frequently considered to be overlapped, despite the fact that they are mutually exclusive strength is a stress representing the intrinsic capability of a material to resist to irreversible deformations, while toughness refers to the energy required to induce a fracture [127]. Toughness can also be determined using fracture mechanics methods, which determine the critical value of a crack-driving force, such as the stress intensity K, strain-energy release rate G, or nonlinear elastic J-integral, required to initiate and/or propagate a previously formed crack. However, the intrinsic brittleness of ceramics basically limits the capability to improve the toughness, primarily because they cannot be toughened by promoting plasticity [128].

The compressive strength of the human cortical bone is reportedly in the range 90–209 MPa, while the reported flexural strength is 135–193 MPa [129]. The mechanical strength of bioceramics is reported to be in the range of cortical and cancellous bones. In particular, fracture toughness is important because it refers to the ability of the scaffold to contrast the propagation of a crack defect. Hence, compressive strength and fracture toughness are relevant properties to be considered for effective bone regeneration [130]. The particle size, composition, porosity and crystallinity of bioceramics significantly affect their mechanical performance an increase of porosity and particle size leads to the decrease of mechanical properties [131]. The bone tissue exhibits outstanding mechanical performance thanks to its hierarchic structure, making it both lightweight and strong. The toughness and flexibility of bone tissue can be ascribed to the complex biomineralization of collagen fibers with apatitic crystals, associated to the multi-scale hierarchical architecture. The fracture toughness of cortical bone (K_{Ic}=2–12 MPa·$m^{0.5}$) is higher than that of ceramics. Numerous methods have been developed over time to measure the fracture toughness and hardness [132]. The low fracture toughness and poor mechanical strength of bioceramics limit their usage in load-bearing applications. Porous bone scaffolds strive to closely replicate the intricate structure of natural bone. However, a significant challenge arises due to the inherent brittleness

of ceramics, which lack plastic behavior, poses a notable limitation that researchers are actively engaged in exploring strategies to address this limitation and enhance the mechanical properties of ceramic scaffolds [129].

1.6.2. Bone cements

Low-temperature self-hardening techniques for the production of bioactive bone cement has been extensively studied for injectable orthopaedic procedures such as spinal fusion, vertebroplasty and kyphoplasty [133] (Figure 1.16). The term "cement" is a misnomer, since it often refers to a material that bonds two things together. Bone cements do not possess inherent adhesive features; rather, they depend on the establishment of a strong mechanical interlock between the rough bone surface and the prosthesis. In 1870, Themistokles Gluck used a knee prosthesis composed of ivory, which was fixed using a cement mixture consisting of plaster and colophony. Otto Rohm and Kulzer were key players in the early stages of research and development related to the physical qualities and applications of bone cement [134].

In 1958, famous English surgeon John Charnley performed the first complete hip arthroplasty using bone cement [135]. He used cold-cured polymethyl methacrylate (PMMA) to attach an acrylic cup to the femoral head and to secure a metallic femoral prosthesis. This was a significant breakthrough in the development of Orthopaedic surgical techniques. Charnley was also the first to recognise that PMMA might be used to fill the medullary canal because of its excellent compatibility with bone shape. During the 1970s, the United States food and drug administration (FDA) approved the use of bone cement in the fixing of hip and knee prosthetics. Later on, bone cement has gained great popularity for fixing prostheses to healthy bone, with significant shifts observed in the patterns of bone cement use [134, 136].

In the past few decades, vertebral fractures resulting from trauma or osteoporosis-related bone weakening have primarily been treated using vertebroplasty and kyphoplasty surgeries. However, complete spine bone regeneration remains an unresolved clinical need, primarily due to the lack of bone cements that possess optimal bioactivity, osteoconductivity and bioresorption properties.

Bone cements are commonly classified into two main categories based on their composition: those made of polymers, particularly acrylic formulations and those composed of calcium phosphates [137].

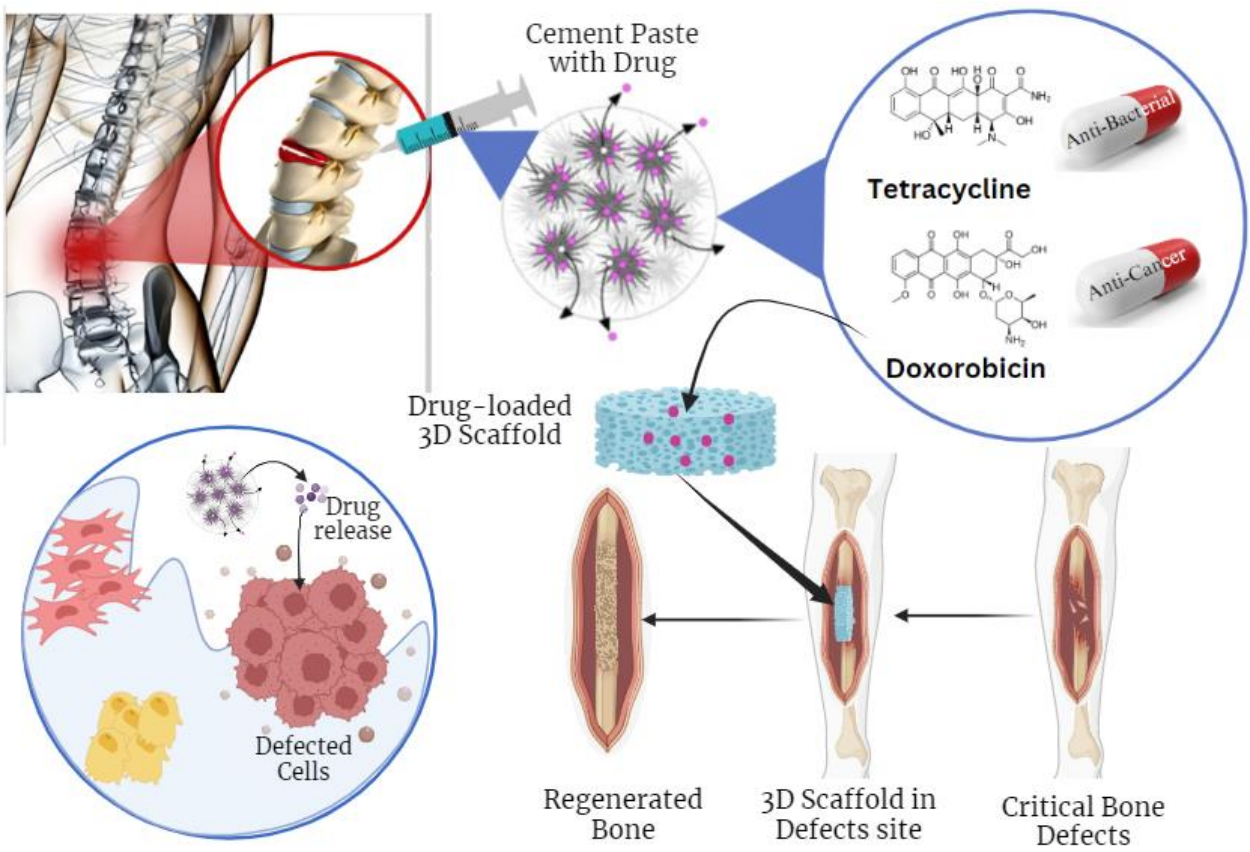

Figure 1-16: bone cement for different functions.

Acrylic bone cement, also known as (poly methyl methacrylate) (PMMA) has been extensively used to secure total joint replacement prostheses to the periprosthetic bone. The development of contemporary PMMA bone cements may be traced back to the patent by Degussa and Kulzer, (1943), who described the process of polymerization of methyl methacrylate (MMA) at ambient temperature, provided a co-initiator, such as a tertiary aromatic amine, is included [138]. Acrylic bone cement is typically composed of two distinct components: a liquid and a powder. These two components are combined in the operating room temperature until they achieve a dough-like consistency, which can then be employed to stabilize a joint replacement prosthesis or infused into damaged vertebral bodies. The primary constituent of acrylic bone cement is methyl methacrylate (MMA), which is an ester of methacrylic acid [139]. Although PMMA-based cements have favourable properties in terms of handling, setting periods and mechanical performance, but they lack osteogenic and bioresorbable properties. To address the shortcomings of PMMA cements in terms of exothermic polymerization hardening and chemical composition, Brown and Chow developed calcium phosphate cements (CPC) in the 1980s. Particularly, CPCs are a promising material due to excellent bioactivity and biodegradability and demonstrate a

physiological hardening at 37°C, while also allowing for the incorporation of biomolecules. It is in the form of powder and liquid component, upon mixing, undergoes a setting process resulting in the formation of hydroxyapatite as the primary phase and sometimes mixed with unreacted particles and other phases. They have been extensively studied, due to their desirable biological features, potential resorbability, molding abilities, simple manipulation and close resemblance to chemical composition of bone inorganic phase [140].

1.6.2.1. Calcium phosphate cements (CPCs)

Calcium phosphate bone cements (CPCs) are recognized for their in vivo self-setting ability, which makes them advantageous for use as injectable materials in minimally invasive surgeries [141]. CPCs may be classified based on a number of factors, including as the number of components present in the solid phase, the type of the setting reaction and the type of the final product shown in Table 1-XII.

Table 1-XII: Classification of CPC.

	Apatitic CPC		**Brushitic CPC**
	Single Component		Multiple Components
Reactive	α -TCP	TTCP + DCPA/DCPD	β-TCP + MCPM.MCPA
Reaction type	Hydrolysis	Acid-Base	
Reaction	$3\alpha - Ca3(PO_4)_2 + H_2O \rightarrow Ca_9(HPO_4)(PO_4)_5(OH)$	$Ca_4(PO_4)_2O + 2CaHPO_4 \rightarrow Ca_{10}(PO_4)_6(OH)$	$\beta\text{-}Ca_3(PO_4)_2 + Ca(H_2PO_4)_2 . H_20 + 7H_20 \rightarrow 4CaHPO_4 . 2H_20$

Many formulations of calcium phosphate cements (CPCs) have been developed and they may be classified into two different types depending on the resulting product: brushite (DCPD) and apatite (HA or CDHA) cements. Brushite and apatite CPCs are formed by mixing one or more calcium phosphate powders with aqueous solutions. This process leads to the dissolution of the initial calcium phosphates, followed by the precipitation of DCPD, HA, or CDHA crystals, depending on the powder compositions and the subsequent setting reactions. During precipitation process, the formation of fresh apatitic crystals occurs, which then undergoes physical entanglement. This entanglement phenomenon leads to the hardening or setting of the crystals at body temperature [133].

Apatite cements can be synthesized by the combination of single or multiple components with aqueous solutions, which then undergo hydrolysis or acid-base reactions, respectively [142]. Calcium-deficient hydroxyapatite (CDHA) is the final product in the first case, whereas stoichiometric hydroxyapatite (HA) is the final result. Some examples are shown below:

Hydrolysis of metastable α-TCP:

$$3\ \alpha\text{-}Ca_3(PO_4)_2 + H_2O \rightarrow Ca_9(HPO_4)(PO_4)_5(OH)$$

The acid-base reaction occurs between tetra calcium phosphate (TTCP), which has basic properties and di calcium phosphate anhydrous (DCPA) with acidic characteristics:

$$Ca_4(PO_4)_2O + CaHPO_4 \rightarrow Ca_5(PO_4)_3(OH)$$

Brushite CPC is synthesized by an acid-base reaction involving tricalcium phosphate (TCP), which is almost neutral and monocalcium phosphate monohydrate (MCPM), which is acidic:

$$\beta\text{-}Ca_3(PO_4)_2 + Ca(H_2PO_4)_2{\cdot}H_2O + 7H_2O \rightarrow 4\ CaHPO_4{\cdot}2H_2O$$

The liquid-to-powder ratio (LPR) and the particle size of the initial powder are two crucial elements that significantly influence the final CPCs features are shown in Table 1-XIII. The setting time, injectability, cohesion, mechanical characteristics and porosity of harder calcium phosphate cements (CPCs) are also influenced by LPR ratio. The setting time, as defined by ISO/DIS 18531 for CaPs, refers to the time from the start of the blending process of powdered agent and liquid agent to the hardening of the cement. This parameter significantly affects the clinical viability and injectability of both apatite and brushite cements. The final surface morphology of brushite or apatite crystals and the total porosity of the final scaffolds are influenced by both particle size and the liquid-to-powder ratio (LPR). These factors have an impact on the mechanical performance, resorbability and overall bioactivity of the scaffolds [143]. The decrease in the particle size of calcium phosphates (CaPs) leads to an increase in the surface area, which in turn influences the reaction kinetics, which results in the formation of small needle-shaped crystals, as compared to larger plate-shaped crystals that are frequently observed when larger CaP precursor particles are used. Furthermore, porosity can be related to the amount of liquid phase used. Consequently, an increase in LPR leads to a decrease in the amount of liquid phase, resulting in an increase in porosity. This effect of LPR shows the difference between brushite and apatite cement in relation to microstructure porosity. Specifically, the consumption of water during the setting reaction of brushite cement is greater than that of apatite cement, resulting in the formation of larger crystal sizes. Consequently, the total porosity of brushite cement is reduced, while the average pore size is increased compared to apatite

cements. The porosity of calcium phosphate cement (CPC) is usually within the range of nano- to sub-micrometer sizes. This porosity enables the flow of physiological fluids through the cement's microstructure. However, the size of these holes is insufficient to support the formation of bone tissue. Consequently, porogens are often used to address this limitation [140].

Table 1-XIII: Influence of particles size and liquid/powder ratio on the particle's morphology and pore size distribution *[95]*.

	Particle Size		**Liquid-to-Powder Ratio**	
	Fine Particles	Coarse Particles	Low L/P	High L/P
Final crystal morphology	Needle-like crystals	Plate-like crystals	Low inter-aggregate distance	High inter-aggregate distance
Pore size distribution	Fine	Coarse	Fine	Coarse

As mentioned above, increasing porosity causes mechanical strength to decrease, thus it is necessary to find a compromise between mechanical performance and porosity level.

Various modifications have been researched and applied to injectable CPCs in order to improve both their physicochemical, mechanical and biological properties for clinical applications, as illustrated schematically [122] in Figure 1.17.

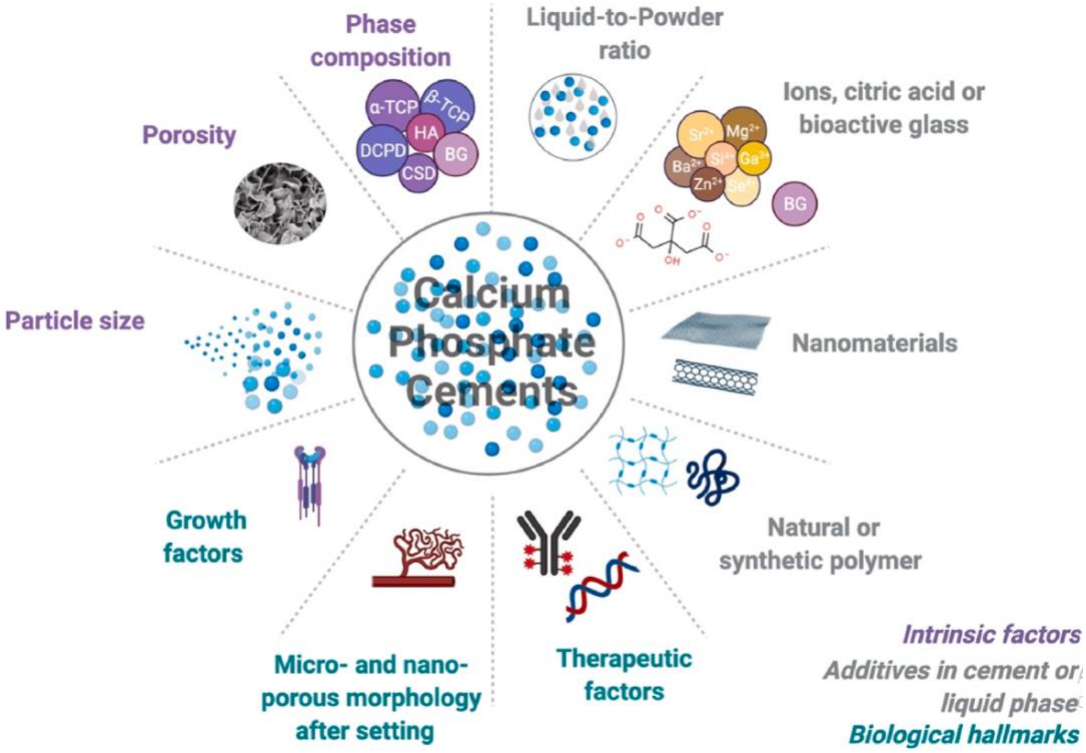

Figure 1-17: Brief overview of the improvement approaches put forward for calcium phosphate cements *[122]*.

The combination with polymeric and additives solutions has been extensively studied to improve their cohesiveness and injectability while maintaining adequate mechanical properties and setting time. Chitosan, a natural amino polysaccharide, has been used to modify the physical properties of CPCs, including injectability, setting time, rheology and in vivo bioactivity. Other natural polymers such as sodium alginate, collagen, gelatine, hyaluronic acid and cellulose derivatives such as methylcellulose (MC), (hydroxypropyl methylcellulose (HPMC) and carboxy methylcellulose (CMC)) have also been utilized as liquid phases for CPC formation. These additives have been shown to improve the mechanical properties and degree of CPC bioactivity. Indeed, the addition of various additives to CPCs has been shown to improve their physicochemical and biological properties [144], making them more suitable for clinical applications. For example, the addition of glycerol has been shown to improve the injectability and workability of CPCs, while strontium carbonate has been used to enhance their osteo-inductive properties. Polyethylene glycol (PEG) has also been utilized to improve the cohesion and setting time of CPCs and the addition of a foaming agent has been shown to promote the formation of interconnected pores within the cement, which can be beneficial for bone regeneration. β-dicalcium silicate has also been investigated as an additive to improve the mechanical properties and bioactivity of CPCs [145].

Overall, the addition of various additives and biopolymers has allowed for the customization and optimization of CPCs for specific applications, bringing them closer to clinical use in orthopaedics [146]. One of the primary limitations hindering the clinical use of CPCs refers to their poor mechanical properties, hence restricting their applicability to situations with mild or non-load-bearing requirements. Some commercial bone cements developed by α-TCP are listed in Table 1-XIV. The detail physio-chemical and biological properties of α-TCP-based bone cements are discussed in previous reviews [147-149].

Table 1-XIV: Commercial bone cements developed using α-TCP.

Brand name	Manufacturer	Powder composition
Calcibon®	Biomet, Europe	α-TCP + DCP + CC + PHA
Norian SRS®	Norian, USA	α-TCP + CC + MCPM
Mimix®	Biomet, USA	α-TCP + TTCP
MCPC	Biomatlante, France	α-TCP + ACP + BCP
Cementek®	Teknimed SA, France	α-TCP + TTCP
Biopex®	Mitsubishi Materials Co., Japan	α-TCP + TTCP + DCPD + HAp
Callos™	Skeletal Kinetics, USA	α-TCP + CC + MCPM

1.6.2.2. Drug Delivery

One notable benefit of CPCs is its ability to self-harden at room temperature. This characteristic, when combined with its inherent porosity, enables the incorporation of drugs, biologically active compounds and cells, resulting in the development of drug delivery materials. A significant advantage of using CPCs as a carrier of active substances is their non-exothermic setting reaction, which is beneficial for temperature-sensitive drugs. Typically, drug loading strategies for implanted materials involve incorporating drugs into the material before fabrication, trapping drugs into basic drug carriers such as nanoparticles and adding them to the implantable material, immersing the scaffold into a drug solution, physically adsorbing drugs onto the material, or coating the scaffold in a polymeric or composite solution. CPCs have been used to deliver anti-cancer drugs since the 1990s (Figure 1.18) [150]. The rate at which the drugs are released is dependent upon the functionalization, microstructure and resorbability of the CPCs matrix.

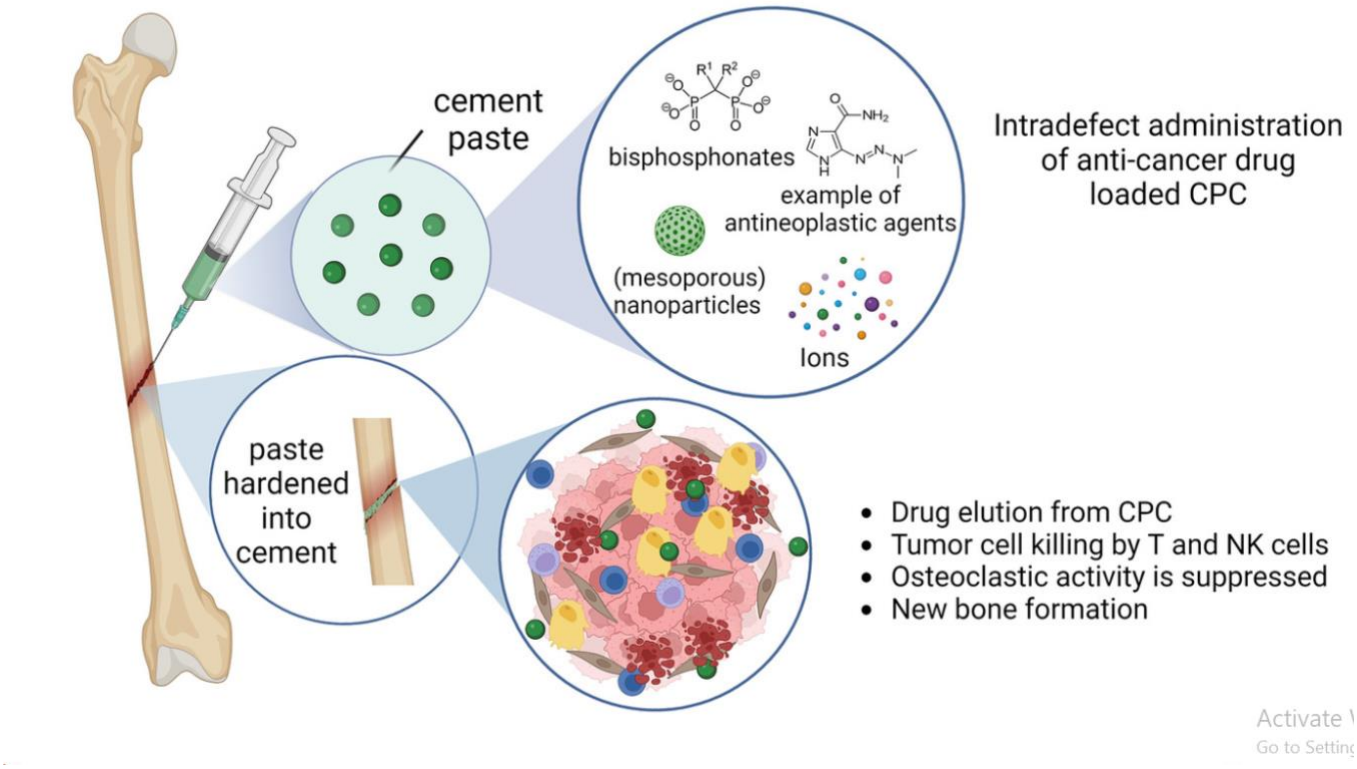

Figure 1-18: Apatite cement for drug delivery.

Drug incorporation in CPCs can occur through various methods, such as mixing the drug in the powder phase, dissolving it in the liquid phase, or editing the cement with microencapsulated drug forms. If the drug is to be incorporated in the liquid phase, it must be soluble in it. For instance, in the study by Ginebra et al., a water-soluble meth acrylamide, poly(4-HMA), was used as a model drug. However, in most cases, the drug is mixed with the cement powder during the powder phase incorporation method. The use of microparticles as drug delivery vehicles offers another advantage, as it can prolong the lifetime of the delivery system and reduce the initial burst release of the drug [151].

Drug release kinetics can be categorized based on how the drug elution is regulated. These categories include diffusion, adsorption-desorption, breakage of chemical bonds and materials erosion. In diffusion-controlled release, the drug is integrated into a matrix material, which is typically non-biodegradable or degrades more slowly than the release of the drug. On the other hand, chemical processes control drug release when the drug is integrated into a biodegradable material, which is connected to the kinetics of the material degradation. The drug solubility, microstructure and porosity of the material also significantly affect drug release. Increased porosity typically leads to increased drug release, while any

changes to the pore structure during the elution period can ultimately impact the overall release pattern [152].

1.7. Fabrication methods for bioceramic scaffolds

Several processing techniques to prepare bone scaffolds with complex shapes and morphology have been proposed and described in literature, including replica method, sacrificial template and direct foaming method [153]. In addition, 3D printing was proposed as effective method for the preparation of scaffolds with controlled morphology and porosity [154]. All these processes involve the precise manipulation of slurries, whose flow behaviour is highly affected by the content of solid particles and their degree of agglomeration. The viscoelastic properties and state of dispersion of such colloidal systems are related to attractive and repulsive forces between the surface of the particles [155].

1.7.1. Preparation of bioceramic slurries

A comprehensive rheological characterization of bioceramics-based slurries is highly desired, as smart and precise adaptations to the process conditions are mostly required. In this respect, the inter-particle repulsion can be considered as main actor in tuning the flow behavior of slurries. Furthermore, other factors greatly affect the rheology of bioceramic slurries, including the calcination temperature, the powder content, the amount of dispersant agents and ion-doping for bioceramics [156].

Ionic substitution during synthesis is also a valuable approach to modulate some features of slurries. These ions are capable to influence the crystallinity, grain size, morphology and surface characteristics of bioceramic material powders which alter the bioactivity, mechanical and solubility of scaffolds [89, 157-159]. In this context, the development of stable and fully injectable slurries for 3D printing technology still represents a big challenge.

Additive manufacturing process could be the most promising technique to have the potential to manufacture bulk bioceramic scaffolds having 3D complex shapes through carefully controlling the extruded material. In particular, the preparation of ceramic suspensions with adequate rheological properties for extrusion-based 3D printing requires a careful optimization of the physical characteristics of bioceramics and various process parameters such as zeta potential, viscosity and elastic modulus [160, 161].

1.7.2. Porous bioceramic scaffolds

Tailored porosity in materials allows for the emergence of a wide range of desirable qualities and features that are not possible in conventionally dense materials. Many processing techniques were developed for

preparing porous ceramics and they have been the subject of substantial research over the last several centuries for a number of different applications. Because of the extreme difficulty in mimicking natural bone qualities, artificial bone replacements are among the most demanding applications [162]. Because of its high biocompatibility, capacity to facilitate new bone formation and adhesion and near resemblance to the inorganic element of bone, hydroxyapatite (HA) is commonly regarded as the material of choice for bone and tooth regeneration [163]. While several scaffold development methods have been studied so far, producing HA scaffolds with a pore structure that mimics bone and appropriate mechanical strength is still difficult. Partial sintering, sacrificial fugitives, replication patterns and direct foaming are the classic methods described in the literature for developing microporous ceramics are showed in Figure 1.19 [78].

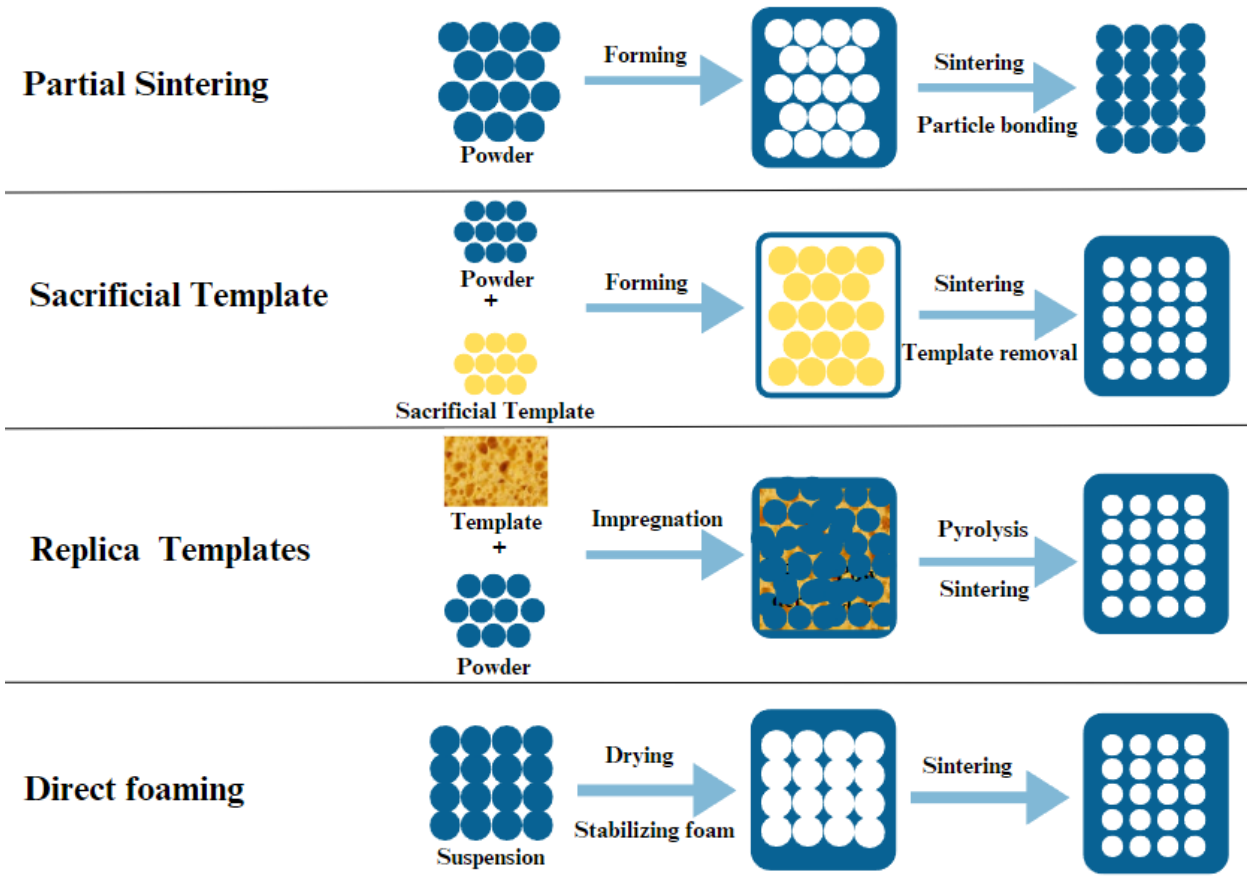

Figure 1-19: Different processing techniques for the development of porous bone scaffolds

Partial sintering

For decades, the gold standard method for producing porous ceramics has been the partial sintering of powder compact. A homogeneous porous structure is produced when sintering is stopped before the material has fully densified as a result of the high-temperature thermal treatment inducing surface diffusion or evaporation-condensation reactions. The pore size and porosity may be modified by altering the starting powder size and the level of partial sintering.

Sacrificial fugitives

The sacrificial template method typically involves preparing a biphasic composite out of a continuous ceramic powder matrix as well as a dispersed sacrificial stage that is first uniformly distributed across the matrix before being removed to produce pores within the microstructure. The amount of agents' present determines the degree of porosity. This method is very helpful for achieving a high degree of open porosity.

Replica Templates

The Replica method was the first technique utilized to create macroporous ceramics. In this method, a ceramic suspension is impregnated into a polymeric cellular structure to create a macroporous ceramic with the same shape as the original template. Because of its adaptability and ease of implementation, this strategy has been found to be very effective. The rheological properties of the ceramic solutions (shear-thinning), the inclusion of binders or plasticizers in the prior suspension to prevent the strut breaking during pyrolisis and the ultimate thermal treatment factors (like heating rate and high temperature) are all crucial features that must be carefully regulated and controlled. Thus, one drawback of this approach is that, after thermal treatment, the struts often crack, drastically reducing the mechanical effectiveness of the structure.

Direct foaming

The direct foaming technique, in which a gas (such as air) is incorporated into a ceramic solution before drying and sintering, has been described as a simple and low-cost procedure that can provide pore volumes in the range of 40-97%. Directly foamed ceramics have a total porosity that is directly related to the volume of gas introduced into the foaming suspension or liquid medium. However, the stability of the wet foam just before setting determines the pore size.

The mechanical strength of cellular structures prepared by direct foaming is typically much greater than that achieved by conventional template-based approaches, mostly because of the drastically decreased incidence of flaws in the cell struts. Because of the large gas-liquid interface present in liquid foams, these systems are unstable from a thermodynamic viewpoint. Destabilization of wet foams occurs from a number of physical processes that work together to lower the free energy of the whole system. The main processes of destabilization are known as drainage, coalescence and Ostwald ripening. Drainage is the physical separation of the gaseous and liquid phases of the foam due to the force of gravity, with the lighter gas bubbles rising to create a denser foam layer on top and the heavier liquid phase accumulating at the bottom [31].

When the thin films produced by drainage are insufficiently stable to keep contacting cells apart, the result is the connection of nearby bubbles, which is known as coalescence. The stability of the thin films is determined by the attractive and repulsive interactions between the bubbles (Fig. 1.19d). Coalescence is facilitated by attractive van der Waals forces and may be prevented by introducing steric and/or electrostatic repulsion between the interacting bubbles. While foams may be tailored to minimize drainage and coalescence processes, the Ostwald ripening phenomena can eventually occur, leading to system destabilization due to the Laplace pressure difference between bubbles of various sizes. The coarsening process may be slowed by the adsorption of surfactants and biomolecules at the gas-liquid interface, which reduces the interfacial energy [162].

3D-Printing

Additive manufacturing technology can develop customized scaffolds that are highly desired to repair damaged tissue [164]. Among various additive manufacturing techniques, selective laser sintering, stereolithography, 3D printing and direct-ink writing are the most commonly used for the development of bioceramic scaffolds [165, 166]. These fabrication methods are generally categorized as powdered-based and suspension-based. In powdered-based methods such as 3D printing and selective laser sintering, bioceramic particles are spread over a printing bed and locally bonded by a binder and laser, while in suspension-based methods such as stereolithography and direct-ink writing, fine bioceramic particles are dispersed in a liquid phase to form paste or ink [167]. Among these techniques, direct ink writing is faster and cost-effective where the complete process, including fabrication, drying and sintering can be done within a day [168]. It involves extrusion of water-based suspension with high ceramic powder content, layer by layer from moving nozzle, that has a capacity to maintain its physical

integrity and support its weight without distortion (Figure 1.20). However, the challenge is to develop a ceramic slurries that is well suited for deposition process, with shear thinning behavior and capacity to retain its structure after extrusion [169]. Slurries must have high rigidity and fluid-like consistency during passing through narrow nozzle. Generally, 50 wt% to 60 wt% of powder content is used for slurry preparation, this high powder content prevents crack formation in scaffolds during drying and sintering. Slurries should have a tailor viscoelastic characteristic (homogenous) to favor the continuous flow through narrow nozzle, while maintaining strength of extruded slurries. However, surface of ceramic particles can be modified by dispersing agents to prevent aggregation in slurries. The most popular dispersing/binding agent used in direct ink-writing is methylcellulose-based binders that are nonionic and promote the shear-thinning behavior [170].

Direct ink writing has been considered as one of the most extensively investigated techniques for the development of bioceramic scaffolds for bone regeneration applications. A wide range of structures for bioceramic scaffolds have been successfully fabricated and subjected to both in-vitro and in-vivo testing. The versatility of the direct ink writing technique is a fascinating feature, enabling the printing of a wide array of bioceramics that range from calcium phosphates and bioactive glasses to calcium silicates. Particularly, this technique provides precise control over lattice arrangement, pore dimensions and pore orientations. Furthermore, it offers the advantage of cost-effective operation, enhancing its appeal as a versatile and efficient fabricating method [164].

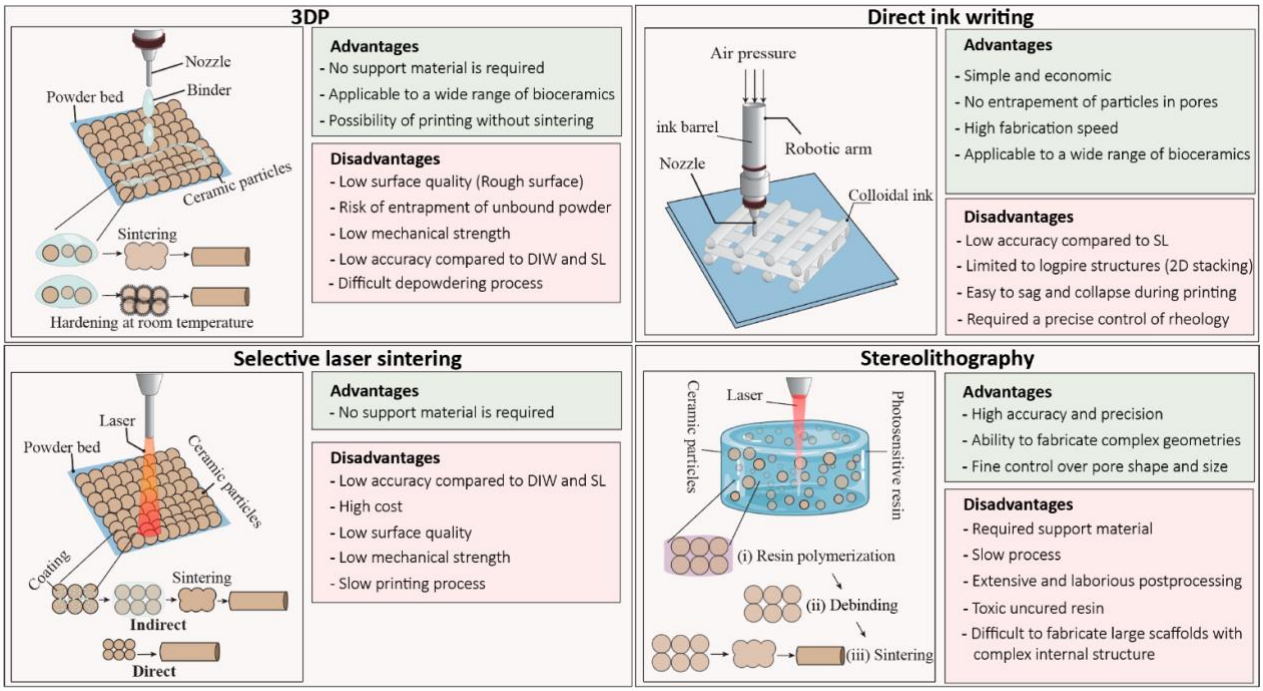

Figure 1-20: Schematic diagram of common additive manufacturing techniques including 3D printing (3DP), stereolithography (SL), direct-ink writing (DIW) and selective laser sintering (SLS) for the development of 3D bioceramic scaffolds.

Despite the excellent bioactive properties of bioceramics, the major disadvantages of them are their low mechanical strength and fracture toughness due to brittleness. These features typically restrict their use to non-load bearing bone applications.

However, several approaches have been developed to improve the mechanical properties of bioceramics [95]. The accurate processing of toughened bioceramic composites involves many steps, from raw materials to the semi-finished processing, including the synthesis of powders, controlled drying, calcination, the debonding of organic components, the addition of second phases and thermal sintering. The intrinsic features of the ceramic powders significantly influence each physical (e.g., density, porosity), microstructural (e.g., shape of grains, grain size, grain boundaries), mechanical (e.g., strength, hardness, toughness, resistance to fatigue failure,) and chemical (e.g., dissolution, hydrolysis) property of the final bioceramic composite scaffold [171].

A promising approach for the toughening of bioceramics is the addition of fibers into the matrix. The manipulation of fibers can be performed by the solution powder mixing technique to prepare polymer–carbon composite materials or biomimetic mineralization to improve the biocompatibility and bone inductivity [172].

The preparation of bioceramic powders involves several approaches, classified into dry and wet chemical methods. The formulation technique has a significant impact on surface characteristics, powder morphology, stoichiometry and crystallinity. Dry methods involve three main types of chemical reactions: thermal decomposition, oxidation/reduction and solid-state reactions. In contrast, various methods can be used for the liquid or wet reaction of bioceramic powders such as hydrothermal synthesis, precipitation, liquid drying and sol–gel synthesis [173]. The preparation of bioceramic powders, in particular hydroxyapatite, mainly involves wet chemical methods, especially hydrothermal synthesis and solid-state reactions [174].

Essential criteria for the effective preparation and reinforcement of bioceramic scaffolds are the homogeneous mixing of the matrix and reinforcement phase and a controlled particle size distribution to optimize the packing density of particles while avoiding agglomeration.

The consolidation of bioceramic scaffolds is modulated by thermal treatments capable of improving the interactions among the particles. Sintering is a high-temperature treatment that can compact the ceramic particles of a pre-shaped green body or powder to consolidate a solid structure [175]. The major goal of sintering is densification; fine and uniform microstructure and bioceramics are typically sintered at temperatures ranging from 500 to 1200°C. The high temperature of sintering provides adequate energy to force material transport processes such as the migration of grain boundaries via the diffusion of atoms or evaporation–condensation phenomena, with the aim of reducing the superficial energy of ceramic particles and eliminating the pores. The sintering can be performed in different atmospheres, including inert gas or air [176].

Semi-finished processing techniques for bioceramic composites involve a myriad of techniques, including hand layup, spray up, injection molding, resign transfer molding, compression molding, filament winding and pultrusion, according to the type of filler (particles, whiskers and fibers) [177]. A recently reported approach also explored the possibility to increase the toughness of bioceramics by introducing a large and controlled density of dislocations, thus leading to local plasticity [178]. It was observed that conventional sintering, the standard densification method for ceramics, actually yields ceramics virtually free of dislocations and dislocation sources. In other words, the brittleness of ceramics appears as merely a consequence of the established conventional production method.

1.8. Toughening Strategies for bone scaffolds

The brittleness of calcium phosphate based bioceramics and cement, significantly limits their applications because in addition to strength, adequate toughness is required to sustain the biomechanical loads. Any crystallographic defect or irregularity within the crystal structure represents the main cause for dislocations, the mechanisms of which are related to the Peierls–Nabarro (PN) barrier energy that defines the fracture toughness of a material. Metals contain mobile dislocations, leading to local plasticity and desirable toughness, while ceramics are characterized by the immobility of dislocations and low fracture toughness, especially at room temperature. In this respect, the high-strength ionic bond typical for ceramic structures plays a crucial role, limiting atomic slip systems [179].

The mechanical properties of bioceramics and bone cement can be improved by including additional biocompatible phases. The dispersion of bioceramics secondary phase such as fibers, whiskers and particles improves their toughness and also affects their inflammatory response [177]. The homogenous distributed secondary phase enhances the integration with bone tissue, hence lowering inflammation by minimising the accumulation of stress and the start of cracks. Non-homogenous dispersion, however, might result in particle irritation and activation of macrophages, followed to initiate the inflammatory reaction [180].

The mechanisms for increasing the toughness of ceramics can be classified as either intrinsic or extrinsic. Intrinsic toughening is primarily related to plasticity, that is, enlarging the plastic zone, mainly against the initiation of a crack. Conversely, extrinsic toughening acts to limit an initiated crack, reduce the stress and strain fields at the crack tip, preventing further opening, including crack bridging by fibers or ductile phases in composites. A significant increase of flexural strength, flexural modulus and fracture toughness of ceramic dental composites was also reported through the addition of zirconia-silica (ZS) or zirconia-yttria-silica (ZYS) nanofibers (2.5 wt % or 5.0 wt %). Bioceramic composites made from HA and TZP (tetragonal zirconia polycrystal) powders coated with Al_2O_3 also exhibited significantly higher strength and fracture toughness, due to the integration of ZrO_2 (15 vol %) and Al_2O_3 (30 vol %) [181].

The microstructural and mechanical changes of Al_2O_3 matrixes, after the incorporation of Cr_2O_3, was also studied, resulting in improved hardness and elastic modulus, while fracture toughness deteriorated with the addition of 2 mol % Cr_2O_3 particles. It was also reported that Zr–Ti–Nb–Cu–Be glasses containing 42–67 vol % dendrites exhibited 100–160 MPa$\sqrt{m}$ toughness at tensile yield strengths of 1.1–1.5 GPa. A monolithic and amorphous Pd–Ag–P–Si–Ge glass alloy with 1.5 GPa tensile strength and

200 MPa·m0.5 toughness properties was also recently reported; its properties were a result of the generation of shear band after loading, which resembles large-scale plasticity. Nevertheless, it has drawbacks related to critical processing and production costs [182]. Moreover, researchers produced novel dental restorative composites by using hydroxyapatite whiskers. They reported that the efficiency of reinforcement depends on the filler morphology. Hydroxyapatite has good wettability with polymer which leads to increased toughness in comparison to nano-size HA powder [182].

The mechanical performance of bioceramics and cement are closely related to several factors, including microstructure, chemical composition, ionic impurities and structural defects. The strategies to improve the toughness or fracture strength of ceramics refer to the capacity to control or limit the propagation of cracks along the powder particles and grains. Several methods have been reported to improve the toughness of ceramics, including crack-bridging, crack-deflection, microcrack-induced toughening, generation of phase transformations and reduction of the defect size (Figure 1.21).

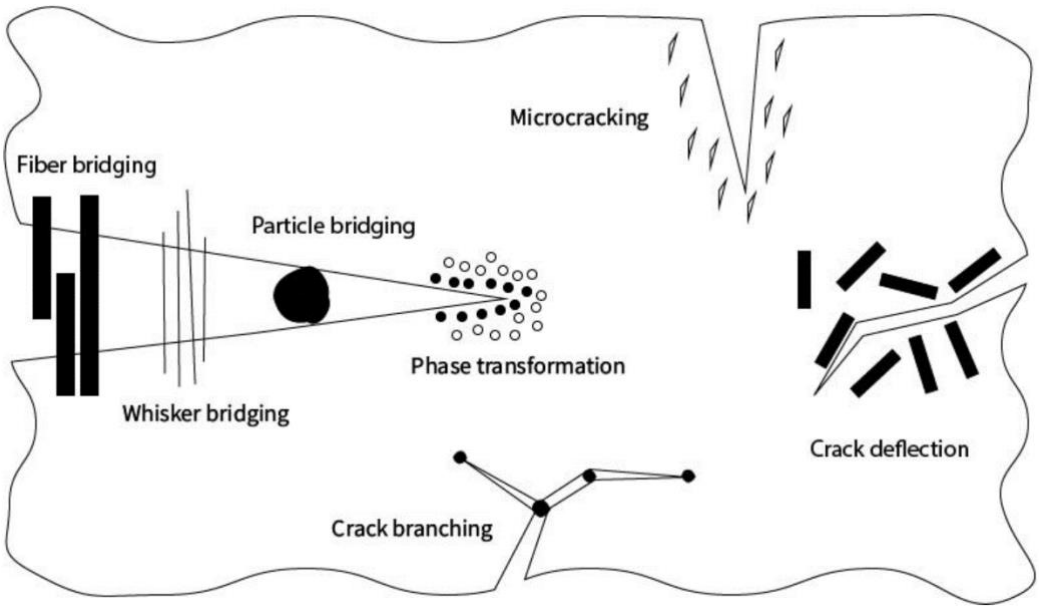

Figure 1-21: Different strategies to improve the toughness of bioceramics and cements *[123]*.

Moreover, the basic scaffold structure can be combined with polymer coatings, or interpenetrating polymer-bioactive ceramic microstructures can be formed to improve the toughness of the ceramic as a simple and effective approach.

1.8.1. Phase Transformation

Toughening phenomena related to phase transformation are well known for zirconia-containing composites, where the phase transition from the tetragonal to monoclinic phase is the essential mechanism behind the enhanced toughness of zirconia used for the development of dental and orthopedic implants. This approach is based on stress induced phase transformations, which are mainly responsible for microstructural additional compressive stresses during the propagation of cracks, which increase the crack growth resistance KIc [183].

Similar to precipitation hardening, the stabilization of particles in a metastable and thermodynamically unfavorable state requires overcoming an energy nucleation barrier. In this case, the modulation of particle volume can be achieved by the application of adequate tensile stress at the crack tip. Phase transformation is initiated by the presence of sufficiently large elastic energy. As the particle was metastable prior to the transformation, the decrease in stress due to an increase in volume does not hamper the process of transformation. Moreover, compressive stress in radial direction and tensile stress in circumferential direction around a particle are superimposed to the external load during the transformation. These compressive residual stresses may result in the reduction of stress on the crack and hence may partially or completely close the crack. In addition, as the tensile stress is applied in circumferential direction around a particle it can generate microcracks, further leading to the dissipation of energy [184].

The stress induced transformation is also related to the free enthalpy reduction. The addition of hydrostatic tensile stress strongly decreases the enthalpy of the phase with a larger volume. This, in turn, increases the driving force for the transformation, enabling the particle to overcome the nucleation barrier [185].

1.8.2. Defect Size Reduction

The main limitation of calcium phosphate material' is mechanical properties related to their brittleness. Ceramics generally exhibit higher compressive strength than tensile strength, essentially due to limitations in stress concentrations and crack propagation when micropores are flattened instead of dilated. Bioceramics are characterized by very limited strain to failure and toughness, compared with ductile material counterparts (e.g., metals, polymers). Tensile stress could cause a fracture to propagate through the material, often causing failure in ceramic material. Many defects can occur during the

production, finishing and application of ceramic because of the foreign particles, porous regions, or large grain sizes. A great research effort has been dedicated to the design of ceramic microstructures with increased toughness and damage tolerance. In this context, the reduction of defect sizes can also be obtained by the incorporation of various ions such as nickel, silver, tantalum and strontium. Some requirements for reducing the size of defects include an efficient, fast and reliable fine grinding, a compact design and the versatility of the process [78].

The fracture mechanics of bioceramics and cement is mainly affected by the powder particle size distribution. Grain size is usually tuned towards monomodal or multimodal distributions, in order to increase the packing density of particles. It was reported that the largest grain may control the size of largest flaw. Alternatively, grain size can be measured at the fracture origin. The microstructure is affected by multiple factors (e.g., powder impurities, thermal treatments of powders, sieving size), complicating the possibility to understand the role of each factor. This methodology has been in use for the production of ceramics to obtain a more homogenous microstructure [29].

1.8.3. Crack Deflection

The propagation of cracks in bioceramics and cement is a critical issue that can cause sudden failure of large structures. Crack deflection can be used as a strategy to increase the toughness of bioceramics. Some local areas in the bioceramics and cement exhibit low resistance to crack propagation, resulting in crack deflection. In particular, when a crack is deflected, the surface of the crack increases, leading to more energy required for crack propagation and an increase of fracture toughness. The prediction of a crack path as the crack approaches a fiber can be based on an energy criterion or a stress criterion. Young's modulus mismatches are also reported as mechanisms of crack deflection. The microstructural paths for crack propagation in bioceramics and cement generally reflect the grain boundaries [186].

The evaluation of crack deflection by disks, rods and spheres showed that (1) increased toughness as a result of crack deflection is dependent on particle shape and volume fraction and is independent of particle size; (2) a rod-shaped morphology is the most effective, followed by disk and sphere, for increasing the toughness. An increase in volume fraction of up to 20% increases the toughness, however, very little increase was observed with a higher volume fraction. The toughness significantly increases when using rods compared to toughness without deflecting particles. Another cause of crack deflection is partial bridging by grains, occurring when a grain/whisker causes the deflection of a crack around it, hence leaving the grain/whisker to bridge the crack. Interactions between crack bridging and crack

deflection in silicon nitride containing rod-shaped grains and whiskers toughened alumina were observed, demonstrating that crack deflection is crucial for the development of crack bridging [187].

1.8.4. Microcrack Formation and Crack Branching

Stress-induced microcrack formation and crack branching represent irretrievable deformation phenomena associated with energy dissipation. Microcracks appear to debond at a poorly bonded matrix particle interface. The stress energy near the tip of the fracture can result in the formation of micro cracks at weak areas in the calcium phosphate material, for example, due to the undesired orientation of grain boundaries. It was observed that a microcrack can decrease crack resistance at the macrocrack tip, which encourages crack progression. The microcrack's effect on fracture propagation can be examined in two ways: energy dissipation owing to microcrack generation and change in local stress intensity factor by simulating the interaction of microcracks with the main cracks. The crack shielding phenomena has a role in microcrack toughening because of two aspects: the material's lower elastic modulus as a result of microcracking and the microcracking-induced dilatation [188].

1.8.5. Crack Bridges Formation

A variety of reinforcing phases can improve the fracture toughness of bioceramic and bone cement composites. The reinforcement in this case bridges the crack surfaces that effectively pins the crack and increases resistance for any further extension of the crack. It was observed that these reinforcing phases bridge the crack in the region behind the crack tip. When the two opposing crack surfaces interact during crack propagation, an increase in energy dissipation occurs during the propagation of a crack. This behavior was observed in coarse-grained microstructures with intercrystallite crack propagation. Different varieties of ceramic whiskers (high-strength crystals with length/diameter ratios of 10 or more), particulates, or fibers can be added to the matrix material of the host in order to generate a composite that can improve fracture toughness. This reinforcement strategy relies on two different mechanisms: (i) the presence of additional particles or fibers represents a deflection stimulus for opening cracks, against its propagation; (ii) in case of weak bonds between the matrix and reinforcement phase, crack propagation energy can be absorbed by pulling out the fiber from its original location, thus preventing crack propagation by forming a bridge in a crack and holding the two face together [189].

Particles

Crack bridging is generally induced by the addition of particles that can confer ductile behavior (e.g., particles with lower Young's Modulus), as in this condition, additional work is required to achieve deformations and crack propagation. Moreover, the addition of ductile particles in bioceramics or cement can also significantly increase their fracture toughness by forming crack bridging behind the crack tip via a discontinuous but strong reinforcing second phase that imposes a closure force on the crack. The mathematical description of non-linear fracture processes and stress transfer across cracks was proposed in the Dugdale–Barenblatt model, useful for estimating the effect of particles addition in increasing toughness. This model encounters the behavior of crack extension when intersecting the particles: the primary crack propagation is impeded by particles, thus retarding its interaction with the surrounding cracks [190].

The doping of HA with strontium-doped particles can improve the mechanical properties. The compressive strength was improved from 50 MPa to 66.57 MPa up to 5 mol % Sr/(Sr + Ca) doping. The incorporation of Sr^{2+} in HA lattice replaces Ca^{2+} with Sr^{2+} and form a $Ca10{-}nSrn(PO_4)_6(OH)2$ (Sr-HA). This decreases the crystallization size and crystallization rate of HA and changes the lattice constant [191].

The addition of titanium particles was also proposed as a promising approach to improve the mechanical properties. Titanium and its alloys are considered as some of the most attractive and important materials due to their unique properties, such as high tensile strength, resistance to body fluid effects, flexibility and high corrosion resistance. They exhibit a unique combination of strength and biocompatibility, which makes them suitable for biomedical applications. Commercially pure titanium (Ti) is prominent in dental implants and Ti-6Al-4V is dominant in orthopedics applications [192].

Whiskers

A whisker is a single crystal in the form of a fiber. Whiskers can be considered as a sub-group of random fibers, possessing shorter lengths compared to conventional fibers. They are defect free and thus stronger and stiffer than fibers. Due to these properties, there is a more pronounced difference in the mechanical properties of a whisker when compared to bulk materials. Materials are crystallized on a very small scale for the production of whiskers. Internal alignment within each whisker is observed to be extremely high.

The processes that cause toughening in whisker-reinforced ceramics are considered to be fundamentally similar to those in ceramic matrix reinforced with aligned continuous fibers [193].

Nanosheets

Recently, regenerative medicine focused on nanosheets applications owing to their excellent biocompatibility and unique mechanical and physicochemical properties. Two-dimensional (2D) structures of nanosheets (e.g., 1–100 nm thickness) are characterized by a large surface-to-volume ratio, ultrathin structure and enhanced mechanical strength, which can be substituted with a large number of functional biomolecules. They express a greater ability to interact with polymers through hydrophobic interaction, Van der Waals force, physical adsorption and electrostatic attraction. The mechanical strength and biocompatibility of scaffolds can be improved by combinations of nanosheets with ceramics polymers [194, 195].

Nanosheets are categorized into monolayered hydroxide nanosheets (MLDHs), polymeric nanosheets, metallic nanosheets and nonmetallic nanosheets. Metallic and non-metallic nanosheets are used for tissue engineering. They have desirable features for tissue engineering, such as biocompatibility, mechanical strength and photothermal and colloidal stability. Molybdenum disulfide (MoS_2), manganese dioxide (MnO_2) and magnesium phosphate ($MgPO_4$) are frequently used metallic compounds, while the commonly used non-metallic components include graphene (GN), graphene oxide (GO) and black phosphorus (BP) [196, 197].

Graphene oxide nanosheets (GOns) have improved mechanical ability, a large surface-to-volume ratio, protein adsorption and biocompatibility, all of which are important properties required in tissue engineering. Surface roughness, protein absorption, hydrophilicity and cell adhesion can be improved by adding extracellular matrix (ECM) components such as Col and HAp to the above nanostructured composites [198].

Molybdenum disulfide (MoS_2) nanosheets exhibit excellent mechanical properties, including 300 GPa Young's modulus, a tensile strength of over 23 GPa and excellent elasticity. Graphene nanosheets are mostly used to strengthen HAp scaffolds. After nanosheets were incorporated into the scaffolds, the elastic modulus of the composite was increased by 40% to 141 ± 8.50 GPa and the fracture toughness was increased by 80% to 1.06 ± 0.03 MPa [199]. Plasma spray was used to create a graphene nanosheet (GNS) reinforced HA on Ti6Al4V substrate. The resulting GNS/HA composite coating has increased

strength and toughness, with ~32.3% and ~54.7%, increases in fracture toughness and indentation yield strength, respectively. The composite coating's improved strength and toughness were attributed to synergetic toughening and strengthening mechanisms such as load transfer, graphene nanosheet (GNS) pull-out, GNS inter-layer sliding, crack branching and GNS bridging. Moreover, the frequent crack deflection when a crack comes into contact with GNS could tailor the trade-off between strength and toughness through crack branching and GNS bridging [200].

Fibers

Fibers in ceramic matrix composites (CMC) help increase the fracture toughness, due to their excellent mechanical properties. Different types of fibers on the basis of length, i.e., particulates and fiber network, continuous fibers and short fibers, can be used for the processing of ceramic matrix composites. For bridging by brittle short fibers, an increase in interfacial shear forces is observed until it either causes the particle to break or debond from the matrix [201]. This interfacial debonding, when followed by the subsequent frictional pulling out process, has a great impact on the toughness of the material. Hull and Clyne (1996) expressed the fracture energy related to fibers pull-out with the following formula:

$$\Delta G_{PULL-OUT} = \int_0^l \frac{N\pi r x^2 \tau_i}{l} dx = \frac{V_f l^2 \tau_i}{3r}$$

where G represents the interfacial shear strength, r is fiber radius, l is pull-out length and N is the number of fibers per unit area.

In bioceramics or cement, the mechanism for fiber reinforcement involves fiber bridging the crack after its appearance due to stress, impeding its further propagation. Furthermore, the frictional sliding of fibers against the matrix during pullout further consumes the applied force that results in increased fracture toughness. The addition of different types of fibers (e.g., carbon, e-glass, aramid and polyglactin) increased the strength of bioceramics or cement and resulted in an increase of approximately two orders of magnitude in the fracture work [202].

Carbon fibers are the preferred choice among researchers compared to all other types of fibers due to their high strength-to-weight ratio, thermophysical properties, sorption and high elastic modulus. Carbon fibers are crystalline filaments of carbon that have a regular hexagonal pattern of carbon sheets. Moreover, due to their inherent biocompatibility (in vivo and in vitro), they are extensively used in the

production of artificial heart valves, purulent wounds, in the treatment of bone fractures and for making bio composites. Carbon fibers are produced by high temperature conversion during the pyrolysis of carbon-rich precursors [203].

The fracture toughness of bioceramic or cement composites can be increased by adding carbon fibers. A 300% increase in fracture toughness of alumina-single-walled carbon nanotubes (SWCNTs) composites was reported [204]. In another report, a 69% improvement in fracture toughness for silica-CNT composites by loading only 0.05 wt % CNTs was obtained [205]. A significant increase in the fracture toughness of $BaTiO_3$-CNTs composites was described when loading 0.5, 1 and 3 wt %, respectively [206]. Wang also reported a moderate improvement of 15% for ZrB_2-SiC-multi-walled carbon nanotube (MWCNT) nanocomposite (2 wt %) [206]. He successfully manufactured composites comprising of micrometer-sized carbon fibers (CFs) and also made biocompatible nanocrystalline calcium hydroxyapatite that contained carbon fibers by 1.0, 2.0 and 5.0 wt %. Moreover, he reported the manufacturing of a HA-carbon fiber composite via hot pressing by using high temperature, pressure and argon atmosphere. The resulting composite had improved fracture toughness and strength [207]. In another instance, the microabrasion resistance of carbon fiber based reinforced and non-reinforced hydroxyapatite was worked on. Commercial grade Hap and carbon fibers were used by hot pressing. The researchers used a temperature of 1000–1150°C and 25 MPa pressure with 15 min pressing time in an argon atmosphere. Most researchers have used the microhardness indentation method to measure fracture toughness (KIc) of carbon-based bioceramic or cement composites due to the small sample sizes [208].

A chemical treatment performed to activate the fiber surface to improve the adhesion adhesion with surrounding matrix concerned the conditioning of the fibers surface, using molecules such as carboxylic acid, sulfuric acid, nitric acid, alkali, formaldehyde and isocyanate [209, 210].

The main drawbacks associated with the use of fiber-reinforced bioceramics or cement include the tendency of fibers to agglomerate due to their high Van-der-Walls forces of interaction among carbon particles and light weight and the low interfacial adhesion between the fibers and the matrix. This tendency to agglomerate has obstructed their application in various fields. In this context, surface functionalization/modification processes that can reduce this agglomeration tendency and increase the fiber–bioceramics interfacial adhesion through covalent or ionic bonding were proposed [207]. Several functionalization strategies were reported for fibers, including wet oxidation (oxidation using potassium

permanganate, hydrogen peroxide, sulfuric acid, nitric acid, etc.), dry oxidation (oxidation by using plasma, air, ozone, etc.), surface adsorption and encapsulation [211].

The oxidation of carbon fibers can be carried out in both wet and dry conditions. Strong acids, such as H_2SO_4, HNO_3 or a mixture of the two with a strong oxidant, i.e., $KMnO_4$, is used for the wet oxidation of CFs and ozone or reactive plasma is used for the oxidation of CFs in dry conditions. Wet oxidation is the most cost-effective process for the surface modification of CFs. A few studies have indicated that the addition/activation of some functional groups on CF surface favors the bonding between material and carbon fibers; in particular, defects caused by oxidants on the surface of carbon fibers are stabilized by bonding with hydroxyl (-OH) or carboxylic acid (COOH) [211, 212].

1.9. References

1. BLOG, F.A. *What Are The Functions Of The Skeletal System?* 2019; Available from: https://www.firstaidforfree.com/what-are-the-functions-of-the-skeletal-system/.
2. Everts, V., et al., *The bone lining cell: its role in cleaning Howship's lacunae and initiating bone formation.* Journal of Bone and Mineral Research, 2002. 17(1): p. 77-90.
3. Jerome, C., B. Hoch, and C.S. Carlson, *Skeletal system*, in *Comparative Anatomy and Histology*. 2018, Elsevier. p. 67-88.
4. Barnabas, J. and P. Raj, *The human body: A digital twin of the cyber physical systems*, in *Advances in Computers*. 2020, Elsevier. p. 219-246.
5. Frontera, W.R. and J. Ochala, *Skeletal muscle: a brief review of structure and function.* Calcified tissue international, 2015. 96: p. 183-195.
6. Hossain, M.A., *Significance of the structure of human skeleton.* American Journal of Medical Science and Medicine, 2018. 6(1): p. 1-4.
7. Carretero, J.M., C. Lorenzo, and J.L. Arsuaga, *Axial and appendicular skeleton of Homo antecessor*. Journal of Human Evolution, 1999. 37(3-4): p. 459-499.
8. Black, J.D. and B.J. Tadros, *Bone structure: from cortical to calcium.* Orthopaedics and Trauma, 2020. 34(3): p. 113-119.
9. Buckwalter, J. and R. Cooper, *Bone structure and function.* Instructional course lectures, 1987. 36: p. 27-48.
10. El-Ganzuri, M.A., R.R. Ahmed, and E.M. Bastawy, *Regulatory Mechanisms of Bone Development and Function.* International Journal, 2015. 3(9): p. 280-303.
11. Clarke, B., *Normal bone anatomy and physiology*. Clinical journal of the American Society of Nephrology, 2008. 3(Supplement 3): p. S131-S139.
12. Feng, X., *Chemical and biochemical basis of cell-bone matrix interaction in health and disease.* Current chemical biology, 2009. 3(2): p. 189-196.
13. Zhao, X., et al., *Carbon fiber reinforced hydroxyapatite composites with excellent mechanical properties and biological activities prepared by spark plasma sintering.* 2020. 46(17): p. 27446-27456.
14. Mohamed, A.M.J.T.M.j.o.m.s.M., *An overview of bone cells and their regulating factors of differentiation.* 2008. 15(1): p. 4.
15. Hadjidakis, D.J. and I.I.J.A.o.t.N.Y.a.o.s. Androulakis, *Bone remodeling.* 2006. 1092(1): p. 385-396.
16. Bosch, P., et al., *Osteoprogenitor cells within skeletal muscle.* Journal of Orthopaedic Research, 2000. 18(6): p. 933-944.
17. Bonewald, L.F., *Osteocytes as dynamic multifunctional cells.* Annals of the New York Academy of Sciences, 2007. 1116(1): p. 281-290.
18. Caetano-Lopes, J., H. Canhao, and J.E. Fonseca, *Osteoblasts and bone formation.* Acta reumatológica portuguesa, 2007. 32(2): p. 103-110.
19. Boyle, W.J., W.S. Simonet, and D.L. Lacey, *Osteoclast differentiation and activation.* Nature, 2003. 423(6937): p. 337-342.
20. Setiawati, R., P.J.O. Rahardjo, and b. regeneration, *Bone development and growth.* 2019. 10.
21. Sensiate, L. and H.J.S.r. Marques-Souza, *Bone growth as the main determinant of mouse digit tip regeneration after amputation.* 2019. 9(1): p. 9720.
22. Robling, A.G. and C.H. Turner, *Mechanical signaling for bone modeling and remodeling.* Critical Reviews™ in Eukaryotic Gene Expression, 2009. 19(4).

23. Saasen, A. and J.D.J.A.R. Ytrehus, *Rheological properties of drilling fluids: use of dimensionless shear rates in herschel-bulkley and power-law models.* 2018. 28(5): p. 201854515.
24. Roberts, W.E., S. Huja, and J.A. Roberts. *Bone modeling: biomechanics, molecular mechanisms, and clinical perspectives*. in *Seminars in orthodontics*. 2004. Elsevier.
25. Maruyama, M., et al., *Modulation of the inflammatory response and bone healing.* 2020. 11: p. 386.
26. Furuhata, M., et al., *Real-time assessment of guided bone regeneration in critical size mandibular bone defects in rats using collagen membranes with adjunct fibroblast growth factor-2.* 2021. 16(4): p. 1170-1181.
27. Dimitriou, R., et al., *Bone regeneration: current concepts and future directions.* 2011. 9(1): p. 1-10.
28. Roddy, E., et al., *Treatment of critical-sized bone defects: clinical and tissue engineering perspectives.* 2018. 28: p. 351-362.
29. Gui, X., et al., *3D-printed degradable hydroxyapatite bioactive ceramics for skull regeneration.* 2023. 2(2): p. e41.
30. Thavornyutikarn, B., et al., *Bone tissue engineering scaffolding: computer-aided scaffolding techniques.* 2014. 3: p. 61-102.
31. Chen, Y., et al., *Recent developments of biomaterials for additive manufacturing of bone scaffolds.* 2020. 9(23): p. 2000724.
32. Kanwar, S. and S.J.B. Vijayavenkataraman, *Design of 3D printed scaffolds for bone tissue engineering: A review.* 2021. 24: p. e00167.
33. Kinoshita, Y. and H.J.T.S.W.J. Maeda, *Recent developments of functional scaffolds for craniomaxillofacial bone tissue engineering applications.* 2013. 2013.
34. Krishani, M., et al., *Development of scaffolds from bio-based natural materials for tissue regeneration applications: A review.* 2023. 9(2): p. 100.
35. Prasadh, S. and R.C.W.J.O.S.I. Wong, *Unraveling the mechanical strength of biomaterials used as a bone scaffold in oral and maxillofacial defects.* 2018. 15(2): p. 48-55.
36. Prévôt, M. and E. Hegmann, *From biomaterial, biomimetic, and polymer to biodegradable and biocompatible liquid crystal elastomer cell scaffolds*, in *Advances in Bioinspired and Biomedical Materials Volume 2*. 2017, ACS Publications. p. 3-45.
37. Aghali, A.J.C., *Craniofacial bone tissue engineering: current approaches and potential therapy.* 2021. 10(11): p. 2993.
38. Huang, M.F., et al., *The use of patient-specific implants in oral and maxillofacial surgery.* 2019. 31(4): p. 593-600.
39. Petrovic, V., et al., *Craniofacial bone tissue engineering.* 2012. 114(3): p. e1-e9.
40. Ha, S.H. and J.Y. Choi, *Restoration of Facial Bone Defect using Patient-Specific Implant.* J Craniofac Surg, 2022. 33(7): p. 2063-2066.
41. Brunski, J.B.J.I.J.o.O. and M. Implants, *Biomaterials and biomechanics in dental implant design.* 1988. 3(2).
42. Cai, H., et al., *3D printing in spine surgery.* 2018: p. 345-359.
43. Zheng, X., et al., *Gelatin/gentamicin sulfate-modified PMMA bone cement with proper mechanical properties and high antibacterial ability.* 2022. 9(3): p. 035405.
44. Hendricks, B.K., et al., *Operative anatomy of the human skull: a virtual reality expedition.* 2018. 15(4): p. 368-377.
45. Anderson, B.W., M.W. Kortz, and K.A. Al Kharazi, *Anatomy, head and neck, skull.* 2018.
46. Costello, B.J., et al., *Regenerative medicine for craniomaxillofacial surgery.* 2010. 22(1): p. 33-42.

47. Elsalanty, M.E., D.G.J.C.t. Genecov, and reconstruction, *Bone grafts in craniofacial surgery.* 2009. 2(3-4): p. 125-134.
48. Ricalde, P. and T.A. Turvey, *History of craniofacial surgery in the United States: the role of the oral and maxillofacial surgeon.* Journal of Oral and Maxillofacial Surgery, 2018. 76(9): p. 1842-1846.
49. Pape, H.-C. and M.J.J.o.o.t. Bottlang, *Flexible fixation with locking plates*. 2011, LWW. p. S1-S3.
50. Hamdy, R.C., J.S. Rendon, and M.J.B.r. Tabrizian, *Distraction osteogenesis and its challenges in bone regeneration.* 2012. 8: p. 177-204.
51. Ingawale, S. and T.J.A.o.b.e. Goswami, *Temporomandibular joint: disorders, treatments, and biomechanics.* 2009. 37: p. 976-996.
52. Haben Fesseha, M.J.O.R.O.J., *Bone grafting, its principle and application: A review.* 2020. 1: p. 43-50.
53. Haglin, J.M., et al., *Patient-Specific Orthopaedic Implants.* 2016. 8(4): p. 417-424.
54. Schieker, M., et al., *Biomaterials as scaffold for bone tissue engineering.* 2006. 32: p. 114-124.
55. reportlinker. 2023; Available from: https://www.reportlinker.com/p06422337/Global-Craniomaxillofacial-Devices-Market-Size-Share-Industry-Trends-Analysis-Report-By-Material-By-Application-By-Product-By-Regional-Outlook-and-Forecast.html?utm_source=GNW.
56. Dewey, M.J. and B.A.J.R.a. Harley, *Biomaterial design strategies to address obstacles in craniomaxillofacial bone repair.* 2021. 11(29): p. 17809-17827.
57. Oryan, A., et al., *Bone regenerative medicine: classic options, novel strategies, and future directions.* 2014. 9(1): p. 1-27.
58. Song, T., Z.-Y. Qiu, and F.-Z.J.F.o.M.S. Cui, *Biomaterials for reconstruction of cranial defects.* 2015. 9: p. 346-354.
59. Wang, W. and K.W.J.B.m. Yeung, *Bone grafts and biomaterials substitutes for bone defect repair: A review.* 2017. 2(4): p. 224-247.
60. Raheem, A.A., et al., *A review on development of bio-inspired implants using 3D printing.* 2021. 6(4): p. 65.
61. Bogduk, N.J.H.o.c.n., *Functional anatomy of the spine.* 2016. 136: p. 675-688.
62. Rahman, S. and J.M. Das, *Anatomy, head and neck, cervical spine*, in *StatPearls [Internet]*. 2021, StatPearls Publishing.
63. Ginebra, M.-P., et al., *Bioceramics and bone healing.* EFORT open reviews, 2018. 3(5): p. 173-183.
64. Deyo, R.A. and W.R.J.S. Phillips, *Low back pain: a primary care challenge.* 1996. 21(24): p. 2826-2832.
65. Sabino, J. and J.N.J.C.r.i.m.m. Grauer, *Pregnancy and low back pain.* 2008. 1: p. 137-141.
66. Evans, L., et al., *The role of spinal surgery in the treatment of low back pain.* 2023. 218(1): p. 40-45.
67. Mobbs, R.J., et al., *The utility of 3D printing for surgical planning and patient-specific implant design for complex spinal pathologies: case report.* 2017. 26(4): p. 513-518.
68. Martz, E.O., et al., *Materials and design of spinal implants—a review.* 1997. 38(3): p. 267-288.
69. Oppenheimer, J.H., I. DeCastro, and D.E.J.N.f. McDonnell, *Minimally invasive spine technology and minimally invasive spine surgery: a historical review.* 2009. 27(3): p. E9.
70. McAfee, P.C., et al., *Minimally invasive spine surgery.* 2010. 35(26S): p. S271-S273.
71. Baliga, S., K. Treon, and N.J.A.J.A.s.j. Craig, *Low back pain: current surgical approaches.* 2015. 9(4): p. 645.
72. Medtronic. 2002; Available from: https://global.medtronic.com/xg-en/e/response/infuse-bone-graft.html.
73. Suamte, L., et al., *Various manufacturing methods and ideal properties of scaffolds for tissue engineering applications.* 2023. 1: p. 100011.
74. Burg, K.J., S. Porter, and J.F.J.B. Kellam, *Biomaterial developments for bone tissue engineering.* 2000. 21(23): p. 2347-2359.

75. Malhotra, A. and P.J.T.i.b. Habibovic, *Calcium phosphates and angiogenesis: implications and advances for bone regeneration.* 2016. 34(12): p. 983-992.
76. Punj, S., J. Singh, and K. Singh, *Ceramic biomaterials: Properties, state of the art and future prospectives.* Ceramics International, 2021. 47(20): p. 28059-28074.
77. Ielo, I., et al., *Recent advances in hydroxyapatite-based biocomposites for bone tissue regeneration in orthopedics.* International Journal of Molecular Sciences, 2022. 23(17): p. 9721.
78. Bai, R., et al., *Ceramic Toughening Strategies for Biomedical Applications.* Frontiers in Bioengineering and Biotechnology, 2022. 10.
79. Cacciotti, I., et al., *Mg-substituted hydroxyapatite nanopowders: synthesis, thermal stability and sintering behaviour.* 2009. 29(14): p. 2969-2978.
80. Matias, P., et al., *Hypomagnesemia: a potential underlooked cause of persistent vitamin D deficiency in chronic kidney disease.* Clinical Kidney Journal, 2023: p. sfad123.
81. Fihri, A., et al., *Hydroxyapatite: A review of syntheses, structure and applications in heterogeneous catalysis.* Coordination Chemistry Reviews, 2017. 347: p. 48-76.
82. Sadat-Shojai, M., M.-T. Khorasani, and A. Jamshidi, *Hydrothermal processing of hydroxyapatite nanoparticles—A Taguchi experimental design approach.* Journal of Crystal Growth, 2012. 361: p. 73-84.
83. Kattimani, V.S., S. Kondaka, and K.P. Lingamaneni, *Hydroxyapatite–-Past, present, and future in bone regeneration.* Bone and Tissue Regeneration Insights, 2016. 7: p. BTRI. S36138.
84. Granito, R.N., et al., *Hydroxyapatite from fish for bone tissue engineering: A promising approach.* International journal of molecular and cellular medicine, 2018. 7(2): p. 80.
85. Eslami, H., M. Solati-Hashjin, and M. Tahriri, *The comparison of powder characteristics and physicochemical, mechanical and biological properties between nanostructure ceramics of hydroxyapatite and fluoridated hydroxyapatite.* Materials Science and Engineering: C, 2009. 29(4): p. 1387-1398.
86. Sulaiman, S.B., et al., *Tricalcium phosphate/hydroxyapatite (TCP-HA) bone scaffold as potential candidate for the formation of tissue engineered bone.* The Indian journal of medical research, 2013. 137(6): p. 1093.
87. Ahn, E.S., et al., *Nanostructure processing of hydroxyapatite-based bioceramics.* Nano Letters, 2001. 1(3): p. 149-153.
88. Cacciotti, I., *Cationic and Anionic Substitutions in Hydroxyapatite*, in *Handbook of Bioceramics and Biocomposites*, I.V. Antoniac, Editor. 2016, Springer International Publishing: Cham. p. 145-211.
89. Reger, N.C., et al., *Structural and phase analysis of multi-ion doped hydroxyapatite for biomedical applications.* Ceramics International, 2019. 45(1): p. 252-263.
90. Nagyne-Kovacs, T., et al., *Synthesis and characterization of Sr and Mg-doped hydroxyapatite by a simple precipitation method.* Ceramics International, 2018. 44(18): p. 22976-22982.
91. Jin, W., et al., *Synergic effect of Sr2+ and Mg2+ on the stabilization of amorphous calcium phosphate.* Crystal Growth & Design, 2018. 18(10): p. 6054-6060.
92. Aina, V., et al., *Magnesium-and strontium-co-substituted hydroxyapatite: the effects of doped-ions on the structure and chemico-physical properties.* Journal of Materials Science: Materials in Medicine, 2012. 23: p. 2867-2879.
93. Landi, E., et al., *Mg, Sr-Cosubstituted Hydroxyapatite with Improved Structural Properties.* Applied Sciences, 2021. 11(11): p. 4930.
94. Kadhim, M.M., et al., *Effect of Sr/Mg co-substitution on corrosion resistance properties of hydroxyapatite coated on Ti–6Al–4V dental alloys.* Journal of Physics and Chemistry of Solids, 2022. 161: p. 110450.

95. Tavoni, M., et al., *Bioactive calcium phosphate-based composites for bone regeneration.* 2021. 5(9): p. 227.
96. Predoi, D., et al., *Influence of the Biological Medium on the Properties of Magnesium Doped Hydroxyapatite Composite Coatings.* Coatings, 2023. 13(2): p. 409.
97. Yuan, X., et al., *Wet-chemical synthesis of Mg-doped hydroxyapatite nanoparticles by step reaction and ion exchange processes.* 2013. 1(47): p. 6551-6559.
98. Bricha, M., et al., *Hydrothermal synthesis and appraisal of mg-doped hydroxyapatite nanopowders.* 2013. 3(5): p. 570-580.
99. Ziani, S., S. Meski, and H.J.I.J.o.A.C.T. Khireddine, *Characterization of Magnesium-Doped Hydroxyapatite prepared by sol-gel process.* 2014. 11(1): p. 83-91.
100. Mishra, V.K., et al., *Mg-doped hydroxyapatite nanoplates for biomedical applications: a surfactant assisted microwave synthesis and spectroscopic investigations.* 2014. 614: p. 283-288.
101. Papargyris, A.D., A. Botis, and S. Papargyri, *Synthetic routes for hydroxyapatite powder production.* Key Engineering Materials, 2002. 206.
102. Pu'ad, N.M., et al., *Synthesis method of hydroxyapatite: A review.* Materials Today: Proceedings, 2020. 29: p. 233-239.
103. Pu'ad, N.M., et al., *Syntheses of hydroxyapatite from natural sources.* Heliyon, 2019. 5(5): p. e01588.
104. Nowicki, D.A., J.M. Skakle, and I.R. Gibson, *Faster synthesis of A-type carbonated hydroxyapatite powders prepared by high-temperature reaction.* Advanced Powder Technology, 2020. 31(8): p. 3318-3327.
105. Ressler, A., et al., *Ionic substituted hydroxyapatite for bone regeneration applications: A review.* Open Ceramics, 2021. 6: p. 100122.
106. Bohner, M., et al., *A physical approach to modify the hydraulic reactivity of α-tricalcium phosphate powder.* 2009. 5(9): p. 3524-3535.
107. Carrodeguas, R.G. and S.J.A.b. De Aza, *α-Tricalcium phosphate: Synthesis, properties and biomedical applications.* 2011. 7(10): p. 3536-3546.
108. Kavaliauskienė, L., *Tricalcium phosphate polymorphs: the role of ionic substitutions and processing conditions on phase selective synthesis and properties*. 2021, Vilniaus universitetas.
109. Gallinetti, S., C. Canal, and M.P.J.J.o.t.A.C.S. Ginebra, *Development and characterization of biphasic hydroxyapatite/β-TCP cements.* 2014. 97(4): p. 1065-1073.
110. Tronco, M.C., J.B. Cassel, and L.A.J.A.b. Dos Santos, *α-TCP-based calcium phosphate cements: A critical review.* 2022.
111. Szurkowska, K., Ł. Szeleszczuk, and J.J.I.J.o.M.S. Kolmas, *Effects of synthesis conditions on the formation of Si-substituted alpha tricalcium phosphates.* 2020. 21(23): p. 9164.
112. Jokić, B., et al., *Synthesis and settings behavior of alpha-TCP from calcium deficient hyroxyapatite obtained by hydrothermal method.* 2007. 9(6): p. 1904-1910.
113. Cicek, G., et al., *Alpha-tricalcium phosphate (α-TCP): solid state synthesis from different calcium precursors and the hydraulic reactivity*. 2011. 22: p. 809-817.
114. Marew, T. and G.J.R.T. Birhanu, *Three dimensional printed nanostructure biomaterials for bone tissue engineering.* 2021. 18: p. 102-111.
115. Abbasi, N., et al., *Porous scaffolds for bone regeneration.* 2020. 5(1): p. 1-9.
116. Fillingham, Y., J.J.T.b. Jacobs, and j. journal, *Bone grafts and their substitutes.* 2016. 98(1_Supple_A): p. 6-9.
117. De Witte, T.-M., et al., *Bone tissue engineering via growth factor delivery: from scaffolds to complex matrices.* 2018. 5(4): p. 197-211.

118. Garot, C., G. Bettega, and C.J.A.f.m. Picart, *Additive manufacturing of material scaffolds for bone regeneration: toward application in the clinics.* 2021. 31(5): p. 2006967.
119. Bencherif, S.A., et al., *Advances in the design of macroporous polymer scaffolds for potential applications in dentistry*. 2013. 43(6): p. 251-261.
120. Turnbull, G., et al., *3D bioactive composite scaffolds for bone tissue engineering.* 2018. 3(3): p. 278-314.
121. Blokhuis, T.J., et al., *Properties of calcium phosphate ceramics in relation to their in vivo behavior.* 2000. 48(1): p. 179.
122. Demir-Oğuz, Ö., A.R. Boccaccini, and D.J.B.M. Loca, *Injectable bone cements: What benefits the combination of calcium phosphates and bioactive glasses could bring?* 2023. 19: p. 217-236.
123. Abbas, Z., et al., *Toughening of bioceramic composites for bone regeneration.* 2021. 5(10): p. 259.
124. Punj, S., J. Singh, and K.J.C.I. Singh, *Ceramic biomaterials: Properties, state of the art and future prospectives.* 2021. 47(20): p. 28059-28074.
125. Tagandurdyeva, N. and V.J.N.i.R. Yudin, *Bioresorbable Composites for Bone Reconstruction.* 2020. 15: p. 400-414.
126. Gul, H., M. Khan, and A.S. Khan, *Bioceramics: Types and clinical applications*, in *Handbook of ionic substituted hydroxyapatites*. 2020, Elsevier. p. 53-83.
127. Ritchie, R.O., *The conflicts between strength and toughness.* Nature materials, 2011. 10(11): p. 817-822.
128. Evans, A.G., *Perspective on the development of high-toughness ceramics.* Journal of the American Ceramic society, 1990. 73(2): p. 187-206.
129. Fu, Q., et al., *Toward strong and tough glass and ceramic scaffolds for bone repair.* 2013. 23(44): p. 5461-5476.
130. Gerhardt, L.-C. and A.R.J.M. Boccaccini, *Bioactive glass and glass-ceramic scaffolds for bone tissue engineering.* 2010. 3(7): p. 3867-3910.
131. Barralet, J.E., et al., *High-strength apatitic cement by modification with α-hydroxy acid salts.* Advanced Materials, 2003. 15(24): p. 2091-2094.
132. Liu, Y., D. Luo, and T.J.S. Wang, *Hierarchical structures of bone and bioinspired bone tissue engineering.* 2016. 12(34): p. 4611-4632.
133. Ginebra, M.-P., et al., *Calcium phosphate cements as drug delivery materials.* 2012. 64(12): p. 1090-1110.
134. Vaishya, R., et al., *Bone cement.* 2013. 4(4): p. 157-163.
135. Patel, R., et al., *An overview of bone cement: Perioperative considerations, complications, outcomes and future implications.* 2023: p. 17504589231169861.
136. Carpenter, W., et al., *The Evolution of Cement Fixation in Total Knee Arthroplasty*. 2019. 35: p. 355-362.
137. Wang, X.-H., S.-J. Jia, and D.-J.J.C.m.j. Hao, *Advances in the modification of injectable calcium-phosphate-based bone cements for clinical application.* 2020. 133(21): p. 2610-2612.
138. Webb, J., R.J.T.J.o.B. Spencer, and J.S.B. Volume, *The role of polymethylmethacrylate bone cement in modern orthopaedic surgery*. 2007. 89(7): p. 851-857.
139. Wang, Q., et al., *Application and modification of bone cement in vertebroplasty: A literature review.* 2022. 33(2): p. 467.
140. Zhang, J., et al., *Calcium phosphate cements for bone substitution: Chemistry, handling and mechanical properties.* 2014. 10(3): p. 1035-1049.
141. Ginebra, M.-P., T. Traykova, and J.A.J.B. Planell, *Calcium phosphate cements: competitive drug carriers for the musculoskeletal system?* 2006. 27(10): p. 2171-2177.
142. Ginebra, M.-P., et al., *New processing approaches in calcium phosphate cements and their applications in regenerative medicine.* 2010. 6(8): p. 2863-2873.

143. de Almeida Pina, S.C., *Cements of doped calcium phosphates for bone implantation*. 2009, Universidade de Aveiro (Portugal).
144. Low, K.L., et al., *Calcium phosphate-based composites as injectable bone substitute materials.* 2010. 94(1): p. 273-286.
145. Sarda, S., et al., *Kinetic study of citric acid influence on calcium phosphate bone cements as water-reducing agent.* 2002. 61(4): p. 653-659.
146. Wang, X., J. Ye, and Y.J.A.b. Wang, *Influence of a novel radiopacifier on the properties of an injectable calcium phosphate cement.* 2007. 3(5): p. 757-763.
147. Bohner, M.J.I., *Calcium orthophosphates in medicine: from ceramics to calcium phosphate cements.* 2000. 31: p. D37-D47.
148. Dorozhkin, S.V.J.J.o.M.S., *Calcium orthophosphate cements for biomedical application.* 2008. 43(9): p. 3028-3057.
149. Chow, L.C.J.J.o.t.C.s.o.J., *Development of self-setting calcium phosphate cements.* 1991. 99(1154): p. 954-964.
150. Wu, Y., et al., *3D printed calcium phosphate cement (CPC) scaffolds for anti-cancer drug delivery*. 2020. 12(11): p. 1077.
151. Fosca, M., J.V. Rau, and V.J.B.M. Uskoković, *Factors influencing the drug release from calcium phosphate cements.* 2022. 7: p. 341-363.
152. Fu, Y. and W.J.J.E.o.o.d.d. Kao, *Drug release kinetics and transport mechanisms of non-degradable and degradable polymeric delivery systems.* 2010. 7(4): p. 429-444.
153. He, X., et al., *The comparison of macroporous ceramics fabricated through the protein direct foaming and sponge replica methods.* 2012. 19: p. 761-766.
154. Gopinathan, J. and I.J.B.r. Noh, *Recent trends in bioinks for 3D printing.* 2018. 22: p. 1-15.
155. Bao, Y., et al., *Rheological behavior of aqueous suspensions of hydroxyapatite (HAP).* 2002. 13: p. 639-643.
156. Amin, A.M., et al., *Role of heat treatment of hydroxyapatite powder prior to suspension preparation on the suspension flow behavior*. 2022. 9: p. 100239.
157. Bose, S., et al., *Trace element doping in calcium phosphate ceramics to understand osteogenesis and angiogenesis.* Trends in biotechnology, 2013. 31(10).
158. Yilmaz, B., A.Z. Alshemary, and Z. Evis, *Co-doped hydroxyapatites as potential materials for biomedical applications.* Microchemical Journal, 2019. 144: p. 443-453.
159. Balakrishnan, S., et al., *Influence of iron doping towards the physicochemical and biological characteristics of hydroxyapatite*. Ceramics International, 2021. 47(4): p. 5061-5070.
160. Amin, A.M., et al., *Role of heat treatment of hydroxyapatite powder prior to suspension preparation on the suspension flow behavior*. Open Ceramics, 2022. 9: p. 100239.
161. Maas, M., U. Hess, and K. Rezwan, *The contribution of rheology for designing hydroxyapatite biomaterials.* Current opinion in colloid & interface science, 2014. 19(6): p. 585-593.
162. Shao, H., et al., *Bone regeneration in 3D printing bioactive ceramic scaffolds with improved tissue/material interface pore architecture in thin-wall bone defect.* Biofabrication, 2017. 9(2): p. 025003.
163. Gao, C., et al., *Advances in biocermets for bone implant applications.* Bio-Design and Manufacturing, 2020. 3: p. 307-330.
164. Lin, K., et al., *3D printing of bioceramic scaffolds—Barriers to the clinical translation: From promise to reality, and future perspectives.* 2019. 12(17): p. 2660.
165. Lewis, J.A.J.A.F.M., *Direct ink writing of 3D functional materials.* 2006. 16(17): p. 2193-2204.
166. Feilden, E., et al., *Robocasting of structural ceramic parts with hydrogel inks.* 2016. 36(10): p. 2525-2533.

167. Cesarano, J., R. Segalman, and P.J.C.i. Calvert, *Robocasting provides MOULDLESS fabrication from slurry deposition.* 1998. 148(4): p. 94-96.
168. Miranda, P., et al., *Sintering and robocasting of β-tricalcium phosphate scaffolds for orthopaedic applications.* 2006. 2(4): p. 457-466.
169. Lewis, J.A.J.J.o.t.A.C.S., *Colloidal processing of ceramics.* 2000. 83(10): p. 2341-2359.
170. Lewis, J.A.J.C.O.i.S.S. and M. Science, *Direct-write assembly of ceramics from colloidal inks.* 2002. 6(3): p. 245-250.
171. Agrawal, D., *Microwave sintering of ceramics, composites and metal powders*, in *Sintering of advanced materials*. 2010, Elsevier. p. 222-248.
172. Ning, W., et al., *1-Allyl-3-methylimidazolium chloride plasticized-corn starch as solid biopolymer electrolytes.* 2009. 76(3): p. 482-484.
173. Ring, T.A., *Ceramic powder synthesis.* Fundamentals of Ceramic Powder Processing and Synthesis, 1996: p. 81-83.
174. Hench, L.L., *An introduction to bioceramics*. Vol. 1. 1993: World scientific.
175. Rahaman, M.N., *Sintering of ceramics*. 2007: CRC press.
176. Boda, S.K., et al., *Structural and magnetic phase transformations of hydroxyapatite-magnetite composites under inert and ambient sintering atmospheres.* The Journal of Physical Chemistry C, 2015. 119(12): p. 6539-6555.
177. Wu, M., et al., *Biomimetic synthesis and characterization of carbon nanofiber/hydroxyapatite composite scaffolds.* Carbon, 2013. 51: p. 335-345.
178. Porz, L., et al., *Dislocation-toughened ceramics.* Materials Horizons, 2021. 8(5): p. 1528-1537.
179. Chan, K.S., *Relationships of fracture toughness and dislocation mobility in intermetallics.* Metallurgical and Materials Transactions A, 2003. 34: p. 2315-2328.
180. Dong, J., et al., *Extrusion-based additive manufacturing of Mg-Zn/bioceramic composite scaffolds.* 2022. 151: p. 628-646.
181. Kong, Y.M., et al., *Reinforcement of hydroxyapatite bioceramic by addition of ZrO2 coated with Al2O3.* Journal of the American Ceramic Society, 1999. 82(11): p. 2963-2968.
182. Juhasz, J., et al., *Mechanical properties of glass-ceramic AW-polyethylene composites: effect of filler content.* Key Engineering Materials, 2002. 240: p. 947-950.
183. Philippart, A., et al., *Toughening and functionalization of bioactive ceramic and glass bone scaffolds by biopolymer coatings and infiltration: a review of the last 5 years.* Expert review of medical devices, 2015. 12(1): p. 93-111.
184. Raut, V., et al., *Stress-induced phase transformation in shape memory ceramic nanoparticles.* Journal of Applied Physics, 2019. 126(21): p. 215109.
185. Marshall, D., A. Evans, and M. Drory, *Transformation toughening in ceramics.* Fracture Mechanics of Ceramics, 1983. 6: p. 289-307.
186. Shi, S.L., et al., *Reinforcement of hydroxyapatite bioceramic by addition of Ti3SiC2.* Journal of the American Ceramic Society, 2006. 89(2): p. 743-745.
187. Rödel, J., *Interaction between crack deflection and crack bridging.* Journal of the European Ceramic Society, 1992. 10(3): p. 143-150.
188. Bengisu, M. and O.T. Inal, *Whisker toughening of ceramics: toughening mechanisms, fabrication, and composite properties.* Annual Review of Materials Science, 1994. 24(1): p. 83-124.
189. Phillips, D., *Interfacial bonding and the toughness of carbon fibre reinforced glass and glass-ceramics.* Journal of Materials Science, 1974. 9: p. 1847-1854.

190. Zhang, X., et al., *Toughening of calcium hydroxyapatite with silver particles.* Journal of materials science, 1997. 32(1): p. 235-243.
191. Schumacher, M. and M. Gelinsky, *Strontium modified calcium phosphate cements–approaches towards targeted stimulation of bone turnover.* Journal of Materials Chemistry B, 2015. 3(23): p. 4626-4640.
192. Kulkarni, M., et al., *Titanium nanostructures for biomedical applications.* Nanotechnology, 2015. 26(6): p. 062002.
193. Wereszczak, A.A., *Toughening mechanisms in whisker/short fiber-reinforced ceramic matrix composites at elevated temperatures*. 1992: University of Delaware.
194. Zhao, C.-Z., et al., *An anion-immobilized composite electrolyte for dendrite-free lithium metal anodes.* 2017. 114(42): p. 11069-11074.
195. Wu, J., et al., *Functionalization of silk fibroin electrospun scaffolds via BMSC affinity peptide grafting through oxidative self-polymerization of dopamine for bone regeneration.* ACS applied materials & interfaces, 2019. 11(9): p. 8878-8895.
196. Fujie, T., et al., *Evaluation of substrata effect on cell adhesion properties using freestanding poly (l-lactic acid) nanosheets.* Langmuir, 2011. 27(21): p. 13173-13182.
197. Fujie, K., et al., *Introduction of an ionic liquid into the micropores of a metal–organic framework and its anomalous phase behavior.* Angewandte Chemie, 2014. 126(42): p. 11484-11487.
198. Feng, L.-L., et al., *High-index faceted Ni3S2 nanosheet arrays as highly active and ultrastable electrocatalysts for water splitting.* Journal of the American Chemical Society, 2015. 137(44): p. 14023-14026.
199. Zhang, X., et al., *Enhanced photoresponsive ultrathin graphitic-phase C3N4 nanosheets for bioimaging.* Journal of the American Chemical Society, 2013. 135(1): p. 18-21.
200. Li, C., et al., *An advance review of solid-state battery: Challenges, progress and prospects.* 2021. 29: p. e00297.
201. Zhang, J., et al., *Calcium phosphate cements for bone substitution: chemistry, handling and mechanical properties.* Acta biomaterialia, 2014. 10(3): p. 1035-1049.
202. Mittal, G., et al., *Reinforcements in multi-scale polymer composites: Processing, properties, and applications.* Composites Part B: Engineering, 2018. 138: p. 122-139.
203. Prashanth, S., et al., *Fiber reinforced composites-a review.* J. Mater. Sci. Eng, 2017. 6(03): p. 2-6.
204. Shah, M.B., *Mechanistic aspects of fracture and fatigue in resin based dental restorative composites*. 2009: Oregon State University.
205. Berguiga, L., et al., *Carbon nanotube silica glass composites in thin films by the sol–gel technique.* Optical Materials, 2006. 28(3): p. 167-171.
206. Huang, Q., L. Gao, and J. Sun, *Effect of adding carbon nanotubes on microstructure, phase transformation, and mechanical property of BaTiO3 ceramics.* Journal of the American Ceramic Society, 2005. 88(12): p. 3515-3518.
207. Zakharov, N., et al., *Synthesis and properties of calcium hydroxyapatite/carbon fiber composites.* Russian Journal of Inorganic Chemistry, 2017. 62: p. 1162-1172.
208. Tian, W.-B., et al., *Effect of carbon nanotubes on the properties of ZrB2–SiC ceramics.* Materials Science and Engineering: A, 2008. 487(1-2): p. 568-573.
209. Shen, L., et al., *Preparation and mechanical properties of carbon fiber reinforced hydroxyapatite/polylactide biocomposites.* Journal of Materials Science: Materials in Medicine, 2009. 20: p. 2259-2265.

210. Uddin, M.N., P.S. Dhanasekaran, and R. Asmatulu, *Mechanical properties of highly porous PEEK bionanocomposites incorporated with carbon and hydroxyapatite nanoparticles for scaffold applications.* Progress in biomaterials, 2019. 8: p. 211-221.
211. Nayak, L., M. Rahaman, and R. Giri, *Surface modification/functionalization of carbon materials by different techniques: An overview.* Carbon-containing polymer composites, 2019: p. 65-98.
212. Rasheed, A., et al., *The efficiency of the oxidation of carbon nanofibers with various oxidizing agents.* Carbon, 2007. 45(5): p. 1072-1080.

CHAPTER 2: DEVELOPMENT OF MECHANICALLY REINFORCED POROUS APATITE SCAFFOLDS

Calcium phosphates, particularly hydroxyapatite (HA) have been widely investigated and recognized as suitable material to develop scaffolds for bone regeneration applications, mainly due to optimal chemical mimicry with the natural inorganic component of bones [1-9]. In addition to chemical mimicry, the presence of wide open and interconnected porosity represents a major factor contribution to the complete integration of the scaffold with the surrounding biological tissue and the achievement of effective mechanical stability, overtime.

In spite of such a great potential, the main drawback associated to hydroxyapatite is its intrinsic brittleness poses significant limitation to their clinical use, as it can result in irreparable mechanical damages and sudden failure of the scaffolds. This is a major reason making the regeneration of load-bearing bone defects such as maxillofacial regions and spine region, a still unmet clinical need of great socio-economic relevance [10-13]. The maximum fracture toughness of dense HA bioceramics is reported as approximately 1.0 $MPa \cdot m^{1/2}$, which is only half of the minimum reported fracture toughness of cortical bone, previously reported in the range 2.0-12.0 $MPa \cdot m^{1/2}$ [14]. In fact, the human cortical bone can be considered as a composite material mainly composed by type-I collagen and biological HA. However, biological HA significantly differ from synthetic, stoichiometric HA in terms of chemical composition and bio-functional abilities, due to multiple substitutions of Ca^{2+} and PO_4^{3-} ions with various foreign ions such as Mg^{2+}, Zn^{2+}, K^{+}, Sr^{2+}, Fe^{2+}, Mn^{2+}, Mo^{3+}, Cu^{2+}, Ni^{2+}, and CO_3^{2-} which in biological HA are relevant drivers and modulators of the bone tissue metabolism[15, 16].

To mimic the chemical composition of biological HA, various foreign ions can be introduced into the HA crystal lattice during synthesis, seeking to improve key biologically relevant features of HA-based biomedical devices. In particular, the doping with Mg^{2+} and Sr^{2+} ions is considered as particularly relevant, since they are major bioactive player in the processes of new bone formation and turnover [10]. These ions are capable to influence the crystallinity, grain size, morphology, thermal stability and degradation rate of HA powders which reflect on the bioactivity, mechanical and solubility of HA scaffolds [17-20]. Ion-doped HA has been widely studied in terms of their microstructure, mechanical and biological properties because can provide combined benefits when doped at appropriate concentration [21-24]. The ion doping of HA powders also affects the surface charge of the particles, resulting in different flow behavior of the slurries [25, 26]. In particular, considering the preparation of

hydroxyapatite slurries, previous studies highlighted that the ion doping in apatite reduces the crystallinity extent, inhibits the grain growth and alter the surface state in terms of charged groups, thus affecting the affinity with water and in turn the rheological properties[27-30].

Several processing techniques have been described in literature to prepare porous bone scaffolds with complex shapes and morphology, including replica method, sacrificial template and direct foaming method [31, 32]. Moreover, 3D printing was established as an effective method for the preparation of scaffolds with controlled morphology and porosity [33, 34]. The design of porous bioactive scaffolds based on hydroxyapatite basically involves the preparation of powders, then manipulated in form of aqueous slurries, that are ternary systems involving water, powder particles and organic dispersants. For this reason, the preparation of stable, homogeneous and handleable colloidal dispersions of powders in water is required to prevent final structural defects. The flow behaviour of hydroxyapatite slurries is mainly affected by the content of solid particles, due to the attractive and repulsive forces between the surface of the particles and their degree of agglomeration [35, 36]. The capability to prevent the agglomeration of powder particles is mandatory to control the homogeneity of the slurry and the final scaffolds, avoiding density gradients or undesired air entrapping [37].

On this basis, a significant contribution of my research activity was focused on rheological characterizations of hydroxyapatite (HA) slurries, towards the fine control of the rheology based on powder amount, calcination temperature, dispersant amount as well as ion-doping and then on a forming process based on direct foaming of ceramic suspensions.

In terms of mechanical reinforcement, a useful approach to enhance the mechanical properties of bioceramics, such as the energy required for fracture generation, is reported as the incorporation of secondary phases (e.g. zirconia, bioglass, fibers, HA whiskers) [10]. Among the various reinforcement materials, carbon fibers has been considered as an excellent choice due to its remarkable strength, excellent biocompatibility and toughening performance [38]. Carbon fibers (CF) have found extensive applications in clinical biomedicine owing to their inherent biocompatibility, chemical stability, favorable mechanical characteristics, low density and resistance to corrosion [39] [40, 41]. Some studies reported moderate inflammatory response of carbon fibers in the body. In the majority of cases the inflammatory responses were associated with considerable length and a high aspect ratio of carbon fibers, can be diminished by other factors like homogenous dispersion in biocompatible and bioactive materials such as apatite's [42] .

In this contest, I investigated novel approaches for the reinforcement of HA scaffolds by addition of fibers, particularly carbon and alumina fibers into the apatite slurries as toughening agents.

2.1. Materials and Methods

2.1.1. Rheology of hydroxyapatite slurries

Commercial HA powder (Merck, Germany) was used as a starting material in this study. The XRD patterns exhibited pure apatite phase (JCPDS Card No. 09-0432). The HA powders were thermally treated at 800°C and 1000°C (heating rate=100°C/h, dwell time=1 hour) and sieved under 150 µm. Then, the preparation of slurries was performed by dispersing HA in distilled water, by using the alkali-free polyelectrolyte polymer "Dolapix CA" (Zschimmer and Schwartz, Germany) as dispersant agent, according to a previously reported route [43].

Several combinations of slurries prepared with HAcom (non-thermally treated powders), HA800 and HA1000 were characterized to investigate the effect of different calcination temperature (T), powder amount (P) and dispersant amount (D) on the flow behaviour of slurries, according to Table 2-I. The dispersant was calculated as dispersant/water ratio (vol%).

Table 2-I: Composition of slurries with respective sample codes.

Sample Code	Powder	Dispersant/water
	wt% (vol%)	(vol%)
24/0	50 (24)	0
24/0.2	50 (24)	0.2
24/2	50 (24)	2
16/0	37 (16)	0
16/0.2	37 (16)	0.2
16/2	37 (16)	2
6/0	17 (6)	0
6/0.2	17 (6)	0.2
6/2	17 (6)	2

2.1.2. Rheology of ion-doped hydroxyapatite slurries

Stoichiometric HA was synthesized by co-precipitation method [44, 45], using calcium hydroxide ($Ca(OH)_2$, Sigma Aldrich, St. Louis, MO, USA) and orthophosphoric acid (H_3PO_4, Sigma Aldrich) as a raw material shown in Figure 2.1. In particular, an aqueous solution of 3 mM $Ca(OH)_2$ (99%) was

prepared in a 500 mL Florence flask and stirred for 30 min at 40°C. Then, a dilute 1 mM H_3PO_4 (95%) aqueous solution was added to the continuously stirred calcium hydroxide solution, with controlled peristaltic pump (1 ml/min). The mixture was stirred for a further 2 h, followed by aging overnight at room temperature. After this, the precipitates were washed with distilled water until the pH = 7. The resulting precipitate was dried overnight at 40°C to remove excess water and sieved below 150 μm.

For the synthesis of ion-doped HA [46-48], the same route was repeated by introducing salts ($MgCl_2 \cdot 6H_2O$ and $SrCl_2 \cdot 6H_2O$, Sigma Aldrich) containing the doping ions in appropriate amounts to prepare Mg-doped HA (Mg/(Ca+Mg) = 5 mol%), Sr-doped HA (Sr/(Ca+Sr) = 5 mol%) and co-doped Mg-Sr-HA (Mg/(Ca+Mg+Sr) = Sr/(Ca+Mg+Sr) = 2.5 mol%).

Various combinations of slurries were prepared by dispersing stoichiometric and ion-doped HA powder in milliQ water upon addition of an anionic polyelectrolyte as dispersant agent (Dolapix CA, 25 wt% of active ingredient, density 1.1 g/mL, Zschimmer and Schwartz, Germany). Slurries with different powder amounts and dispersant amounts calculated with respect to the total slurry weight were studied, according to Table 2-II.

Table 2-II:Composition of stochiometric and ion-doped HA slurries, with respective sample codes

Sample Code	Powder	Dispersant	Water
	wt% (vol%)	(wt%)	(wt%)
49/0	49 (23)	0	51
49/3	49 (23)	3	48
49/6	49 (23)	6	45
33/0	33 (13)	0	67
33/3	33 (13)	3	64
33/6	33 (13)	6	61

The correlation of the zeta potential (ζ) with rheological behavior with a comprehensive compositional parameter for the dispersant was achieved by introducing the parameter β defined as the mass of active dispersant molecule (m_d) per unit of total surface area of the powder:

$$\beta = \frac{m_d}{SSA \cdot m_p} \quad (1)$$

where SSA is the specific surface area of the powder and m_p is the mass of powder.

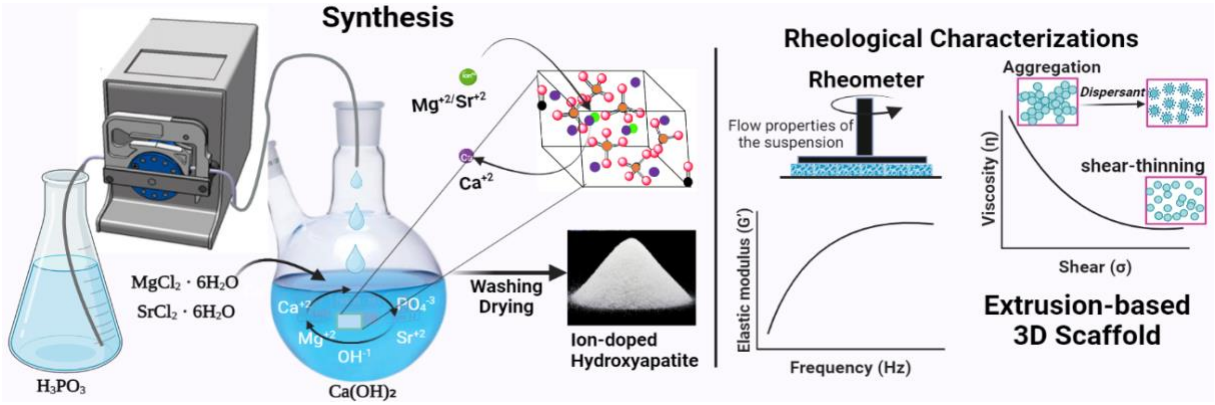

Figure 2-1:schematic diagram of Ion-doped HA synthesis and their rheological characterizations

2.1.3. Mechanically reinforced HA scaffold with fibers

Reinforced HA scaffold with carbon fibers: Carbon fiber-reinforced HA composite was prepared by pressureless sintering. For the development of composite, commercial HA powder were calcinated at 1000°C for 1 hour and sieved under 150 µm. Carbon fibers (C.F) with tensile strength of 3500 MPa and average diameters 7 µm (TohoTenax Co, Ltd) were ultrasonically cleaned in acetone at room temperature, washed by distilled water until the pH=7, referred to untreated C-fibers.

To enhance the surface properties, the C-fibers were treated with a combination of various acids at 100°C for 1 hour [49], shown in Table 2-III. Then, treated C-fibers were thoroughly washed with distilled water, before testing the surface characteristics of different C-fibers in order to remove physically absorbed acids or residues.

Table 2-III: Combinations of different acids for surface activation of carbon fibers.

Sample Code	Acid solutions	Volume ratios
A	HNO_3	10
B	HNO_3: H_2SO_4	6:4
C	HNO_3: H_2SO_4 : H_3PO_4	2: 4 : 4
D	HNO_3: H_2O_2	8: 2
E	3*HCl: 1*HNO_3 (aquaregia)	7.5: 2.5
F	Control (untreated)	10

Then, acids-activated C-fibers were immersed in $CaCl_2$ solution and then, added into buffered Phosphate solutions [50] (Figure 2.2).

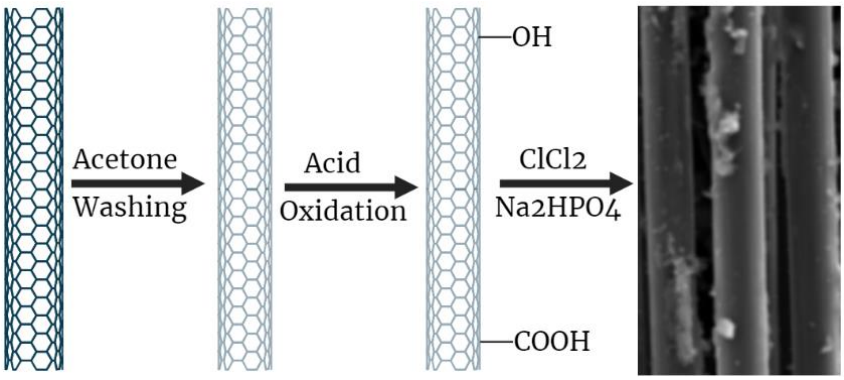

Figure 2-2: Activation and mineralization of carbon fibers

Mineralized C-fibers were manually cut up to 2-3 mm and mixed into HA slurries by wt% ratio of HA: H_2O: Dispersant: C-fibers (72: 23: 4: 1). The resulting fibers containing slurries were dried in dedicated moulds at room temperature for 24 hours and sintered at 1200°C for 1h in N_2 atmosphere.

Reinforced HA scaffold with alumina fibers; Alumina fibers with two different compositions were explored for the development of alumina-fiber reinforced HA composite, showed in Table 2-IV.

Table 2-IV: Alumina fibers blanket with different composition.

Fiber type	Al_2O_3 (wt%)	SiO_2 (wt%)	Fe_2O_3 (wt%)	CaO (wt%)
Alumina-Silica Blanket	56	27	<1	11
Pure alumina saffil blanket	96	3	<1	0

a. The slurries containing hydroxyapatite and alumina-silica fibers were prepared by varying the HA content, upon the addition of dispersant and fibers amount. The alumina-silica fibers were added to the slurry by two different methods, namely impregnation and mixing. The impregnation method involved the addition of alumina blankets into HA slurries, followed by manual deformation of the resulting composite, to achieve complete impregnation.

Conversely, the mixing method involved the addition of chopped small pieces of blankets during the mixing procedure of a slurry with a high-energy planetary ball mixing device or high-energy shear-mixing device without grinding media.

Different combinations of slurries were prepared by mixing HA powder calcinated at different temperatures, dispersant and alumina blanket amount, to analyse the mechanical strength of alumina fibers reinforced HA composite, shown in Table 2-V.

Table 2-V: Combination of samples for mechanical strength tests with respective sample codes. (*) Replica method; (**) Direct foaming method

Sample Code	Calcination Temperature (°C)	Slurry composition (wt%)			Alumina fibers (wt%) wrt HA powder
		HA	Water	Dolapix	
C1	-	52	43	5	20
C2	-	52	43	5	40
D1 (*)	1000	73	23	4	
D2	1000	52	43	5	15
D3	1000	67	27	6	
D4	1000	67	27	6	30
D5	1000	77	19	4	26
D6 (**)	1000	64	32	4	15

b. Similarly, several combinations of pure alumina fibers-reinforced HA slurries were prepared by mixing HA powder, dispersant and fibers (2-3mm) amount using high energy share mixing, shown in Table 2-VI.

Table 2-VI: Combinations of alumina fibers reinforced HA slurries

Sample code	HA (wt%)	Water (wt%)	Dolapix (wt%)	Alumina Fibers (wt%) wrt powder
A0	72	22	6	0
A2	72	22	6	7
A5	72	22	6	17
A10	72	22	6	34

Then, the final fiber-reinforced HA slurries were dried at room temperature in dedicated moulds and sintered at 1200°C for 1h.

Direct Foaming Method

Sample D6 in Table 2.V was prepared using direct foaming process. HA powder calcined at 1000℃ was dispersed in distilled water with a dispersant and chopped alumina fibers (2-3mm), in 250ml zirconia jar containing 6 zirconia balls (15mm diameter), a high-energy ball milling (Pulverisette 6, Fritsch, Germany) treatment were used for 30 minutes at 400 rpm to prepare the slurry. Following this, foaming agents containing 1.87 wt% Olimpicon A (Olimpia Tensioattivi, Italy) and 0.87 wt% W53 (Zschimmer and Schwartz, Germany) were added to slurry in proportion to the powder amount. After 5 minutes of continuous mixing at 400 rpm, a foamed suspension was formed, poured into paper moulds and dried for 2 days at room temperature to produce stable ceramic foams.

Replica Method

Macroporous apatitic specimens prepared by replica method (coded as D1 in Table 2. V) were used as control samples for compressive strength tests. Briefly, commercial HA powders were mixed in distilled water with dispersant through energy shear mixture. Then, cellulose sponges were impregnated into slurries. To achieve the appropriate infiltration of the slurry, various techniques of sponge manipulation, including wringing out, rolling up and twisting were performed. Subsequently, the sponges underwent a drying process under gentle vacuum circumstances at a temperature of 37°C. Then, it was followed by sintering, in order to remove the organic matrix of the sponge and simultaneously enhance the structural integrity of the final apatite-based formations, while preserving the original shape of the sponge.

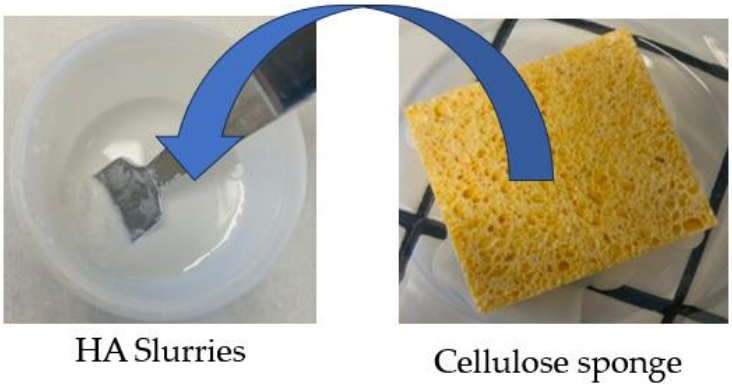

Figure 2-3: Impregnation of Cellulose sponge in HA slurry.

Finally, the sample were subjected to a high-temperature thermal treatment, as indicated in Table 2-VII, which included an initial debonding phase, remove the organic matrix (sponge) and simultaneously enhance the structural integrity of the final apatite-based formations.

Table 2-VII: Sintering cycle

Temperature(°C)	Temperature rate(°C/h)
25 - 1250	100
1250	1 h (dwell time)

Three specimens (size: 2 cm x 1 cm x 1cm) were prepared for compression test. The relative porosity of each specimen was calculated according to geometric method with the theoretical density of HA (3.16 g/cm^3).

2.1.4. Characterizations

The phase composition of samples were investigated by X-Ray diffraction (D8 Advance, Bruker, Karlsruhe, Germany, equipped with a LINXEYE detector using monochromator CuKα radiation) in the 2θ range 10° to 80° with a scanning step of 0.02°. The lattice parameters refinement was performed according to the Rietveld method. The Fourier-transform infrared spectroscopy (FTIR) was performed by a spectrometer (Nicolet IS5, Thermo Fisher Scientific, U.S.A.) to investigate the presence of specific functional groups. For FTIR analysis, sample were grinded with 5% KBr in an agate mortar and compressed to small pellets, analysed within range from 500 to 4000 cm^{-1}. Thermogravimetric analysis were performed using Simultaneous Thermal Analyzer TG-DSC (STA 449 F3 Jupiter, Netzsch Geraetebau) within temperature range (20-1200℃) under N_2 atmosphere. Particles size distribution was analysed using an X-ray instrument based on the Stokes' sedimentation equation (SediGraph 5100 instrument, Micromeritics, USA), by dispersing of powder into aqueous solutions of sodium hexametaphosphate (0.05 wt%). The specific surface area (SSA) was calculated by nitrogen adsorption, with Brunauer–Emmett–Teller (BET) method (Surfer, Thermo Scientific, USA). The porosity of the powders was evaluated by Thermofinnigan 240 Pa on the intrusion of mercury through controlled pressure (0.1-200 MPa). Inductively Coupled Plasma-Optical Emission Spectroscopy (ICP-OES) (5100. Agilent) was used to determine the elemental composition of the powders. Field Emission Scanning electron microscopy (FE-SEM) (Zeiss-SIGMA, Carl Zeiss Microscopy GmbH) was employed to study the morphology of the powders.

The stability of HA slurries was assessed by pH and ζ-potential measurements, as well as viscosity and viscoelasticity tests. The zeta potential (ζ) was studied as indicator of the colloidal stability of the slurries,

as the electrostatic repulsion between particles comes directly related to the value of ζ, resulting in a more stable slurry with increasing the dispersant amount. The pH and Zeta potential of suspension was measured by zeta potential (DT-310, Dispersion Technology Inc.). The viscosity of HA slurries was measured with a Bohlin CVOR controlled stress rheometer (Bohlin Instruments Limited) with a rough parallel plate geometry (25 mm diameter) and 1000 μm gap size between plate and lower disk. The shear viscosity data were recorded as a function of shear rate applying a sequence of discrete steps, after 60 s of equilibration step time, in stress viscometry mode. Continuous shear stress measurements were performed by increasing shear rate in the range 0.1–1000 Pa. To improve the reproducibility of the tests, the slurries were pre-sheared for 30 seconds at an appropriate shear rate. The measurements were carried out at a constant temperature of 25°C, with a solvent trap to prevent water evaporation during the tests. Dynamic tests were performed in an oscillatory mode, to investigate the linear viscoelastic region (LVER), that is the range of proportionality between stress and strain until non-linearity and microstructural breakages. The amplitude sweep tests were performed at a constant frequency of 1 Hz, with increasing the shear stress in the range 0.1-1000 Pa. In this way, 1, 10 and 25 Pa was selected as adequate stress for HA1000, HA800 and HACom respectively, preventing microstructural damage and used as constant during the frequency sweep in the range 0.1-10 Hz.

The mechanical properties of samples were evaluated by compressive and 4-point bending tests. Five parallelepiped specimens with size/volume (1 x 1 x 2 cm / 2 cm^3) for compressive strength and five rectangular specimens with dimension (1 x 1 x 6 cm / 6 cm^3) for 4-point bending strength of each sample were prepared, grinded and polished. A schematic illustration and equation for compressive tests is presented in given Figure 2.4.

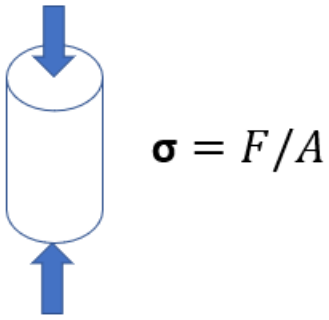

Figure 2-4: schematic illustration and equation for compressive tests

where σ is compression strength (MPa), F is applied load (N) and A is area (cm^2) of the specimen.

A schematic illustration and equation for 4-point bending tests is presented in given Figure 2.5.

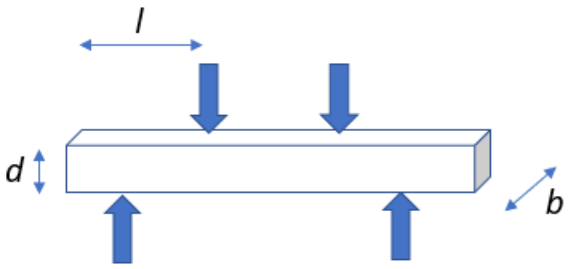

$$\sigma = 3Fl/bd^2$$

Figure 2-5: schematic illustration and equation for 4-point bending tests

where σ = Bending strength (MPa), F = load (N), l = support span (mm), b = Width of test sample (cm) (b>d), d = Height of tested sample (cm).

A Zwick Roell Z050 machine was used to perform compressive and 4 point-bending tests, in displacement control, with a speed of 1 mm/min.

2.2. Results and Discussion

2.2.1. Rheology of hydroxyapatite slurries

The XRD, FTIR and SEM analysis of non-calcinated HA and calcinated HA powders are reported in Figure 2.6. The XRD spectra of HA_0, HA_800 and HA_1000 show strong peaks at 2θ values of 25.87°, 31.78° and 32.98 which are characteristic peaks of pure HA according to JCPDS Card No. 09–0432. The thermally treated powders exhibited higher crystallinity, confirmed higher intensity of the peaks, peak narrowing and splitting with increasing the diffraction angles, ascribed to the coalescence of small grains through grain boundary diffusion [24]. The A complete assignment of FTIR bands of non-calcinated and calcinated HA powders confirmed the pure HA, in absence of phase transformation (Figure 2.6 b), in agreement with XRD results. The FTIR peaks detected between 560-620cm^{-1} correspond to P-O bending, while peaks at 1091cm^{-1} are attributed to stretching of PO_3^{-4}. Moreover, a broad peak at 3435 cm^{-1} is attributed to H-O-H group [51]. The intensity of peaks increase, while also sharpening, with increasing calcination temperatures of HA, indicating heigh degree of crystallinity in the resulting calcined powder [52].

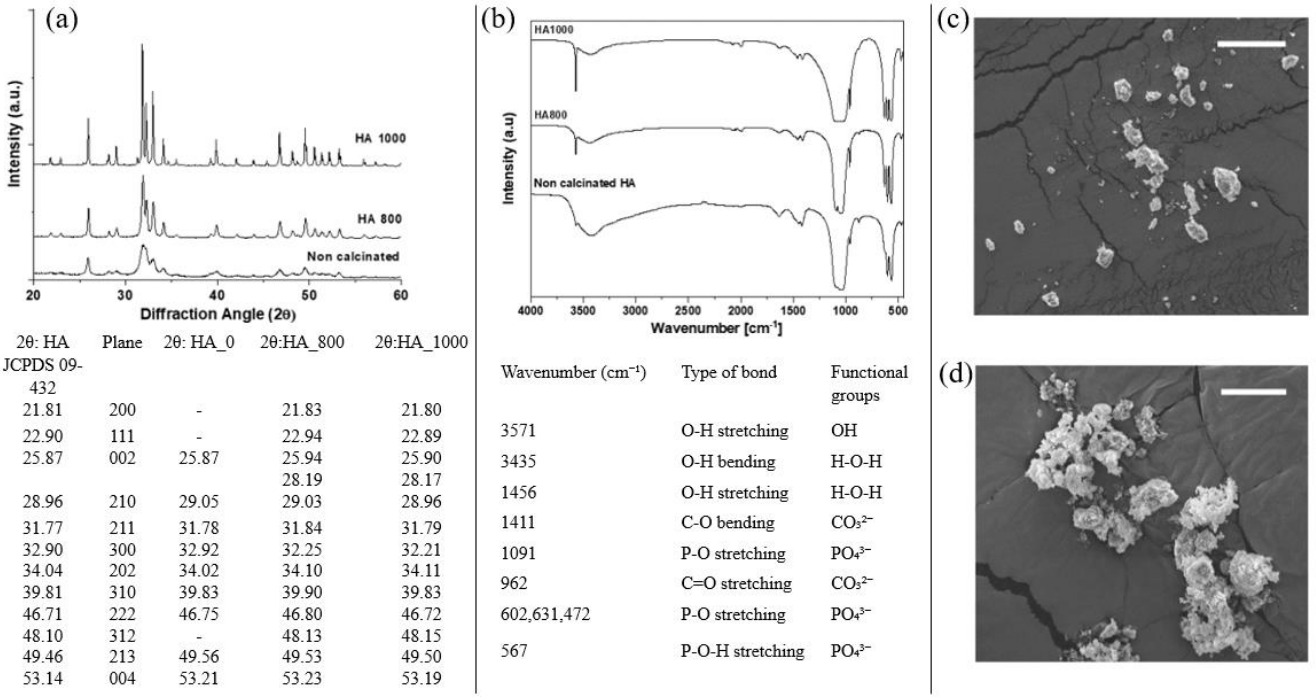

2θ: HA JCPDS 09-432	Plane	2θ: HA_0	2θ:HA_800	2θ:HA_1000
21.81	200	-	21.83	21.80
22.90	111	-	22.94	22.89
25.87	002	25.87	25.94	25.90
			28.19	28.17
28.96	210	29.05	29.03	28.96
31.77	211	31.78	31.84	31.79
32.90	300	32.92	32.25	32.21
34.04	202	34.02	34.10	34.11
39.81	310	39.83	39.90	39.83
46.71	222	46.75	46.80	46.72
48.10	312	-	48.13	48.15
49.46	213	49.56	49.53	49.50
53.14	004	53.21	53.23	53.19

Wavenumber (cm^{-1})	Type of bond	Functional groups
3571	O-H stretching	OH
3435	O-H bending	H-O-H
1456	O-H stretching	H-O-H
1411	C-O bending	CO_3^{2-}
1091	P-O stretching	PO_4^{3-}
962	C=O stretching	CO_3^{2-}
602,631,472	P-O stretching	PO_4^{3-}
567	P-O-H stretching	PO_4^{3-}

Figure 2-6: Physico-chemical characterization of HA: a) XRD, b) FTIR, c) morphology of HA800, d) morphology of HA1000 (scale bar = 20µm)

The morphology of HA powders was also investigated by SEM (Figure 2.6 c & d), demonstrating that particle size and grain growth significantly increased with increasing the calcination temperature [53]. The specific surface area (SSA), particle size and crystalline size of HA powders were calculated in Table 2-VIII. The calcination of HA powder resulted in a significant decrease of specific surface area as compared to the non-calcinated HA due to particles densification and coalescence.

Table 2-VIII: Effect of different calcination temperatures on the crystalline size and SSA of HA powder

Calcination (°C)	Particle size (µm)			SSA (m^2/g)	Crystalline size (nm)	Crystallinity (%)
	d10	d50	d90			
0	-	0.48	3.30	96.88	24	11
800	0.32	1.12	2.86	29.24	65	34
1000	0.51	1.52	5.05	5.12	97	80

The HA slurries can be defined as ternary systems involving aqueous dispersions of powder particles and dispersants. Here, we introduced some physically relevant parameters to describe their preparation and characterization:

$$\varphi_p = \frac{V_p}{V_s} \quad (1)$$

where V_p refers to the volume of powder and V_s to the overall volume of the slurries and

$$\beta = \frac{m_d}{A_p} \quad (2)$$

where m_d refers to the Dolapix active molecule mass and A_p to the specific surface area (SSA) of the powder content (m_p) in the sample ($A_p = SSA \cdot m_p$).

Two other parameters were also introduced, according to an operative point of view.

$$R_p = \frac{m_p}{m_w^0} \quad (3)$$

where m_p refers to the mass of powder and $m_W{}^0$ to the mass of water and

$$R_{vd} = \frac{V_{d.sol}}{V_w^0} \quad (4)$$

where $V_{d.sol}$ refers to the volume of Dolapix and $V_W{}^0$ to the mass of water.

Furthermore, a dependance among the parameters can be also identified as follows.

$$\varphi_p = \frac{R_p \rho_w}{R_p \rho_w + (1 + R_{vd})\rho_p} \quad (5)$$

where ρ_w and ρ_p refers to the densities of water (1 g/cm^3) and HA (3.16 g/cm^3), respectively and

$$\beta = \frac{\omega_d^{d.sol} \rho_{d.sol}}{SSA \cdot \rho_w} \frac{R_{vd}}{R_p} \quad (6)$$

where $\omega_d^{d.sol}$ refers to the concentration of dispersant active molecule (25 wt%) and $\rho_{d.sol}$ refers to the density of Dolapix (1.1 g/cm^3).

The effect of calcination temperature, powder and dispersant amount on the colloidal stability of the HA slurries was determined by zeta potential and pH measurements (Figure 2.7).

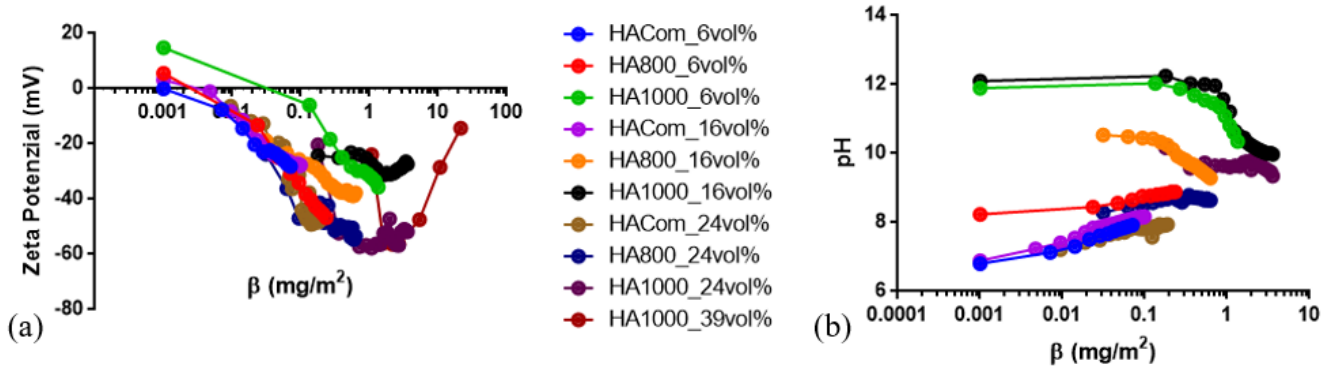

Figure 2-7: a) zeta potential; b) pH as function of β for non-calcined and calcined HA powder

In particular, the parameter β was introduced, defined as the mass of active dispersant molecule (m_d) per unit of total surface area of the powder.

As increasing calcination temperature up to maximum value 1000°C, the slurries become more stable, resulting in decreased of corresponding absolute zeta potential curve due to repulsion of large HA particles. As shown in Fig. 2.7 (a), the HA1000 suspension with powder concentration 24 vol% showed a absolute minimum zeta potential value. The amount of dispersant used was referred to the particle specific surface area, because the degree of stabilization also depends mainly on the amount of dispersant adsorbed on the solid particle's surfaces. Additionally, it is worthwhile to consider this parameter with the comparison of specific surface area of calcined and non-calcined HA powder.

The zeta potential of HA slurries was decreased as amount of dispersant "Dolapix CA" increased, so consequently maximum zeta potential in absolute value was observed at 2.43mg/m^2 of β. Meanwhile, the pH of slurries leads toward average value 9 by increasing dispersant amount shown in Figure 2.8.

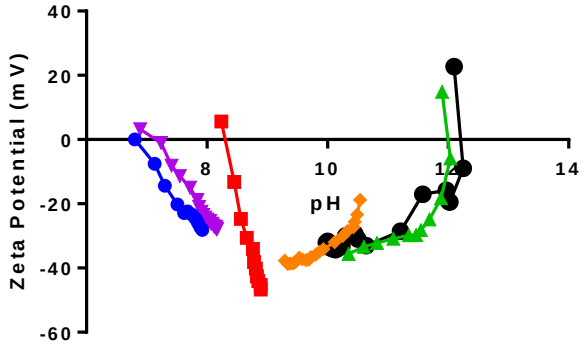

Figure 2-8: pH as function of zeta potential for non-calcined and calcined HA powder

The effect of solid loading on the flow behavior of slurries prepared from calcinated HA at 0, 800 and 1000°C were thoroughly investigated by measuring the viscosity against shear-stress. Figure 2.9. shows the viscosity-shear rate curves of slurries prepared from different volume percentage such as 6, 16 and 24 vol% of solid loading of HA, respectively. We observed that viscosity of all the prepared slurries shown in Table 3.1, was decreased significantly as increasing the shear rate from 0.1 to 1000 pa, that exhibit the shear thinning behavior of slurries. At 0.1pa, the continuous phase liquid was immobilized within large flocs network of HA slurries. At specific high shear rate, the flocs network breaks down into small and more order flocs in trapped liquid phase, suddenly a large drop in viscosity was observed. Additionally, it is clearly demonstrating that, for a given shear rate, an increase in the slurry solid loading results in a significant rise in the slurry viscosity. Figure 2.9 a. shows the viscosity-shear stress curves of slurries prepared from different volume percentages (6, 16 and 24 vol%) of solid loading of non-calcinated HA. The maximum solid loading of non-calcinated HA was observed 24vol%, because of more flocculated behavior of non-calcinated HA slurry as compared to calcinated HA slurry.

A significant decreased in the viscosity was observed in same range of shear stress when calcinated HA at both 800 and 1000°C slurries were studied. This significant reduction in viscosity is corelated with large reduction in specific surface area and specific increase in particle size of HA powder after treating at 800 and 1000°C. It was observed that the tremendous improvement in the flow behavior of calcinated HA slurries. However, the highest solid loading for calcinated HA at 1000°C was found to be 39vol%. Because calcination at high temperature changes the physical properties of power give the chance to prepare the high solid loading slurries.

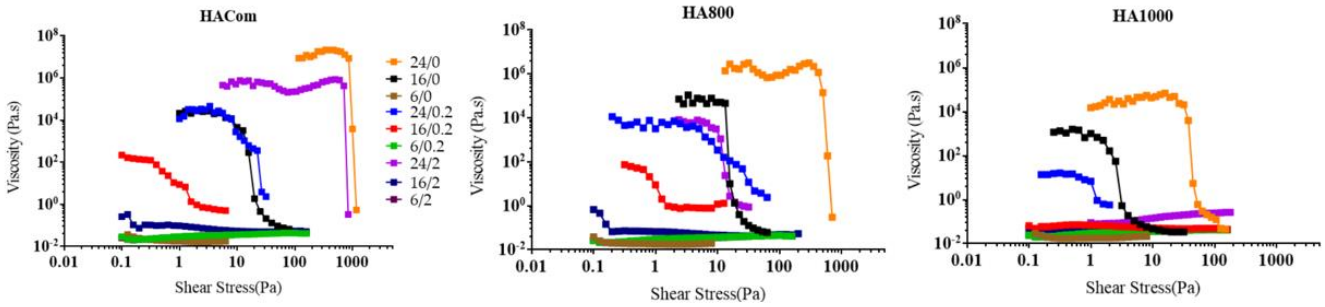

Figure 2-9: Viscosity-shear rate relationship of slurries prepared with a) non calcinated HA, b) HA calcinated at 800°C and c) HA calcinated at 1000°C.

The same results are also qualitatively represented in Figure 2.10, where viscosity was calculated at constant shear stress 10Pa against dolapix/water (vol%) with different solid loading. It is appreciable that with increasing the solid content both dispersant and calcination temperature play crucial role in tuning the viscosity, particularly the thermal treatment, showed a tremendous effect on rheological properties of HA slurries.

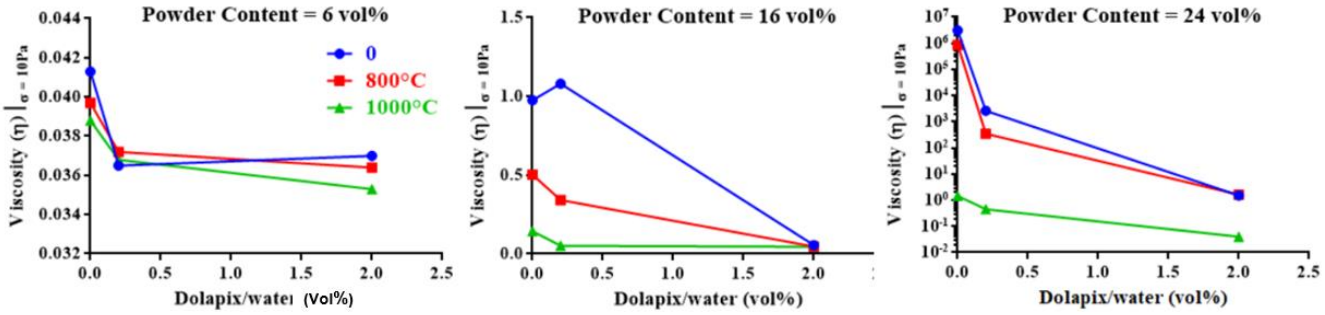

Figure 2-10: viscosity as a function of "β" at shear stress 10pa for the HA slurries to studies the effect of solid loading, calcination temperature and dispersant amount.

To highlight the differences between the behaviour of the slurries of various calcinated powders, as well as the effect of the solid loading and dispersant amount, the rheological data were also co-related with β coefficient (Figure 2-11).

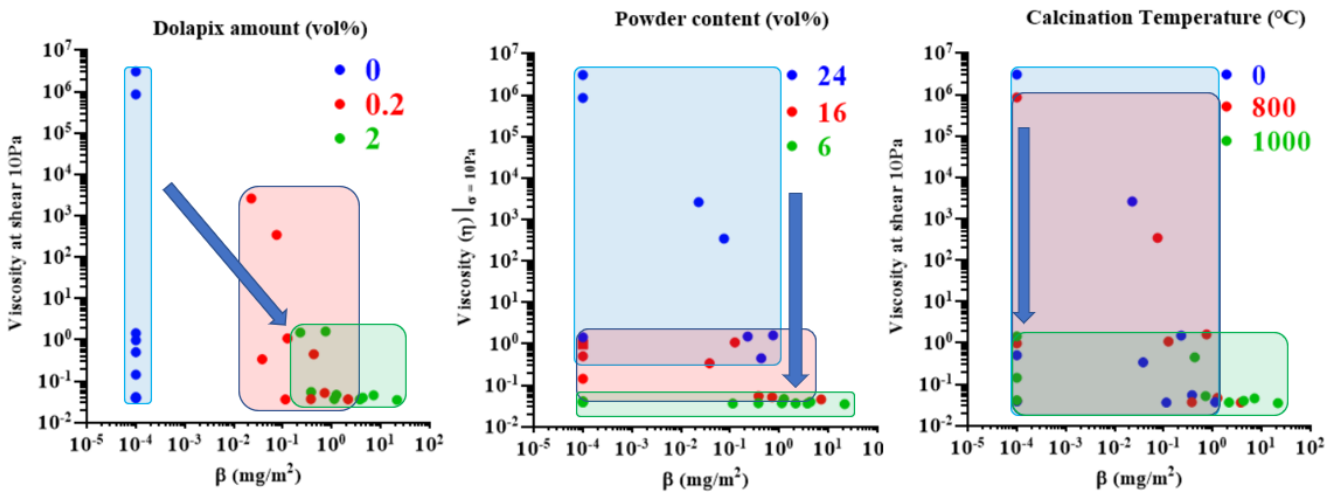

Figure 2-11: Viscosity – β relationship of HA slurries

As a general behaviour for all the slurries, the viscosity increases with increasing solid phase. For low solid loadings, the distance between particles in slurries allows water molecules to flow easier, thus reducing the stress required to move the slurry. At higher solid loadings, less liquid is available between the particles, causing the particles to collide and stick together, leading even to massive agglomeration. The lowest viscosity was observed by HA1000 slurry prepared with solid loading 24 vol% and 2 vol% of dispersants, in agreement with its lower specific surface area. However, at 6 vol% the HA1000 slurries have the lowest viscosity. The calcination temperature is capable to vary the physical properties of powders, namely reducing the SSA, allowing the preparation of higher solid loading slurries.

In addition, dynamic frequency sweep measurements of slurries were performed in order to understand the flow behaviour of prepared slurries by non-calcinated and calcinated HA at 800 and 1000°C. These experiments examine the elastic and viscous moduli against frequency sweep at controlled shear stress 10Pa for different solid loading of non-calcinated and calcinated HA at 800 and 1000°C with various vol% of solid loading and dispersant amount. Nevertheless, it is widely recognized that the estimation of the yield strength of a ceramic suspension can be achieved through the analysis of dynamic stress sweep curves. One potential approach for measuring the yield strength of a ceramic suspension involves identifying the point at which the elastic modulus curve intersects with the viscous modulus curve [54].

Figure 2-12a shows the elastic moduli as a function of frequency at constant shear stress for different volume percent (6, 16, 24 vol%) of solid loading of HA and Figure 2.12b shows the elastic moduli as a function of frequency at constant shear stress for non-calcinated and different calcinated HA slurries.

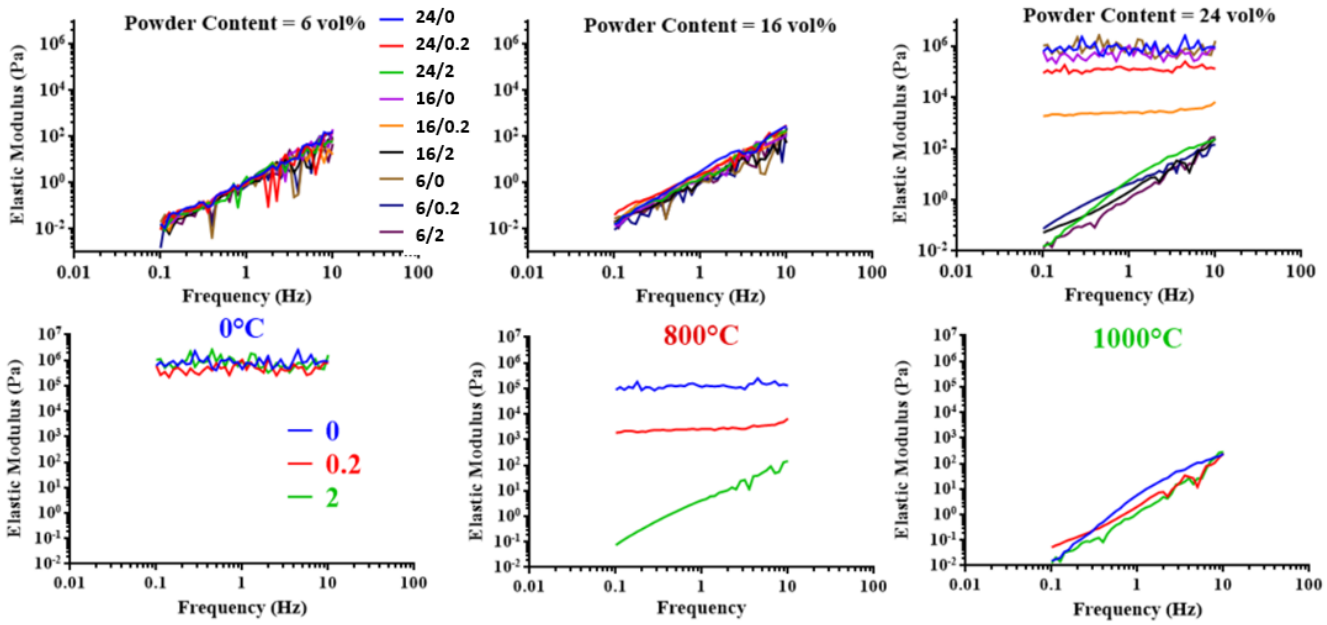

Figure 2-12: Elastic moduli as a function of frequency (a) for different powder content (b) for non-calcinated and different calcinated HA slurries at constant shear stress.

Minor changes in dispersant amount were associated to significant variations of the rheological properties of HA slurries. The calcination temperature had also a significant contribution on suspension stability, while dispersant showed a clear transition as the powder concentration increased. This improvement in rheological behaviour is ascribed to large decrease in the specific surface area of HA powder by heat treatment. It was observed that the surface area of the non-calcinated HA powder, that was approximately 96 m^2/g, was significantly decreased to 29 m^2/g and 5 m2/g for powder heat-treated at 800 and 1000 ℃, respectively. In addition, the non-calcinated powder is distinguished by a large pore volume percentage when compared to those heat-treated at 800 and 1000 ℃ [24, 37]. Figure 2.13 shows the elastic moduli was calculated at constant frequency 1Hz against dolapix/water (vol%) with different powder concentrations. It is appreciable that with increasing the solid content both dispersant and calcination temperature play an important role in tuning the elastic moduli, particularly the thermal treatment, showed a tremendous effect on rheological properties of HA slurries.

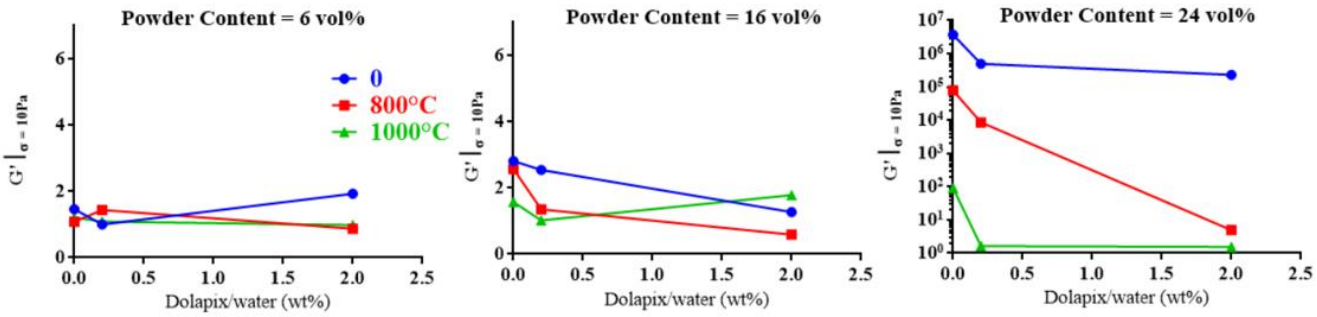

Figure 2-13: Elastic moduli as a function of dispersant/water for non-calcinated and different calcinated HA slurries at constant frequency 1Hz for different powder content.

Based on the results, it is feasible to prepare HA slurries with a substantial solid loading of 39vol% using HA powder subjected to heat treatment at 1000°C, exhibiting favourable rheological properties suitable for casting and 3D printing process.

The calcination treatment of the HA powder resulted in the formation of more rounded particles intercalated to micron-size pores (Figure 2.14) because of thermal activation of surface diffusion processes, which only slightly reduced the initial powder particles' coalescence and prevented grain growth. SEM pictures indicate that HA grains are tightly linked together and have a spherical pore structure, demonstrating that the calcination treatment was successful in conserving enough driving energy to produce widespread surface and grain-boundary diffusion and full neck growth between particles.

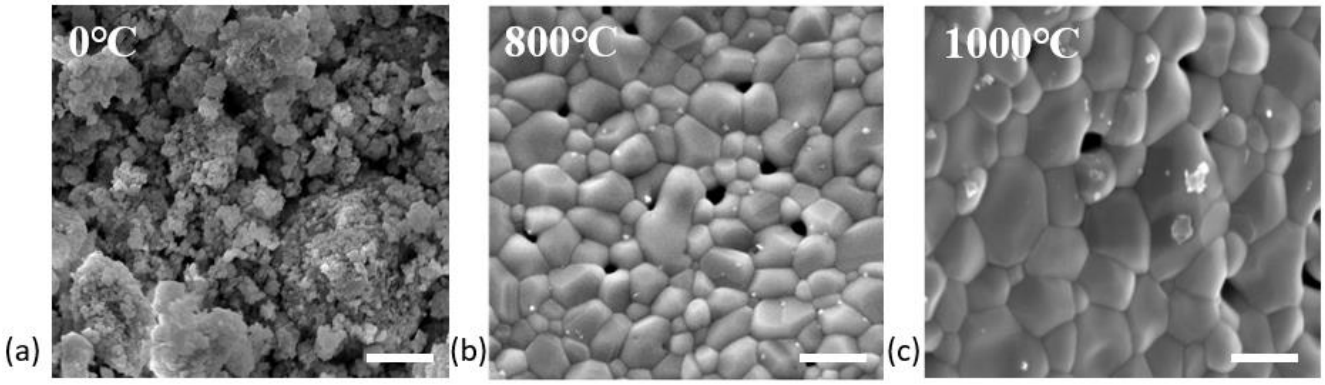

Figure 2-14: SEM image of surface of a) HA calcinated at 800°C and b) HA calcinated at 1000°C bodies

2.2.2. Rheology of ion-doped hydroxyapatite slurries

The stoichiometric and ion-doped HA powders exhibited similar XRD diffraction patterns, in accordance with JCPDS Card No. 09–0432, with no secondary crystalline phases (Figure 2.15). The XRD patterns exhibits strong peaks at 25.87°, 28.96°, 31.77°, 32.90°, and 39.85° values, which correspond to the planes of the HA crystal lattice. The XRD pattern of MgHA has strong peaks at 25.87°, 28.96°, 31.74°, and 34.04° angle. The observed peaks have a resemblance to the peaks seen in the XRD pattern of HA, but with a minor shift towards lower angles. This suggests that the introduction of magnesium ions has caused a slight expansion of the HA lattice because of smaller ionic radius of strontium compared to calcium. The XRD pattern of SrHA has main peaks at 2θ values of 25.87°, 29.28°, 31.81°, 32.99°, and 39.84°, which have been somehow displaced towards higher angles. This suggests that the incorporation of strontium ions has caused a slight contraction of the size of the HA lattice due to larger ionic radius of strontium compared to calcium. While XRD pattern of MgSrHA has significant peaks at 25.84°, 31.71°, 32.88°, and 34.01°, positioned in between the XRD patterns of MgHA and SrHA. This suggests that the presence of magnesium and strontium ions has caused an intermediate effect on the HA lattice. This intermediate effect is likely due to the combined influence of the smaller ionic radius of magnesium and the larger ionic radius of strontium.

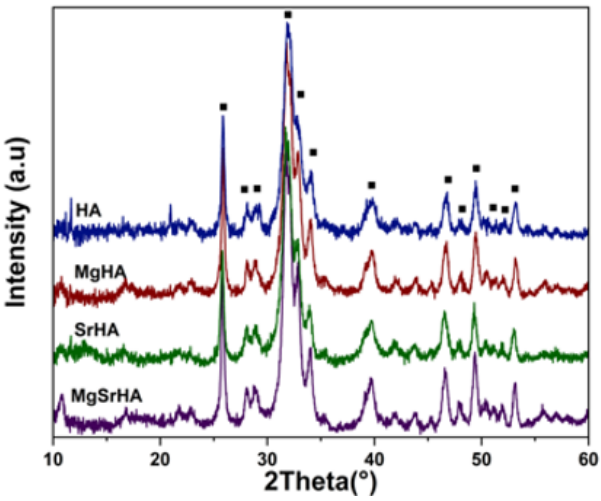

2θ: HA JCPDS 09-432	Plane	2θ: HA	2θ: MgHA	2θ: SrHA	2θ: MgSrHA
25.87	002	25.87	25.87	25.87	25.84
28.96	210	29.08	29.12	29.28	
31.77	211	31.80	31.74	31.81	31.71
32.90	300	32.98	32.92	32.99	32.88
34.04	202	34.08	34.04	34.10	34.01
39.81	310	39.84	39.64	39.89	39.72
46.71	222	46.78	46.71	46.82	46.64
49.46	213	49.52	49.52	49.62	49.40
53.14	004	53.27	53.19	53.96	53.11

Figure 2-15: XRD analysis of stoichiometric and ion-doped HA.

The analysis of the crystal structure by Rietveld analysis (Table 2-IX) reported slightly modified cell parameters in ion-doped HA with respect to the stoichiometric HA, in compliance with partial substitution of calcium with foreign ions [55]. In particular, a slight decrease of c axis was associated to Mg-doping [56], while higher cell volume were calculated for Sr-doped HA [57]. Here, the co-doping

with Mg and Sr was associated to higher volumes, even if lower than reported [58]. Given the constant c/a, no significant lattice distortions were observed with ion-doping.

Table 2-IX: Refined lattice parameters and calculated cell volume for HA and ion-doped HA.

	a-axis (Å)	*c-axis (Å)*	*c/a (-)*	*Vol ($Å^3$)*
HA	9.4297	6.8953	0.731	530.99
MgHA	9.4357	6.8860	0.730	530.94
SrHA	9.4496	6.9159	0.732	534.83
Mg-Sr-HA	9.4521	6.9000	0.730	533.88

The FTIR analysis also presented the typical patterns of hydroxyapatite (Figure 2.16). The vibrational bands appeared at 562 and 603 cm^{-1} were ascribed to O-P-O bending, while peaks at 962 and 1034 cm^{-1} were both attributed to the stretching of PO_3^{-4}, despite a slight calcium deficiency. In addition, the peaks at 874, 1339 and 1456 cm^{-1} associated to CO_3^{2-} group were also found in all patterns. The peak at 632 cm^{-1} and the broad peak at 3427cm^{-1} were attributed to OH^- or structural H_2O [59, 60]. The doping of Sr^{2+} or Mg^{2+} ions did not cause a shift in the position of the characteristic bands, but it affected the intensity of the broad peak at 3427cm^{-1} associated to OH^{-1}, indicating that the samples had slight calcium deficiency due to the ion doping [61].

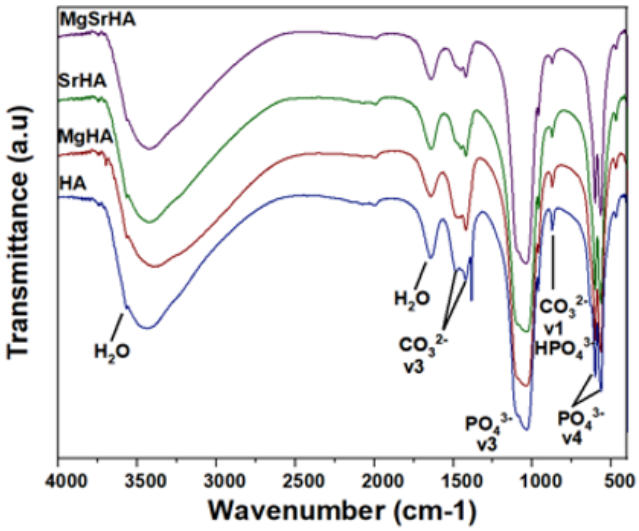

Wavenumber (cm^{-1})	Type of bond	Functional groups
3429	O-H bending	H-O-H
1642	O-H stretching	H-O-H
1419	C-O bending	CO_3^{2-}
1035	P-O stretching	PO_4^{3-}
960	C=O stretching	CO_3^{2-}
602	P-O stretching	PO_4^{3-}
564	P-O-H stretching	PO_4^{3-}

Figure 2-16: FTIR analysis of stoichiometric and ion-doped HA.

The weight loss (~ 4-6%) observed by TGA (Figure 2.17) below 200°C is attributed to the evaporation of physiosorbed/structural water; the one recorded at higher temperatures was ascribed to the evaporation of carbonate groups [27] also confirmed in FTIR analysis.

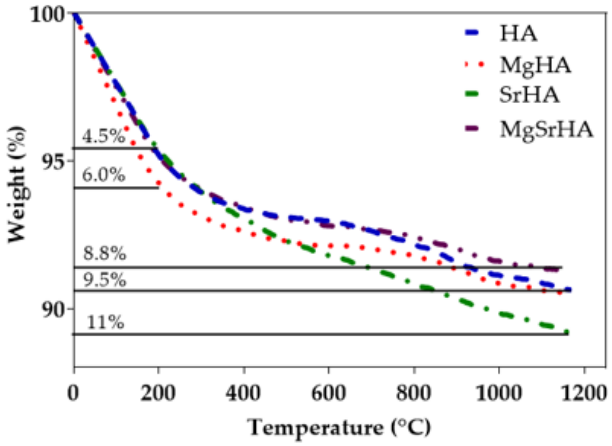

Sample	Mass Change 20-200°C (wt%)	Mass change 200-1200°C (wt%)
HA	-4.5	-9.5
MgHA	-6.0	-9.5
SrHA	-4.5	-11.0
MgSrHA	-4.5	-8.8

Figure 2-17: Thermogravimetric analysis (TGA) of stoichiometric and ion-doped HA.

The thermal analysis revealed the highest weight losses for SrHA, perhaps caused by the strain and disruption in the lattice structure of HA owing to the incorporation of bigger Sr^{2+} instead of the native Ca^{2+} [62]. These flaws may serve as starting points for thermal decomposition by the breaking of bonds and the release of chemically bonded water molecules during heating. SrHA exhibits a higher susceptibility to carbonation compared to pure HA and MgHA. Sr^{2+} serve as nucleation sites for the formation of carbonate, resulting in higher weight loss due to decomposition of carbonates at higher

temperature. Mg-doped HA showed the highest weight loss below 200°C, possibly ascribable to the higher affinity of Mg^{2+} exposed at the surface with water[63].

The elemental composition confirmed the presence of the doping ions in amounts very close to the nominal composition of the starting mixture (Table 2-X), as well as the calcium-deficiency, with Cations/P mole ratios lower than 1.67 as shown by FTIR analysis.

Table 2-X: Elemental analysis of stoichiometric and ion-doped HA.

Sample	Ca/P (mol%)	(Ca+Mg+Sr)/P (mol%)	Mg/(Ca+Mg) (mol%)	Sr/(Ca+Sr) (mol%)
HA	1.64±0.01	1.64±0.01	0	0
MgHA	1.54±0.01	1.61±0.01	4.91±0.02	-
SrHA	1.52±0.00	1.61±0.00	-	5.29±0.03
Sr-Mg-HA	1.53±0.01	1.57±0.01	2.41±0.07	2.67±0.07

The specific surface area (SSA), particle size distribution and porosity of stoichiometric and ion-doped HA powders were measured (Table 2-XI).

Table 2-XI: Particle size, specific surface area and porosity measurements.

Sample	Particle size (μm)			SSA	Porosity
	d10	d50	d90	(m^2/g)	(%)
HA	0.24	0.68	5.15	115.95	51.35
MgHA	0.32	0.72	3.44	87.29	60.91
SrHA	0.24	1.37	10.21	94.06	44.50
MgSrHA	0.23	0.64	4.59	85.86	40.77

The specific surface area of powders decreased with ion doping compared to the stoichiometric HA. The different specific surface area is ascribable to different particle size and porosity of the HA particles [64, 65] (see Table 2. XI). MgHA powder with greater medium particle size (d50) than the stoichiometric HA exhibits a corresponding increase of porosity due to the increased interparticle spacing and reduced densification efficiency associated with larger particles, while MgSrHA powder exhibits the opposite effect.

The microstructure of the powders evidenced a size range 50-100 nm for the samples and a transition from needle-like to rod-like morphology of the particles in the case of ion-doped HA [66, 67], as reported in Figure 2.18.

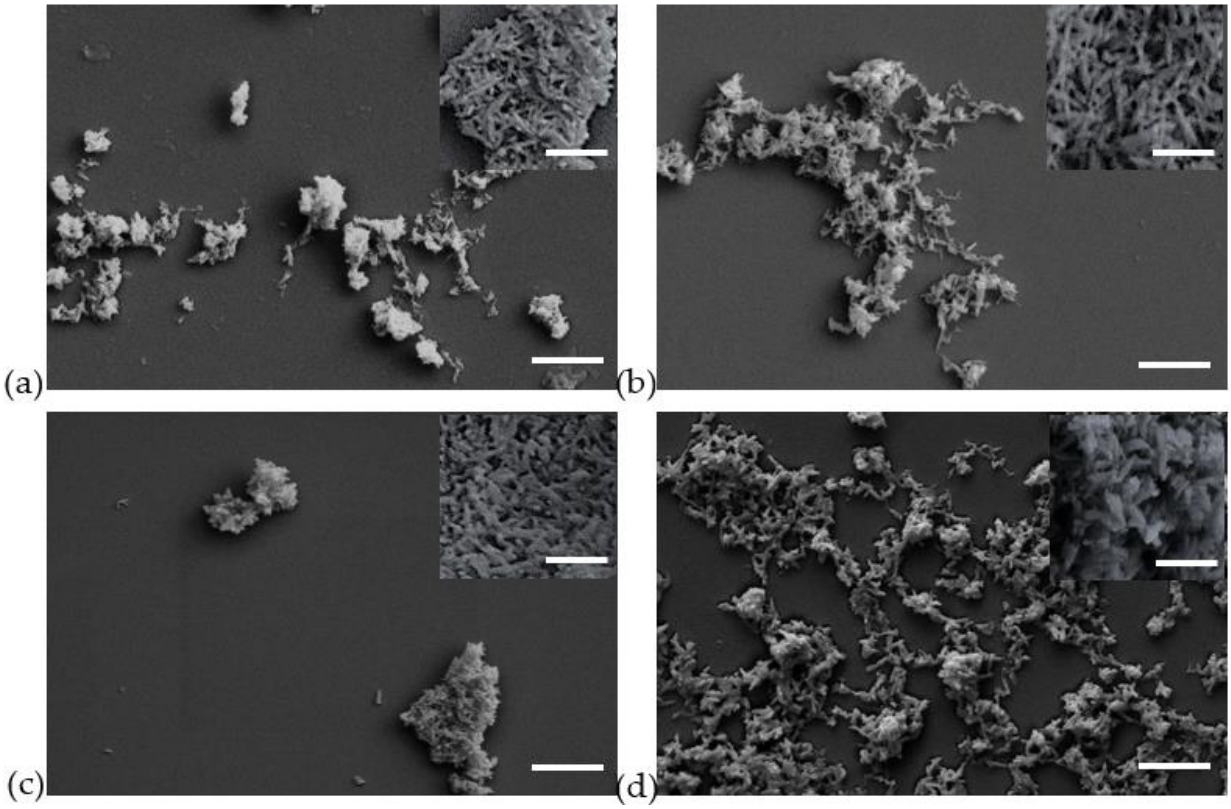

Figure 2-18: SEM micrographs of HA (a), MgHA (b), SrHA (c) and MgSrHA (d). Figure scale bars = 1 µm, Inset scale bar = 200 nm.

Two concentrations of HA slurries, 33 wt% and 49 wt%, were selected for rheological study because they represent two crucial phases in the manufacturing of HA ceramics. With a concentration of 33 wt%, the slurry maintains a relatively fluid consistency, which is crucial for processing methods such as vat photopolymerization [68-70]. The slurry, when it reaches a concentration of 49 wt%, exhibits a higher viscosity, which is essential for processing techniques like extrusion [71] and compression moulding [72]. Highly concentrated ceramic slurries are crucial for the development of scaffold due to more viscous and consistent mixture, which is important for fabricating complex-shape scaffolds through various fabrication techniques like injection moulding and 3D printing. The increased particle packing density further improves the mechanical strength, resilience, and elasticity modulus of the scaffolds, allowing them to withstand the stresses and strains experienced inside the human body.

The colloidal stability of the slurries, as estimated by the measured ζ potential values, increased with increasing the amount of dispersant and the extent of Mg^{2+} ions incorporated into HA, especially in the case of 33 wt% slurries (Figure 2.19).

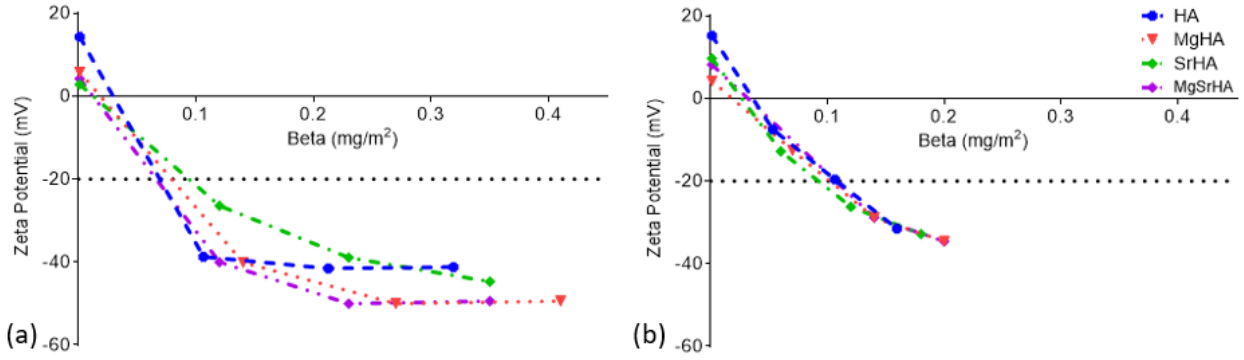

Figure 2-19: ζ potential as function of β for slurries with increasing powder amount of stoichiometric and ion-doped HA: a) 33 wt% and b) 49 wt%.

The variation of β was obtained by keeping constant the amount of powder and increasing the amount of dispersant. Positive zeta potentials were obtained in absence of dispersant (i.e., β = 0); significant variations were obtained by adding even small amounts of dispersant, up to values in the range -30 to -40 mV, according to good stability of sample.

Viscosity-shear stress curves and 3D surface response of the stoichiometric and ion-doped HA slurries at different solid loading (33 and 49 wt%) and dispersant amount (0, 3, 6 wt%) were collected (Figure 2.20).

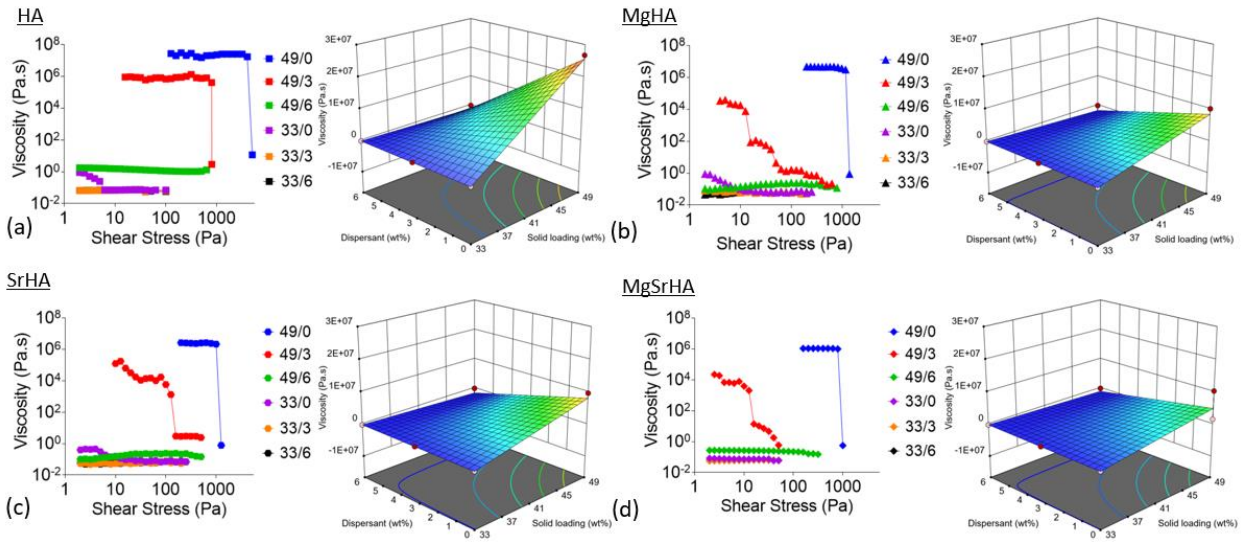

Figure 2-20: Viscosity curves as a function of shear stress and 3D surface plots for the effect of solid loading and dispersant on the viscosity at a shear stress of 5 Pa for HA (a), MgHA (b), SrHA (c) and MgSrHA (d) slurries.

At low shear stresses the high viscosities for the more concentrated suspensions (49 wt%) is the result of the aggregation of the solid particles to form complex three-dimensional networks. Upon increasing the shear stress, the viscosity of the slurries gradually decreases, due to the partial to complete breaking of agglomerates, thus revealing a shear-thinning behavior of the slurries, except for the ones of stoichiometric HA whose viscosity remains almost constant till the highest stresses applied. The liquid within agglomerates remains locally immobilized at low shear stresses, but when shear stress rises, it is released decreasing the friction in the flow direction. The stoichiometric and ion-doped HA slurries showed significant variation in viscosity in relation with their zeta potential and specific surface area, particularly at the highest solid loading (49 wt%). The stoichiometric HA slurries exhibited the highest viscosities as compared to ion-doped HA at constant solid loading and dispersant concentration, possibly caused by particle flocculation. The MgHA and MgSrHA slurries exhibited lower viscosities, possibly ascribable to the higher zeta potential (in absolute value) and lower SSA, associated also to the higher affinity of Mg ions with water molecules [73]. At the lowest solid loading (33 wt%) the viscosities are several orders of magnitude lower (even lower than 1 Pa·s) and a Newtonian behavior is observed. The 3D surface response graphs of stoichiometric and ion-doped HA slurries come helpful in observing the significant increase in viscosity at constant shear stress (5 Pa) passing from 33 to 49 wt% of solid loading. On the other hand, the increase of dispersant in the range 0-6 wt%, significantly decreased the viscosity of the slurries, mainly due to the efficient role of the anionic polyelectrolyte absorbed on the surface of

the particles in reducing the mean agglomerate size. It was also noticed that the dispersant amount was more effective at the highest solid loading.

Considering stoichiometric HA, the threshold of solid loading to obtain a homogeneous and flowable paste was represented by 49 wt% (i.e., 23 vol%). Interestingly, higher maximum solid loading was experienced for ion-doped HA slurries (e.g. 59 wt%), mainly ascribable to the lower SSA.

The oscillatory tests performed on stoichiometric and ion-doped HA slurries to investigate their viscoelastic behavior are shown in Figure 2.21 and Figure 2.22. In Figure 2.20, typical results of the amplitude sweep tests on stoichiometric and ion-doped HA slurries for the formulation 49/0 are plotted; in such tests the shear stress was gradually increased from 1 to 1000 Pa at constant frequency of 1 Hz. The critical shear stress at which the moduli decrease occurs at different values for the different slurries, but a linear viscoelastic behavior was observed between 1 and 100 Pa of shear stress for all the slurries, except for the MgSrHA, for which the breaking of agglomerates occurred at lower stress (around 50 Pa). A shear stress of 5 Pa was selected as amplitude of oscillation in the frequency sweep tests for all the samples.

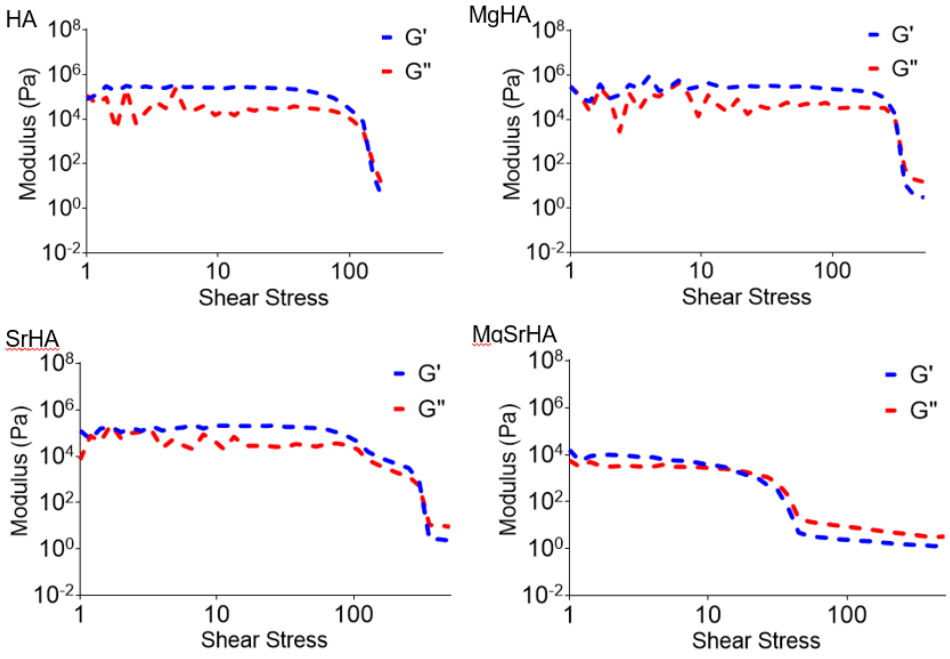

Figure 2-21: Mechanical moduli curves as a function of shear stress for 49/0 slurries: (a) HA, (b) MgHA, (c) SrHA and (d) MgSrHA.

The effect of solid loading and dispersant amount on the elastic moduli of the materials as a function of shear stress are shown in Figure 2.21. The more diluted slurries (33 wt%) have elastic moduli around 1-

10 Pa and their values are almost not dependent on the dispersant amount. Conversely, the addition of small amounts of dispersant in the concentrated (49 wt%) ion-doped HA slurries significantly decreased the values of elastic moduli, even more than stoichiometric HA slurries, bringing them from values around 10^5 Pa down to values similar to the ones for the diluted slurries with the addition of 6 wt% of dispersant, except for the MgHA slurry.

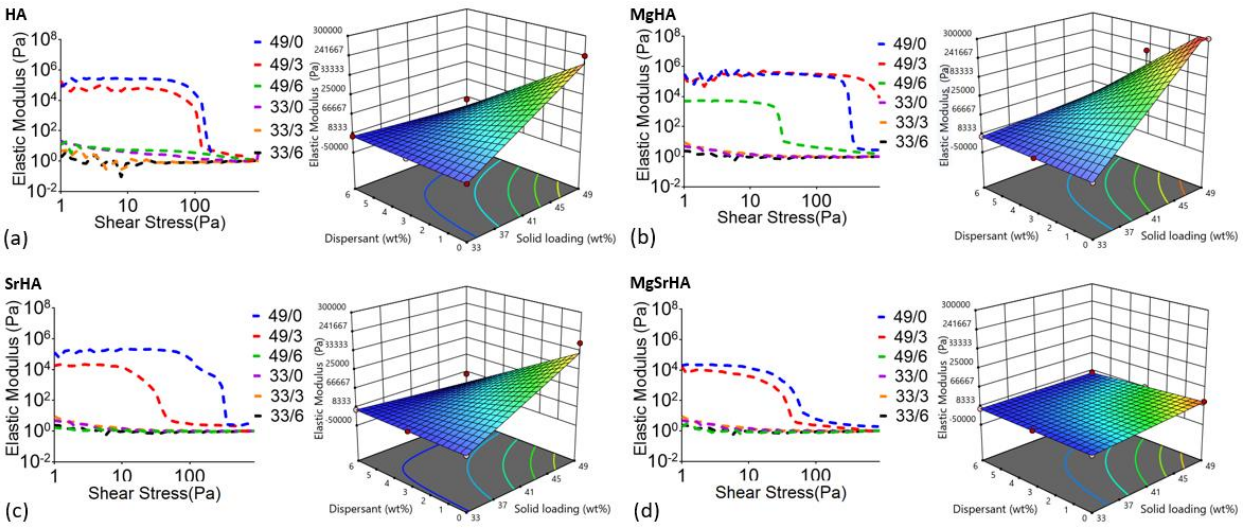

Figure 2-22: Elastic moduli curves as a function of stress and 3D surface plots for the effect of solid loading and dispersant on the elastic moduli at a shear stress of 5 Pa for HA (a), MgHA (b), SrHA (c) and MgSrHA (d) slurries.

The dependence of elastic moduli on frequency of oscillation for the different slurries was also studied to investigate the stiffness of the materials (Figure 2.23). Also in this case, the effect of the dispersant on the more diluted slurries (33 wt%) is negligible, while the addition of small amounts of dispersant in the more concentrated slurries (49 wt%) significantly decreases the value of the elastic moduli. In general, we observed that for the samples at 33 wt% of solid loading (33/0, 33/3, 33/6) and for the samples at 49 wt% with the highest amount of dispersant (49/6) the elastic modulus increases with the frequency of oscillation, while the samples 49/0 (and the samples 49/3 for the HA and MgSrHA slurries) the elastic modulus is constant with the frequency. This suggests a transition between a solid-like behavior to a gel-like behavior by changing solid loading and dispersant amount.

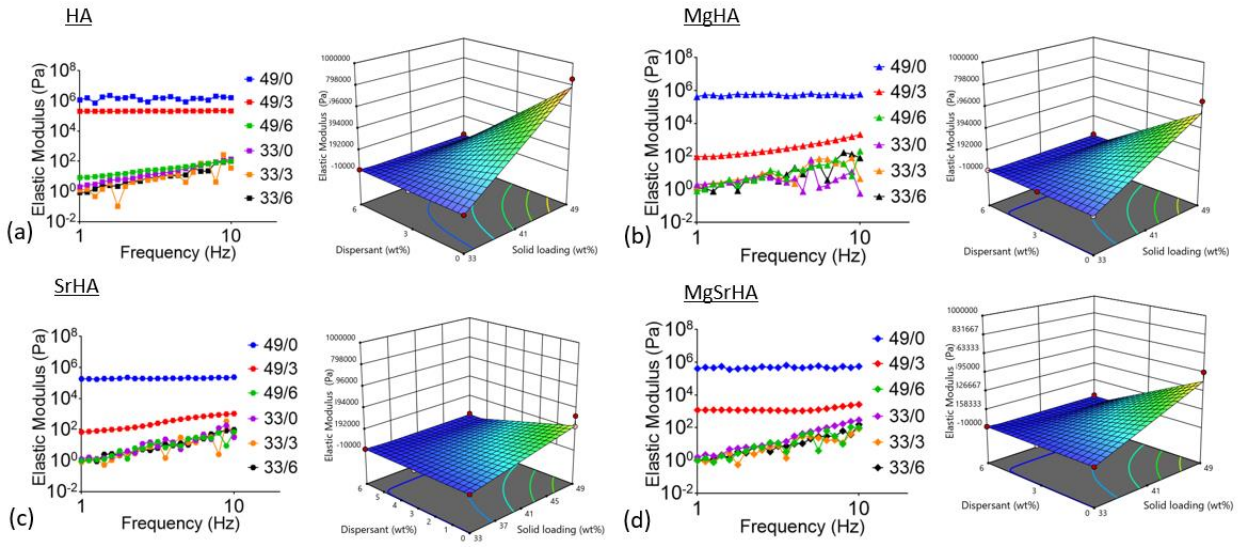

Figure 2-23: Elastic moduli curves as a function of frequency and 3D surface plots for the effect of solid loading and dispersant on the elastic moduli at the frequency of 5 Hz for HA (a), MgHA (b), SrHA (c) and MgSrHA (d) slurries.

To highlight the differences between the behavior of the slurries of different powders, as well as the effect of the solid loading and dispersant amount, the rheological properties previously collected have been variously compared. In Figure 2.24 is shown the dependence of viscosity on solid loading at different concentration amounts for the slurries of the four powders.

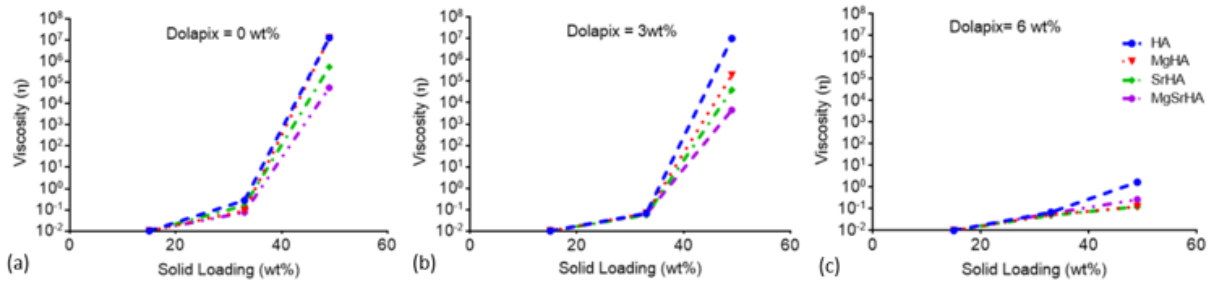

Figure 2-24: Viscosity (at shear stress 5 Pa)-solid loading curves of stoichiometric and ion-doped HA slurries with dispersant. (a) 0 wt%, (b) 3 wt% and (c) 6 wt%.

The common features of all slurries is that the viscosity increases with increasing solid phase. For low solid loadings, the distance between particles in slurries allows water molecules to flow easier, thus reducing the stress required to move the slurry. At higher solid loadings, less liquid is available between the particles, causing the particles to collide and stick together, leading even to massive agglomeration. The lowest viscosity was observed for MgSrHA slurry prepared with solid loading 49 wt% and 0 and 3

wt% of dispersant, in agreement with its lower specific surface area. However, at 6 wt% the MgHA and SrHA slurries have the lower viscosities. The ion-doping in HA result in change the physical properties, low SSA and high zeta potential which allows the preparation of higher solid loading slurries.

The effect of powder amount on the elastic modulus of slurries was also studied (Figure 2.25). Comparable elastic modulus for stoichiometric and ion-doped HA slurries were observed for slurries prepared with highest solid loading, in absence of dispersant. Upon addition of 3 wt% of dispersant, a significant decrease in elastic modulus was observed for ion-doped HA slurries at 49 wt%, while at 6 wt% all the slurries show the same elastic modulus.

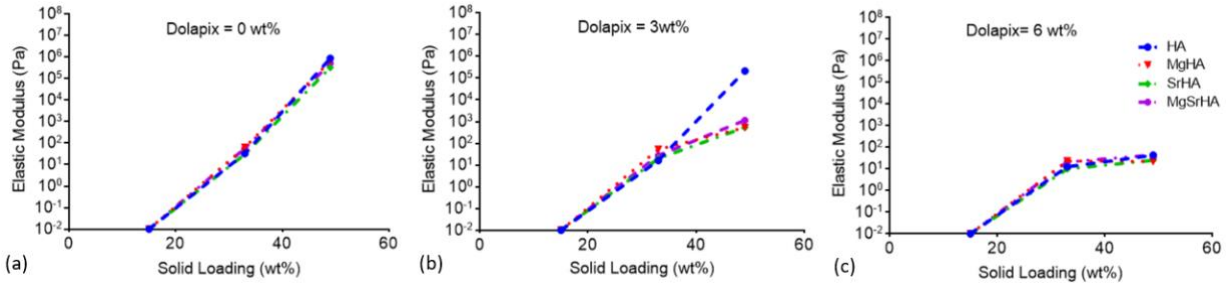

Figure 2-25: Elastic moduli (at frequency 5 Hz) - solid loading curves of stoichiometric and ion-doped HA slurries with dispersant. (a) 0 wt%, (b) 3 wt% and (c) 6 wt%.

The effect of dispersant amount on viscosity and elastic modulus of stoichiometric and ion-doped HA slurries prepared at 33 and 49 wt% is highlighted in Figure 2-26.

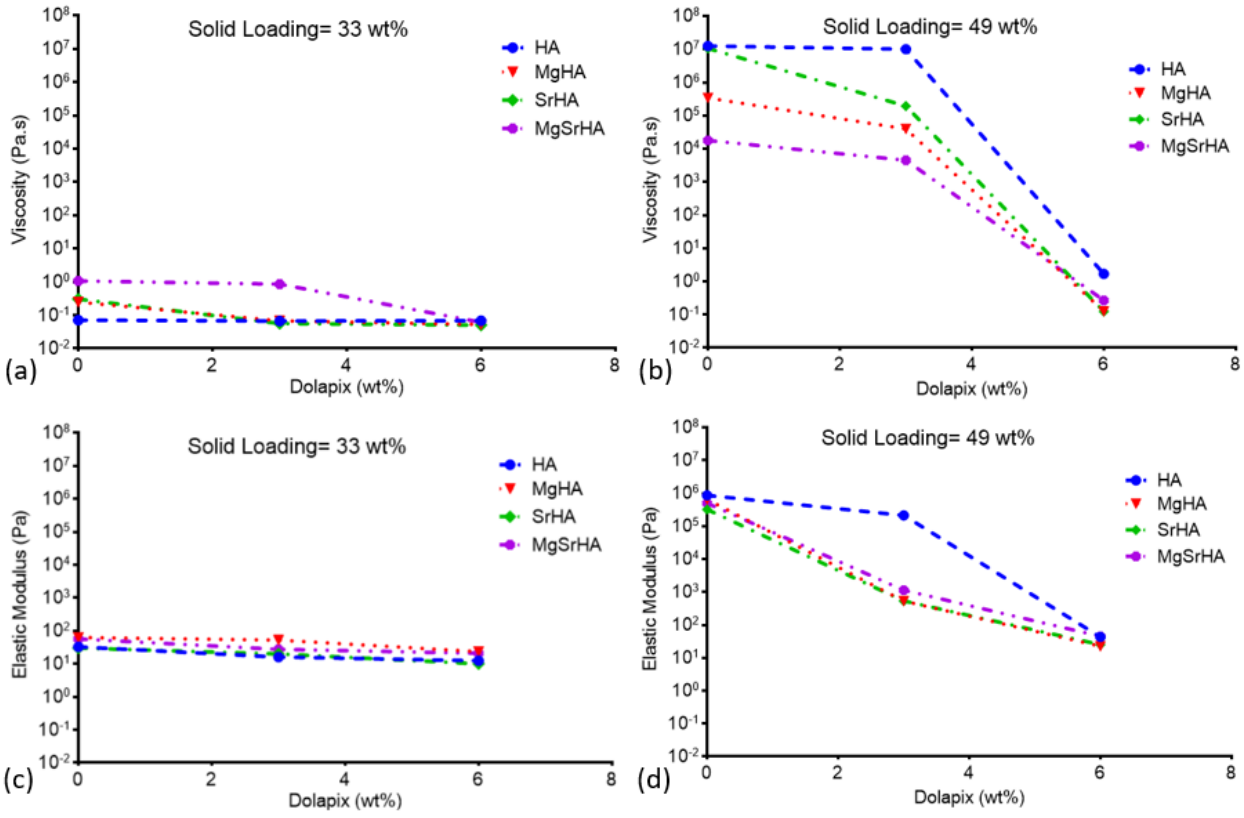

Figure 2-26: Viscosity and elastic modulus of stoichiometric and ion-doped HA slurries at different solid loading

The results revealed that the viscosity and elastic modulus of the high concentrated slurries decreased with increasing amount of dispersant, while is slightly affected for the more diluted ones. Moreover, the effect of dispersant on ion-doped HA slurries was greater than on stoichiometric HA slurries. The dispersant adsorbed on solid particles prevents agglomeration that could cause inhomogeneities into the slurry.

2.2.3. Mechanically reinforced HA scaffold with fibers

Reinforced HA scaffold with carbon fibers

The XRD analysis of carbon fibers and calcinated HA powders are shown in Figure 2.27 a. The XRD patterns exhibited pure HA, with the most prominent peaks corresponding to the (211), (300) and (310) crystallographic planes, as already explained in sub-chapter 2.2.1.

The SEM micrographs of CF and calcinated HA are shown in Figure 2.26b and 3.26c. Micrograph shown in Figure 2.26c, revealed the presence of well-coalesced hydroxyapatite (HA) grains that are interspersed within micron-sized pores.

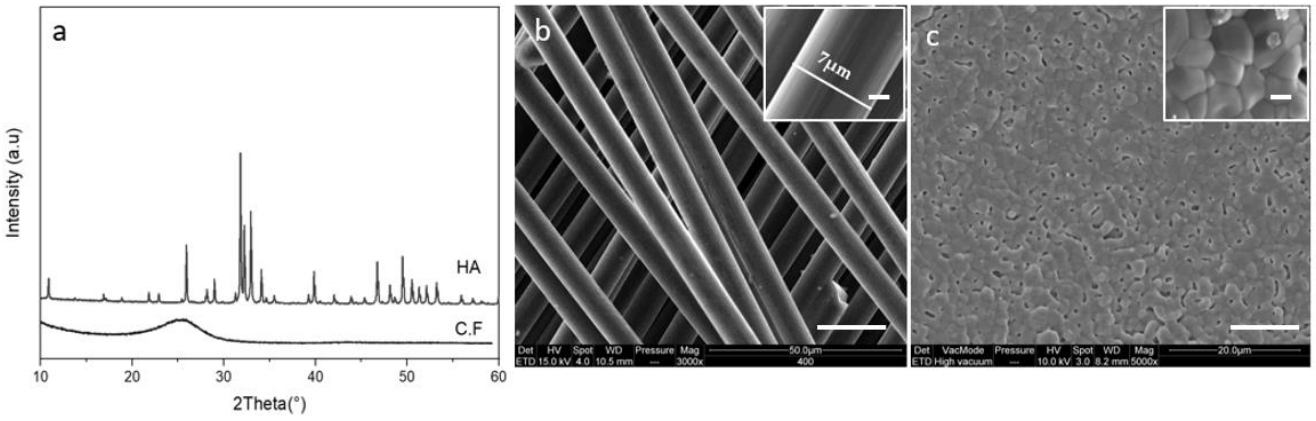

Figure 2-27: (a) XRD (b&c) SEM images of C-fibers and HA, Figure scale bars = 10 µm, Inset scale bar = 1 µm.

C-fibers were protected from decomposition at high temperatures by activation/mineralization of C-fibers. The mineralization of C-fibres by chemical treatments aimed to activate the C fiber surface with COO- groups, suitable for further linking with Ca^{2+} ions and subsequent reaction with PO_4^{-2} groups to achieve fiber coating with HA. This approach is being carried out by using microwave reactors. SEM images of C-fibers after activation through mineralization demonstrate a notable increase in surface roughness, as shown in Figure 2.28. The smooth surface of C-fibers undergoes a transformation to become grooved following the oxidation process, provided deposition sites for the calcium phosphate coating. The surface roughness of carbon fibres enhances their adherence to the matrix by increasing the available bonding area for interfacial interactions between the fibres and the matrix. The formation of grooves or pits on the fibre surface due to oxidation serves as attachment points for the matrix, resulting in a reinforced connection and increased strength of the composite material. Moreover, the presence of roughness on the fibres might enhance their surface energy, hence enhancing adhesion via the formation of hydrogen bonds with the matrix [74].

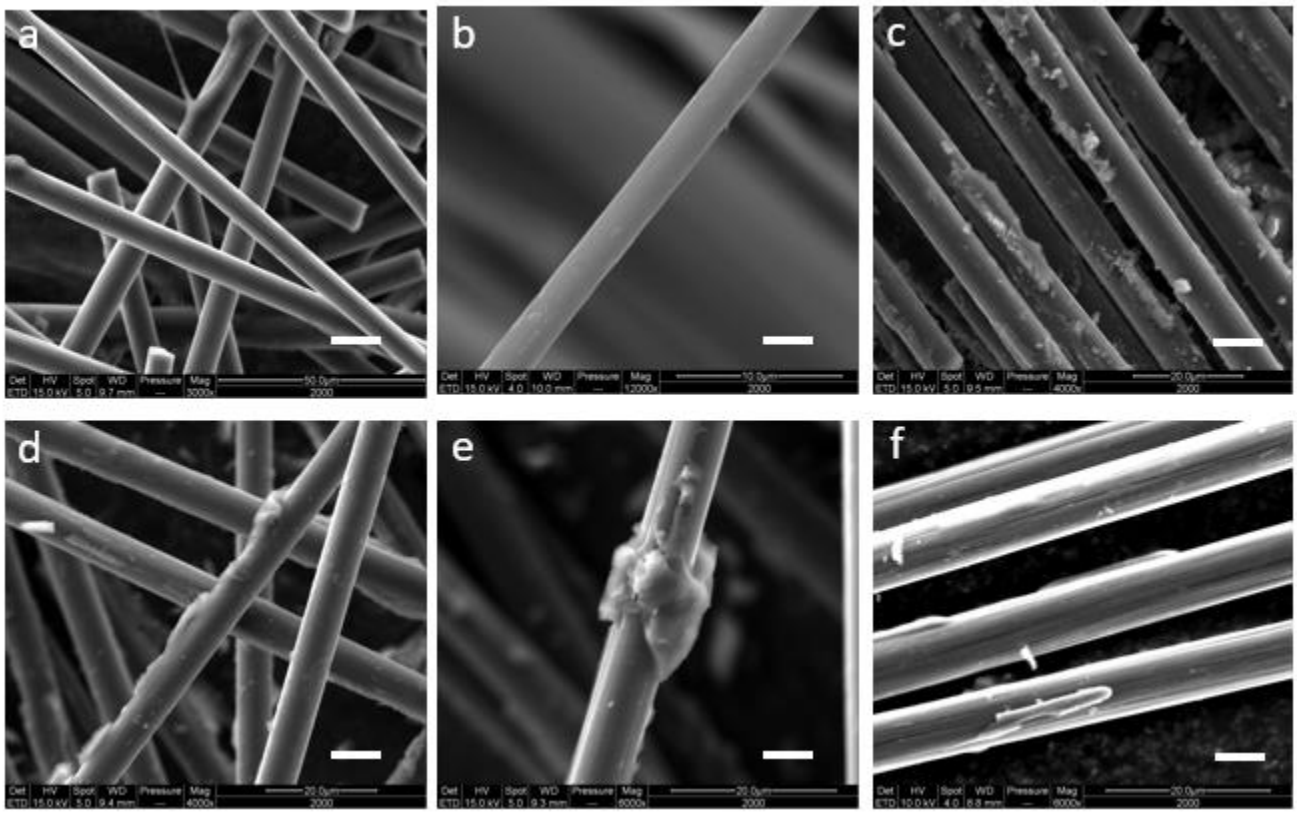

Figure 2-28: SEM images of mineralized carbon fibers (scale bars = 10 µm)

The nature of functional groups on surafce of carbon fibers before and after mineralization was examined by FTIR analysis shown in Figure 2.29. The strong absorbance of C-fibers makes it necessary to use a very low concentration of C-fibers in a KBr powder. The untreated and treated C-fibers was observed to have the stretching vibration of C–H of methyl and methylene groups in the range of 2800–2980 cm^{-1} and the C–C as well as C=C stretching vibration centered at about 1050–1100 cm^{-1} and 1580–1699 cm^{-1}, respectively. After the oxidation treatment of C-fibers with different acids combinations, the broad peak was observed at about 3433 cm^{-1} is assigned to the stretching vibration of hydroxyl groups. New peaks appear at 1368 and 1729 cm^{-1} corresponding to the stretching vibration of C–O and C=O (carboxylic groups, COOH), respectively, which confirm that the surface of C-fibers has been oxidized and etched by the oxidized treatment [23].

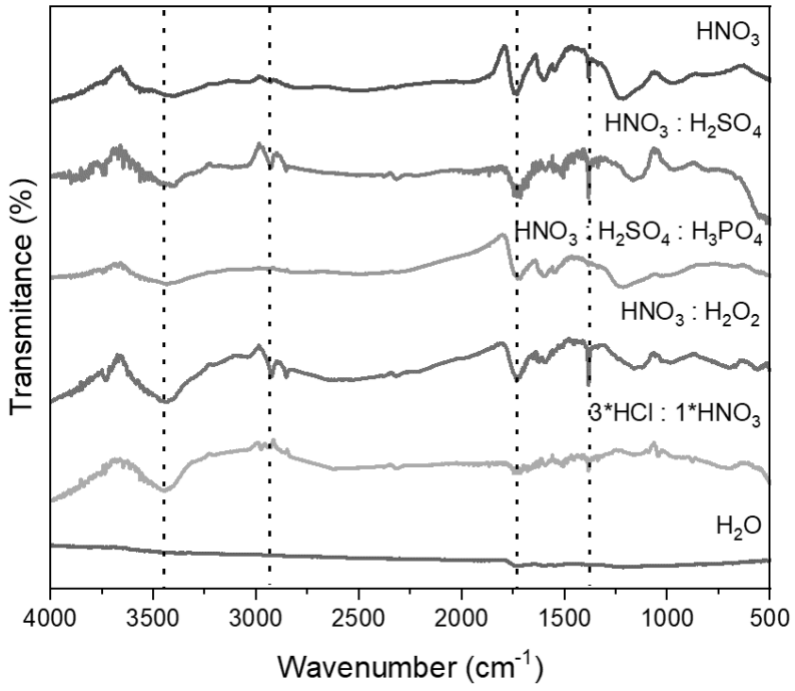

Figure 2-29: XRD of mineralized carbon fibers

SEM images of C-fibers reinforced HA composite before and after sintering are shown in Figure 2.30. C-fibers was observed on the surface of the composite, exposed to N_2 gas flux, were unaffected, while C-fibers embedded in the matrix disappeared after heat treatment. It was hypothesized that decomposition of C-fibers occurs in an oxidative environment activated by HA at high temperatures. Besides, such degradation induced the formation of microporosity in the matrix, as shown by SEM images.

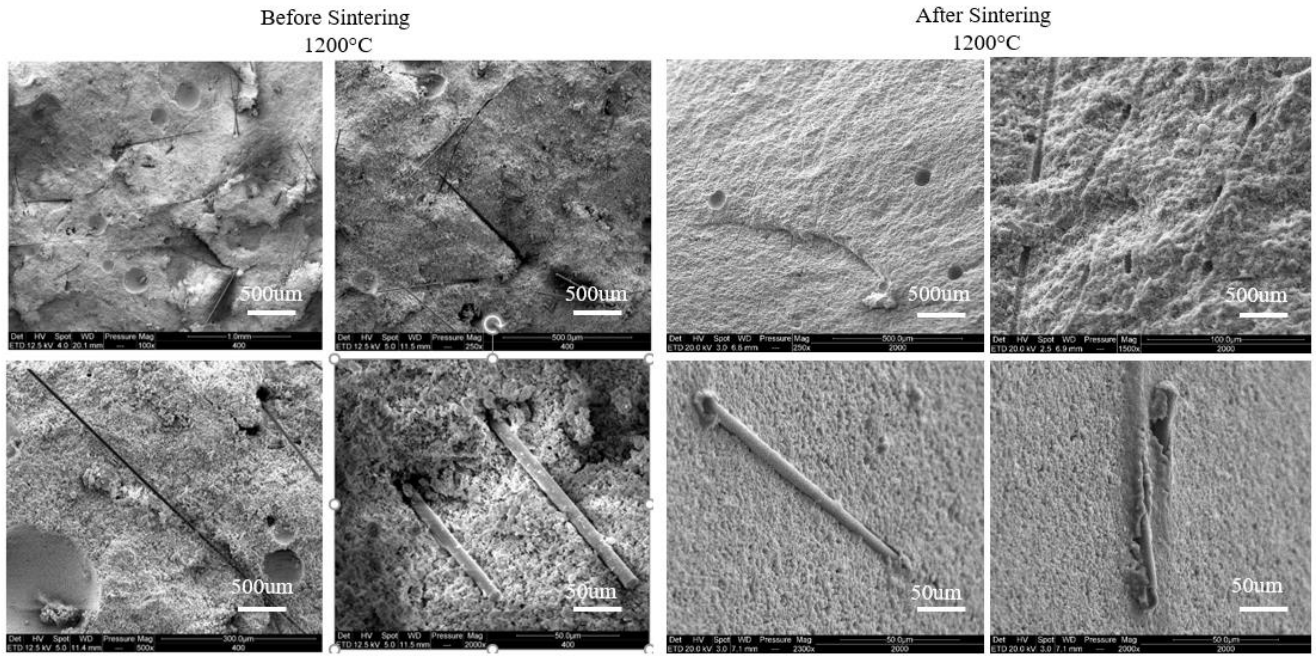

Figure 2-30: SEM images of C-fibers reinforced HA composite before and after sintering.

Mineralized C-fibres introduced into the HA matrix was also decomposed when subjected to high temperature treatment. Due to several technical difficulties in manipulation and processing of the C-fibers, also giving problems in achieving good dispersion of the fibers and also with the purpose to limit excessive complexity in the process, the addition/impregnation of 3D-fibrous structures (alumina + >10% silica), hereinafter called blankets, was considered for the reinforcement of HA.

Reinforced HA scaffold with alumina fibers

I. The XRD patterns of alumina-silica fibers before thermal treatment exhibited amorphous structure (Figure 2.31 a). Conversely, after thermal treatment at 1200°C for 1h a lot of phases were detected, thus the thermal decomposition of fibers was hypothesized, possibly due to the presence of silica ≥ 27 wt%. The micrograph of the sintered alumina-fiber hydroxyapatite composite showed that the fibers had been completely oxidized and were not visible in the micrograph.

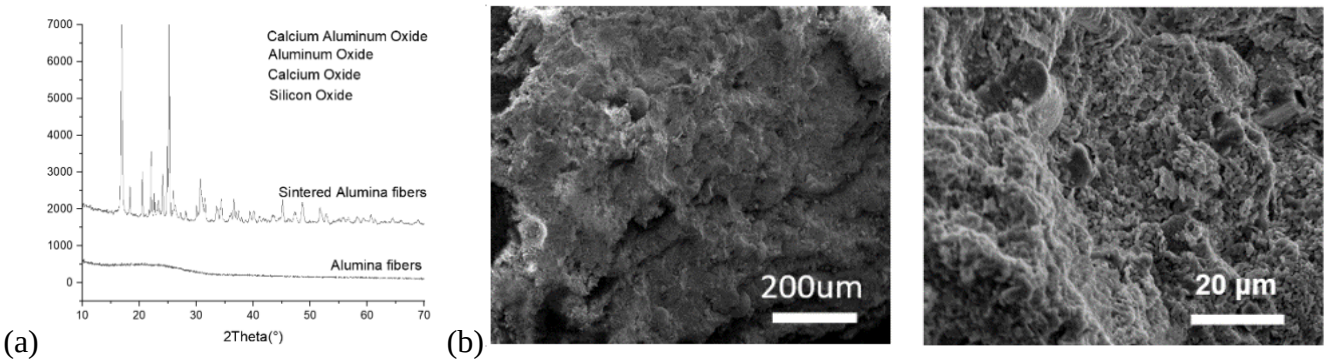

Figure 2-31: (a) XRD and (b) SEM images of alumina-silica fibers reinforced HA composite before and after thermal treatment

Figure 2.32. shows the maximum compressive strength, fracture toughness and porosity of the alumina reinforced HA composite. The work of fracture was calculated from the area under the force-displacement curve. The area of fractured zone was dividing into numerous small rectangles and determined by a definite integral method between two points. Then, the total area was added to obtain the work of fracture. The samples without alumina-silica fibers e.g., D1 and D3 sample, were significantly brittle and easier to break during cutting/polishing, while the samples containing fibers were easy to cut without fracturing.

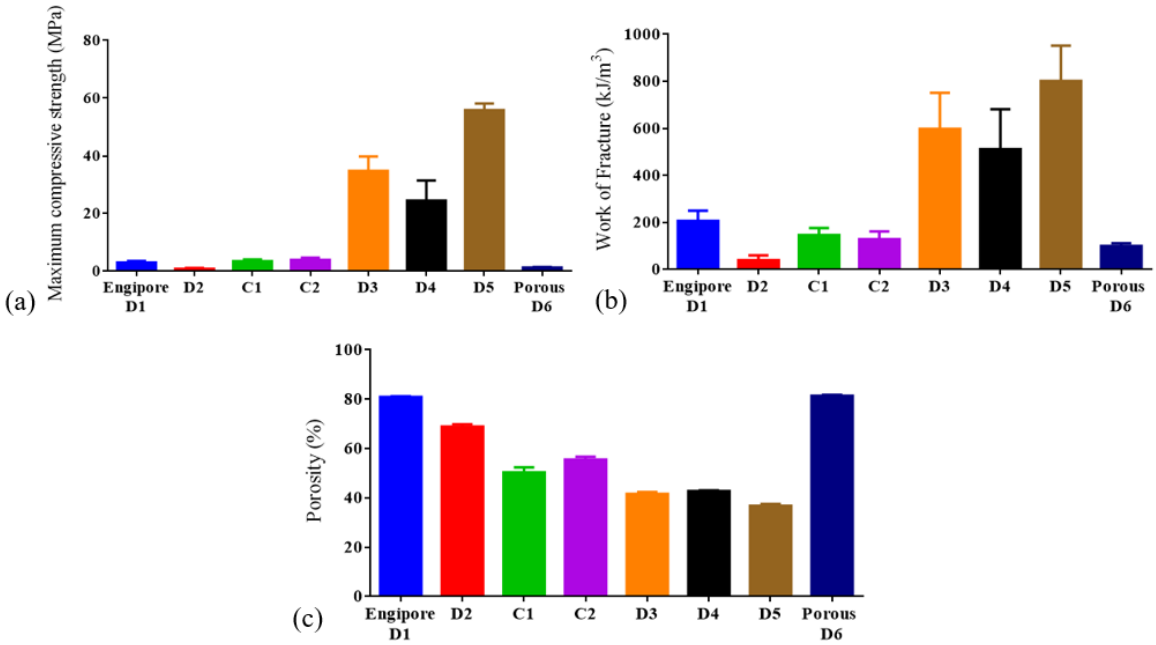

Figure 2-32: Maximum compression strength, work of fracture and porosity of alumina-silica fibers reinforced HA composite.

The maximum compressive strength and work of fracture (WOF) increased with increasing the powder content, while the porosity decreased (Table 2-XII) [75]. The higher powder content led to a more compact material with less empty spaces, enhancing its capacity to withstand compressive forces and tolerate fracture growth [76]. In particular, the sample D5 containing 77 wt% powder content exhibited the highest compressive strength and WOF (56 MPa and 801 kJ/m^3). In general terms, the porosity is inversely related to the compressive strength, where the interrelation is shown by equation.

$$\sigma = k(1-\rho)^3$$

where σ represents the compressive strength, k is a constant that is the compressive strength of the material with no porosity and p is the porosity fraction.

Considering the sample "*D1-Engipore*" porous as a control, fibers containing samples exhibited higher maximum compressive strength and lower porosity. Moreover, the mixing of alumina-silica fibers in HA slurries resulted in a decrease the viscosity of slurries, was considered particularly promising towards the manipulation of high-loaded slurries. This behaviour is strongly related to the interaction forces between the particles and particles-fibres dispersed in water, particularly the equilibrium between the electrostatic repulsive and Van der Waals attractive forces [77].

The stress-strain curves related to the mechanical tests are shown in Figure 3.33.

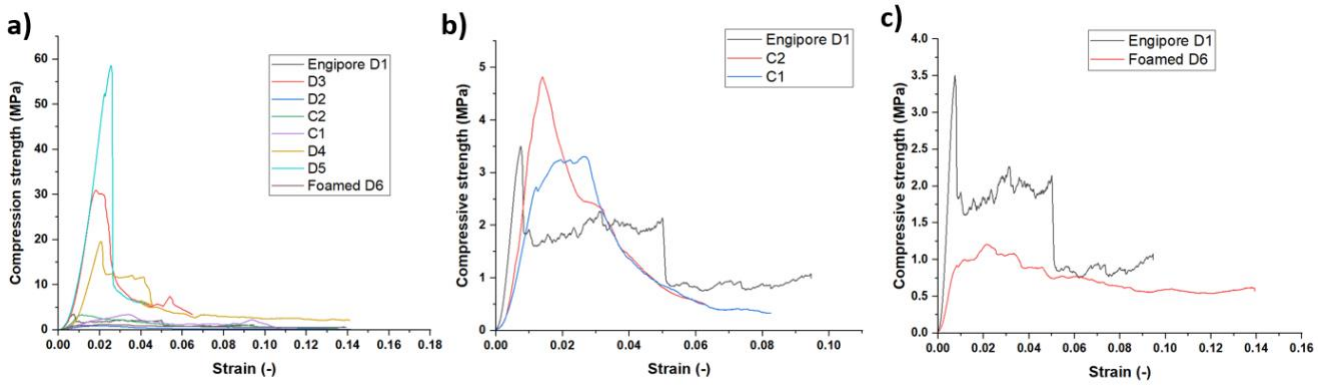

Figure 2-33: Work of fracture of the alumina reinforced HA ceramics

The compressive strength curves of samples without fibers exhibited typical brittle behaviour [78], as significant drops of compressive strength values were experienced with increasing strain in the range 0.02-0.04, associated with the generation and propagation of longitudinal cracks. The comparison between samples "Engipore-D1" and "Foamed D6" comes particularly interesting, as the presence of

alumina silica fibers attenuated the propagation of cracks of brittle materials, while also increasing the strain range associated to the final failure of the samples.

Table 2-XII: Summary of the mechanical tests. (*) commercial direct foaming, (**) experimental direct foaming

Sample Code	Calcination Temperature (°C)	Slurry composition (wt%)			Alumina fibers (g)	Work of Fracture (kJ/m3)	Porosity (%)	Compressive Strength (MPa)
		HA	Water	Dolapix				
C1	-	52	43	5	10	146.1	50.3	3.5
C2	-	52	43	5	20	129.4	55.5	4
D1(*)	1000	73	23	4	-	206.9	80.9	3.1
D2	1000	52	43	5	8	39.5	68.8	0.9
D3	1000	67	27	6	-	598.3	41.6	34.8
D4	1000	67	27	6	20	512.3	42.7	24.5
D5	1000	77	19	4	20	801.2	36.8	55.8
D6 (**)	1000	64	32	4	10	100.5	81.3	1.4

The samples D3, D4 and D5 exhibited significantly higher compressive strength and WOF due to their lower porosity, resulting from higher initial powder content. Nevertheless, all the samples displayed brittle behavior, except for D4, which demonstrated extended range of strain before reaching failure.

Overall, alumina silica fiber-reinforced HA composite exhibited lower maximum compressive strength, compared to the control sample of HA without fibers. However, the high-temperature sintering treatment of fiber-reinforced HA composite at 1200°C for 1h resulted in fibers decomposition and formation of secondary phase, as confirmed by X-ray diffraction analysis. This was ascribed to the presence of more than 20wt% of silica as secondary phase, which possibly lowered the melting point of the fiber construct.

The SEM images of reinforced HA without and with alumina silica fibers were shown in Figure 2.34. The micrographs exhibited a range of porosity from macro- to micro levels for samples D1 and D6. In particular, the porosity in the D1 sample appeared to be extensively interconnected pores with spherical shape, while in the D6 sample, it was less interconnected, potentially attributable to a higher concentration of powder and the inclusion of fibers. The identification of fibers was particularly critical, possibly confirming their thermal decomposition within the samples.

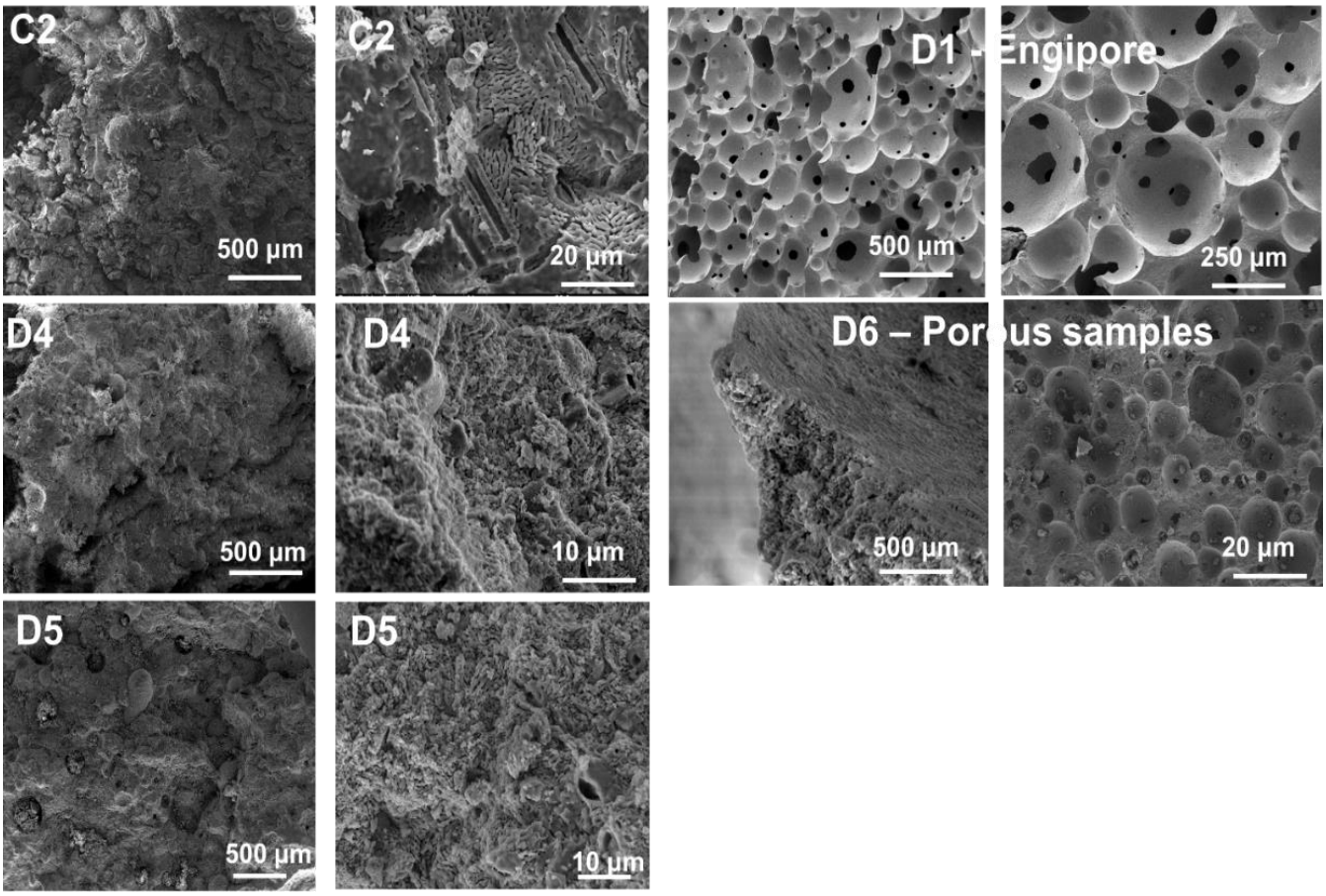

Figure 2-34: The morphology of the HA ceramics without or with Alumina Fiber

II. Due to the thermal decomposition of alumina-silica fibers, we attempted a new type of alumina fibers (SiO_2<5wt%), thermally stable up to 1600°C to achieve proper mechanical reinforcement of apatite scaffolds. Figure 2.35 shows the XRD of alumina fibers with and without heat treatment and SEM images of alumina fibers reinforced HA composite. We found a pure phase of alumina before and after sintering treatment. However, upon thermal treatment up to 1200°C for 1h, these new fibers also exhibited brittle character.

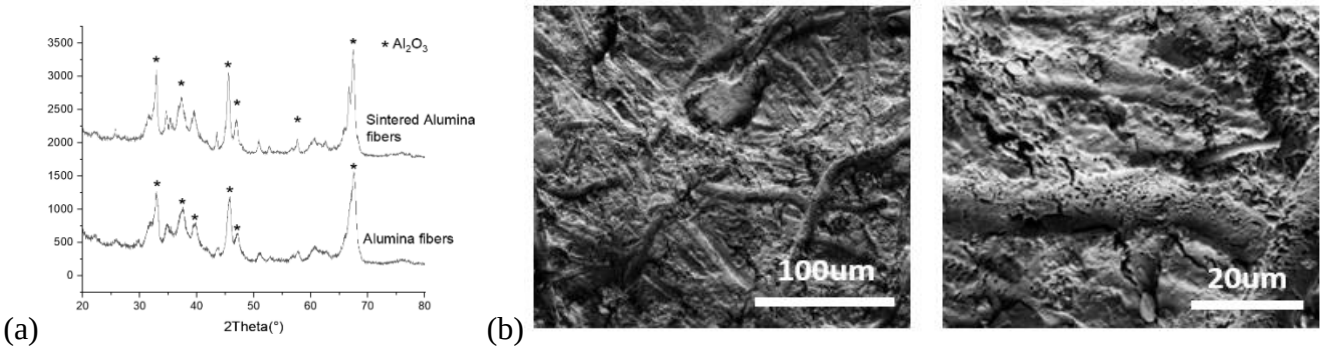

Figure 2-35: XRD and SEM images of old (a) and new (b) alumina fibers reinforced HA before and after high-temperature treatment

The maximum compressive strength and porosity of both control HA samples without fibers and fibers-reinforced HA samples with different amounts of alumina fibers are shown in Figure 2.36. The control samples (A0) exhibited significantly higher maximum compression strength (≈40.63 ± 5.01 MPa). However, they also exhibited extreme brittleness, with the occurrence of splinters upon fracture.

Conversely, the maximum compression strength of fiber-reinforced HA composite was observed significantly lower, and it exhibited a distinctly different fracture behavior then control. In contrast to the control's splintering, the fiber-reinforced composites demonstrated a damage-tolerant structure, lacking splinters, owing to the promotion of micro void formation, particularly evident with up to 20wt% of added fibers. As the fiber content increased further, there was a significant improvement in compressive strength, accompanied by a reduction in porosity. Considering the control, both the maximum compressive strength and overall porosity decreased, attributed to microstructural interactions between the fibers and powder particles.

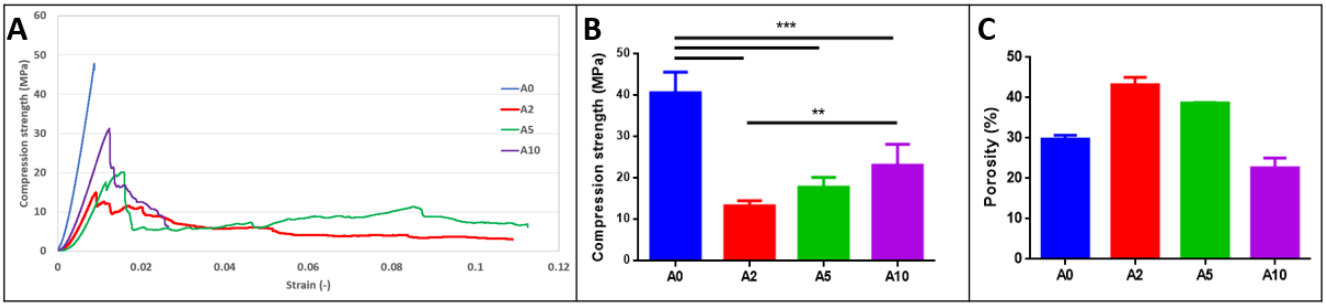

Figure 2-36: Compressive tests of alumina-fibers reinforced hydroxyapatite samples: a) compressive strength, b) maximum compressive strength, c) porosity

In this context, it was observed that the incorporation of fibers into the slurry, followed by drying and sintering, can cause microstructural defects, resulting in a reduction of the maximum compressive

strength. However, as the fiber content increased, the compressive strength also increases, but still lower than control sample of HA without fibers.

4-point bending tests

In accordance with compressive strength results, the 4-point bending tests highlighted a significant increase of bending strength by increasing the amount of alumina fibers, shown in Figure 3.37. During the 4-point bending tests, the samples experienced a combination of both compression and tensile stresses, making these test more representative than compression tests. The preparation of samples without fibers (A0) proved to be challenging, especially during the drying phase, leading to compromised specimen integrity. In particular, the 4-point bending stress exhibited significantly higher values by increasing the amount of fibers, as illustrated in Figure 2.37b.

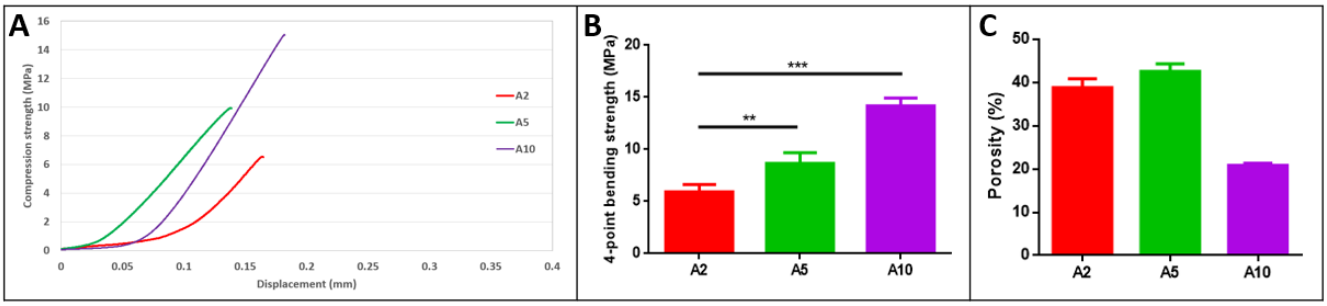

remov

Figure 2-37: Four-point bending tests of alumina-fibers reinforced hydroxyapatite samples: a) compressive strength-displacement curve, b) maximum strength, c) porosity

However, it was pointed out that the preparation and manipulation of such fiber-concentrated slurries was particularly difficult, especially to prevent the formation of agglomerates as well as uncontrollable drying of the slurry, resulting in a noticeable decrease of mechanical performance compared to the control sample without fibers.

2.3. Conclusions

The aim of this work is to develop mechanically reinforced HA composites with fibers. Various formulations of HA slurries were prepared and characterized to investigate the effect of calcination temperature of powder, powder content and dispersant amount as well as ion-doping on the flow behavior of hydroxyapatite slurries. Stoichiometric and ion-doped HA were synthesized by wet method. The calcination treatment of powders resulted in a significant reduction of specific surface area and reactivity, especially up to 1000°C. So, at constant powder amount, the resulting slurries exhibited reduced aggregation, improved colloidal stability and higher absolute zeta potential values with increasing the calcination temperature of powders. The yield points of concentrated slurries were observed to be inversely correlated with calcination temperature at constant powder amount. However, the highest solid loading for calcinated HA at 1000°C was found to be around 39 vol%, definitely higher than the highest solid loading for non-calcinated HA which resulted around 24 vol%. It was observed that with increasing the solid content, both dispersant and calcination temperature play an important role in tuning the viscosity. Ion-doped HA slurries such as Sr-doped HA, Mg-doped HA and Mg-Sr co-doped HA slurries, exhibited lower viscosities compared to stoichiometric HA slurries at constant powder and dispersant amounts, possibly ascribable to altered surface charge and functional groups, also reflecting into significantly higher chemical affinity of ions with water molecules and higher zeta potential, in absolute value. Amplitude sweep tests of all the slurries were performed to determine the respective linear viscoelastic region (LVR), thus indicating the shear stress range preventing significant alterations in the sample powder network. Then, frequency sweep tests were performed, according to LVR, to examine the elastic (G') and viscous (G") modulus against frequency range (0.1-10Hz) at constant shear stress. All slurries exhibited dominant elastic modulus (G') over viscous modulus (G") across the entire range of frequencies tested, except HA calcinated at 1000°C that exhibited viscous modulus dominant over elastic modulus. On this basis, I could observe that with increasing the powder content, both dispersant and calcination temperature of the powder play an important role in tuning the elastic moduli. Moreover, I found that the effect of dispersant amount was more prominent on ion-doped HA slurries than on stoichiometric HA slurries, significantly decreased the values of elastic modulus, bringing them to values similar to the ones for the diluted slurries.

Moreover, the scaffolds obtained by such slurries generally exhibit a brittle mechanical behavior. In this context, I investigated novel approaches for the reinforcement of hydroxyapatite scaffolds. The reinforcement of HA scaffolds with carbon fibers exhibited some limitations, possibly related to the

thermal decomposition of fibers in oxidative environment. In view of that, reinforcement of hydroxyapatite with alumina fibers was considered more suitable than carbon. Alumina fiber-reinforced HA composite exhibited lower maximum compressive strength and flexural strength, compared to the control sample of HA without fibers. However, the high-temperature sintering treatment of fiber-reinforced HA composite at 1200°C for 1h resulted in fibers decomposition and formation of secondary phase. Interestingly, the introduction of alumina fibers in HA slurries resulted in a decrease of viscosity: this behaviour was considered particularly promising towards the manipulation and development of high-solid loaded slurries. Due to the thermal decomposition of alumina-silica fibers, we attempted a new type of "pure" alumina fibers (SiO_2< 5wt%), thermally stable up to 1600°C to achieve proper mechanical reinforcement of apatite scaffolds. However, upon thermal treatment up to 1200°C for 1h, these new fibers also exhibited brittle character, resulting in a noticeable decrease of mechanical performance compared to the control sample without fibers. With increasing the amount of alumina fibers, the compressive strength increases, but still lower than control sample of HA without fibers. In conclusion, both carbon and alumina fibers decomposed after thermal treatment, preventing structural homogeneity and integrity, inducing microstructural defects which in turn caused the decrease of maximum compressive and flexural strength.

2.4. References

1. Mohd Zaffarin, A.S., et al., *Nano-Hydroxyapatite as a Delivery System for Promoting Bone Regeneration In Vivo: A Systematic Review.* 2021. 11(10): p. 2569.
2. Zhong, Z., et al., *Zn/Sr dual ions-collagen co-assembly hydroxyapatite enhances bone regeneration through procedural osteo-immunomodulation and osteogenesis.* 2022. 10: p. 195-206.
3. Nasiri-Tabrizi, B., et al., *Development of the third generation of bioceramics: Doping hydroxyapatite with s-, p-, d-, and f-blocks cations and their potential applications in bone regeneration and void filling.* Ceramics International, 2022.
4. George, S.M., et al., *Multifunctional hydroxyapatite composites for orthopedic applications: a review.* ACS Biomaterials Science & Engineering, 2022. 8(8): p. 3162-3186.
5. Rossini, Z., et al., *Custom-made porous hydroxyapatite cranioplasty in patients with tumor versus traumatic brain injury: a single-center case series.* World Neurosurgery, 2020. 138: p. e922-e929.
6. Aldahak, N., et al., *Hydroxyapatite bone cement application for the reconstruction of retrosigmoid craniectomy in the treatment of cranial nerves disorders.* Surgical Neurology International, 2017. 8.
7. Boyetey, M.-J.B., S. Torgbo, and P.J.E.P.J. Sukyai, *Bio-scaffold for bone tissue engineering with focus on bacterial cellulose, biological materials for hydroxyapatite synthesis and growth factors.* 2023: p. 112168.
8. Song, Y., et al., *Design and fabrication of drug-loaded alginate/hydroxyapatite/collagen composite scaffolds for repairing infected bone defects.* Journal of Materials Science, 2023: p. 1-16.
9. Ozder, M.N., et al., *In situ synthesis and cell line studies of nano-hydroxyapatite/graphene oxide composite materials for bone support applications.* Ceramics International, 2023.
10. Abbas, Z., et al., *Toughening of bioceramic composites for bone regeneration.* 2021. 5(10): p. 259.
11. Ginebra, M.-P., et al., *Bioceramics and bone healing.* EFORT open reviews, 2018. 3(5): p. 173-183.
12. Nicoara, A.I., et al., *Hydroxyapatite/carbon based biocomposite scaffolds as prospective materials for bone tissue engineering.* 2019. 81: p. 107-120.
13. Ielo, I., et al., *Recent advances in hydroxyapatite-based biocomposites for bone tissue regeneration in orthopedics.* 2022. 23(17): p. 9721.
14. Prakasam, M., et al., *Fabrication, properties and applications of dense hydroxyapatite: a review.* 2015. 6(4): p. 1099-1140.
15. Yedekçi, B., et al., *Synthesis and sintering of B, Sr, Mg multi-doped hydroxyapatites: Structural, mechanical and biological characterization.* Journal of the Mechanical Behavior of Biomedical Materials, 2021. 115: p. 104230.
16. Cacciotti, I., *Cationic and Anionic Substitutions in Hydroxyapatite*, in *Handbook of Bioceramics and Biocomposites*, I.V. Antoniac, Editor. 2016, Springer International Publishing: Cham. p. 145-211.
17. Bose, S., et al., *Trace element doping in calcium phosphate ceramics to understand osteogenesis and angiogenesis.* Trends in biotechnology, 2013. 31(10).
18. Yilmaz, B., A.Z. Alshemary, and Z. Evis, *Co-doped hydroxyapatites as potential materials for biomedical applications.* Microchemical Journal, 2019. 144: p. 443-453.
19. Balakrishnan, S., et al., *Influence of iron doping towards the physicochemical and biological characteristics of hydroxyapatite*. Ceramics International, 2021. 47(4): p. 5061-5070.
20. Reger, N.C., et al., *Structural and phase analysis of multi-ion doped hydroxyapatite for biomedical applications.* Ceramics International, 2019. 45(1): p. 252-263.
21. Mahon, O.R., et al., *Nano-particle mediated M2 macrophage polarization enhances bone formation and MSC osteogenesis in an IL-10 dependent manner.* 2020. 239: p. 119833.

22. Yang, G., et al., *Bio-inspired hybrid nanoparticles promote vascularized bone regeneration in a morphology-dependent manner.* 2017. 9(18): p. 5794-5805.
23. Li, Y., et al., *Controllable synthesis of biomimetic hydroxyapatite nanorods with high osteogenic bioactivity*. 2019. 6(1): p. 320-328.
24. Amin, A.M., et al., *Role of heat treatment of hydroxyapatite powder prior to suspension preparation on the suspension flow behavior.* Open Ceramics, 2022. 9: p. 100239.
25. Maqbool, M., et al., *Synthesis, characterization, antibacterial properties, and in vitro studies of selenium and strontium co-substituted hydroxyapatite.* International Journal of Molecular Sciences, 2021. 22(8): p. 4246.
26. Ressler, A., et al., *A multifunctional strontium/silver-co-substituted hydroxyapatite derived from biogenic source as antibacterial biomaterial.* Ceramics International, 2022. 48(13): p. 18361-18373.
27. Sprio, S., et al., *Surface phenomena enhancing the antibacterial and osteogenic ability of nanocrystalline hydroxyapatite, activated by multiple-ion doping.* ACS Biomaterials Science & Engineering, 2019. 5(11): p. 5947-5959.
28. Li, Z., et al., *Chemical composition, crystal size and lattice structural changes after incorporation of strontium into biomimetic apatite*. Biomaterials, 2007. 28(7): p. 1452-1460.
29. Uskoković, V., et al., *Germanium-doped hydroxyapatite: Synthesis and characterization of a new substituted apatite.* Ceramics International, 2022. 48(19): p. 27693-27702.
30. Boanini, E., M. Gazzano, and A. Bigi, *Ionic substitutions in calcium phosphates synthesized at low temperature.* Acta biomaterialia, 2010. 6(6): p. 1882-1894.
31. Kim, I.J., et al., *Wet Foam Stability from Colloidal Suspension to Porous Ceramics: A Review*. J. Korean Ceram. Soc, 2019. 56(3): p. 211-232.
32. Studart, A.R., et al., *Processing Routes to Macroporous Ceramics: A Review.* 2006. 89(6): p. 1771-1789.
33. Ferrage, L., et al., *A review of the additive manufacturing (3DP) of bioceramics: alumina, zirconia (PSZ) and hydroxyapatite.* Journal of the Australian Ceramic Society, 2017. 53(1): p. 11-20.
34. Jodati, H., B. Yılmaz, and Z.J.C.I. Evis, *A review of bioceramic porous scaffolds for hard tissue applications: Effects of structural features.* 2020. 46(10): p. 15725-15739.
35. Gardini, D., C. Galassi, and R. Lapasin, *Rheology of hydroxyapatite dispersions*. Journal of the American Ceramic Society, 2005. 88(2): p. 271-276.
36. Bao, Y., et al., *Rheological behavior of aqueous suspensions of hydroxyapatite (HAP).* 2002. 13: p. 639-643.
37. Amin, A.M., et al., *Role of heat treatment of hydroxyapatite powder prior to suspension preparation on the suspension flow behavior.* 2022. 9: p. 100239.
38. Patel, N.R. and P.P.J.I.J.E.T.A.E. Gohil, *A review on biomaterials: scope, applications & human anatomy significance*. 2012. 2(4): p. 91-101.
39. Petersen, R.J.F., *Carbon fiber biocompatibility for implants.* 2016. 4(1): p. 1.
40. Zhao, X., et al., *3D printing of bioactive macro/microporous continuous carbon fibre reinforced hydroxyapatite composite scaffolds with synchronously enhanced strength and toughness.* 2022. 42(10): p. 4396-4409.
41. Zhao, X., et al., *Carbon fiber reinforced hydroxyapatite composites with excellent mechanical properties and biological activities prepared by spark plasma sintering.* 2020. 46(17): p. 27446-27456.
42. Maciel, C.C.M., et al., *Carbon fiber: Characterization and evaluation of the inflammatory response and toxicity in rats.* J Biomed Mater Res B Appl Biomater, 2023. 111(11): p. 1956-1965.
43. Dapporto, M., et al., *A novel route for the synthesis of macroporous bioceramics for bone regeneration.* Journal of the European Ceramic Society, 2016. 36(9): p. 2383-2388.

44. Yelten-Yilmaz, A. and S.J.C.I. Yilmaz, *Wet chemical precipitation synthesis of hydroxyapatite (HA) powders.* 2018. 44(8): p. 9703-9710.
45. Tampieri, A., et al., *Characteristics of synthetic hydroxyapatites and attempts to improve their thermal stability.* 2000. 64(1): p. 54-61.
46. Ruffini, A., et al., *Synthesis of nanostructured hydroxyapatite via controlled hydrothermal route.* 2019. 10.
47. Landi, E., et al., *Sr-substituted hydroxyapatites for osteoporotic bone replacement.* 2007. 3(6): p. 961-969.
48. Landi, E., et al., *Development of Sr and CO3 co-substituted hydroxyapatites for biomedical applications.* 2008. 4(3): p. 656-663.
49. Hassan, M.F., et al., *Recent trends in activated carbon fibers production from various precursors and applications—A comparative review.* 2020. 145: p. 104715.
50. Fu, R., et al., *Studies on the structure of activated carbon fibers activated by phosphoric acid.* 2003. 87(14): p. 2253-2261.
51. Yusuf, A., et al., *The effect of temperature synthesis on the purity and crystallinity of hydroxyapatite.* 2020. 860: p. 228-233.
52. Ahmed, Y., S. El-Sheikh, and Z.J.B.o.M.S. Zaki, *Changes in hydroxyapatite powder properties via heat treatment.* 2015. 38: p. 1807-1819.
53. Manalu, J.L., F. Tjhay, and T.J.A.J.o.A.S. Kristoforus, *Effect of Calcination Time on Bovine-Derived Hydroxyapatite as Bone Implant Material: An In Vitro Study.* 2020. 8(5).
54. Laura, d.-M.-B. and G. Maria-Pau, *Rheological characterisation of ceramic inks for 3D direct ink writing: A review.* Journal of the European Ceramic Society, 2021. 41(16): p. 18-33.
55. Mahanty, A. and D. Shikha, *Microstructural, biocompatibility and mechanical investigation of MgHAp and AgHAp: Comparative report.* Journal of Materials Science: Materials in Medicine, 2023. 34(5): p. 22.
56. Lala, S., et al., *Magnesium substitution in carbonated hydroxyapatite: Structural and microstructural characterization by Rietveld's refinement.* Materials Chemistry and Physics, 2016. 170: p. 319-329.
57. Cheng, G., et al., *Effects of strontium substitution on the structural distortion of hydroxyapatite by rietveld refinement and Raman Spectroscopy.* Ceramics International, 2019. 45(8): p. 11073-11078.
58. Aina, V., et al., *Magnesium-and strontium-co-substituted hydroxyapatite: the effects of doped-ions on the structure and chemico-physical properties.* Journal of Materials Science: Materials in Medicine, 2012. 23: p. 2867-2879.
59. Antonakos, A., E. Liarokapis, and T. Leventouri, *Micro-Raman and FTIR studies of synthetic and natural apatites.* Biomaterials, 2007. 28(19): p. 3043-3054.
60. Zou, L., et al., *Biomimetic mineralization on natural and synthetic polymers to prepare hybrid scaffolds for bone tissue engineering.* Colloids and Surfaces B: Biointerfaces, 2019. 178: p. 222-229.
61. Zhang, H., et al., *Synthesis and structural characteristics of magnesium and zinc doped hydroxyapatite whiskers.* 2017. 61: p. 244-249.
62. Landi, E., et al., *Mg, Sr-Cosubstituted Hydroxyapatite with Improved Structural Properties.* Applied Sciences, 2021. 11(11): p. 4930.
63. Bertinetti, L., et al., *Surface characteristics of nanocrystalline apatites: effect of Mg surface enrichment on morphology, surface hydration species, and cationic environments.* Langmuir, 2009. 25(10): p. 5647-5654.
64. Cacciotti, I., et al., *Mg-substituted hydroxyapatite nanopowders: synthesis, thermal stability and sintering behaviour.* 2009. 29(14): p. 2969-2978.
65. Zyman, Z., et al., *Magnesium-substituted hydroxyapatite ceramics.* 2006. 37(6): p. 474-477.

66. Nagyne-Kovacs, T., et al., *Synthesis and characterization of Sr and Mg-doped hydroxyapatite by a simple precipitation method.* Ceramics International, 2018. 44(18): p. 22976-22982.
67. Wang, P., et al., *Effects of synthesis conditions on the morphology of hydroxyapatite nanoparticles produced by wet chemical process.* Powder Technology, 2010. 203(2): p. 315-321.
68. Al Rashid, A., et al., *Vat photopolymerization of polymers and polymer composites: Processes and applications.* 2021. 47: p. 102279.
69. Shah, M., et al., *Vat photopolymerization-based 3D printing of polymer nanocomposites: current trends and applications.* 2023. 13(2): p. 1456-1496.
70. Zeng, Y., et al., *3D printing of hydroxyapatite scaffolds with good mechanical and biocompatible properties by digital light processing.* 2018. 53(9): p. 6291-6301.
71. Zavřel, F., et al., *Development of Hot-Melt Extrusion Method to Produce Hydroxyapatite/Polycaprolactone Composite Filaments.* 2022. 24(3): p. 2100820.
72. Ramli, M., et al., *Stainless steel 316L–hydroxyapatite composite via powder injection moulding: rheological and mechanical properties characterisation.* 2014. 18(sup6): p. S6-100-S6-104.
73. Kolev, S.K., et al., *Sodium and Magnesium Ion Location at the Backbone and at the Nucleobase of RNA: Ab Initio Molecular Dynamics in Water Solution.* ACS omega, 2022. 7(27): p. 23234-23244.
74. Liu, J., et al., *Enhancement of fiber–matrix adhesion in carbon fiber reinforced Al-matrix composites with an optimized electroless plating process.* 2021. 142: p. 106258.
75. Zhao, X., et al., *Potential load-bearing bone substitution material: carbon-fiber-reinforced magnesium-doped hydroxyapatite composites with excellent mechanical performance and tailored biological properties.* 2022. 8(2): p. 921-938.
76. Abifarin, J.K. and O.A.J.J.o.t.A.C.S. Owolabi, *New insight to the mechanical reliability of porous and nonporous hydroxyapatite.* 2023. 59(1): p. 43-55.
77. Zhang, Z., *Novel formulations for magnetic-resonance imaging guided theranostics*. 2021, UCL (University College London).
78. Li, H., et al., *Experimental study on compressive behavior and failure characteristics of imitation steel fiber concrete under uniaxial load.* 2023. 399: p. 132599.

CHAPTER 3: DEVELOPMENT OF POROUS APATITIC BONE CEMENT REINFORCED WITH FIBERS.

Calcium phosphate cements (CPC) are obtained by mixing a precursor powder with a liquid phase thus obtaining a paste that can be molded prior to self-hardening. Among inorganic precursors for apatitic CPCs, α-tricalcium phosphate (α-TCP) is especially interesting as a bioactive material because of its ability to react with water and set at body temperature, without any temperature or pH change during setting, thus transforming in nanocrystalline, calcium deficient apatite (CDHA) with a composition close to the mineral component of human bones and a microporous diffuse porosity [1].

For these reasons, α-TCP has been widely investigated as adequate precursor for bone cements due to its biocompatibility, high reactivity, bioresorbability and potential to achieve high mechanical strength upon hardening. Its synthesis involves a high temperature thermal treatment between 1100 and 1500°C, followed by rapid quenching. High-temperature synthesis tends to produce a more crystalline and mechanically stable α-TCP phase, making it suitable for load-bearing orthopedic applications. As crystalline precursors can limit hydraulic and biological reactivity, I investigated the synthesis of α-TCP at much lower temperatures [2].

In order to improve features of the apatitic bone cement, such as osteointegration, mechanical properties and implantation efficacy, CPCs can be doped with small amounts of ions that are found in natural bone minerals. Particularly, Mg and Sr are trace elements naturally found in human bones and play an important role in modulating cell behavior and natural bone turnover [3]. Sr-doped CPCs gained increasing interest due to potential anti-osteoporotic character provided by Sr^{2+} ions, while Mg is one of the most important elements for living organisms, as an essential regulatory factor for coordination of water molecules, pH and calcium ions intake in cells. CPCs are interesting for functionalization with various drugs and biomolecules, particularly due to their nanostructure offering high specific surface area for cell attachment and conduction, towards the generation of multifunctional devices with enhanced therapeutic ability [4]. In addition, carbon fibers (CF) have the advantages of high mechanical properties and excellent biocompatibility, so that it is considered as a good candidate for the reinforcement of bone scaffold as a toughening agent.

This activity involves three main goals including:

i) Apatitic cement from precursors obtained by low and high-temperature processing.
ii) Magnesium-doped apatite cement with intrinsic antibacterial properties.
iii) Mechanically reinforced magnesium and strontium-doped apatite cement with carbon fibers.

3.1. Apatitic cements from precursors obtained by low and high-temperature processing.

The phase equilibrium diagram of the system $CaO–P_2O_5$ reveals the presence of three distinct polymorphs corresponding to the tricalcium phosphate composition $Ca_3(PO_4)_2$ known as α-TCP, β-TCP and α'-TCP phases, based on the temperature [5-7]. The α'-TCP phase is only present at temperatures above 1430°C and currently lacks practical significance as it has not been stabilized at room temperature. The β-TCP phase remains stable up to 1120°C, while above this temperature, it undergoes a transformation into the monoclinic α-TCP. However, the synthesis of α-TCP phase by solid state reaction is a difficult process as its thermodynamically stable within temperature range 1130-1470°C, has to be rapidly cooled by quenching to avoid the β-TCP phase formation [8].

Indeed, metastable α-TCP can also be obtained by an alternative method involving the heating of amorphous tricalcium phosphate (ACP). Despite the fact that the maximum temperature during this formation process is significantly lower than the stability domain of α-TCP (1130 to 1470°C), it is still possible to produce α-TCP by heating ACP within the temperature range of 650 to 700°C [9]. This method offers a cost-effective approach and expands the low-temperature domain for α-TCP formation, which helps in limiting grain growth and sintering. Despite these advantages, the potential of low-temperature a-TCP in cement production has been barely exploited when compared to the conventional high-temperature process [10].

The objectives of this study were to compare the structural, physicochemical and hydraulic reactivity of α-TCP obtained through two different routes: high-temperature solid-state reaction at 1400°C and "low-temperature" conversion from amorphous calcium phosphate at 650°C (LT-αTCP). In addition, I investigated the crystallization and phase evolution of ACP partially substituted with Mg^{2+}, Sr^{2+}, Si^{2+} and co-doped with $Sr^{2+}$and Si^{2+} as well as effect of citrate. Then, cement was prepared by mixing low and high temperature precursor powder in setting solution (5wt% $NaHPO_4$, 2wt% Na-Alginate) with liquid-to-powder (L/P) ratio equals to 0.8. Moreover, addition of 4wt% carbon fibers with 5mm-length in both cements were investigated to enhance mechanical properties.

3.1.1. Materials and methods

Amorphous calcium phosphate (ACP) was synthesized by precipitation method involve quick mixing of aqueous solution of $Ca(NO_3)_2{\cdot}4H_2O$ (15.25 g in 160 mL of water) with a aqueous solution of $(NH_4)_2HPO_4$ (5.10 g in 400 mL of water) at room temperature and keep pH close to 10 by adding NH_4OH 30%. The resulting precipitate was filtered, washed and lyophilized for 48 hours. Then ACP were thermal treated at different temperature 500, 550, 600, 650, and 700°C. In particular, ACP was converted into α-TCP at 650°C, referred as low temperature α-tricalcium phosphate (LT- αTCP)

For the synthesis of ion-doped ACP, the same route was repeated by introducing salts ($MgCl_2{\cdot}6H_2O$, $SrCl_2{\cdot}6H_2O$, SiO_2 Sigma Aldrich) containing the doping ions in appropriate amounts to prepare Mg-doped ACP (Mg/(Ca+Mg) = 2 mol%), Sr-doped ACP (Sr/(Ca+Sr) = 2 mol%), Si-doped ACP (Si/(Ca+Si) = 2

mol%) and co-doped SrSi-ACP (Sr/(Ca+Si+Sr) = Si/(Ca+Si+Sr) = 1 mol%). Sodium-citrate were also added in 2mole% with respective calcium, in Sr-doped ACP solutions to investigate the effect of citrate on stability of ACP and then αTCP.

While, high-temperature α-tricalcium phosphate (HT-αTCP) was synthesized by a solid-state reaction [11] of calcium phosphate dibasic ($CaHPO_4$, Sigma Aldrich, US) and calcium carbonate ($CaCO_3$, Sigma Aldrich, US) mixture with a molar ratio of 2:1. Subsequently, the mixture was thermally treated at 1400°C for 1 h, followed by rapid cooling. The resulting powder was milled in ethanol (98%, Sigma Aldrich, US) using a planetary ball milling (Pulverisette 6 classic line, Germany) with alumina grinding balls (2 mm diameter) at 400 rpm for 50 min. Ethanol was evaporated using a rotavator with a vacuum pump.

Then, cements were prepared by mixing precursor powder synthesized at two different temperature, in setting solution with liquid-to-powder (L/P) ratio equals to 0.8. Setting solution was prepared by mixing 5 wt% of sodium phosphate dibasic dihydrate ($Na_2HPO_4{\cdot}2H_2O$, Fluka, UK) and 2 wt% sodium alginate (Sodium Salt of Alginic Acid from Brown Algae, Sigma Aldrich, US) in water.

In addition, 5mm carbon fibers of 4wt% were mixed in both powder before mixing in setting solution. The compressive strength of the calcium phosphate cement (CPC) with and without carbon fibers were investigated by cylindrical specimens, after being hardened in Teflon moulds for 30 minutes, the specimens were left in a thermostatic bath for 72h. Five cylindrical specimens for each sample were prepared, with a diameter of 6 mm and a height of 12 mm in Teflon moulds.

3.1.2. Characterizations

To analyze the phase composition of samples, XRD were used to investigate the diffraction peaks on a D8 Advance diffractometer (Bruker, Karlsruhe, Germany), with CuKα radiation, in 2θ range of 10° to 80° with a scanning step of 0.02°. The average crystal size was determined using the Scherrer equation ($D=k\lambda/B{\cdot}\cos\theta$), where D represents the crystalline diameter (Å), k is the Scherrer constant (≈0.9), λ is the X-ray wavelength ≈1.5406 Å, θ is the Bragg angle and B represents the full width at half maximum intensity of the observed peak.

To investigate the chemical composition and functional groups, Fourier-transform infrared spectroscopy (FTIR) was performed using a Nicolet IS5 spectrometer (Thermo Fisher Scientific, U.S.A.). The samples were ground with 5 wt% KBr in an agate mortar, compressed into tablets and analysed in the spectral range of 500 to 4000 cm^{-1}.

The specific surface area (SSA) was calculated using the Brunauer–Emmett–Teller (BET) method (Surfer, Thermo Scientific, United States) by nitrogen adsorption at a relative pressure of 0.03 Torr.

Particle size distribution was determined by dispersing the powder in aqueous solutions of sodium hexametaphosphate (0.05 wt%). The measurements were performed using an X-ray instrument based on the Stokes sedimentation equation (Sedigraph 5100 instrument, Micromeritics, US).

The Thermofinnigan 240 Pa instrument was used to measure the porosity of the powders by the intrusion of mercury under controlled pressure (0.1-200 MPa).

Thermogravimetric analysis were performed using Simultaneous Thermal Analyzer TG-DSC (STA 449 F3 Jupiter, Netzsch Geraetebau) under the N_2 atmosphere within temperature range (20-1200℃).

Elemental composition analysis of the powders was performed using Inductively Coupled Plasma-Optical Emission Spectroscopy (ICP-OES) with an Agilent 5100 instrument.

The morphology of the powders was studied using Field Emission Scanning Electron Microscopy (FE-SEM) using the Zeiss-SIGMA instrument (Carl Zeiss Microscopy GmbH) at 20 kV acceleration voltage.

The initial and final setting times of the cement formulations were investigated using the Gillmore needles apparatus, following the guidelines in the standard ASTM C266-99.

Zwick Roell Z050 machine was used to perform compressive tests in displacement control, with a speed of 1 mm/min.

3.1.3. Results and Discussion

The X-ray diffraction analysis of ACP powders exhibited the typical patterns of amorphous calcium phosphate phases, showing broad peaks in the angular range 30-50̊. Thermogravimetric (TGA) analysis of ACP powders is shown in Figure 3.1a, exhibits two obvious mass losses. The first below ~500°C was related to the evaporation of adsorbed structural water and second occurred above 500℃ was referred to the decomposition of calcium carbonate. The intense exothermic peak start at 710°C was observed in the DSC heat-flow curve, attributed to the transformations and crystallization of the ACP into α-TCP.

To investigate the structural changes of ACP powder upon heating, 1 g of the powder was subjected to constant temperatures in an oven at different temperature points 550, 600, 650 and 700°C for 1 hour (Figure 3.1b) [2][12].

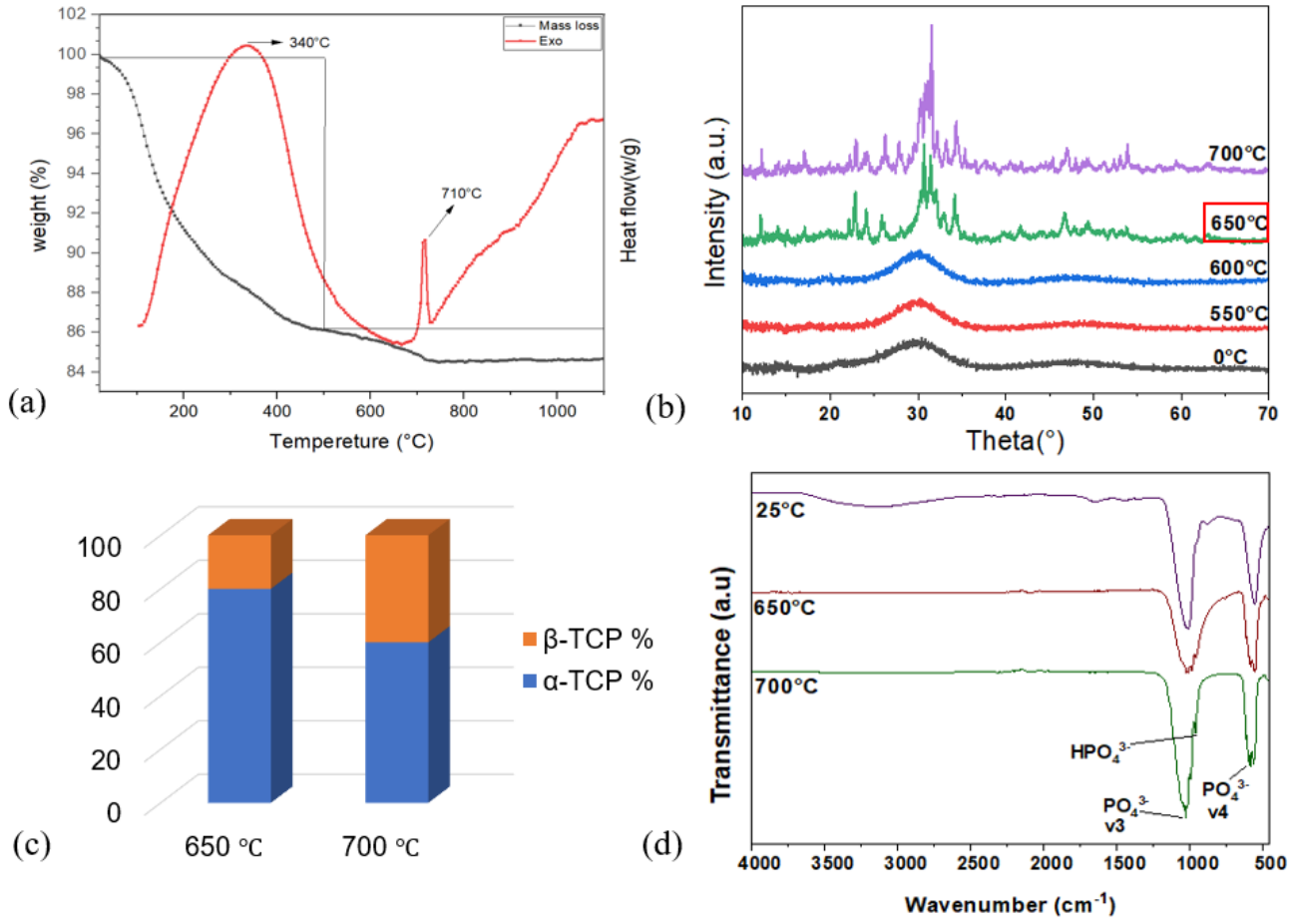

Figure 3-1:(a) TGA/DSC of amorphous calcium phosphate (b) XRD (d) FTIR analysis of calcinated amorphous calcium phosphate at different temperatures points (550, 600, 650, 700°C), and (c) phase composition % of αTCP and βTCP at 650°C and 700°C.

Table 3. I show 2θ angle, planes of calcinated amorphous calcium phosphate in the XRD spectra. Based on the XRD results, ACP remains in its amorphous state until 600°C and the level of crystallinity of calcinated amorphous calcium phosphate increases with increasing calcination temperature. The crystallization into α-TCP occurs between 600 and 650°C, is lower temperature than the crystallization peak observed in the thermal analysis, a difference often observed between dynamic and static heating modes. Afterward, the metastable α -TCP starts to recrystallize into the stable β-TCP phase and both α and β phases coexist between 700 and 800°C (Figure 3. 1 c). This sequence of thermodynamically unstable phase forming first aligns with the Ostwald step rule.

Table 3-I: The 2θ angle spacing and planes of calcinated amorphous calcium phosphate.

2θ: α-TCP JCPDS 29-359	Plane	2θ: ACP_650℃
12.10	031	12.12
14.02	201	14.05
14.41	002	14.51
17.09	131	17.12
22.13	201	22.15
22.89	132	22.78
24.10	261	24.13
29.66	361	29.71
30.70	100	30.73
31.26	335	31.27
34.46	203	34.53

The wavenumber, type of bond, and functional groups of calcinated amorphous calcium phosphate at different temperatures points (550, 600, 650, 700℃) based on FTIR spectroscopy is given in Table 3. II.

Table 3-II: FTIR band assignment and functional groups of calcinated amorphous calcium phosphate.

Wavenumber (cm^{-1})	Type of bond	Functional groups
3429	O-H bending	H-O-H
1035, 1024	P-O stretching	PO_4^{3-}
961	C=O stretching	CO_3^{2-}
594, 580	P-O stretching	PO_4^{3-}
564	P-O-H stretching	PO_4^{3-}

XRD pattern of the HT-αTCP revealed the typical phases of α-TCP at 2θ angle of 22.15°, 22.91°, 24.12°, 30.72°, and 31.28°, according to JCPDS. NO 29-0359 (Figure 3.2a and Table 3-III).

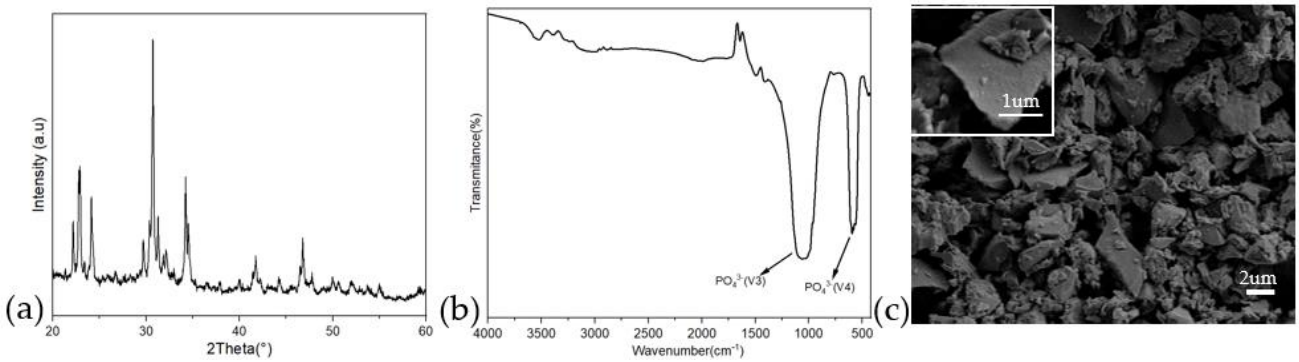

Figure 3-2: (a) X-ray diffraction pattern; (b) FTIR-ATR spectrum; (C) SEM micrograph, of α-TCP (scale bar = 500 nm)

Table 3-III: The 2θ angle spacing and planes of α-TCP.

2θ: α-TCP JCPDS 29-359	Plane	2θ: α-TCP
22.13	201	22.15
22.76	162	22.76
22.89	132	22.91
24.10	261	24.12
29.66	361	29.71
30.70	100	30.72
31.26	335	31.28
34.46	203	34.21

The FTIR spectrum and complete assignment of FTIR bands of the HT-αTCP is shown in Figure 3.2b and Table 3-IV, presented the characteristic bands of the OH^{-1}, $PO^{4-}(V_4)$ and $PO^{4-}(V_3)$. The SEM micrograph of α-TCP shows a plate-like particle are shown in Figure 3.7c.

Table 3-IV: FTIR band assignment and functional groups of α-TCP.

Wavenumber (cm^{-1})	Type of bond	Functional groups
3429	O-H bending	OH
1035, 1024	P-O stretching	PO_4^{3-}
594, 580	P-O stretching	PO_4^{3-}
564	P-O-H stretching	PO_4^{3-}

The specific surface area of LT-αTCP was observed to be significantly higher than that of α-TCP synthesized at high temperature (HT-αTCP); such a feature was the main cause of a reduced initial setting time are shown in Table 3-V.

Table 3-V: SSA, Initial and final setting time of LT and HT-αTCP.

Samples	SSA (m^2/g)	Initial setting minutes	Final setting minutes
LT- αTCP	12.46	7	22
HT- αTCP	3.03	18	35

The reactivity of a-TCP powders was investigated in deionized water at 37 ℃ using pH measurements over a period of approximately 12 hours. The hydrolysis reaction was stopped after 12, 48 and 96 hours by immersing the powders in ethanol, followed by XRD analysis (Figure 3.3). The initial event seen in all cases was powder dissolution, followed by proton absorption and a significant increase in pH. This pH rise was attributed to the hydrolysis of dissolved PO_4^{3-} ions, leading to the formation of HPO_4^{2-} and PO_4^{2-} ions.

Calcium-deficient apatite (CDHA) was detected in HT-αTCP samples only after 24 hours and no α-TCP was left after 48 hours (Figure 3.2 a). On the other hand, CDHA was detected in LT-αTCP samples faster, with a small amount visible at 12 hours. However, once this phase has nucleated, the hydrolysis reaction completes within a few hours, resulting in the presence of only CDHA at 24 hours [2]. The transformation of α-TCP into calcium deficient hydroxyapatite (CDHA) appears to be generally faster for LT-αTCP, if compared to HT-αTCP, possibly due to higher specific surface area and lower crystallinity.

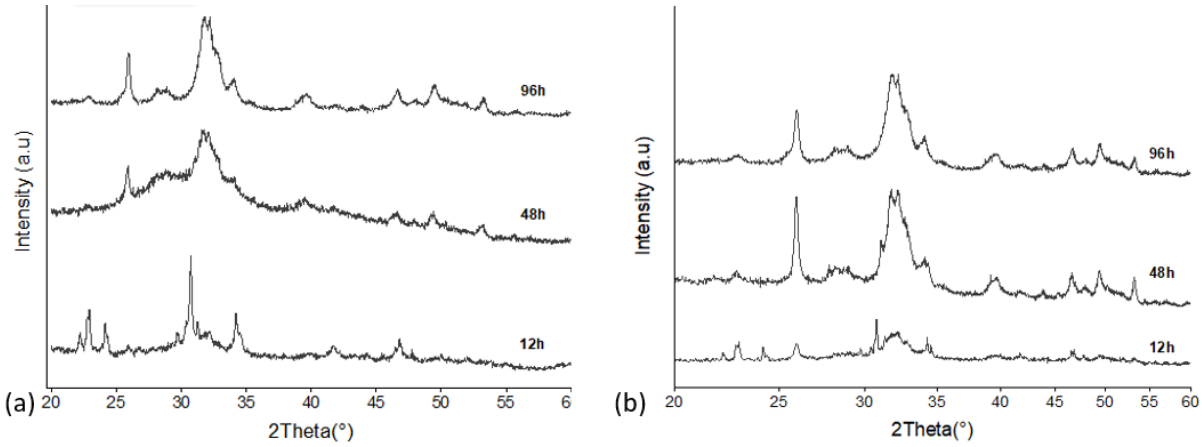

Figure 3-3: XRD analysis of cement at different hardening time from (a) HT-αTCP (b) LT-αTCP

Cements obtained from LT-αTCP precursors exhibit higher specific surface area respectively smaller particle size compared to HT-αTCP cements. The cements obtained from HT-αTCP have larger particle size and pore size than LT-αTCP cements, are shown in Table. 3-VI. Despite these differences, the overall porosity of both cements remained comparable. In HT-αTCP cement, crystal growth was observed like multiple needle-like patterns, whereas in LT-αTCP cement, crystal growth appeared even smaller, shown in Figure 3.4.

Table 3-VI: SSA, Initial and final setting time of cement from LT and HT-αTCP.

Samples	SSA (m^2/g)	Pore size (µm)	Porosity (cm^3/g)
LT-CPC	113	0.02	0.54
HT-CPC	61	0.3	0.50

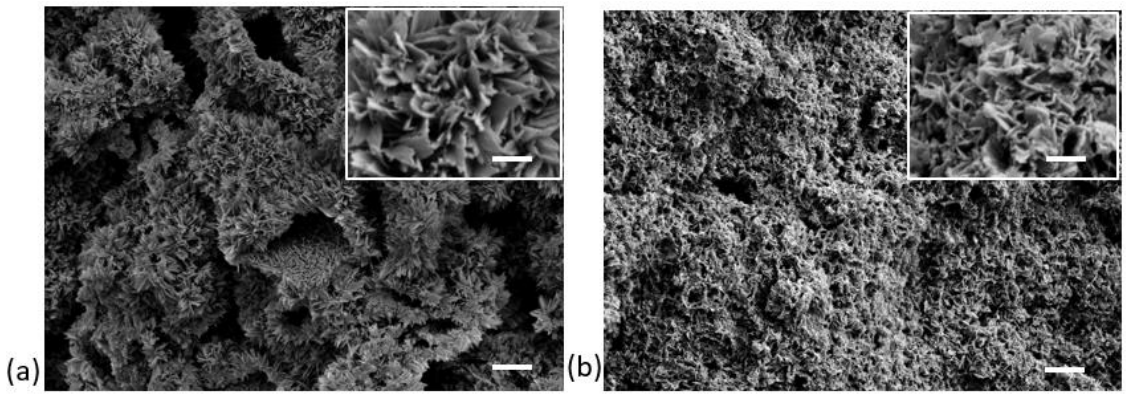

Figure 3-4: SEM images of cement from (a) HT-αTCP (b) LT-αTCP (Figure scale bars = 1µm, Inset scale bar = 200 nm.)

The XRD patterns of ACP substituted with 2 mol% of Mg, Sr, Si and co-doped with Sr and Si ions, as well as Cit-stabilized Sr-ACP are shown in Figure 3.5. All samples, regardless of the doped ions, were amorphous, with no distinct diffraction peaks corresponding to any crystalline material. After heat treatment at 500°C, all ion-doped ACP remained amorphous [13]. However, upon treatment at 650°C, all samples crystallized directly to α-TCP and β-TCP phases without an intermediate phase. The substitution of ions induced different crystallization behavior compared to ACP, leading to the coexistence of two polymorphs. Mg substitutions promote the formation of β-TCP. All of the diffraction peaks in the XRD pattern of the Mg-doped sample correspond to β-TCP and there are no signals from α-TCP. Sr and Si doping in ACP promote the formation of α-TCP [14].

All samples showed the presence of α-tricalcium phosphate (α-TCP) except Mg-doped sample, with a minor crystal phase of β-tricalcium phosphate (β-TCP) detected. Co-doped ACP samples exhibited a prominent α-TCP phase and citrate play important role in stabilizing the α-TCP phase.

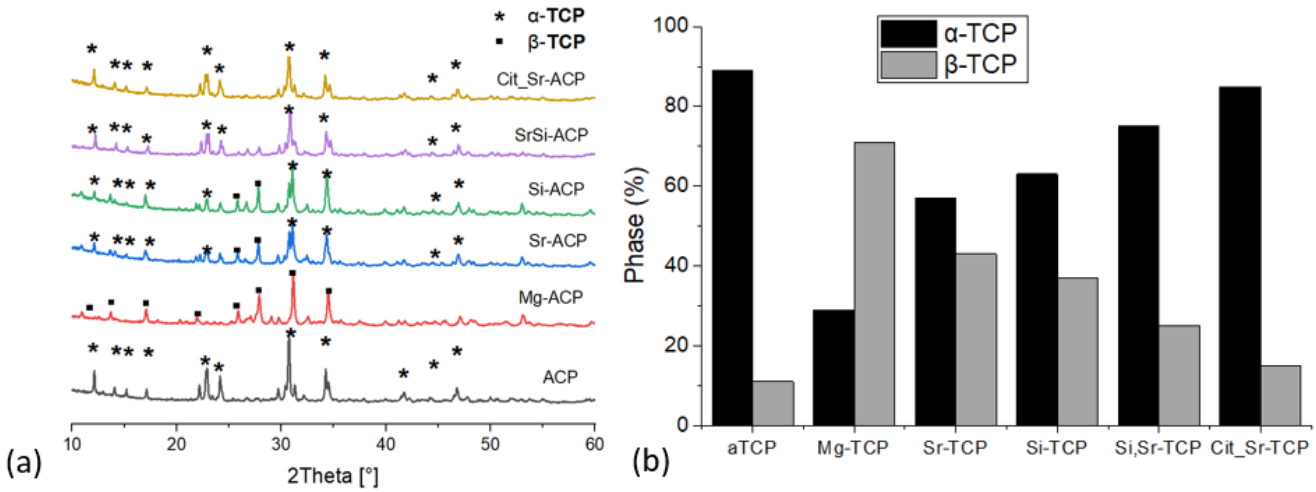

Figure 3-5: (a) Phase transformation (b) phase % of TCP by different ions doping treated at 650℃.

The compressive and flexural strength of cement from LT-αTCP and HT-αTCP with and without carbon fibers were analysed (Figure 3.6). The cements from HT-αTCP showed the slightly higher maximum

compressive strength of 7.57 ± 1.38 MPa compared to 5.15±1.02 MPa for LT-αTCP cements. This slight enhancement in strength is attributable to the improved crystal structure and sintering behavior associated with high temperatures synthesis. The presence of carbon fibers into both cement improved the compressive strength, with the greatest increase observed for LT-αTCP cement due to possibly higher specific area.

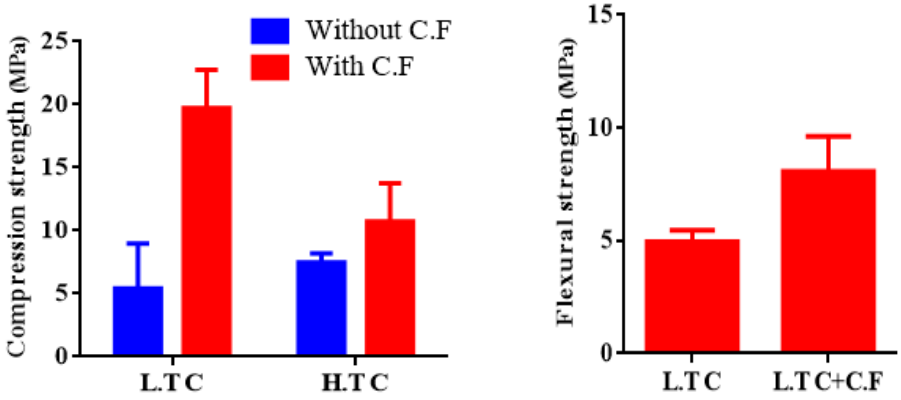

Figure 3-6: Mechanical performance of cement from low temperature cement (L.T C) and high temperature cement (H.T C) (a) maximum compressive strength (b) maximum 3point bending strength with and without carbon fibers.

3.2. Magnesium-doped apatite cement with intrinsic antibacterial properties.

Post-operative infections are one of the most common problems associated with implanting scaffolds for bone regeneration, in particular infectious diseases and biofilm formation on the surface of implants, usually lead to implant failure and osteomyelitis [15-17]. The development of bioactive bone scaffolds with improved osteogenesis, angiogenesis and long-time antibiofilm properties is strongly encouraged in bone regeneration applications [18, 19]. However, Mg-doped apatite cement (CPCs) is considered a promising material for medical implants due to its biocompatibility and biodegradability, considering that the mineral phase of bone is mainly composed of muti-substituted hydroxyapatite. While, Mg has been reported in literature as good antimicrobial agent against gram-positive and gram-negative bacteria [20].

Apatite cement (CPC) has the advantage to fill the bone defects of various geometries and shapes through mini-invasive surgery, as they are characterized by their inherent ability to set and harden in situ [18]. Much effort has been made to improve the biological response of CPCs by functionalization with different drugs, ion doping and/or nanoparticles [19].

In the last decade, numerous studies have attempted to introduce bioactive ions in apatite to improve the osteogenesis and angiogenesis [21-24]. Among all ions doping, magnesium ions stand as the most crucial cation substituting calcium in apatite, as they are the fourth most prevalent cations in the human body [24, 25]. Its deficiency adversely affects all stages of skeletal metabolism, causing cessation of bone growth and decreasing osteoclast and increased osteoblast [26, 27]. It is also reported that magnesium (Mg) has a substantial impact on preventing potential risk factors associated with osteoporosis in humans [28-30].

Furthermore, the release of Mg^{2+} ions in apatitic cement (CPC) has been shown to stimulate osteogenesis and promote angiogenesis [31].

However, the direct doping of Mg^{2+} in α-TCP phase used as a precursor for CPC is reported as particularly challenging, due to the intrinsic character of Mg to stabilize β-TCP. Commonly, Mg^{2+} increased the transformation temperature of the β-phase to the α-polymorph from 1150°C to 1540°C [32].

The functionalization of calcium phosphate cement (CPC) with different drugs has recently gained increasing interest in biomedical applications [33]. They are inherently biocompatible and biodegradable and have been greatly studied in the delivery of drugs or biomolecules for therapeutic applications [34-37]. CPC blended with therapeutic agents exhibits a sustained and controllable release kinetics through passive drug diffusion which has been commercialized for the treatment of osteomyelitis [38]. They have a significant advantage as a drugs carrier due to their non-exothermic setting reaction because many drugs possess temperature sensitive nature [39]. Moreover, higher specific surface area and porous-nano structure of CPC also play a key role in linking and controlling the release of various drugs compared with sintered hydroxyapatite (HA) scaffolds [40].

The development of drug-loaded CPCs is previously studied by mixing the drug in solid component of cement [41]. However, the preparation of drug-loaded CPC is considered as a more challenging than CPCs without drugs, in terms of setting time, flowability and injectability [42-45]. For instance, the loading of the antibiotic tetracycline (TC) on CPC was found to cause a delaying effect on the hardening and the rate of transformation into HA [38, 46, 47]. This delay was attributed to the chemical affinity between TC and Ca^{2+} ions, which could interfere with the dissolution-reprecipitation process responsible for the conversion of calcium phosphate precursors into HA, as well as the overall setting times of the cement [16]. However, slow degradation of CPC can result in prolonged retention of antibiotics and may lead to inactivation or limitations in the pharmaceutical effects and bacterial resistance on final release [37].

To the best of my knowledge, the role of Mg^{+2} in modifying TC release behaviour from Mg-doped CPC has not been studied.

The aim of this study was to develop Mg-doped apatite cement (Mg-CPC) with tuneable antibacterial properties. Therefore, we synthesized a self-hardening paste based on Mg-doped CPC by mixing α-tricalcium phosphate powders $Ca_3(PO_4)_2$ as unique solid precursor and MgHA nanoparticles. First, the effect of MgHA nanoparticles on the setting time, physico-chemical and mechanical properties of CPCs, as well as the role of magnesium on antibacterial properties was investigated. Then, we optimized tetracycline (TC) adsorption process on MgHA nanoparticles and release profile from Mg-doped CPCs functionalized with TC-loaded MgHA nanoparticles. Finally, antibacterial activity of TC-loaded Mg-doped CPC against *Escherichia coli* and *Staphylococcus aureus* were evaluated.

3.2.1. Materials and Methods

α-tricalcium phosphate (αTCP), solid precursor of CPC was synthesized by a high-temperature solid-state reaction of calcium phosphate dibasic ($CaHPO_4$, Sigma Aldrich, US) and calcium carbonate ($CaCO_3$, Sigma Aldrich, US) mixture with a molar ratio of 2:1. Subsequently, the mixture was thermally treated at 1400°C for 1 h, followed by rapid cooling. The resulting powder was milled in ethanol (98%, Sigma Aldrich, US) using a planetary ball milling (Pulverisette 6 classic line, Germany) with alumina grinding balls (5 mm diameter) at 400 rpm for 50 min. Ethanol was evaporated using a rotavator with a vacuum pump.

Magnesium-doped hydroxyapatite (MgHA) nanoparticles were synthesized by wet process, using calcium hydroxide ($Ca(OH)_2$, Sigma Aldrich, US), orthophosphoric acid (H_3PO_4, Sigma Aldrich, US) and magnesium chloride hexahydrate ($MgCl_2 \cdot 6H_2O$, Sigma Aldrich, US). To initiate the synthesis, 3 mM aqueous solution of $Ca(OH)_2$ (99%) was prepared in a 500 mL flask by introducing the appropriate amounts of salts ($MgCl_2 \cdot 6H_2O$) to achieve a Mg-doped HA composition with a magnesium-to-calcium ratio of 10 mol%. The mixture was stirred for 30 minutes on a magnetic stirrer at 40°C. Subsequently, a dilute aqueous solution of 1 mM H_3PO_4 (95%) was added to the continuously stirred calcium hydroxide solution using a controlled peristaltic pump at a rate of 1 ml/min. The solution was stirred for an additional 2 hours and left overnight at room temperature. Then, three-time washed with double distilled water by centrifuging at 10,000 rpm for 10 min. The resulting precipitate was dried overnight at 40°C to remove excess water. Finally, the dried powders were sieved through a 150 μm mesh sieve.

Different powder mixtures were prepared by adding 5 wt%, 10 wt%, 20 wt% of MgHA nanoparticles in respect to α-TCP, respectively. Setting solution, liquid component of CPCs is prepared by mixing 5 wt% sodium phosphate dibasic dihydrate ($Na_2HPO_4 \cdot 2H_2O$, Fluka, UK) and 2 wt% sodium alginate (Sodium Salt of Alginic Acid from Brown Algae, Sigma Aldrich, US) in distilled water.

Finally, the appropriate amounts of the powder mixture and liquid, based on a liquid-to-powder (L/P) ratio of 0.5, were manually mixed to produce the CPC are labelled as Mg-CPC (0%), Mg-CPC(5%), Mg-CPC(10%) and Mg-CPC(20%) are shown in Table 3.VII.

Table 3-VII: Different combinations of cements

Sample code	αTCP powder (wt%)	MgHA powder (wt%)
Mg-CPC (0%)	100	0
Mg-CPC (5%)	95	5
Mg-CPC (10%)	90	10
Mg-CPC (20%)	80	20

3.2.2. Characterizations

To analyse the phase composition of samples, X-Ray powder diffraction (XRD) was used to investigate the diffraction peaks on a D8 Advance diffractometer (Bruker, Karlsruhe, Germany), with CuKα radiation, in 2θ range of 10° to 80° with a scanning step of 0.02°.

To investigate the chemical composition and functional groups, Fourier-transform infrared spectroscopy (FTIR) was performed using a Nicolet IS5 spectrometer (Thermo Fisher Scientific, U.S.A.). The samples were ground with 5% KBr in an agate mortar, compressed into tablets and analysed in the spectral range of 500 to 4000 cm^{-1}.

The specific surface area (SSA) was calculated using the Brunauer–Emmett–Teller (BET) method (Surfer, ThermoScientific, United States) by nitrogen adsorption at a relative pressure of 0.03 Torr.

Particle size distribution was determined by dispersing the powder in aqueous solutions of sodium hexametaphosphate (0.05 wt%). The measurements were performed using an X-ray instrument based o' the Stokes' sedimentation equation (SediGraph 5100 instrument, Micromeritics, US).

The Thermofinnigan 240 Pa instrument was used to measure the porosity of the powders by the intrusion of mercury under controlled pressure (0.1-200 MPa).

Elemental composition analysis of the powders was performed using Inductively Coupled Plasma-Optical Emission Spectroscopy (ICP-OES) with an Agilent 5100 instrument.

The morphology of the powders was studied using Field Emission Scanning Electron Microscopy (FE-SEM) using the Zeiss-SIGMA instrument (Carl Zeiss Microscopy GmbH) at 20 kV acceleration voltage.

The zeta potential of the samples was determined using Dynamic Light Scattering (DLS, Malvern, Zetasizer Nano ZSP). To perform the analysis, the nanoparticles (NPs) were dispersed in a buffer solution at a concentration of 1 mg/ml and maintained at pH 7.4.

The initial and final setting times of the cement formulations were investigated using the Gillmore needles apparatus, following the guidelines in the standard ASTM C266-99.

The compressive strength of the CPCs was evaluated by compressed cylindrical specimens, after being hardened in Teflon moulds for 30 minutes, the specimens were left in a thermostatic bath for 72h. Five cylindrical specimens for each sample were prepared, with a diameter of 6 mm and a height of 12 mm in Teflon moulds. Zwick Roell Z050 machine was used to perform compressive tests in displacement control, with a speed of 1 mm/min.

Functionalization of MgHA nanoparticles with tetracycline (TC)

Firstly, a calibration curve of tetracycline (TC, $C_{22}H_{25}ClN_2O_8$, Sigma Aldrich) was investigated in 4-(2-hydroxyethyl)-1-piperazineethanesulfonic acid (HEPES) buffer solutions (0.01M, with KCl 0.01M, pH 7.4), for concentrations in the range 0.5–2 $mg \cdot ml^{-1}$, in dark conditions to prevent the photo-degradability of the drug when exposed to UV radiation (Gomez-Pacheco et al., 2012). The resulted line (R2 = 0.998)

was obtained by monitoring the optical density at 70 nm by Nanodrop spectrophotometer, ThermoFisher Scientific considering a molar adsorption coefficient of TC of ε = 136 L $mol^{-1} \cdot cm^{-1}$. Then, the adsorption kinetic of TC on MgHA nanoparticles was investigated by dispersing 20 mg of MgHA nanoparticles into 5 ml of TC solutions (1 mg/mL), in a thermostatic stirrer at 37°C up to 24 h. The supernatant was collected at several time-points after centrifuging the suspensions at 5000 rpm for 2 min, then analysed by UV spectroscopy and completely refreshed. In this way, the adequate incubation time to maximize the TC adsorption on MgHA nanoparticles was found. Then, the adsorption of increasing amount of TC was also explored (0.5, 1 and 2 mg/mL), with the same solid/liquid ratio and temperature used to determine the adsorption kinetic. According to this protocol, the optimal incubation time and TC concentration to optimize the drug loading were defined. As control samples, TC-free MgHA nanoparticles solutions were also prepared and analysed.

Preliminary experiments were carried out to evaluate the effect of the dry addition of increasing amounts of MgHA nanoparticles, in the range 0–20 wt% in respect to the αTCP precursor, on the setting times and injectability of the CPC. In this way, the maximum number of NPs capable to avoid significant variations of CPC setting times and viscosity was identified. Then, the same amount of MgHA nanoparticles functionalized with TC (hereafter code as TC-MgHA) was dry mixed with CPC in different amounts, before mixing with the liquid component, to prepare TC-MgHA loaded cements (hereinafter coded as TC-MgCPC).

A calibration curve of TC in HCl (0.1 M, pH 1) for the concentration range 0.1-500 μg/mL was investigated under dark conditions to prevent photodegradation of the drug when exposed to UV radiation. The resulting line (R2 = 0,999) was obtained by monitoring the optical density at 355 nm by UV-vis spectrophotometry (LAMBDA™ 750 UV/Vis/NIR spectrophotometer from PerkinElmer). TC-release experiments were performed by incubating TC-loaded CPC in 10 mL of HEPES buffer solution. At each time point, the 50% of the solution was collected and refreshed. The collected solutions were acidified with HCl 1M to pH 1 and analysed by UV spectroscopy to evaluate the kinetic release of TC. Subsequently, same solutions were analysed by ICP-OES spectrometer (Agilent Technologies, Santa Clara, CA, USA) to evaluate the release of ions (calcium, phosphate and magnesium).

Furthermore, to evaluate the mechanism governing the release of TC from the CPC matrix, the mathematical interpretation of our result was proposed, according to the semiempirical models able to describe drug release from polymeric or monolithic systems, such as Korsmayer-Peppas or Power-Law model ($x_i = Kt^n$) [48, 49], where x_i is the fraction of the released drug by time t, K is a parameter including geometrical and structural features of the matrix and n is the factor related to the mechanism governing the release kinetics, according to Table 3.VIII.

Table 3-VIII: mechanism of release of TC from the CPC matrix

n exponent value	Release regime	Release kinetic and mechanisms
0 < n < 0,45	Hindered Fickian diffusion	Representative of system characterized by diffusive regime with hampered release.
n = 0,45	Fickian diffusion (case I)	Representative of first-order kinetic where diffusion is the main release mechanism
0,45 < n < 1	Anomalous transport	Characteristic of those case where in addition to diffusion, other mechanisms contribute to the drug release (e.g. matrix erosion or Swelling).
n = 1	Non-Fickian transport (case II)	Corresponds to a zeroth order kinetic and is typical of kinetics governing by phenomena of polymer degradation and relaxation or degradation/dissolution of monolithic system
n > 1	Super case II	Extreme form of transport that usually occurs when severe modification in the matrix take place

Antibacterial tests

The pellets of HA and Mg-doped HA (7 mol %) were prepared with dimension 1cm*2mm and were incubated in simulated body fluid (PBS) solution for 24h at 37°C, while CPC and Mg-CPC (20 wt%) pellets were incubated for 72h at 37°C in PBS solution. After separating of PBS solution, E. coli ATCC 25922 and S. aureus 25923 were seeded on pellets for 3h, 12h and 24h. Viability has been determined through MTT assay on bacteria suspension and adhesion to the scaffolds. Data represented as % of bacterial viability on scaffolds over the number of bacteria grown in the medium (TCP-red hatching). Statistical analysis (*) was performed using two-way analysis of variance (ANOVA), followed by Bonferroni's multiple comparisons test within the same group. ****$p<0.0001$ and *$p<0.05$.

3.2.3. Results and Discussions

The elemental analysis confirmed the presence of magnesium ions in quantities that closely matched the nominal composition of the initial mixture (Table 3-IX). Additionally, the analysis revealed calcium deficiency, indicated by Ca/P mole ratios 1.54.

Table 3-IX: Elemental composition by ICP of MgHA-NPs (After grinding).

Sample	Ca/P (mol%)	(Ca+Mg)/P (mol%)	Mg/(Ca+Mg) (mol%)	Mg (wt%)
MgHA	1.58±0.01	1.69±0.01	7.00±0.02	1.34±0.11

XRD patterns of MgHA nanoparticles demonstrating diffraction peaks matching JCPDS No. 09-0432. No other crystalline phases were detected are shown in Figure 3.7a. FTIR analysis also revealed typical hydroxyapatite patterns is shown in Figure 3.7b. Vibrational bands at 562 and 603 cm^{-1} indicated O-P-O bending, while peaks at 962 and 1034 cm^{-1} represented PO_3^{-4} stretching, despite minor calcium deficiency.

Additionally, peaks at 874, 1339 and 1456 cm^{-1} associated with CO_3^{2-} group were observed in pattern. The peak at 632 cm^{-1} and broad peak at 3427 cm^{-1} indicated OH^- or absorbed H_2O. SEM analysis of MgHA confirms the nano-size and the needle-like morphology (Figure 3.7c), which is consistent with the high SSA value.

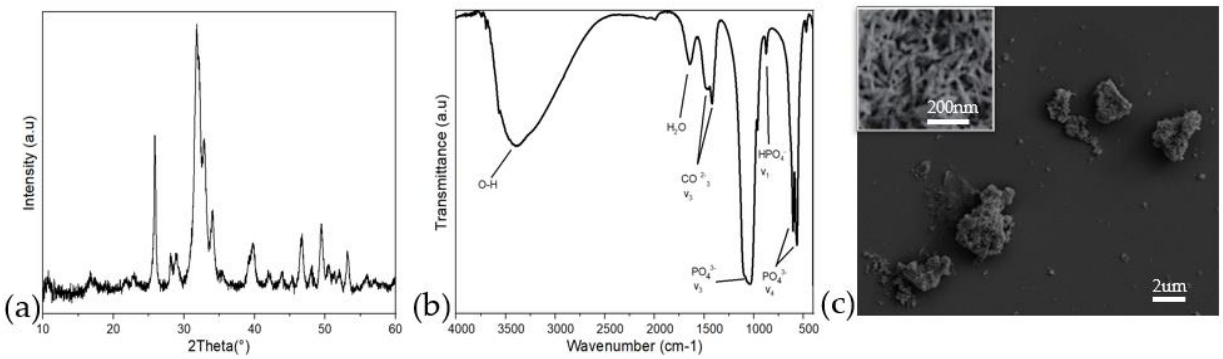

Figure 3-7:(a) X-ray diffraction pattern; (b) FTIR-ATR spectrum; (c) SEM micrograph, of MgHA-NPs.

The XRD pattern, FTIR and SEM analysis of the α-TCP revealed the typical phases of α-TCP (sub-chapter 3.1.3) (Figure 3.8).

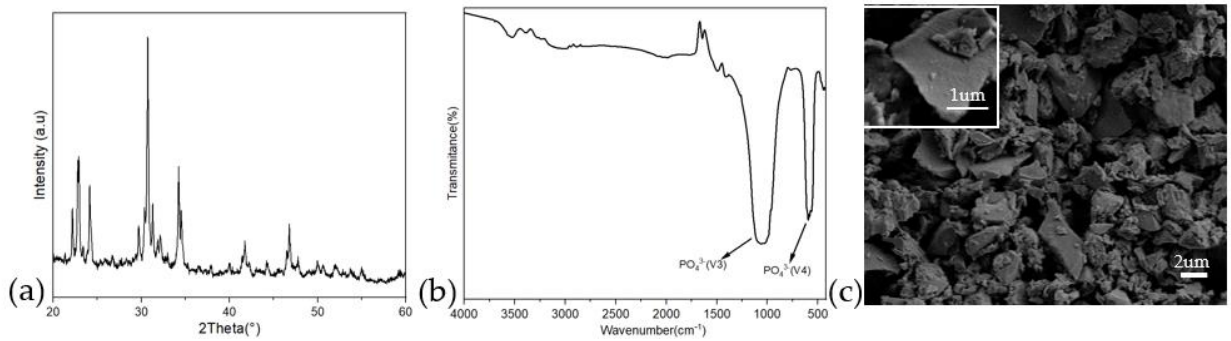

Figure 3-8: (a) X-ray diffraction pattern; (b) FTIR-ATR spectrum; (C) SEM micrograph, of α-TCP (scale bar = 500 nm)

The average agglomerate particle size of the MgHA nanoparticles and α-TCP was 0.72 μm and 2.2 μm respectivily are shown in Table 3-X. The specific surface area of MgHA was much higher than that of α-TCP.

Table 3-X: Particle size, specific surface area and porosity of MgHA nanoparticles and α-TCP

Sample	Particle size (μm) d50	SSA (m^2/g)	Porosity (%)
MgHA	0.72	87.29	60.91
α-TCP	2.2	3.03	57.02

Initial experiments were conducted to find the maximum amount of MgHA nanoparticles that could be incorporated into CPCs without causing significant changes in setting times, injectability and hardening, to maintain an initial setting time of approximately 15-30 minutes, which is considered appropriate for clinical applications. A slight increase in initial setting times and a noticeable increase in final setting time was obsereved, in particular when the amount of MgHA nanoparticles was increased up to 20 wt% in the cement (Table 3-XI)

Table 3-XI: Initial and final setting time of Mg-CPC

Sample code	Initial setting time (min)	Final setting time (min)
Mg-CPC (0%)	10±1.5	22±2.0
Mg-CPC (5%)	18±2.0	65±3.0
Mg-CPC (10%)	23±2.5	90±3.0
Mg-CPC (20%)	40±2.5	220±5.0

Elemental analysis confirmed the amount of each doping ion in the final cement was very close to the amount in the starting mixture (Table 3-XII). The final product was also calcium-deficient, with a calcium-to-phosphorus mole ratio lower than 1.67.

Table 3-XII: ICP analysis of Mg-CPC

Sample	Ca/P	(Ca+Mg) /P	Mg/(Ca+Mg) (mol%)	Mg (wt%)
Mg-CPC (0%)	1.40	1.40		
Mg-CPC (5%)	1.39	1.40	0.62	0.11
Mg-CPC (10%)	1.40	1.42	1.03	0.22
Mg-CPC (20%)	1.40	1.41	2.08	0.44

The XRD analysis was conducted on the cements at various time points 16h, 30h, 48h and 72h, to investigate the extent of transformations into CDHA. The incorporation of MgHA nanoparticles into CPCs prolonged both initial and final setting times, resulting in a delayed in the complete transformation of α-TCP into calcium-deficient apatite. As the concentration of MgHA nanoparticles increased from 5 wt% to 20 wt% in cements, a greater delayed in HA formation was observed (Figure 3.9). Especially, the presence of MgHA nanoparticles led to a decrease in the crystallinity of the HA phase within the cement. These results indicates that the addition of MgHA nanoparticles not only favoring the cement setting and phase transformation process, also impede the crystal growth of the new HA phase, could be potentially good for enhancing bioactivity.

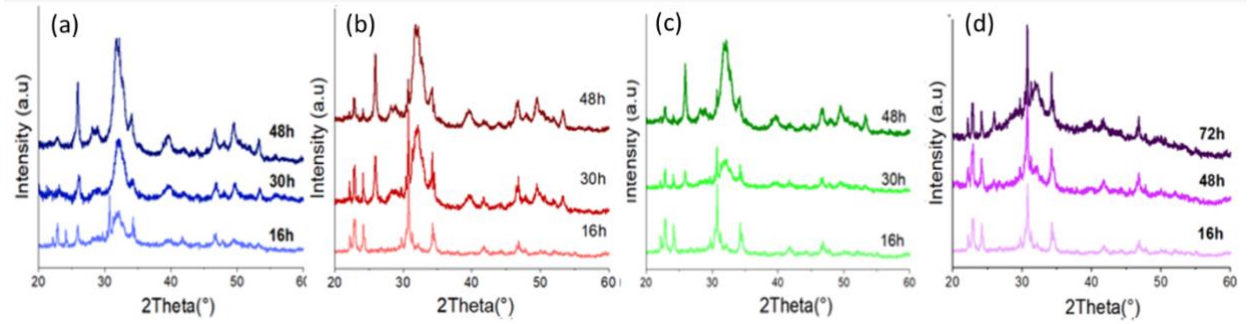

Figure 3-9: X-ray diffraction pattern of CPC (a); Mg-CPC (5%); Mg-CPC (10%) and Mg-CPC (20%) after (0h, 16h, 30h, 48h, 72h) setting at 37°C.

Extent of HA formation at different time points 16h, 30h, 48h and 72h was also invesigated by FTIR analyses. Figure 3.10 shows the patterns for all cements formed by hydrolysis of a-TCP powder with different concentartions of MgHA nanoparticles (5 wt%, 10 wt%, 20 wt%). In all patterns, pure phases of HA was confirmed with no any other phase detected. The presence of structural OH^- groups in the hydrated composite is suggested by the absorption peaks at 650 and 3473 cm^{-1} in Mg-CPCs. The peak at 650 cm^{-1} corresponds to the OH vibrational mode, while the peaks at 3473 cm^{-1} represents the stretching mode, which appears as a symmetrical and broad peak, falling within the range of weakly hydrogen-bonded groups. A more distinct OH peak is observed in the librational mode, located near the principal $PO4^{3-}$ absorption peaks at 650 cm^{-1} confirming the HA formation from αTCP hydrolysis. The increased absorption intensity of the OH^- band at 3473 cm^{-1} with increasing hardening time suggests the formation of calcium-deficient hydroxyapatite. While with increasing concentartions of MgHA nanoparticles in cements, resulted in delayed of transformation into CDHA , as confirmed in above XRD analysis.

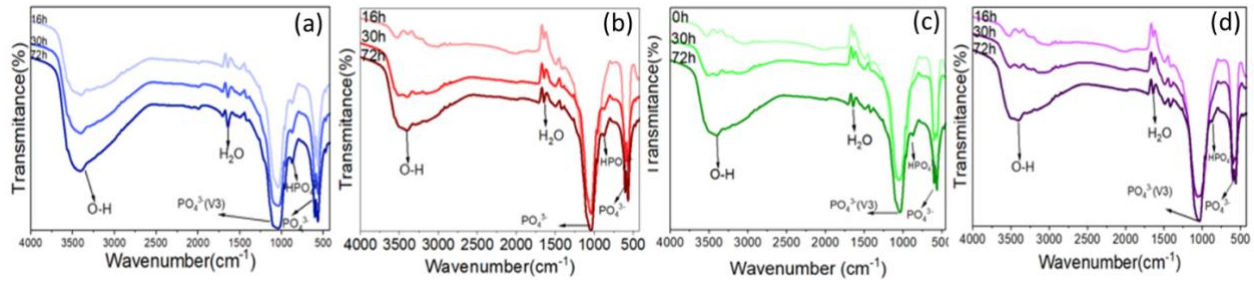

Figure 3-10: FTIR spectrum of CPC (a); Mg-CPC (5%); Mg-CPC (10%) and Mg-CPC (20%) after (0h, 16h, 30h, 48h, 72h) setting at 37°C.

The morphology of the cements was examined using SEM, shown in Figure 3.11a. It was observed that the addition of MgHA nanoparticles up to a concentration of 10wt%, the morphology of the cements appeared similar after 72h. However, when the concentration was increased to 20wt% of MgHA nanoparticles, only larger particles of αTCP and nanoparticles of MgHA were observed, indicating that the cement did not fully

harden after 72h. The complete transformation of Mg-CPC (20%) occurred after 96 h, morphology transformed from a plate-like to a rod-like shape.

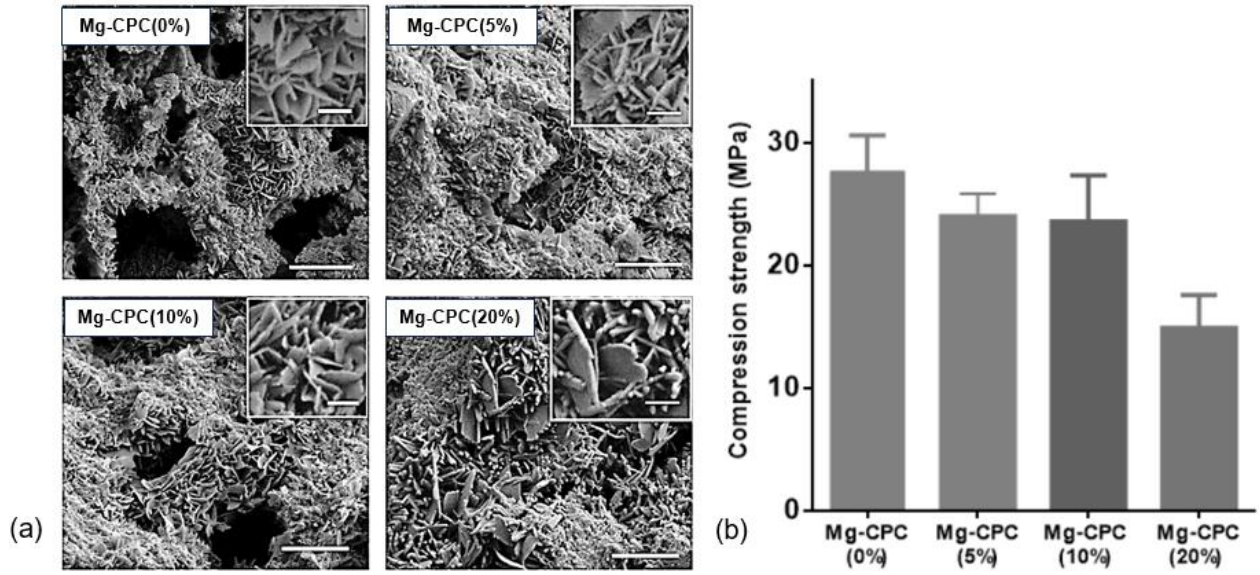

Figure 3-11: (a) SEM images with Scale bar 1µm and insert bar is 200nm, (b) Maximum compressive strength of Mg-CPC (0%): Mg-CPC (5%); Mg-CPC (10%) and Mg-CPC (20%) after 72h setting at 37°C.

Furthermore, the compressive strength of the cements was evaluated are shown in Figure 3.11b. It was found that with the addition of up to 10wt% of MgHA-NPs in cements, the compressive strength slightly decreased after 72h hardening. This decrease may be attributed to the incorporation of the MgHA nanoparticles, which can affect the overall structure and bonding within the cements. However, when 20 wt% of MgHA nanoparticles were added, the compressive strength decreased significantly. This suggests that the addition of 20 wt% of MgHA nanoparticles, delayed the hardening and have not completely transformed into HA after 72 hours, leading to a considerable decrease in its strength. These results indicate that while the addition of lower concentrations of MgHA nanoparticles (up to 20wt%) had a limited effect on the morphology and compressive strength of the cement, higher concentrations (30wt%) resulted in non-hardened cement and a substantial reduction in strength. These findings are important for determining the optimal concentration of MgHA nanoparticles for achieving desirable cement properties in terms of both morphology and mechanical strength.

On the basis these results, the 20wt% Mg-CPC was evaluated for antibacterial tests and release of tetracycline (TC).

The antibacterial analysis of MgHA and Mg-CPC scaffolds was assessed by evaluating the viability of *E. coli* and *S. aureus* bacteria in the supernatant after incubation with the scaffolds for different time periods. Both scaffolds had a substantial antibacterial effect on both bacteria during a short incubation period of 3 hours, as shown in Figure 3.12. However, the antibacterial activity of the scaffolds decreased progressively as the incubation duration increased. The antibacterial efficacy against E. coli decreased to 30% after 24

hours in MgHA scaffolds and to 10% after 24 hours in Mg-CPC scaffolds. Conversely, the antibacterial effect of MgHA scaffolds on *S. aureus* decreased to 50% after 24 hours, but the antibacterial effect of Mg-CPC scaffolds persisted at 70% even after 24 hours [50]. The findings suggest that Mg-CPC scaffolds have a prolonged antibacterial activity against S. aureus in comparison to MgHA scaffolds. The variation in antibacterial efficacy may be attributed to the inherent characteristics of the scaffolds, such as their surface chemistry and porous structure [51]. The surface chemistry of Mg-CPC scaffolds might potentially interfere with bacterial cells by impeding their metabolism or inhibiting cell wall production. The porosity nature of Mg-CPC scaffolds may further serve as a physical barrier that inhibits bacterial adhesion and proliferation [52]. Mg-CPC scaffolds possess a commendable capability to sustain their antibacterial efficacy against S. aureus over long periods of incubation, making them a very promising material for applications in bone tissue engineering. Their capacity to prevent S. aureus infection might have an important impact on the success of orthopedic therapies.

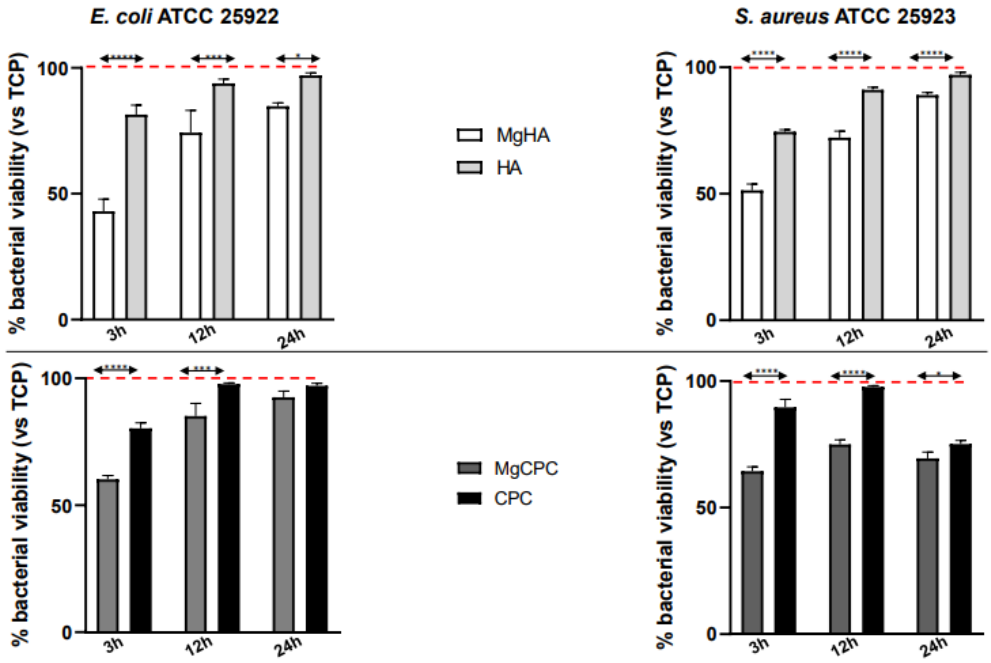

Figure 3-12: The statistical analysis of supernatant composed of planktonic bacteria.

The activity of MgHA and Mg-CPC scaffolds prevents the bacterial attachment at higher incubation times for *E. coli* S. aureus at 24 h (Figure 3.13). The addition of magnesium in scaffold significantly increases the antibacterial activity of the material [53]. This effect is seen for both *E. coli* and *S. aureus* bacteria, with the greatest effect seen at 24 hours. At 24 hours, MgHA reduced the viability of *E. coli* by 60% and *S. aureus* by 35%, compared to 30% and 10% for HA, respectively. While Mg-CPC reduced the viability of *E. coli* by 90% and *S. aureus* by 35%, compared to 70% and 10% for CPC, respectively. HA scaffold also exerts an important antibacterial action [54]. Mg-CPC scaffolds are able to reduce the bacterial viability

up to 70% in both suspension and adhesion against gram-negative bacteria *E coli* and gram-positive bacteria *S aureus* at 24h.

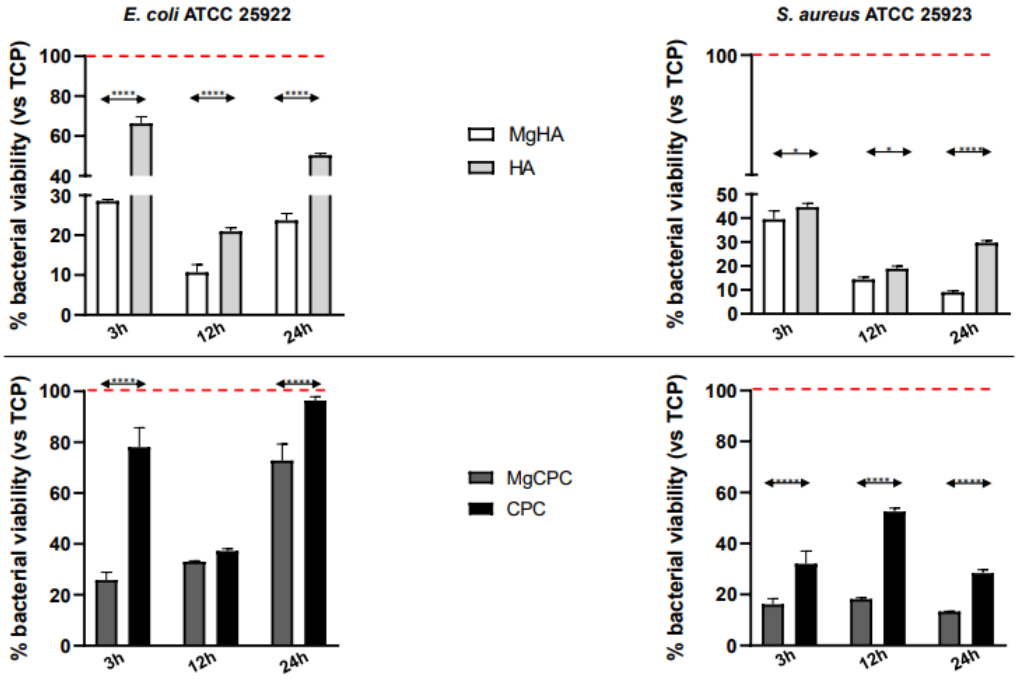

Figure 3-13: The statistical analysis of bacterial adhesion on the scaffold

Experiments were conducted to optimize the adsorption of TC onto MgHA nanoparticles. The adsorption rate of a TC solution onto MgHA nanoparticles was studied at various incubation times, revealed that a soaking time of 2 hours is sufficient to reach a quasi-equilibrium condition. After given optimal contact time 2 hours, the adsorption of TC was evaluated at different concentrations of TC in solution (Figure 3.14a). The amount of TC adsorbed on the MgHA nanoparticles increased as the concentration of TC in solution increased, reaching a maximum of about 1 mg/m^2. MgHA nanoparticles exhibited negative zeta potential, but the zeta potential in absolute value decreased as the concentration of TC increased are shown in Figure 3.14b.

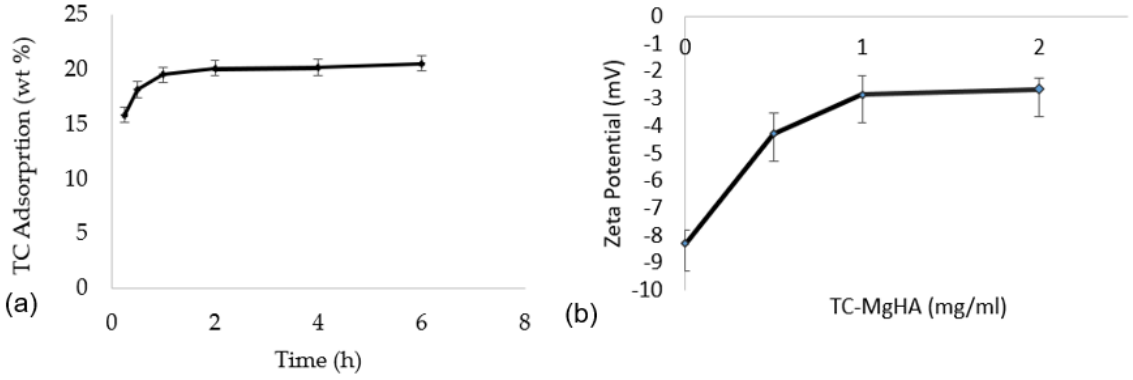

Figure 3-14: TC absorption and zeta potential o magnesium doped cement.

TC release profile of Mg-CPC (20wt%) are shown in Figure 3.15. Magnesium doped cements were functionalized with tetracycline, a commonly used broad-spectrum antibiotic, while combining it with magnesium effect to achieve an effective antibacterial outcome.

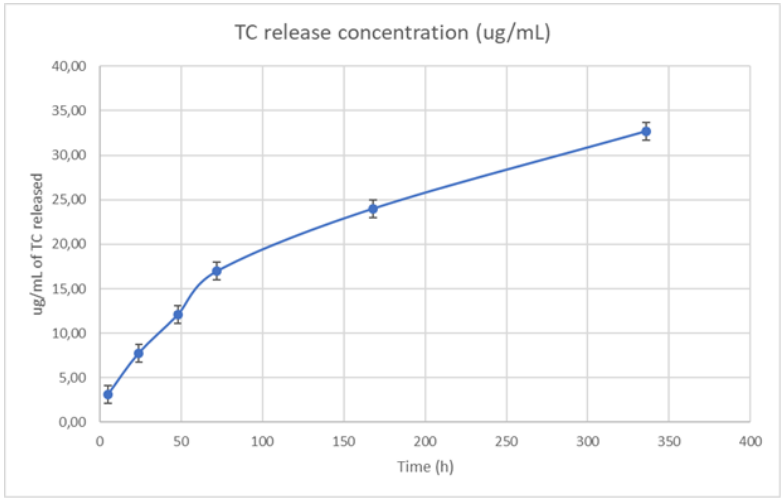

Figure 3-15: TC release from magnesium doped cement

Degradation tests of the bone cements were also performed up to 14 days, in terms of Ca^{2+} and Mg^{2+} ions release, exhibiting lower calcium and magnesium release for the TC-containing formulations (Figure 3.16). Mg-CPC exhibited higher calcium release than control CPC, will have higher solubility.

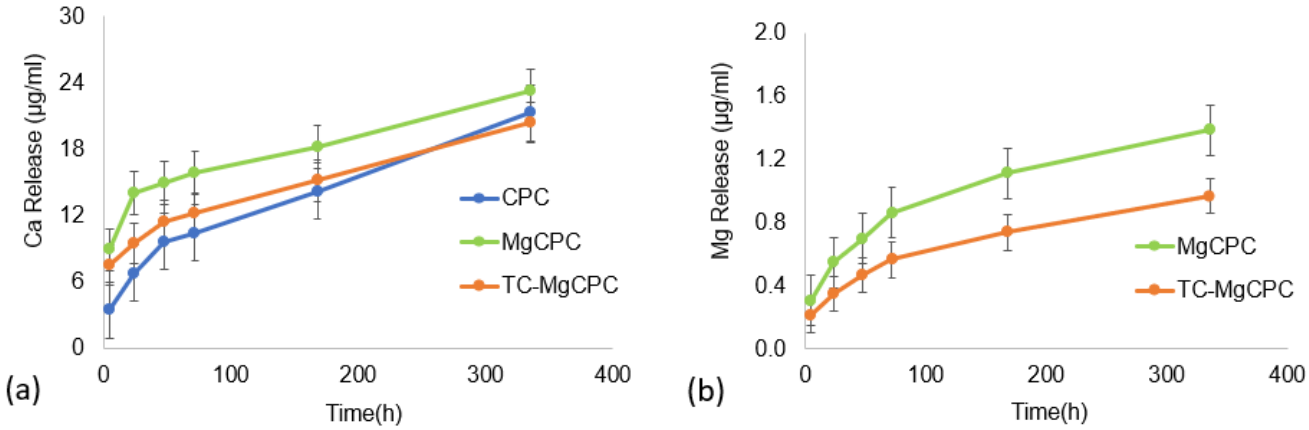

Figure 3-16: Ion releases up to 14 days: (a) Calcium, (b) Magnesium.

3.3. Mechanically reinforced magnesium and strontium-doped apatite cement with carbon fibers.

The major challenges concerning the mechanical properties of calcium phosphate cements (CPC) scaffold is related to their inherent brittleness, which limits their usage to non-load bearing bone applications. Among various toughening approaches, fiber reinforcement is intriguing method due to its unique mechanism. They can bridge cracks after its appearance due to stress, impeding its further propagation. Furthermore, the frictional sliding of fibers against the matrix during pullout further consumes the applied force that results in increased fracture toughness. The addition of different types of fibers (e.g., carbon, e-glass, aramid, and polyglactin) increased the strength of cement and resulted in an increase of approximately two orders of magnitude in the fracture work [55]. Carbon fibers are the preferred choice among researchers compared to all other types of fibers due to their high strength-to-weight ratio, thermophysical properties, sorption, and high elastic modulus. These advances are potential and are actively being investigated by researchers to develop cement composite with improved interlaminar toughness [56]. These non-degradable fibers can significantly improve the fracture toughness of CPCs, but their low biodegradability can hinder the new bone formation [57].

In this context, this study will explore the balance between suitable mechanical strength and biological properties.

Therefore, the aim of this activity was to develop carbon fiber-reinforced calcium phosphate cements by mixing αTCP or Sr-αTCP with MgHA nanoparticles as inorganic precursors. Here, MgHA nanoparticles were mixed in αTCP or Sr-αTCP powder because the direct doping of Mg^{2+} in α-TCP phase used as a precursor for CPC is reported as particularly challenging, due to the intrinsic character of Mg to stabilize β-TCP. The addition of carbon fibers in cement was investigated to achieve appropriate mechanical properties.

3.3.1. Materials and Methods

α-tricalcium phosphate (αTCP), solid precursor of CPC were synthesized by a high-temperature solid-state reaction of calcium phosphate dibasic ($CaHPO_4$, Sigma Aldrich, US) and calcium carbonate ($CaCO_3$, Sigma Aldrich, US) mixture with a molar ratio of 2:1 [11, 58-60]. Subsequently, the mixture was thermally treated at 1400°C for 1 h, followed by rapid cooling. The resulting powder was milled in ethanol (98%, Sigma Aldrich, US) using a planetary ball milling (Pulverisette 6 classic line, Germany) with alumina grinding balls (2 mm diameter) at 400 rpm for 50 min. Ethanol was evaporated using a rotavator with a vacuum pump.

Sr-αTCP were synthesized by repeating the same route by introducing strontium carbonate (CaCO3, Sigma Aldrich, US) containing the doping ions in appropriate amounts to prepare Sr-αTCP (Sr/(Ca+Sr) = 2wt%) [1, 58].

Magnesium-doped hydroxyapatite (MgHA) nanoparticles were synthesized by co-precipitation method [61], using calcium hydroxide (Ca(OH)2, Sigma Aldrich, US), orthophosphoric acid (H3PO4, Sigma Aldrich, US) and magnesium chloride hexahydrate (MgCl2·6H2O, Sigma Aldrich, US). To initiate the synthesis, 3 mM aqueous solution of Ca(OH)2 (99%) was prepared in a 500 mL flask by introducing the appropriate amounts of salts (MgCl2·6H2O) to achieve a Mg-doped HA composition with a magnesium-to-calcium ratio of 10 mol%. The mixture was stirred for 30 minutes on a magnetic stirrer at 40°C. Subsequently, a dilute aqueous solution of 1 mM H3PO4 (95%) was added to the continuously stirred calcium hydroxide solution using a controlled peristaltic pump at a rate of 1 ml/min. The solution was stirred for an additional 2 hours and left overnight at room temperature. Then, three-time washed with double distilled water by centrifuging at 10,000 rpm for 10 min. The resulting precipitate was dried overnight at 40°C to remove excess water. Finally, the dried powders were sieved through a 150 μm mesh sieve.

Different powder mixtures were prepared by adding 10 wt% of MgHA nanoparticles to α-TCP and Sr-αTCP, respectively (Table I). Setting solution, liquid component of CPCs is prepared by mixing 5 wt% sodium phosphate dibasic dihydrate (Na2HPO4·2H2O, Fluka, UK) and 2 wt% sodium alginate (Sodium Salt of Alginic Acid from Brown Algae, Sigma Aldrich, US) in distilled water.

Finally, the appropriate amounts of the powder mixture and liquid, based on a liquid-to-powder (L/P) ratio of 0.6, were manually mixed to produce the CPC are labelled as CPC, Mg-CPC, Sr-CPC, MgSr-CPC are shown in Table 3-XIII.

Table 3-XIII: Different combinations of cements

Sample code	αTCP powder (wt%)	Sr-αTCP powder (wt%)	MgHA powder (wt%)
CPC	100	0	0
Mg-CPC	90	0	10
Sr-CPC	0	100	0
MgSr-CPC	0	90	10

Different combinations of carbon fibers reinforced cement were prepared by varying the amount (4wt%, 2wt%) and length (5mm, 2.5mm) of fibers for compressive and 3-point-bending tests of CPC (Table 3-XIV).

Table 3-XIV:Composition of CPC contains different amount and length of carbon fibers.

Sample Name	Powder (wt%)	Carbon Fibers (wt%)	Carbon Fibers length (mm)
CPC	100	-	-
CPC/CF4/2.5	96	4	2.5
CPC/CF4/5	96	4	5
CPC/CF2/5	98	2	5

On the base of these mechanical test, 4 wt% of carbon fibers with 5mm were selected to reinforced CPC, Mg-CPC, Sr-CPC and MgSr-CPC.

Characterizations

To analyse the phase composition of samples, X-Ray powder diffraction (XRD) was used to investigate the diffraction peaks on a D8 Advance diffractometer (Bruker, Karlsruhe, Germany), with CuKα radiation, in 2θ range of 10° to 80° with a scanning step of 0.02°. Fourier-transform infrared spectroscopy (FTIR) was performed using a Nicolet IS5 spectrometer (Thermo Fisher Scientific, U.S.A.) to investigate the chemical composition and functional groups of powder. For this, samples were ground with 5% KBr in an agate mortar, compressed into tablets and analysed in the spectral range of 500 to 4000 cm−1. The specific surface area (SSA) was calculated using the Brunauer–Emmett–Teller (BET) method (Surfer, ThermoScientific, United States) by nitrogen adsorption at a relative pressure of 0.03 Torr. Particle size distribution was determined by dispersing the powder in aqueous solutions of sodium hexametaphosphate (0.05 wt%). The measurements were performed using an X-ray instrument-based o' the Stokes' sedimentation equation (SediGraph 5100 instrument, Micromeritics, US). The Thermofinnigan 240 Pa instrument was used to measure the porosity of the powders by the intrusion of mercury under controlled pressure (0.1-200 MPa). Elemental composition analysis of the powders was performed using Inductively Coupled Plasma-Optical Emission Spectroscopy (ICP-OES) with an Agilent 5100 instrument. The morphology of the powders was studied using Field Emission Scanning Electron Microscopy (FE-SEM) using the Zeiss-SIGMA instrument (Carl Zeiss Microscopy GmbH) at 20 kV acceleration voltage. The initial and final setting times of the cement formulations were investigated using the Gillmore needles apparatus, following the guidelines in the standard ASTM C266-99. The compressive strength of the CPCs was evaluated by compressed cylindrical specimens, after being hardened in Teflon moulds for 30 minutes, the specimens were left in a thermostatic bath for 72h. Five cylindrical specimens for each sample were prepared, with a diameter of 6 mm and a height of 12 mm in Teflon moulds.

The equation for calculating the compression strength is:

$$\sigma = - \frac{F}{A}$$

Where $\boldsymbol{\sigma}$ is compression strength (MPa), F is applied load (N) and A is area (mm) of the specimen undergoing the mechanical stress.

Conversely, the 3-point bending strength of the CPCs was evaluated by rectangular bar with dimension 60mm*12mm*10mm. The 3-point bending strength was calculated by the equation:

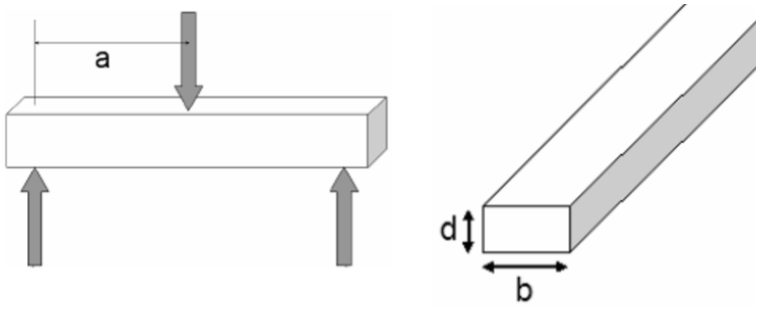

$$\boldsymbol{\sigma = \frac{3Fl}{bd^2}}$$

where $\boldsymbol{\sigma}$ = bending strength (MPa), F = load (N), l = support span (mm), b = width of tested specimen (mm) (b>d), d = height of tested specimen (mm).

Zwick Roell Z050 machine was used to perform compressive tests in displacement control, with a speed of 1 mm/min. Macrograph images of mechanical tested specimen were analysed by optical microscopy.

Results and Discussions

Initial experiments were conducted to find the maximum amount of MgHA nanoparticles that could be incorporated into CPCs without causing significant changes in setting times, injectability and hardening, to maintain an initial setting time of approximately 15-30 minutes, which is considered appropriate for clinical applications [62, 63]. A slight increase in initial setting times and a noticeable increase in final setting time was observed, in particular when the amount of MgHA nanoparticles was increased up to 10 wt% in the cement [58].

Elemental analysis confirmed the amount of each doping ion in the final cement was very close to the amount in the starting mixture (Table 3-XV). The final product was also calcium-deficient, with a calcium-to-phosphorus mole ratio lower than 1.67.

Table 3-XV: ICP analysis of CPC, Mg-CPC, Sr-CPC and MgSr-CPC

Sample	Ca/P	(Ca+Mg+Sr) /P	Mg/(Ca+Mg+Sr) (mol%)	Sr/(Ca+Mg+Sr) (mol%)	Mg (wt%)	Sr (wt%)
CPC	1.50	1.50	-	-	-	-
Mg-CPC	1.40	1.42	1.03	-	0.22	-
Sr-CPC	1.39	1.45	-	1.59	-	0.25
MgSr-CPC	1.39	1.45	0.99	1.49	0.19	0.15

The addition of MgHA-NPs (10 wt%) in CPCs resulted in increased initial and final setting time as compared to CPC or Sr-CPC, while the addition of C-fibers (4wt.%) slightly decreased the setting time (as shown in Table 3-XVI).

Table 3-XVI: Composition and setting times of CPC, Sr-CPC containing MgHA nanoparticles and carbon fibers.

Sample Name	Powder (wt%)	MgHA (wt%)	Carbon Fibers (wt%)	Carbon Fibers length (mm)	Initial setting minutes	Final setting minutes
CPC	100	-	-	-	10	22
CPC+C.F	96	-	4	5	8	20
Mg-CPC	90	10	-	-	35	90
Mg-CPC+C.F	86	10	4	5	25	60
Sr-CPC	100	-	-	-	15	22
Sr-CPC+C.F	96	-	4	5	10	20
MgSr-CPC	90	10	-	-	40	90
MgSr-CPC+C.F	86	10	4	5	40	80

To evaluate the phase transformation extent of CPC, Mg-CPC, Sr-CPC and MgSr-CPC, the XRD analysis was performed at 16h and 72h after mixing and hardening. The transformation of α-TCP and Sr-αTCP into calcium-deficient apatite (CDHA) was delayed as a result of the incorporation of MgHA-NPs into α-TCP and Sr-αTCP. It was observed that after 72h, all the samples were completely transformed into HA. On the other hand, the addition of C-fibers did not prevent the transformation into HA [64], but poorly crystalline HA phases were also detected (Figure 3.17).

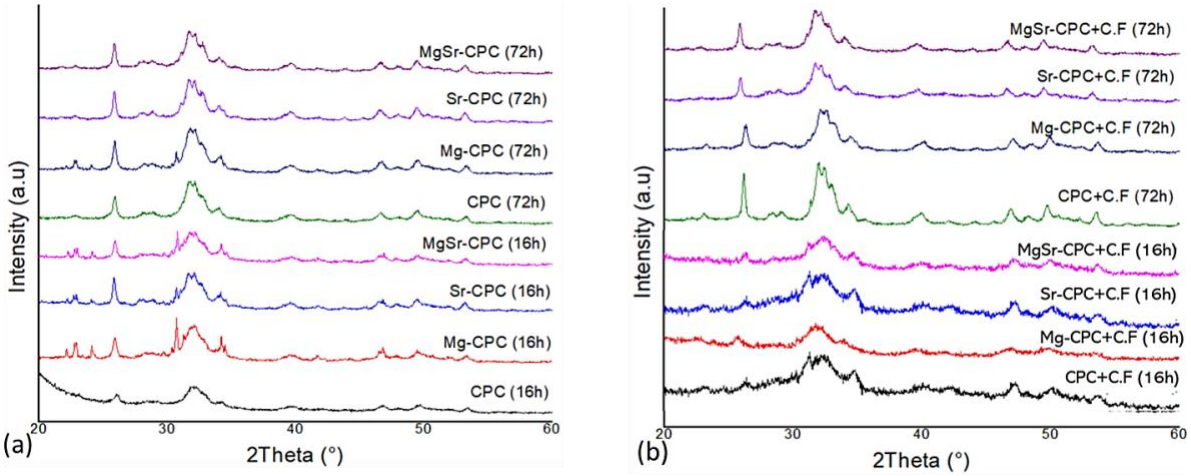

Figure 3-17: X-ray diffraction pattern of CPC, Sr-CPC, Mg-CPC and MgSr-CPC after (16h and 72h) setting at 37°C (a) without (a)carbon fibers (b) with carbon fibers.

The microscopical features of the cements with and without fibers were evaluated by SEM analysis (Figure 3.18). A plate to needle-like morphology were exhibited by all the samples, due to the dissolution and precipitation mechanism at the basis of CPC hardening [65-67]. Plate-like crystals are frequently formed during the first phases of hardening, while needle-like crystals are produced during the latter stages. The plate to needle-like morphology of CPC plays a crucial role in improving mechanical performance, particularly plates-like particles provide tensile strength, and the needles-like offer compressive strength [44].

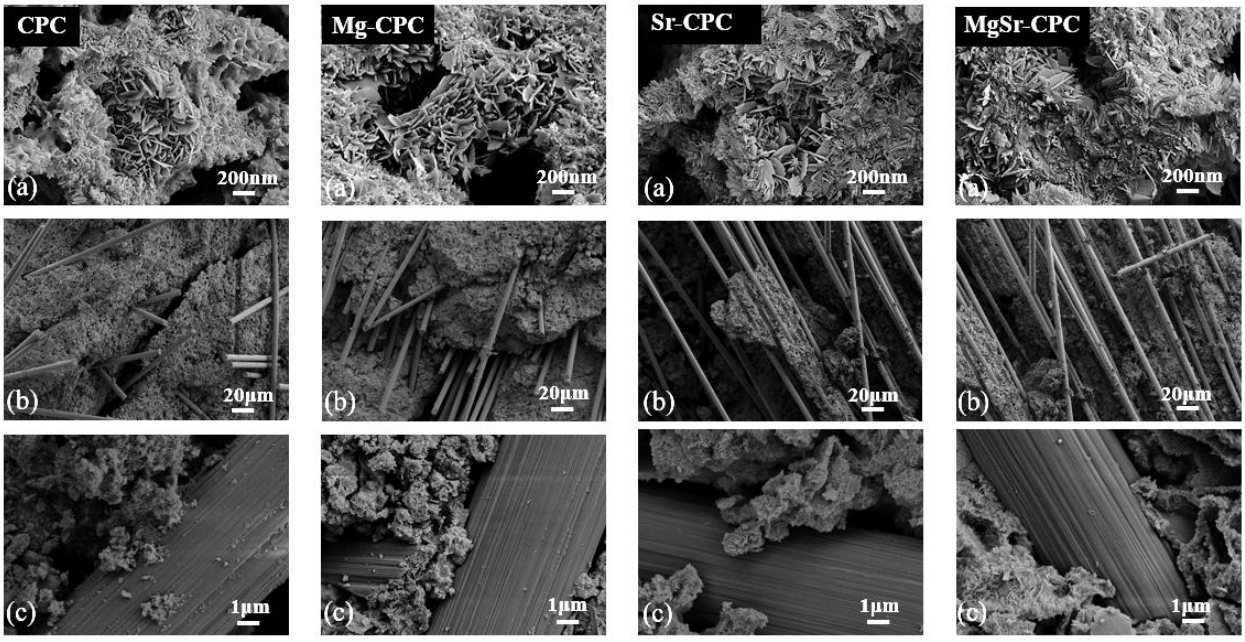

Figure 3-18: SEM images of CPC, Mg-CPC, Sr-CPC and MgSr-CPC without carbon fibers (a) and with 2.5mm carbon fibers at 4 wt% (b, c).

The fiber-containing formulations exhibited tufts of fibers randomly dispersed into the cement matrix due to the aggregation of fibers during the mixing process. The cement-fiber interface exhibited randomly weak interactions between the components because fibers are simply entangled in the cement matrix and not

chemically linked to the cement [68]. However, in particular situations like bone tissue engineering, this weak interface might be advantageous in promoting better integration between the implant and the adjacent bone [69].

The compressive and flexural strength of CPC, Mg-CPC, Sr-CPC and MgSr-CPC were analyzed (Figure 3.19). The maximum compressive strength, and three-point bending strength is a measure of the material's capacity to resist deformation under compressive loading, and bending loading, respectively [68, 70, 71]. The Young's modulus and modulus of resilience were measured using three-point bending tests. Materials with greater three-point bending strengths and maximum compressive strengths are more resistant to crushing and breaking, respectively [72].

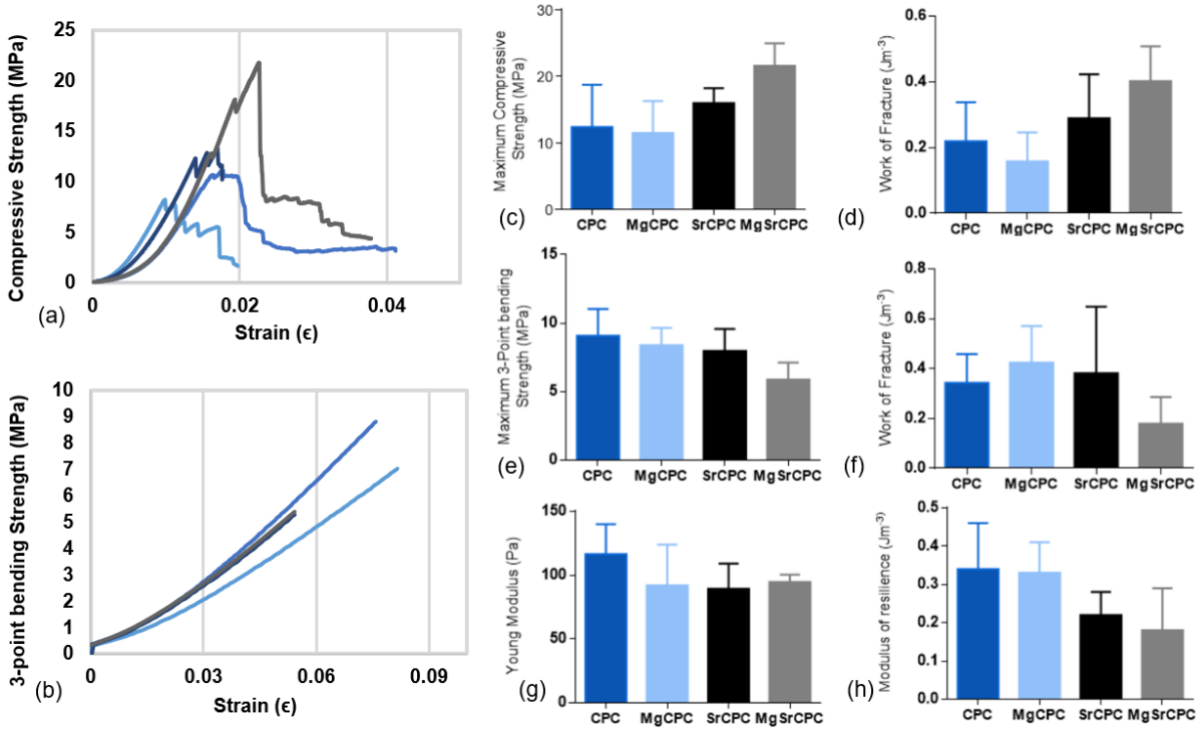

Figure 3-19: Mechanical performance of CPC, Mg-CPC, Sr-CPC and MgSr-CPC (a) compressive strength curves, (b) 3-point bending strength curve (c) maximum compressive strength, (d) work of fracture from compressive tests (e) maximum 3point bending strength (f) work of fracture from 3-point bending tests (g) young modulus from 3-point bending tests (h) bending modulus of resilience from 3-point bending tests.

The MgSr-CPC showed the highest maximum compressive strength (21.57 ± 3.38 MPa) and work of fracture (0.4±0.1 J/m^3), while also the lowest bending strength (5.88 ± 1.23 MPa) and bending work of fracture (0.18 ± 0.10 J/m^3). The CPC exhibited higher Young's modulus and modulus of resilience values than all other samples indicating higher stiffness and energy absorption capacity under tensile stress, are shown in Figure 5 g&h [73].

Mg and Sr doping slightly improved the compressive strength of CPCs by altering crystal lattice properties, introducing additional phase stability.

The low strength of the CPC formulations was due to the intrinsic macro-porosity of the samples [74], as observed in by optical microscopy (Figure 3.20), possibly acting as stress concentration defects, increased stress in the vicinity and initiating the crack, leading to complete brittle breakage of the samples [75]. This concentrated stress may exceed the yield strength of the material, resulting in the development of microcracks. Further loads may cause the propagation and enlargement of these microcracks, leading to the complete collapse of the material [76, 77].

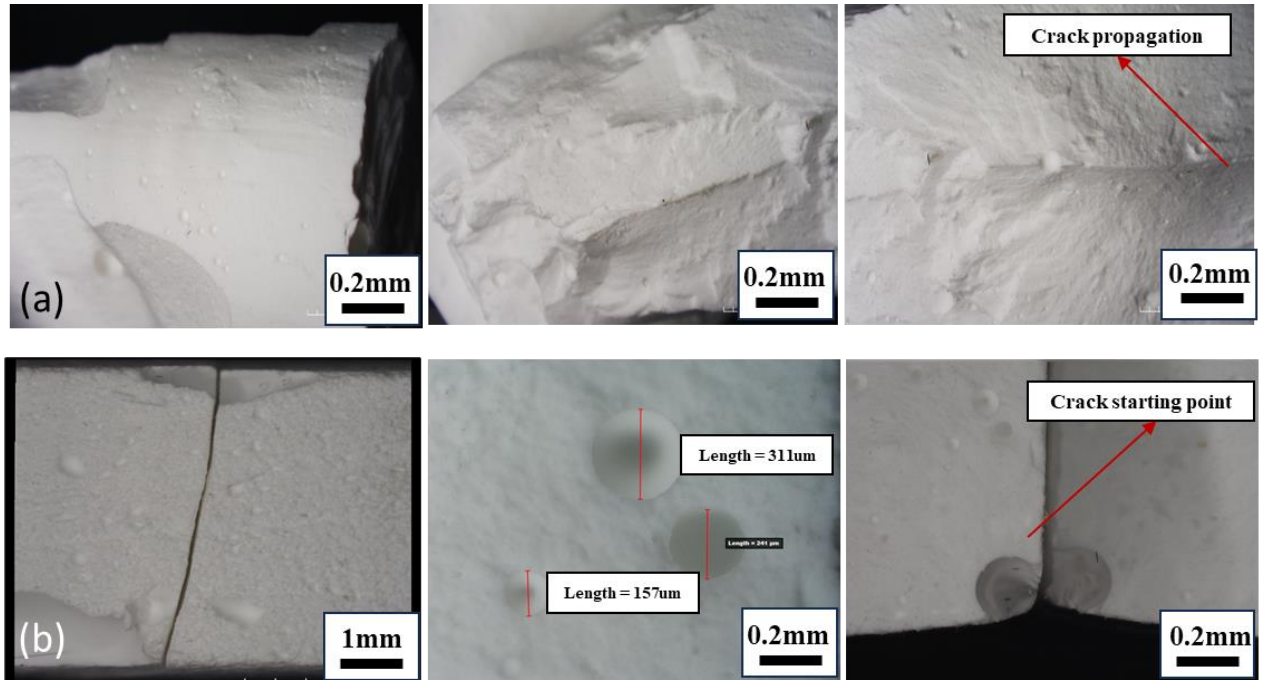

Figure 3-20: Optical images of CPCs after (a) compressive tests and (b) flexural tests.

The presence of carbon fibers into CPCs improved the compressive strength, with the greatest increase observed for samples with 5mm-length carbon fibers at 4wt% concentration, while CPC without carbon fibers observed the lowest compressive strength. The maximum compressive strength and work of fracture of carbon fibers reinforced CPC with respective their fibers amount and length are shown in Table. 3-XVII.

Table 3-XVII: The maximum compressive and flexural strength of CPC contains different amount and length of carbon fibers.

Sample Name	Maximum Compressive strength (MPa)	Maximum Flexural strength (MPa)	Work of fracture from compressive tests	Work of fracture from flexural tests
CPC	12.34±6.38	9.07±1.96	0.219±0.12	0.34±0.11
CPC/CF4/2.5	19.75±0.46	25.55±5.02	2.78±0.97	19.77±5.59
CPC/CF4/5	22.44±4.42	20.97±4.82	2.81±0.46	15.69±3.74
CPC/CF2/5	17.00±1.86	21.57±2.39	1.75±0.51	18.93±7.03

The statistical analysis of maximum compressive strength and work of fracture are shown in Figure 3.21 c&d. The work of fracture from compressive strength of CPC with 4 wt% of carbon-fibers of 5mm and 2mm was about 5time higher than CPCs without fibers (P>0.001). While the work of fracture of CPC with 2 wt% of carbon-fibers of 5mm was about 2time higher than CPCs without fibers (P>0.001). The effect of fiber amount was more pronounced than fiber length on compressive strength of carbon reinforced cement.

The flexural strength of CPC also increased with the addition of carbon fibers, with the highest strength was observed for samples with 2.5mm fibers at 4 wt% and the work of fracture was also significantly increased. This behavior was observed due to a more homogenous dispersion of shorter fibers inside the cement [78], which led to increased flexural strength by bridging the cracks and prevent them from expanding (Table 3-XVII) [79-81]. Such significantly higher performance was determined by energy-dissipation mechanisms related to the pullout of the fibers [82], which depends on the bonding properties between fiber and matrix. The statistical analysis of maximum 3-point bending strength and its work of fracture are shown in Figure 3.21 e&f. The work of fracture from 3-point bending strength of CPC with 4 wt% of carbon-fibers of 5mm and 2mm was about 20time higher than CPCs without fibers (P>0.001). While the work of fracture of CPC with 2 wt% of carbon-fibers of 5mm was about 15time higher than CPCs without fibers (P>0.001).

However, maximum flexural strength and WOF were the same for the samples with 5mm;4wt.% and 5mm;2wt.% carbon fibers, despite the difference in fiber amount [83, 84]. The carbon fibers embedded inside the cement matrix experience tensile stress when a CPC sample is bent. If the fibers are long enough, they may be pulled out from the matrix, which helps to disperse energy and avoid rapid sample fracture. Both the bending of the fibers themselves and the frictional resistance between the fibers and the matrix are responsible for this energy dissipation [55, 85].

The Young modulus of flexural test samples decreased with the addition of fibers, while the modulus of resilience increased except 5mm carbon fibers of 2wt%, where modulus of resilience decreased. Integrating carbon fibers to cement lowers Young’s modulus because the fibers destabilize the matrix's regular arrangement of calcium phosphate crystals, making the material less stiff but more flexible [80, 86]. The overall results suggested that the addition of carbon fibers can significantly improve the flexural strength, modulus of resilience and work of fracture of CPC, even at relatively low fibers amount.

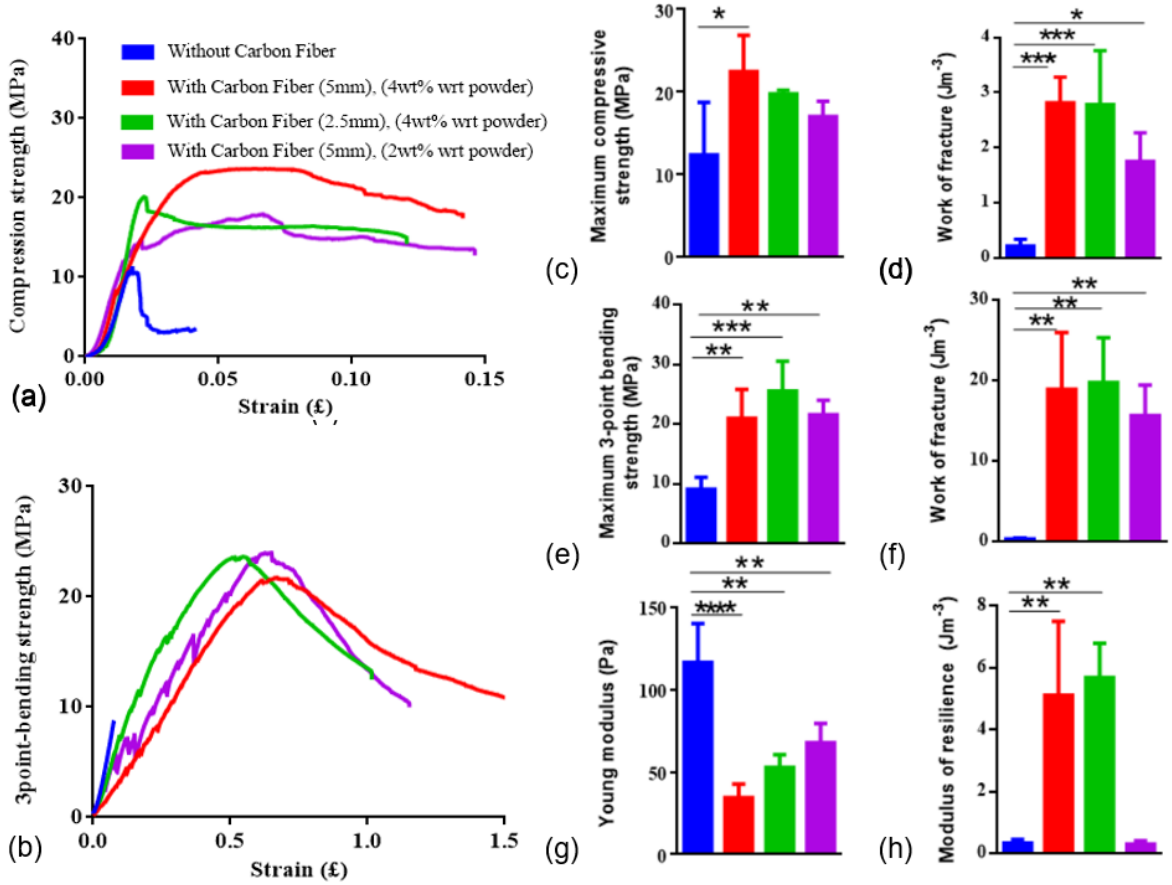

Figure 3-21: Mechanical performance of carbon fibers-reinforced CPCs: (a) compressive strength representative curves; (b) 3-point bending strength representative curves; statistical analysis of (c) maximum compressive strength; (d) work of fracture from compressive tests; (e) maximum 3-point bending strength (f) work of fracture from 3-point bending tests; (g) young modulus from from 3-point bending tests (h) modulus of resilience from 3-point bending tests.

The optical images of flexural and compressive strength tested specimens of carbon fibers-reinforced cements (Figure 3.22) showed that fibers are bridging the cracks at the site of failure, preventing them from widening and keeping the specimens intact. This is very different from the control CPC specimen (Figure 3.20), mainly exhibiting brittleness behavior where the development of one crack generally spread catastrophically. This is because CPC is brittle and is unable to resist plastic deformation or energy absorption prior to cracking [68, 84, 87].

Conversely, in presence fibers-reinforcement, multiple microcracks were experienced in the linear portion of σ-ε diagram, without inducing complete failure, indicating that the composite cement is able to withstand higher loads and dissipate more fracture energy before ultimate cracking [88]. As the fibers efficiently bridge them, these microcracks do not lead to the material's total breakdown. This suggests that before final cracking, the composite cement could withstand larger stresses and release more fracture energy [89, 90].

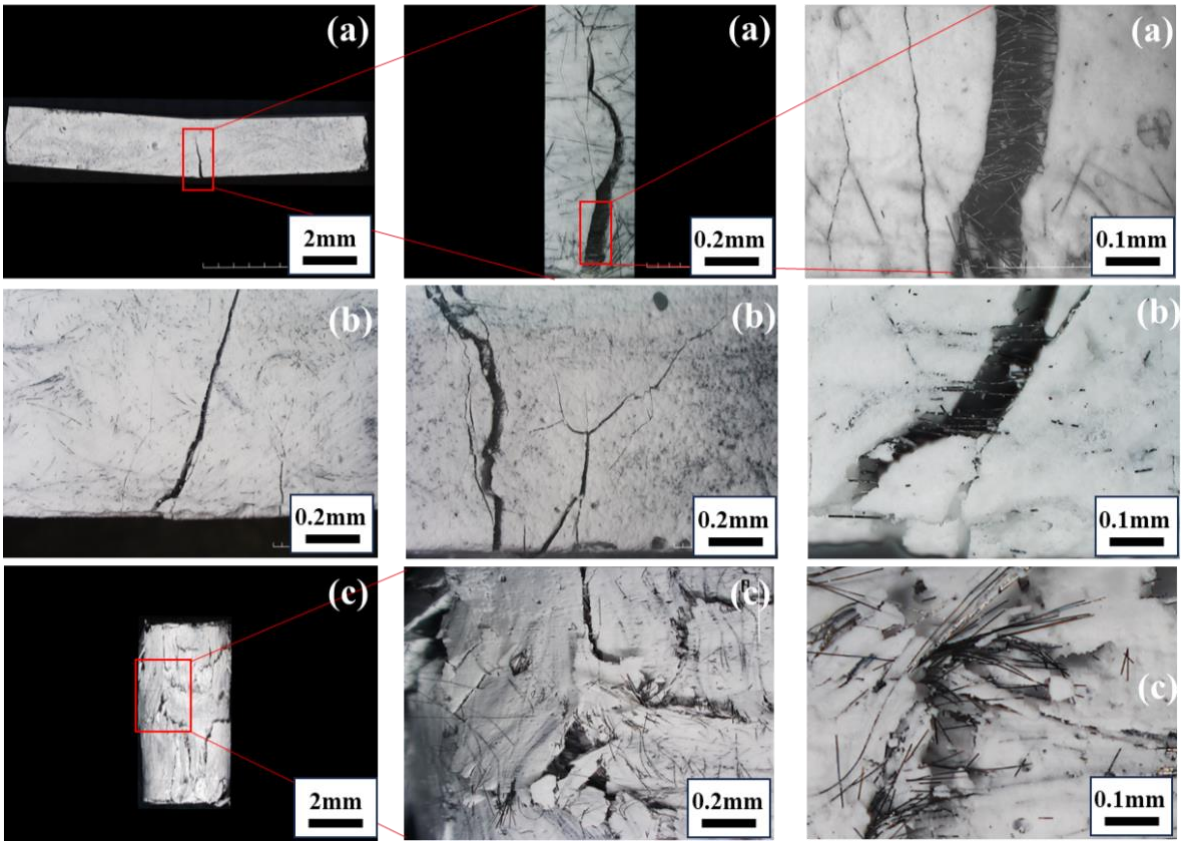

Figure 3-22: Optical images of (a) flexural strength tested CPC samples with (a) CF (5mm, 4wt%), (b) CF (5mm, 2wt%) and (c) compression strength tested CPC sample with CF (5mm, 4wt%).

The mechanical performance of CPC, Mg-CPC, Sr-CPC and MgSr-CPC reinforced with and without 5mm carbon fibers of 4wt% are reported in Figure 3.23. Carbon fiber reinforcement significantly improved the compressive and flexural strength of all types of CPC tested (Table 3-XVIII), with the greatest improvement observed in the MgSr-CPC with carbon fibers [84, 91, 92].

The compressive strength of the Mg-CPC and Sr-CPC with fibers was very close to that of CPC with fibers. This indicates that the addition of magnesium and strontium ions in CPC does not have a substantial impact on the efficacy of carbon fiber reinforcing [44].

Table 3-XVIII: The maximum compressive and flexural strength of CPC, Mg-CPC, Sr-CPC and MgSr-CPC with and without carbon fibers.

Sample Name	Maximum compressive strength (MPa)	Maximum flexural strength (MPa)	Work of fracture from compressive tests ($J \cdot m^{-3}$)	Work of fracture from flexural tests ($J \cdot m^{-3}$)
CPC	12.34±6.38	9.077±1.96	0.21±0.11	0.34±0.11
CPC+C.F	22.44±4.42	20.97±4.82	2.81±0.46	18.93±7.03
Mg-CPC	11.45±4.82	8.37±1.28	0.15±0.08	0.42±0.14
Mg-CPC+C.F	21.87±1.35	24.16±7.80	2.18±0.67	20.86±9.41
Sr-CPC	15.96±2.27	7.96±1.60	0.28±0.13	0.38±0.26
Sr-CPC+C.F	18.31±1.60	29.82±3.62	2.26±1.15	23.06±6.97
MgSr-CPC	21.57±3.38	5.88±1.23	0.40±0.10	0.17±0.10
MgSr-CPC+C.F	10.90±2.55	30.50±2.59	0.72±0.35	24.50±2.69

The flexural strength of carbon-fibers reinforced Mg-CPC, Sr-CPC and MgSr-CPC was much higher than the flexural strength of the control CPC with fibers as reported in Table 3.XVIII. The highest flexural strength of 30.50±2.59 MPa was observed by fiber-reinforced MgSr-CPC, followed by the fiber-reinforced CPC (20.97±4.82), Mg-CPC (24.16±7.80 MPa), Sr-CPC (29.82±3.62 MPa) and CPC (20.97±4.82 MPa). The work of fracture and modulus of resilience from flexural strength of all the carbon fiber reinforced CPC was also significantly greater than the control CPC, indicating more resistance to crack propagation and failure. Figure 3.23 shows a statistical analysis of the mechanical properties of CPC, Mg-CPC, Sr-CPC, and MgSr-CPC reinforced with and without 4 wt% of carbon fibers with 5mm-length. The maximum 3-point bending strength of Sr-CPC and MgSr-CPC with fibers was about 1.5time higher than CPCs with fibers ($P>0.001$).

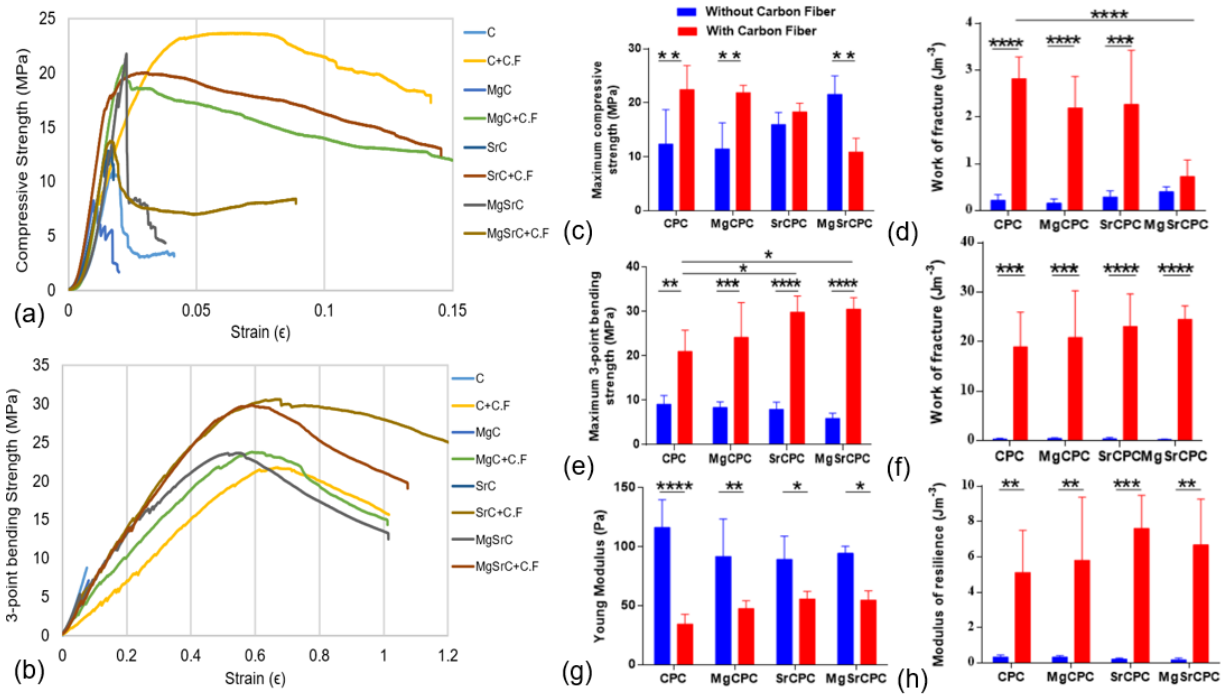

Figure 3-23: Mechanical performance of CPC, Mg-CPC, Sr-CPC and MgSr-CPC reinforced with and without 5mm carbon fibers of 4wt% (a) compressive strength representative curves; (b) 3-point bending strength representative curves; statistical analysis of (c) maximum compressive strength; (d) work of fracture from compressive tests; (e) maximum 3-point bending strength (f) work of fracture from 3-point bending tests; (g) young modulus from from 3-point bending tests (h) modulus of resilience from 3-point bending tests.

3.4. Conclusions

The transformation of α-TCP into calcium deficient hydroxyapatite (CDHA) appears to be generally faster for LT-αTCP, if compared to HT-αTCP, possibly due to higher specific surface area and lower crystallinity. The compressive strength of HT-αTCP cement was observed as significantly higher than that of LT-αTCP cement; this can be ascribed to the smaller grain size of LT-αTCP in respect to the HT-αTCP cement, which also reflects in a smaller pore size that usually gives higher mechanical strength. Incorporation of carbon fibers in both cements resulted in significantly enhanced compressive and flexural strength. However, the carbon fibers were more effective in LT-αTCP cement, observed higher compressive strength than fiber-reinforced HT-αTCP cement. Cements obtained by LT-αTCP may be better suited for applications that need shorter setting times, such as in bone surgery or dental procedures. HT-αTCP cement may be better suited for applications where high compressive strength is required.

Magnesium doped apatite cement (Mg-CPC) was prepared by mixing increasing amount of MgHA nanoparticles to αTCP (i.e. 0, 5, 10, 20 wt% with respect to αTCP) . The incorporation of MgHA nanoparticles into CPCs prolonged both initial and final setting times, resulting in slackening of the complete transformation of α-TCP into CDHA. As the amount of MgHA nanoparticles in the cements increased from 5 wt% to 20 wt%, the compressive strength of Mg-CPC decreased slightly and the morphology of the cements gradually changed from plate-like crystals to needle-like shapes. The degradation tests of bone cements showed that the Mg-containing formulations released more calcium, indicating that they were more soluble than the control CPC.

The microbiological characterization proved a significant antibacterial effect for MgHA (7 mol%) and Mg-CPC (20 wt%) scaffolds after short times (3 hours). Mg-CPC scaffolds were able to reduce bacterial viability by up to 70% against both gram-positive bacteria (S. aureus) and gram-negative bacteria (E. coli) in suspension and on scaffolds after 24 hours.

Carbon fiber-reinforced magnesium and strontium apatite cements were synthesized by mixing αTCP or Sr-αTCP with MgHA nanoparticles as inorganic precursors. The incorporation of carbon fibers into CPCs reduced the setting times without preventing the complete conversion of α-TCP into calcium-deficient hydroxyapatite. In terms of mechanical performance, the addition of carbon fibers into CPCs significantly increased the bending strength and work of fracture, while all cement samples exhibited comparable porosity, about (60.2 ± 1.4) %. The flexural strength of carbon fiber-reinforced cement was about (30.5 ± 2.5) MPa, while pure calcium phosphate cements exhibited only (9 ± 1.9) MPa. Carbon fiber-reinforced magnesium and strontium-doped cement may have potential applications in hard tissue repair and replacement for load-bearing bones. By adjusting the rheological properties, fiber-reinforced magnesium and strontium-doped cement with smaller fiber length (i.e. <2 mm) may also be possible candidates as inks for 3D-printing processes.

Carbon fiber-reinforced calcium phosphate cements (CPCs) are a new kind of biomaterial that combines the strong mechanical features of carbon fibers with the bioactivity and biocompatibility of calcium phosphate ceramics. The incorporation of these fibers has many potential benefits compared to CPC materials, such as improved mechanical strength, greater integration with biological tissues, and less inflammatory reaction. This is especially crucial for load-bearing bone applications, since the scaffold has to withstand substantial mechanical stress. Additionally, the incorporation of carbon fibers with a diameter of 7μm often have surface properties and are generally less likely to elicit an immune response. Moreover, the addition of carbon fibers may provide a more favorable environment for cell adhesion and growth, hence potentially reducing the inflammatory reaction [93].

3.5. References

1. Dapporto, M., et al., *Nanostructured strontium-doped calcium phosphate cements: a multifactorial design.* 2021. 11(5): p. 2075.
2. Tronco, M.C., J.B. Cassel, and L.A.J.A.b. Dos Santos, *α-TCP-based calcium phosphate cements: A critical review.* 2022.
3. Bosch-Rué, E., et al., *Biological roles and delivery strategies for ions to promote osteogenic induction.* 2021: p. 1809.
4. Lourenço, A.F.H.F., *An injectable sr-releasing hybrid system to promote bone regeneration.* 2019.
5. Sever, H.E., *Additive Manufacturing of 3-Dimensional Bioceramic Structures Elaborated By Calcium Phosphate Cement Reactions*. 2022, Middle East Technical University.
6. Tavoni, M., et al., *Bioactive calcium phosphate-based composites for bone regeneration.* 2021. 5(9): p. 227.
7. Kavaliauskienė, L., *Tricalcium phosphate polymorphs: the role of ionic substitutions and processing conditions on phase selective synthesis and properties*. 2021, Vilniaus universitetas.
8. Cestari, F., *3D printing of bone scaffolds using powders derived from biogenic sources.* 2023.
9. Degli Esposti, L., et al., *An in situ study of thermal crystallization of amorphous calcium phosphates.* 2022. 24(39): p. 24514-24523.
10. Dorozhkin, S.V.J.B.S., *Synthetic amorphous calcium phosphates (ACPs): Preparation, structure, properties, and biomedical applications.* 2021. 9(23): p. 7748-7798.
11. Martínez, T., et al., *α-tricalcium phosphate synthesis from amorphous calcium phosphate: structural characterization and hydraulic reactivity.* 2021. 56(24): p. 13509-13523.
12. Benali, B., et al., *Pore-level Ostwald ripening of CO2 foams at reservoir pressure.* 2023: p. 1-19.
13. Degli Esposti, L., et al., *Antimicrobial activity of remineralizing ion-doped amorphous calcium phosphates for preventive dentistry.* 2022. 9: p. 846130.
14. Sinusaite, L., et al., *Thermally induced crystallization and phase evolution of amorphous calcium phosphate substituted with divalent cations having different sizes.* 2021. 21(2): p. 1242-1248.
15. Xu, H.H., et al., *Calcium phosphate cements for bone engineering and their biological properties.* Bone research, 2017. 5(1): p. 1-19.
16. Dapporto, M., et al., *Strontium-doped apatitic bone cements with tunable antibacterial and antibiofilm ability.* Frontiers in Bioengineering and Biotechnology, 2022. 10.
17. Xu, X., et al., *Doping engineering and functionalization of iron oxide nanoclusters for biomedical applications.* 2022: p. 166459.
18. Moussi, H., et al., *Injectable macromolecules-based calcium phosphate bone substitutes.* Materials Advances, 2022.
19. Belluomo, R., A. Khodaei, and S.A. Yavari, *Additively manufactured Bi-functionalized bioceramics for reconstruction of bone tumor defects.* Acta Biomaterialia, 2023. 156: p. 234-249.
20. Nguyen, N.-Y.T., et al., *Antimicrobial activities and mechanisms of magnesium oxide nanoparticles (nMgO) against pathogenic bacteria, yeasts, and biofilms.* 2018. 8(1): p. 16260.
21. Uskoković, V., *Ion-doped hydroxyapatite: an impasse or the road to follow?* Ceramics International, 2020. 46(8): p. 11443-11465.
22. Ratha, I., et al., *Effect of doping in hydroxyapatite as coating material on biomedical implants by plasma spraying method: A review.* Ceramics International, 2021. 47(4): p. 4426-4445.
23. Panda, S., C.K. Biswas, and S. Paul, *A comprehensive review on the preparation and application of calcium hydroxyapatite: A special focus on atomic doping methods for bone tissue engineering.* Ceramics international, 2021. 47(20): p. 28122-28144.
24. Ghosh, R., et al., *A review on the antimicrobial and antibiofilm activity of doped hydroxyapatite and its composites for biomedical applications.* Materials Today Communications, 2022: p. 103311.
25. Glasdam, S.-M., S. Glasdam, and G.H. Peters, *The importance of magnesium in the human body: a systematic literature review.* Advances in clinical chemistry, 2016. 73: p. 169-193.
26. Dermience, M., et al., *Effects of thirty elements on bone metabolism.* Journal of Trace Elements in Medicine and Biology, 2015. 32: p. 86-106.

27. Rude, R.K., F.R. Singer, and H.E. Gruber, *Skeletal and hormonal effects of magnesium deficiency.* Journal of the American College of Nutrition, 2009. 28(2): p. 131-141.
28. Matias, P., et al., *Hypomagnesemia: a potential underlooked cause of persistent vitamin D deficiency in chronic kidney disease.* Clinical Kidney Journal, 2023: p. sfad123.
29. Fritzen, R., et al., *Magnesium Deficiency and Cardiometabolic Disease.* Nutrients, 2023. 15(10): p. 2355.
30. Dominguez, L.J., et al., *Association between Serum Magnesium and Fractures: A Systematic Review and Meta-Analysis of Observational Studies.* Nutrients, 2023. 15(6): p. 1304.
31. Arkin, V.H., et al., *Characterization and In Vitro Evaluations of Injectable Calcium Phosphate Cement Doped with Magnesium and Strontium.* ACS Omega, 2021. 6(4): p. 2477-2486.
32. Enderle, R., et al., *Influence of magnesium doping on the phase transformation temperature of β-TCP ceramics examined by Rietveld refinement.* Biomaterials, 2005. 26(17): p. 3379-3384.
33. Neves, A.R., et al., *Calcium phosphate nanoparticles in therapeutics*, in *Inorganic Nanosystems*. 2023, Elsevier. p. 407-435.
34. Cuylear, D.L., et al., *Calcium Phosphate Delivery Systems for Regeneration and Biomineralization of Mineralized Tissues of the Craniofacial Complex.* Molecular Pharmaceutics, 2023.
35. Hadden, M., et al., *Porous Calcium Carbonates and Calcium Phosphates for Drug Delivery Applications*, in *Advanced Porous Biomaterials for Drug Delivery Applications*. 2022, CRC Press. p. 137-189.
36. Stino, S., *Basic Concept of Bone Cement: A review.* Biomaterials Journal, 2023. 2(4): p. 15-25.
37. Liu, Q., et al., *Tunable calcium phosphate cement formulations for predictable local release of doxycycline.* Materialia, 2023. 28: p. 101769.
38. Lukina, Y., et al., *Calcium Phosphate Cements as Carriers of Functional Substances for the Treatment of Bone Tissue.* Materials, 2023. 16(11): p. 4017.
39. Pylostomou, A., O. Demir-Oguz, and D. Loca, *Calcium phosphate bone cements as local drug delivery systems for bone cancer treatment.* Biomaterials Advances, 2023: p. 213367.
40. Tavoni, M., et al., *Bioactive calcium phosphate-based composites for bone regeneration.* Journal of Composites Science, 2021. 5(9): p. 227.
41. Ribeiro, N., et al., *Improvement of a commercial calcium phosphate bone cement by means of drug delivery and increased injectability.* Ceramics International, 2022. 48(22): p. 33361-33372.
42. Ginebra, M.-P., et al., *New processing approaches in calcium phosphate cements and their applications in regenerative medicine.* Acta biomaterialia, 2010. 6(8): p. 2863-2873.
43. Wang, P., et al., *Stem cells and calcium phosphate cement scaffolds for bone regeneration.* Journal of dental research, 2014. 93(7): p. 618-625.
44. Zhang, J., et al., *Calcium phosphate cements for bone substitution: chemistry, handling and mechanical properties.* Acta biomaterialia, 2014. 10(3): p. 1035-1049.
45. Pastorino, D., C. Canal, and M.-P. Ginebra, *Drug delivery from injectable calcium phosphate foams by tailoring the macroporosity–drug interaction.* Acta biomaterialia, 2015. 12: p. 250-259.
46. Rabiee, S.M., *Development of hydroxyapatite bone cement for controlled drug release via tetracycline hydrochloride.* Bulletin of Materials Science, 2013. 36: p. 171-174.
47. Sampath Kumar, T. and K. Madhumathi, *Antibacterial potential of nanobioceramics used as drug carriers*, in *Handbook of bioceramics and biocomposites*. 2016, Springer. p. 1333-1373.
48. Korsmeyer, R.W., et al., *Mechanisms of solute release from porous hydrophilic polymers.* International journal of pharmaceutics, 1983. 15(1): p. 25-35.
49. Fosca, M., J.V. Rau, and V. Uskoković, *Factors influencing the drug release from calcium phosphate cements.* Bioactive Materials, 2022. 7: p. 341-363.
50. Franco, D., et al., *Antimicrobial effect and cytotoxic evaluation of Mg-doped hydroxyapatite functionalized with Au-nano rods.* 2021. 26(4): p. 1099.
51. Zhang, K., et al., *Synthesis Technology of Magnesium-Doped Nanometer Hydroxyapatite: A Review.* 2023. 8(47): p. 44458-44471.
52. Schnieders, J., et al., *The effect of porosity on drug release kinetics from vancomycin microsphere/calcium phosphate cement composites.* 2011. 99(2): p. 391-398.

53. Deng, K., et al., *Single-ion conducting gel polymer electrolytes: design, preparation and application.* 2020. 8(4): p. 1557-1577.
54. Mulazzi, M., et al., *Medicated hydroxyapatite/collagen hybrid scaffolds for bone regeneration and local antimicrobial therapy to prevent bone infections.* 2021. 13(7): p. 1090.
55. Canal, C. and M. Ginebra, *Fibre-reinforced calcium phosphate cements: a review.* Journal of the mechanical behavior of biomedical materials, 2011. 4(8): p. 1658-1671.
56. Geffers, M., J. Groll, and U. Gbureck, *Reinforcement strategies for load-bearing calcium phosphate biocements.* Materials, 2015. 8(5): p. 2700-2717.
57. Cai, P., et al., *Injectable nanofiber-reinforced bone cement with controlled biodegradability for minimally-invasive bone regeneration.* 2023. 21: p. 267-283.
58. Dapporto, M., et al., *Strontium-doped apatitic bone cements with tunable antibacterial and antibiofilm ability.* 2022. 10: p. 969641.
59. Kolmas, J., et al., *Alpha-tricalcium phosphate synthesized by two different routes: Structural and spectroscopic characterization.* 2015. 41(4): p. 5727-5733.
60. Asadi Tabrizi, R., A. Zamanian, and S.J.A.C.P. Hesaraki, *Effects of time, temperature and precursor on solid state synthesis of α-TCP.* 2015. 1(1): p. 36-39.
61. Karunakaran, G., et al., *Mesoporous Mg-doped hydroxyapatite nanorods prepared from bio-waste blue mussel shells for implant applications.* 2020. 46(18): p. 28514-28527.
62. Schulin, T.J., *Development of Fully Injectable Novel Compositions of Phosphate Cements for Orthopedic Applications*. 2020, The University of Toledo.
63. Demir-Oğuz, Ö., A.R. Boccaccini, and D.J.B.M. Loca, *Injectable bone cements: What benefits the combination of calcium phosphates and bioactive glasses could bring?* 2023. 19: p. 217-236.
64. Canal, C. and M.J.J.o.t.m.b.o.b.m. Ginebra, *Fibre-reinforced calcium phosphate cements: a review.* 2011. 4(8): p. 1658-1671.
65. Liu, J., et al., *Setting behavior, mechanical property and biocompatibility of anti-washout wollastonite/calcium phosphate composite cement.* 2016. 42(12): p. 13670-13681.
66. Ribeiro, N., et al., *Improvement of a commercial calcium phosphate bone cement by means of drug delivery and increased injectability.* 2022. 48(22): p. 33361-33372.
67. Kucko, N.W., et al., *Calcium phosphate bioceramics and cements*, in *Principles of Regenerative Medicine*. 2019, Elsevier. p. 591-611.
68. Krüger, R. and J. Groll, *Fiber reinforced calcium phosphate cements–on the way to degradable load bearing bone substitutes?* Biomaterials, 2012. 33(25): p. 5887-5900.
69. Zuo, Y., et al., *Incorporation of biodegradable electrospun fibers into calcium phosphate cement for bone regeneration.* Acta biomaterialia, 2010. 6(4): p. 1238-1247.
70. Paknahad, A., et al., *Experimental and numerical analysis on bending and tensile failure behavior of calcium phosphate cements.* journal of the mechanical behavior of biomedical materials, 2020. 103: p. 103565.
71. Haque, M.A., B. Chen, and M.R. Ahmad, *Mechanical strength and flexural parameters analysis of micro-steel, polyvinyl and basalt fibre reinforced magnesium phosphate cement mortars.* Construction and Building Materials, 2020. 235: p. 117447.
72. Boehm, A.V., et al., *Self-healing capacity of fiber-reinforced calcium phosphate cements.* Scientific reports, 2020. 10(1): p. 9430.
73. Fada, R., et al., *Mechanical properties improvement and bone regeneration of calcium phosphate bone cement, Polymethyl methacrylate and glass ionomer.* 2021. 8(1): p. 60-79.
74. Lodoso-Torrecilla, I., J.J. van den Beucken, and J.A.J.A.b. Jansen, *Calcium phosphate cements: Optimization toward biodegradability.* 2021. 119: p. 1-12.
75. Eliaz, N. and N. Metoki, *Calcium Phosphate Bioceramics: A Review of Their History, Structure, Properties, Coating Technologies and Biomedical Applications.* 2017. 10(4): p. 334.
76. Wu, F., et al., *Self-setting bioactive calcium–magnesium phosphate cement with high strength and degradability for bone regeneration.* Acta biomaterialia, 2008. 4(6): p. 1873-1884.

77. Schröter, L., et al., *Biological and mechanical performance and degradation characteristics of calcium phosphate cements in large animals and humans.* Acta Biomaterialia, 2020. 117: p. 1-20.
78. Cao, M., W. Si, and C.J.A.M.J. Xie, *Relationship of rheology, fiber dispersion, and strengths of polyvinyl alcohol fiber-reinforced cementitious composites.* 2020. 117(3): p. 191-204.
79. Mobasher, B., *Mechanics of fiber and textile reinforced cement composites*. 2011: CRC press.
80. Paknahad, A., *Calcium phosphate cement reinforced with poly (vinyl alcohol) fibers. Experimental and numerical studies on mechanical failure*. 2020, [Sl]:[Sn].
81. Ajoku, C.A., A. Turatsinze, and A. Abou-Chakra, *Mechanical behaviour of wollastonite-based cement composites incorporating fibres and recycled rubber aggregates.* Construction and Building Materials, 2023. 392: p. 131843.
82. Pei, C., et al., *Pull-out performance of anchored carbon-fiber bundles in cementitious matrix.* 2021. 25(6): p. 04021057.
83. Paknahad, A., et al., *Calcium phosphate cement reinforced with poly (vinyl alcohol) fibers: An experimental and numerical failure analysis.* Acta Biomaterialia, 2021. 119: p. 458-471.
84. Kucko, N.W., et al., *Tough and osteocompatible calcium phosphate cements reinforced with poly (vinyl alcohol) fibers.* ACS Biomaterials Science & Engineering, 2019. 5(5): p. 2491-2505.
85. Xu, H.H., F.C. Eichmiller, and A.A. Giuseppetti, *Reinforcement of a self-setting calcium phosphate cement with different fibers.* Journal of biomedical materials research, 2000. 52(1): p. 107-114.
86. Ritts, W.W., *The study and development of calcium phosphate bone cement and hydroxyapatite nanofibers*. 2012: University of Missouri-Columbia.
87. Wei, M., et al., *Enhanced mechanical properties and anti-washout of calcium phosphate cement/montmorillonite composite bone-cement for bone-repair applications.* Ceramics International, 2022. 48(23): p. 35185-35197.
88. Lancioni, G., R.J.J.o.t.M. Alessi, and P.o. Solids, *Modeling micro-cracking and failure in short fiber-reinforced composites.* 2020. 137: p. 103854.
89. Baudín, C., T. Benet, and P. Pena, *Effect of graphene on setting and mechanical behaviour of tricalcium phosphate bioactive cements.* Journal of the Mechanical Behavior of Biomedical Materials, 2019. 89: p. 33-47.
90. Abolhasani, A., H. Nazarpour, and M. Dehestani, *The fracture behavior and microstructure of calcium aluminate cement concrete with various water-cement ratios.* Theoretical and Applied Fracture Mechanics, 2020. 109: p. 102690.
91. Luo, J., et al., *The addition of poly (vinyl alcohol) fibers to apatitic calcium phosphate cement can improve its toughness.* Materials, 2019. 12(9): p. 1531.
92. Balea, A., et al., *Fiber reinforced cement based composites*, in *Fiber Reinforced Composites*. 2021, Elsevier. p. 597-648.
93. Rajzer, I., et al., *In vitro and in vivo studies on biocompatibility of carbon fibres.* 2010. 21: p. 2611-2622.

FINAL CONCLUSIONS AND FUTURE PERSPECTIVES

Hydroxyapatite (HA) has been widely recognized as suitable material to develop scaffolds for bone regeneration applications, mainly due to optimal chemical mimicry with the natural inorganic component of bones. In spite of such a great potential, the main drawback associated to hydroxyapatite refers to its intrinsic brittleness and limited bioactivity, posing significant limitation to their clinical use mainly due to low degradation rate and irreparable failure of the scaffolds. This is a major reason making the regeneration of load-bearing bone defects such as maxillofacial regions and spine region, a still unmet clinical need of great socio-economic relevance.

Among the various approaches for apatite reinforcement, the use of carbon fibers is an interesting strategy due to their inherent biocompatibility, high strength-to-weight ratio, thermophysical properties, sorption, and high elastic modulus. They can bridge cracks after its appearance due to stress, impeding its further propagation, thus raising the toughness and prevent from sudden failure. In the present work, apatitic bone scaffolds particularly suitable for applications in maxillofacial and spinal bone regions have been developed and optimized following different approaches. In summary:

I) Various formulations of HA slurries were prepared and characterized to investigate the effect of calcination temperature of powder, powder content and dispersant amount as well as ion-doping on the flow behaviour of hydroxyapatite slurries. Stoichiometric and ion-doped HA were synthesized by neutralization method. Calcination of HA powders reduced surface area and reactivity with water, enhancing slurry stability and lowering viscosity. In this respect, the highest solid loading for calcinated HA at 1000°C was found to be ≈39 vol%, significantly higher than the highest solid loading for non-calcinated HA which resulted ≈24 vol%. Ion-doped HA slurries showed lower viscosity compared to stoichiometric HA slurries, possibly ascribable to altered surface charge and functional groups, also reflecting into significantly higher chemical affinity of ions with water molecules and higher zeta potential, in absolute value. The slurries generally exhibited solid behaviour, with dominant elastic modulus (G') over viscous modulus (G") across the entire range of frequencies tested, except HA calcinated at 1000°C. The amount of dispersant and calcination temperature influenced elastic moduli, with a more prominent effect of dispersant on ion-doped HA slurries.

II) Porous HA composites, mechanically reinforced with fibers, were prepared by mixing the previously developed slurries. The reinforcement of HA scaffolds with carbon fibers exhibited some limitations, possibly related to their thermal decomposition in oxidative environments. Interestingly, the introduction of alumina fibers in HA slurries resulted in a decrease of viscosity:

this behaviour was considered particularly promising towards the manipulation and development of high-solid loaded slurries. Alumina fiber-reinforced HA composite exhibited lower maximum compressive strength and flexural strength, compared to the control sample of HA without fibers. With increasing the amount of alumina fibers, the compressive strength increases, but still lower than control sample of HA without fibers. However, the high-temperature sintering treatment of fiber-reinforced HA composite at 1200°C for 1h resulted in fibers decomposition and formation of secondary phase. In conclusion, both carbon and alumina fibers decomposed after thermal treatment, preventing structural homogeneity and integrity, inducing microstructural defects which in turn caused the decrease of maximum compressive and flexural strength.

III) The transformation of α-TCP into calcium deficient hydroxyapatite (CDHA) appears to be generally faster for LT-αTCP, if compared to HT-αTCP, possibly due to higher specific surface area and lower crystallinity. The compressive strength of HT-αTCP cements was observed as significantly higher than that of LT-αTCP cements; this can be ascribed to the smaller grain size, which also reflects in higher hydraulic reactivity, smaller pore size upon hardening and higher mechanical strength. The incorporation of carbon fibers in cements significantly enhanced both compressive and flexural strength, particularly in the case of LT-αTCP cements.

IV) Magnesium doped apatite cements (Mg-CPC) were prepared by mixing increasing amount 0, 5, 10, 20 wt% of MgHA nanoparticles to αTCP. The incorporation of MgHA nanoparticles into CPCs prolonged the setting times, resulting in slackening of the complete transformation of α-TCP into CDHA. The compressive strength of Mg-CPC slightly decreased with increasing the concentration of MgHA nanoparticles, while the microstructure of the cements shifted from plate-like to needle-like crystals. The degradation tests of the cements exhibited higher calcium release for the Mg-containing formulations, as a marker for higher solubility. MgHA (7 mol%) and Mg-CPC (20wt%) scaffolds exhibited a short-time (3h) remarkable antibacterial effect against gram positive and gram-negative bacterial strains, respectively S. aureus and E. coli. Mg-CPC scaffolds are able to reduce the bacterial viability up to 70% in both planktonic and adherent populations at 24h.

V) Carbon fiber-reinforced magnesium and strontium apatite cements were synthesized by mixing αTCP or Sr-αTCP with MgHA nanoparticles as inorganic precursors. The incorporation of carbon fibers into CPCs reduced the setting times without preventing the complete conversion of α-TCP into calcium-deficient apatite. In terms of mechanical performance, the addition of

carbon fibers into CPCs significantly increased the 3-point bending strength and work of fracture, while all cement samples exhibited comparable porosity, about 60.0±1.4 %. The flexural strength of carbon fiber-reinforced cement was about 30.5±2.5 MPa, while pure calcium phosphate cements exhibited only 9.3±1.9 MPa. Carbon fiber-reinforced magnesium and strontium-doped cement may have potential applications in hard tissue repair and replacement for load-bearing bones. By adjusting the rheologic properties, fiber-reinforced magnesium and strontium-doped cement with smaller fiber length (i.e. < 2 mm) may also be possible candidates as inks for 3D-printing processes.

The novelty of fibers-reinforced bioceramic is explored relatively in few reports in literature. Some studies reported moderate inflammatory response of carbon fibers in the body. In most cases the inflammatory responses were associated with considerable length and a high aspect ratio of carbon fibers, that can be diminished by other factors like homogenous dispersion in biocompatible and bioactive materials such as apatite's.

The experiments confirmed that the fiber-reinforcement of sintered hydroxyapatite bodies remains challenging due to high-temperature oxidation and degradation phenomena. However, in consideration of the relevant clinical needs related to large bone reconstruction, that may be solved thanks to the use of reinforced apatite scaffold, efforts are worthy to be dedicated to address the existing drawbacks. As future possible research route, exploring alternative biocompatible fibrous materials like silica, alumina, or zirconia-based compounds could be interesting to unveil new potential materials for reinforcing sintered calcium phosphates, apart from carbon. In this respect, phase degradation at high temperatures is still a problem. To contrast this issue, the development of protective interface layers coating the reinforcing fibers for sake of protection from degradation may be a viable solution to achieve more chemically inert fibres. Besides, the research focus should be put also on the sintering treatment itself, looking for example to faster treatments to limit the reaction time and, possibly, the degradation extent.

Conversely, porous apatitic cements, functioning as bone scaffolds, can be obtained at body temperature, thus offering enhanced possibility of mechanical reinforcement and, even, functionalization with therapeutic drugs. The fiber reinforcement of cements appears much more achievable and promising, likely due to their consolidation not requiring thermal treatment. Though, there are still few studies available on this topic. The possibility to tune the cement formulation rheology, chemical activity and porosity, is also relevant for use of various forming techniques, including 3D printing. This is promising for future development of scaffolds with tailored geometry and bioactivity, relevant for personalized

surgical treatments. Regarding the strengthening of CPCs, further research is required to optimize the processing techniques of carbon fibers reinforced CPC as well as biological properties and verify its long-term effectiveness in clinical contexts. Future research might also venture beyond carbon fibers, investigating other biocompatible fibrous materials, like silica, alumina, or zirconia-based compounds.

ANNEX

ANALYTICAL TECHNIQUES

Several analytical techniques for material characterization reported in this Ph.D. thesis are X-Ray Diffraction (XRD), Fourier-Transform Infrared Spectroscopy (FTIR), Scanning Electron Microscopy (SEM), Inductively Coupled Plasma Optical Emission Spectroscopy, Energy dispersive X-ray spectroscopy (EDS), B.E.T. Technique, Sedigraph, Thermogravimetric analysis (TGA), Rheometer, Zwick Roell Z050 machine, Dynamic Light Scattering (DLS).

X-Ray Diffraction (XRD)

X-ray diffraction (XRD) is a non-destructive technique that is used to determine the composition of a crystalline substance by determining its different phases [1]. The bulk phase composition has been determined after the material has been homogenized and carefully pulverized. Constructive interference between monochromatic X-rays and the crystalline substance is the foundation of the XRD technique. A cathode ray tube acts as the source of the X-rays, which are then filtered to produce monochromatic radiation, collimated to focus and targeted at the sample. When the conditions of Bragg's law are satisfied, the interaction of the incident X-rays with the material results in constructive interference and a diffracted beam (Figure 1).

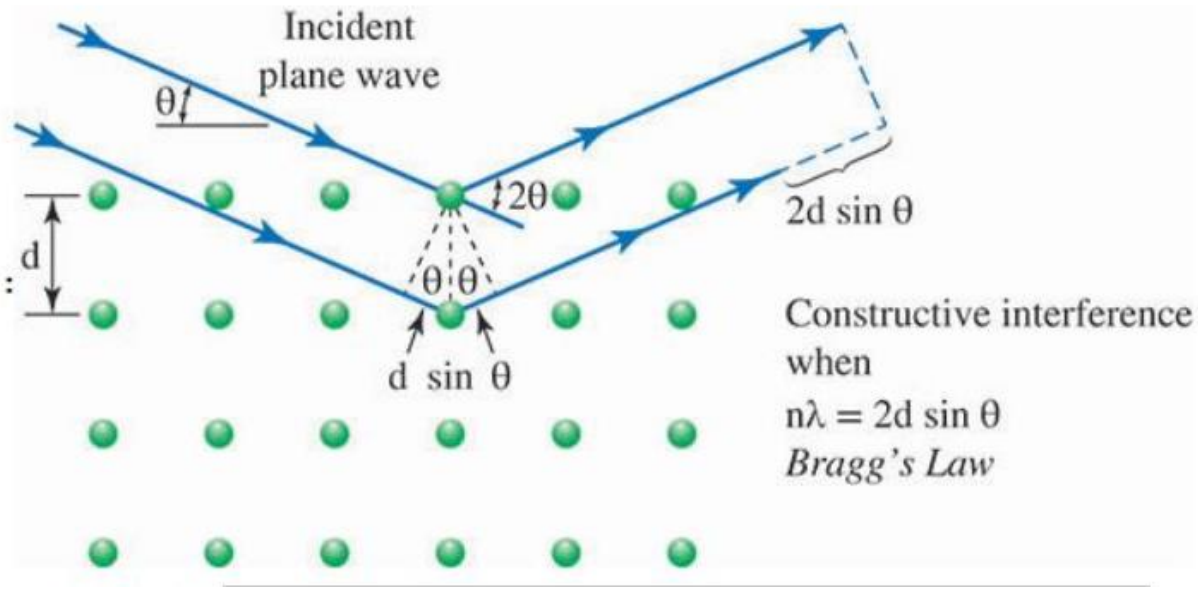

Figure 1: Bragg's law and constructive interference.

To examine the phase composition of the substance, diffraction measurements are compared to a database of powder diffraction files (International Centre for Diffraction Data - ICDD).

Rietveld refinement

When coupled with Rietveld refinement techniques, XRD has the potential to provide additional information about the structure of a material, such as the measurements of the unit cell and lattice strains. Elastic scattering, also called Rayleigh scattering, occurs when X-rays interact with atoms, causing the electronic cloud to move and then re-radiate waves at the same frequency (Figure 2).

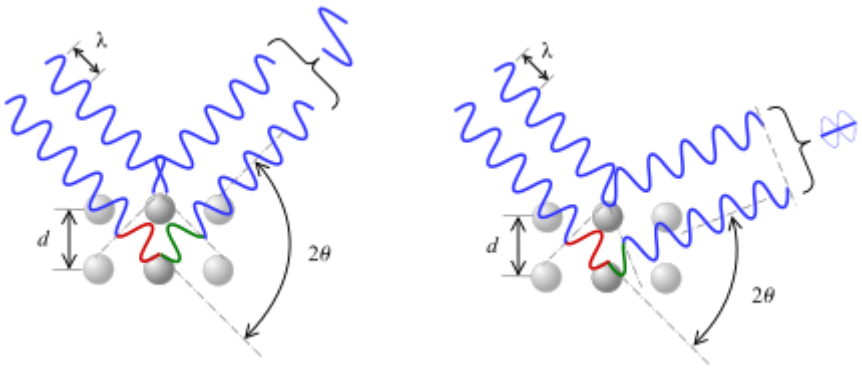

Figure 2: Constructive (left figure) or destructive (right figure) interference in Rayleigh scattering of X-rays.

X-ray diffraction data is usually displayed in the form of diffraction patterns, also known as diffractograms, which illustrate diffracted peaks as a function of the scattering angle 2θ, which occur due to constructive interference between X-rays and the crystalline structure of the material [2]. It is possible to determine the chemical composition of a substance by analysing the position of the peaks, which correlate to the lattice spacing and the relative intensity of the peaks themselves, which are also distinctive of a particular phase.

Crystal Structure

Crystals are a type of solid material characterized by a highly ordered and regular arrangement of atoms. This kind of regularity of arrangement can be characterized in terms of symmetry elements, which reflects the symmetry of the physical characteristics of a material. The unit cell of a material is a representation of its crystal structure, which is characterized by its lattice parameters. These parameters include the length of the cell edges and the angles between them and are used to quantitatively describe the unit cell. The atomic positions within the unit cell can be characterized by a set of coordinates (xi, yi, zi) that are determined relative to a specific lattice point.

Symmetry elements are defined as geometrical entities, such as points, axes, or planes, with respect to which a lattice symmetry occurs. Symmetric elements are required for the representation of symmetry operations, which are the virtual movement of the smallest asymmetric unit about a symmetrical center. The most accurate level to characterize the symmetry characteristics of the crystal, such as cleavage, electronic band structure and optical properties, can be obtained by performing complex symmetry operations, which lead to the formation of space groups.

There is an infinite number of methods for denoting a unit cell, but for each crystal structure there is a conventional unit cell that is selected to demonstrate the full symmetry of the crystal structure. Nonetheless, the unit cell that is commonly used may not always be the smallest possible option. The smallest volume that is fully occupied by a number of atoms in a stacked arrangement is referred to as the primitive unit cell of a specific crystal structure.

In a primitive cell, the local atoms surrounding each atom can be arranged in a variety of different ways, whereas in a unit cell, the local atoms surrounding each atom are arranged in an identical manner. The crystal structure is comprised of the same group of atoms, known as the basis, which is arranged in the same manner around every lattice point. According to the arrangement of one of the 14 Bravais lattices, this atomic group will therefore repeat itself indefinitely across all three dimensions (Figure 3).

The following are some examples of potential lattice centrings:

- P: Primitive centring, with lattice points positioned just on the cell's corners;
- I: Body-centred, additional lattice point at the cell's center;
- F: Face centered, an additional lattice point positioned in the center of each of the cell's faces;
- C: Centred on a single face, an additional lattice point is located in the center of one of the cell faces.

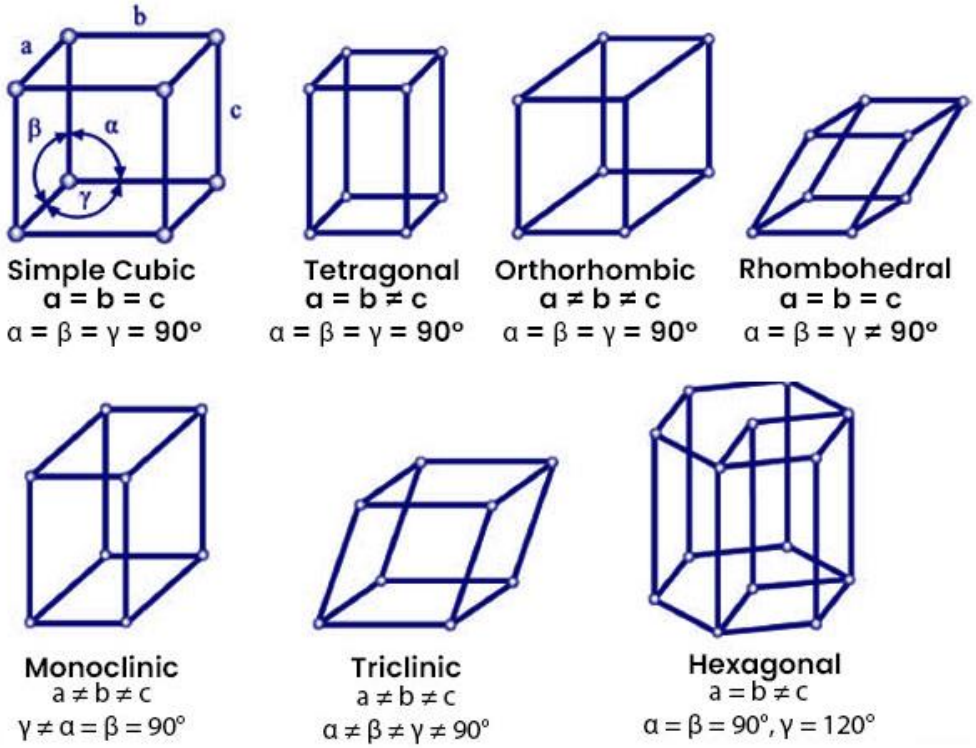

Figure 3: The seven crystalline systems and 14 Bravais lattices.

Miller indices

In crystallography, the Miller indices are a helpful notation tool for determining the orientation and planes of a Bravais lattice. The Miller indices, h, k and l are three integers that are used for identifying a reticular plane. These indices are vectors, which are the reciprocals of the plane's intercepts on the axes x, y and z.

Size and Strain Broadening

The width of a diffraction peak, denoted by B, is dependent on a number of parameters, including the following:

1. instrumental factors
2. the presence of lattice defects
3. strain inhomogeneity among the grains
4. the size of the crystallites

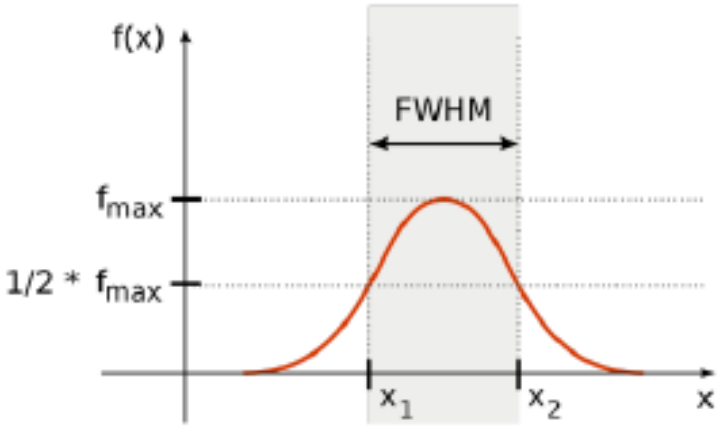

The analysis of X-ray diffraction (XRD) peak profiles has revealed that the full-width at half-maximum (FWHM) is a highly sensitive measure of the changes in both microstructure and stress-strain accumulation in the substance. The presence of tensile stress in a substance result in an increase in the full width at half maximum (FWHM), whereas relaxation of such stress leads to a decrease in FWHM.

Crystallite size can be determined by using the Scherrer equation [1]:

$$B(2\theta) = \frac{K\lambda}{D\ cos}$$

The equation for determining the crystallite average size, denoted as D, involves several variables. Specifically, B represents the peak width that has been adjusted for instrumental broadening, θ refers to the diffraction angle, K is a form factor typically assumed to be 0.9 and λ represents the wavelength of the incident radiation.

Diffractometer

X-ray diffractometers are comprised of three fundamental components, including an X-ray tube, a sample holder and an X-ray detector. X-rays are produced within a cathode ray tube through the process of heating a filament to generate electrons, subsequently accelerating these electrons towards a target by means of voltage application and ultimately subjecting the target material to electron bombardment (Figure 4).

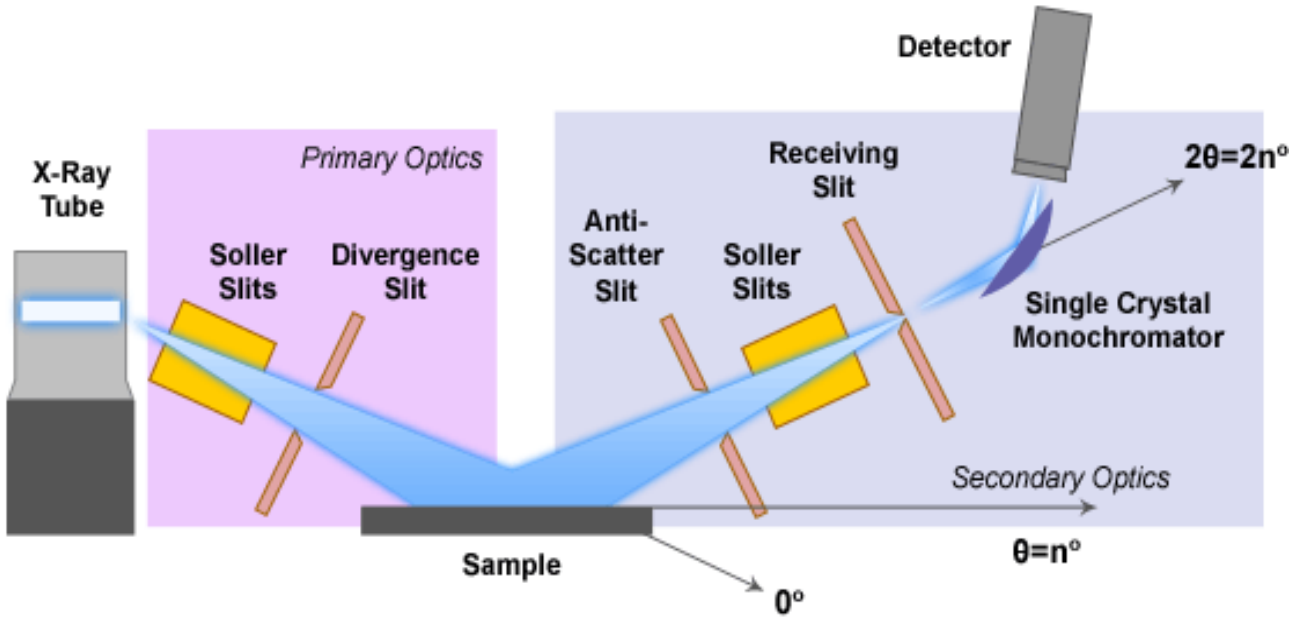

Figure 4: Standard design of a diffractometer of the Bragg-Brentano type.

The diffractometer utilized in this experiment is a D8 Advance diffractometer (CuKα radiation) operating under Bragg-Brentano configuration and supplied with a LINXEYE detector (Bruker, Karlsruhe, Germany). The X-ray diffraction (XRD) patterns have been recorded within the 2θ range of 10°-80°, with a scan step of 0.02° and a step time of 0.5 seconds. The refinement of lattice parameters has been performed using the Rietveld technique (TOPAS 4.2 software).

Fourier-Transform Infrared Spectroscopy (FTIR)

Infrared spectroscopy, often known as IR spectroscopy, refers to the branch of spectroscopy that specifically focuses on the analysis of the infrared region within the electromagnetic spectrum. The electromagnetic spectrum's infrared section is categorised into three distinct areas, namely the near-infrared, mid-infrared and far-infrared, which are named based on their relation to the visible spectrum. The far-infrared region, which covers around 400-10 cm-1 (1000–30 μm) and is located near to the microwave zone, exhibits low energy levels and may be used for the purpose of rotational spectroscopy. The mid-infrared region, covering from roughly 4000-400 cm-1 (30–1.4 μm), may be used for the analysis of basic vibrations and the corresponding rotational-vibrational properties. The near-infrared (IR) region with greater energy, ranging from around 14000-4000 cm-1 (1.4–0.8 μm), has the capability to induce overtone or harmonic vibrations.

Infrared spectroscopy is based on the principle that molecules possess distinct frequencies at which they undergo rotational or vibrational motions, which correspond to distinct energy levels (Figure 5). The

molecular potential energy surfaces, the atomic masses and the coupling of vibrational and electronic interactions all play a role in determining these resonant frequencies. Therefore, the resonant frequencies may be first correlated with the bond strength and the mass of the atoms located at either end of it. Hence, the frequency of the vibrations may be correlated with a certain bond type and used for the characterization of highly complex mixtures.

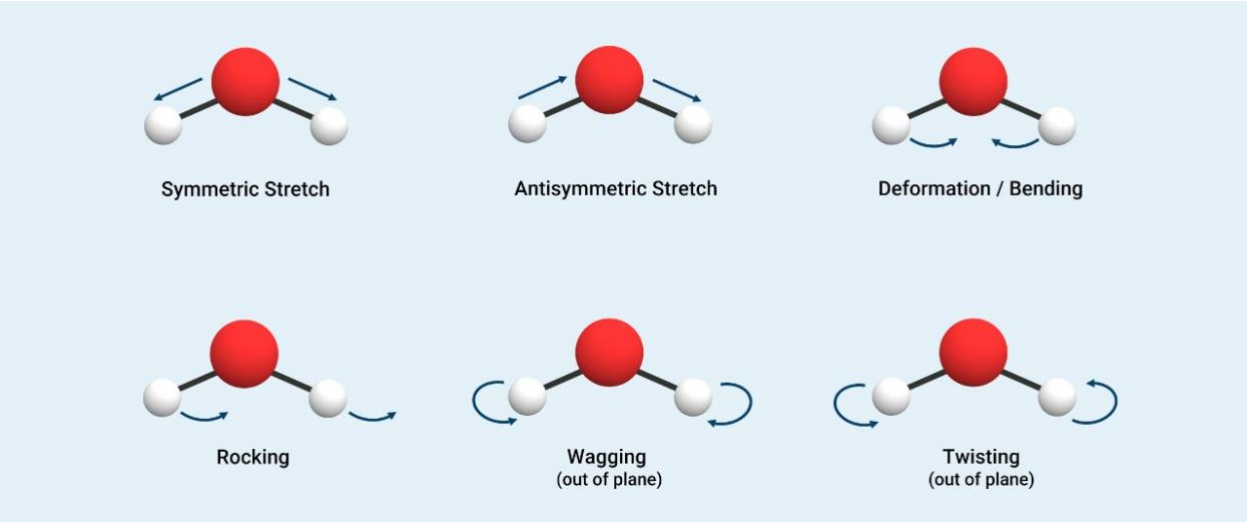

Figure 5: Potential vibrations detected by infrared spectroscopy.

The collection of infrared spectra from a sample involves the transmission of an infrared light beam through the sample. The analysis of the transmitted light provides information on the amount of energy that was absorbed at different wavelengths, shown in Figure 6. This may be accomplished with a monochromatic beam, which varies in wavelength over time, or with a Fourier transform device, which simultaneously measures all wavelengths. This information may be used to generate a transmittance or absorbance spectrum, which reveals the specific infrared (IR) wavelengths that the sample absorbs. The analysis of these absorption properties provides insights about the molecular composition of the sample.

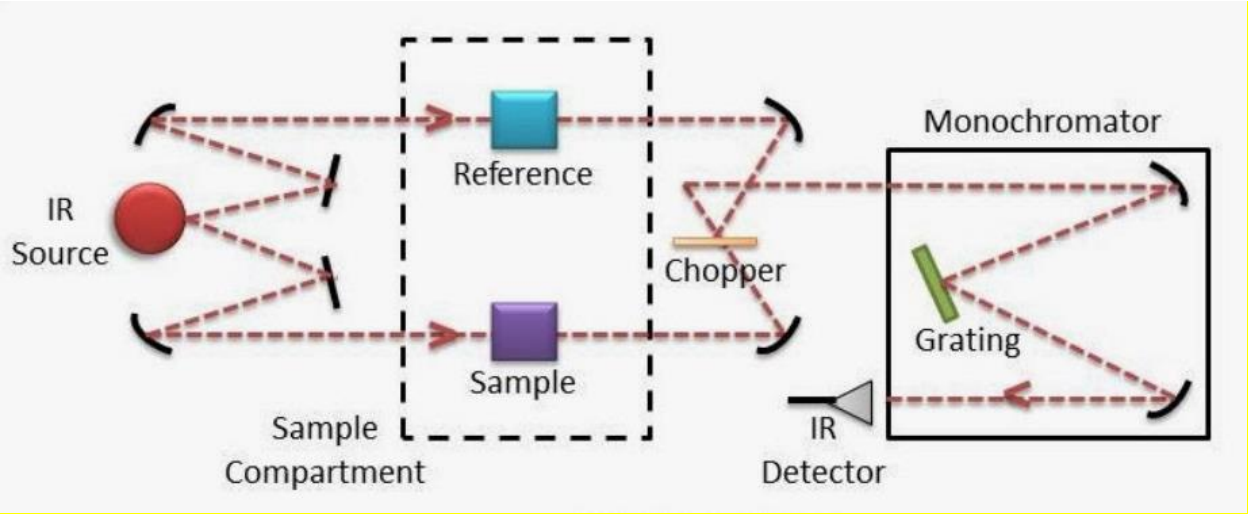

Figure 6: Schematic diagram of the equipment setup for infrared spectroscopy.

Samples are prepared by carefully grinding a portion of the material with potassium bromide (to eliminate scattering effects from large crystals), which is also used as a standard. The powder is then compressed in a mechanical die press to create a transparent pellet that allows the spectrometer's beam to pass through.

There are two primary uses of a reference:

- This reduces the impact of variations in the output of the source on the collected data.
- This enables the cancellation of the solvent's effects, often by using a reference of pure solvent.

This enables the cancellation of the solvent's effects, often by using a reference of pure solvent.

Scanning Electron Microscopy (SEM)

A scanning electron microscope is a tool that is capable of generating high-magnification images of a sample, with an ultimate magnification of up to 200000x [3]. Notably, this device offers superior resolution and field depth compared to the traditional optical microscope. The image is captured by the utilization of a high-energy electron beam to explore the surface of the sample, while also performing a concurrent, real-time assessment of the intensity of the emitted secondary electrons. After directing a high-energy electron beam toward a sample's surface, numerous signals are observed because of the interaction between the incident electrons and the sample (Figure 7).

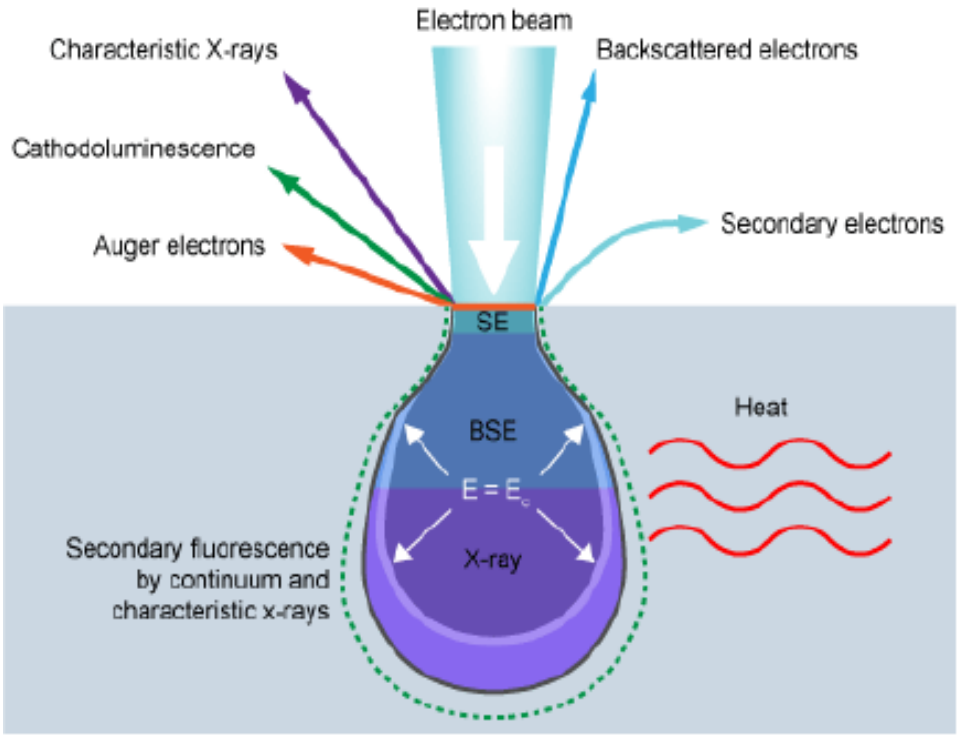

Figure 7: Interaction between electrons and matter.

A portion of the primary electron beam, also known as incident electrons, is reflected resulting in the generation of backscattered electrons while maintaining their initial energy. The primary electrons that do not undergo reflection transfer their energy to select electrons within the samples, thereby enabling them to diffuse toward the surface and subsequently escape the sample with minimal energy (i.e., energy levels < 50 eV), these electrons are commonly referred to as secondary electrons.

Moreover, the emission of characteristic X-ray photons occurs as a result of the primary beam inducing the removal of inner shell electrons from the material and this phenomenon is employed to examine the elemental composition of the sample. The back-scattered electrons that are emitted from the sample can be utilized independently to create an image or in combination with the characteristic x-rays as indicators of atomic number contrast, thereby providing information about the elemental composition of the sample. The scanning electron microscope (SEM) works by releasing thermo-ionic electrons from a tungsten cathode, also referred to as an electron gun, which is then accelerated towards an anode (Figure 8).

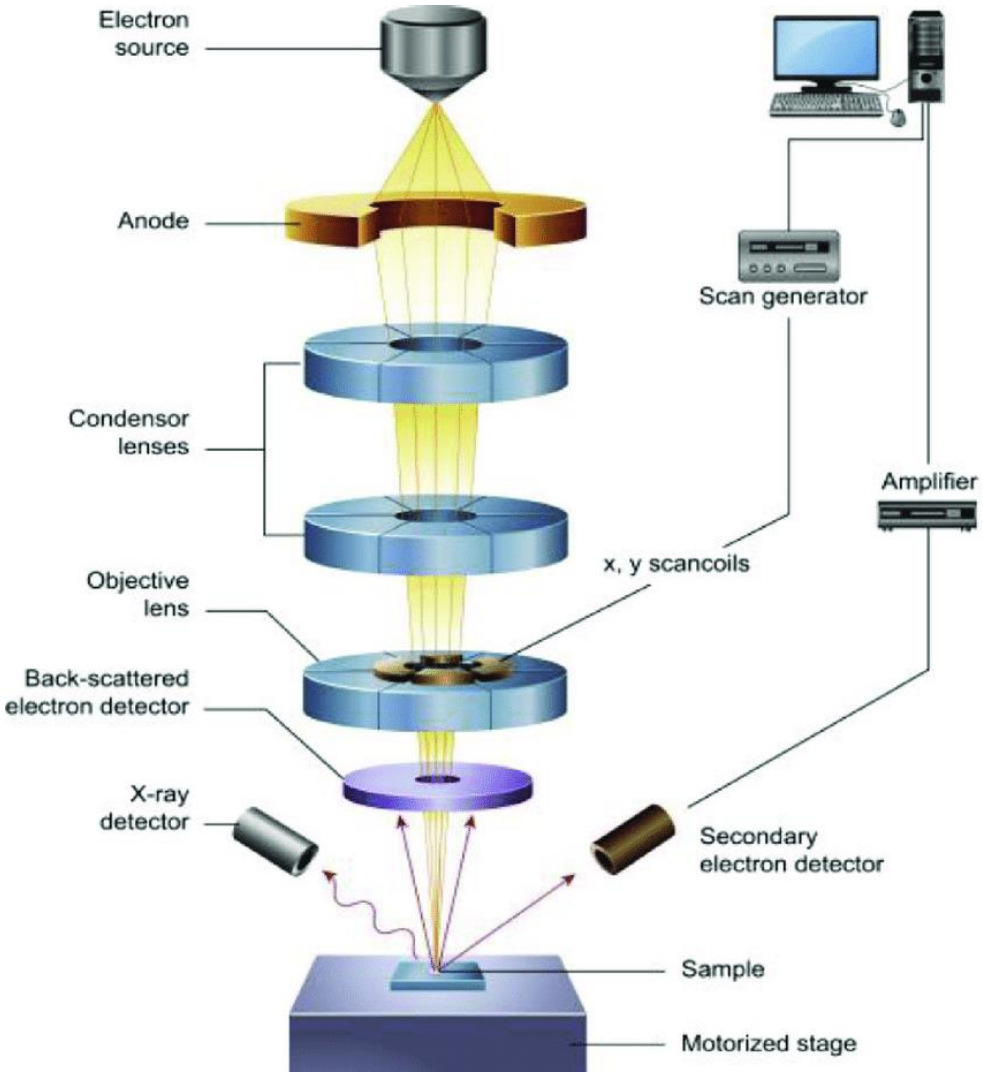

Figure 8: Structure of SEM [4].

Tungsten is a preferred material due to its exceptional qualities such as high melting point and low vapour pressure. The electron beam, with an energy range from a few hundred electron volts to 100KeV, is focused by condenser lenses to produce a beam with a very fine focal spot, monitoring between 0.4 nm and 5 nm in size. To scan the surface of the sample, the beam is deflected by passing via pairs of scanning coils or pairs of deflector plates located in the electron optical column, most often in the objective lens. The interaction volume may be affected by different parameters, including the energy of the electron beam, the atomic number of the sample and the density of the sample. Due to their low energy, secondary electrons are detected by a scintillator photomultiplier device, which then converts the resultant signal into a two-dimensional intensity distribution that may be displayed or saved as a digital image. The intensity of the signal is dependent upon the number of secondary electrons that arrived at the detector. The spatial resolution of the scanning electron microscope (SEM) is dependent upon the electron spot's

dimensions, which are influenced by the wavelength of the electrons and the magnetic electron-optical system responsible for generating the scanning beam.

Inductively Coupled Plasma Optical Emission Spectroscopy

Inductively Coupled Plasma Optical Emission Spectroscopy (ICP-OES) is a highly effective and widely utilized analytical technique in the identification of trace elements [5].

The approach relies on the spontaneous release of photons from atoms and ions that undergo excitation within a radiofrequency (RF) discharge. The instrument can receive liquid and gas samples through direct injection, whereas solid samples involve extraction or acid digestion to ensure the presence of analytes in a solution. The relationship between the radiation intensity and the element concentration is directly proportional and can be determined through calibration using appropriate standard solutions.

A torch comprising three concentric tubes, typically composed of quartz, can be used to maintain an inductively coupled plasma for spectrometry. The end of this torch is inserted into an induction coil that is supplied with a radio-frequency electric current. After introducing a flow of argon gas between the torch's two outermost tubes, an electrical spark is provided for a short period of time to inject free electrons into the argon gas flow (Figure 9).

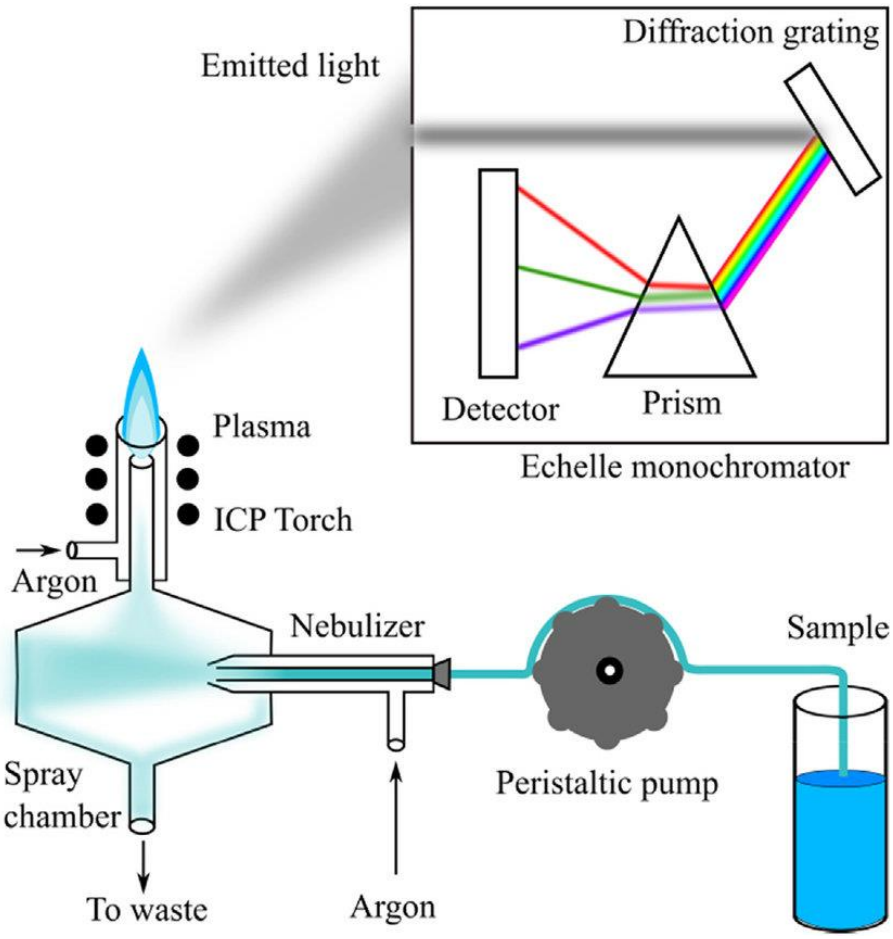

Figure 9: Schematic view of an ICP-OES instrument.

After converting into an aerosol, the sample solution is then introduced into the plasma's central flow channel. The inductively coupled plasma (ICP) maintains a temperature of around 10000K, resulting in rapid vaporization of the aerosol. The analyte elements undergo a process of liberation, resulting in their conversion into free atoms in a gaseous state. Additional energy is provided to the atoms within the plasma through further collisional excitation, which results in their shift to excited states. The availability of sufficient energy often facilitates the conversion of atoms into ions, subsequently resulting in the promotion of these ions to excited states. The emission of photons may then allow the excited atomic and ionic species to return to their ground states. The energies of these photons are unique and can be determined by the quantized energy level arrangement of the atoms or ions. Therefore, the wavelength of the photons may be utilized to determine the elements from where they emerged. A direct correlation is found between the quantity of the emitted element and the total number of photons.

Energy dispersive X-ray spectroscopy (EDS)

The Energy Dispersive X-ray Spectroscopy (EDS) technique is used to identify the constituent elements of a given material by detecting the X-ray fluorescence [6]. When a specimen is stimulated by a high-energy electron beam or other forms of electromagnetic radiation, it results in the ejection of the inner shell of electrons into a vacuum, thus creating a vacancy in that particular shell (figure below).

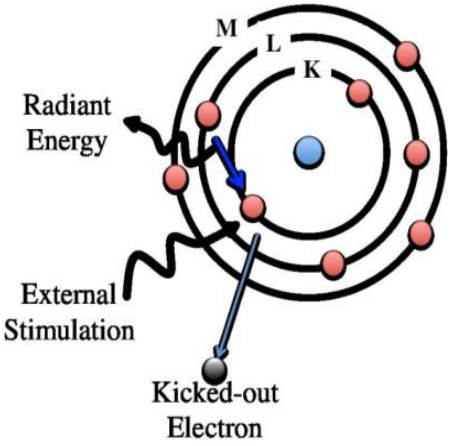

Electrons located in the outermost shell of an atom jump to occupy a vacant site in the inner shell. During this process (radiant energy), the specimen exhibits fluorescence by emitting X-rays with an energy equivalent to the difference between its initial and final states. The unique and discrete energy levels of each atom result in the characteristic X-ray fluorescence of atoms.

SiLi detectors, which operate at the temperature of liquid nitrogen, are frequently used in EDS experiments (as depicted in Figure 10). After interaction with the detector, X-rays generate photoelectrons that subsequently give rise to electron-hole pairs within the Si material. These then travel to the ends of the detectors (with the help of an applied electric field of 1.5 kV), where they generate a current pulse, whose size is directly proportional to the intensity of the incident X-rays.

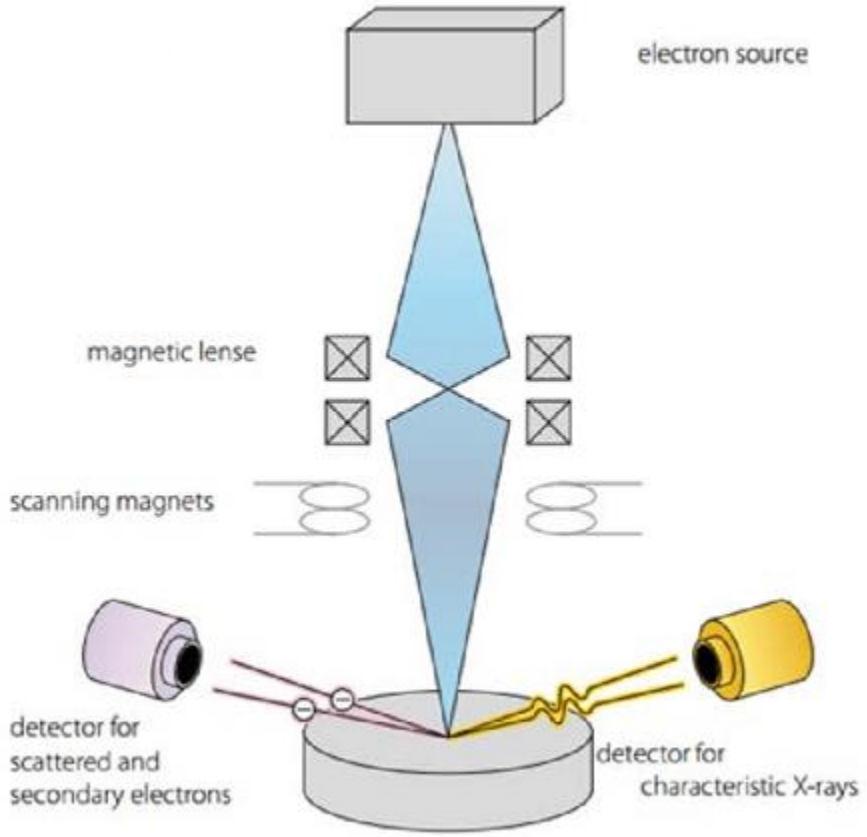

Figure 10: Schematic diagram of principle of EDS device in the scanning electron microscope (SEM) [7].

Specific Surface Area

The production of ceramics is closely related to various parameters, particularly the dimensions, structure and specific surface area (SSA) of the powders. In an ideal scenario, it can be assumed that a powder comprises small spherical particles that have identical diameters. In such a case, the specific surface area (m^2/g) of the powder, denoted by S, can be determined by multiplying the surface area of each particle with the number of particles per unit weight, represented by n ($S = 4\pi r^2 n$). The irregular and unpredictable size and shape of the powder particles prevent the development of a simple surface area model. In this particular case, the determination of specific surface area (SSA) is achieved through the indirect measurement of gas adsorption on the external surface of the particles.

Adsorption process may be divided into two distinct types: physical adsorption and chemical adsorption. The primary distinction involves the characteristics of the interaction forces responsible for the gas's adsorption; in the first case, only weak Van der Waals and electrostatic forces exist, but in other case, stronger chemical bonds are also involved. Because of this, determining SSA by physical adsorption is

believed to be the simplest method, since a reversible process known as desorption can be used to measure the amount of adsorbed gas.

B.E.T. Equation

In 1938, the scientists Stephen Brunauer, Paul Hugh Emmett and Edward Teller proposed a hypothesis as an extension of the Langmuir theory to explain the multilayer adsorption phenomenon [8].

Three primary postulates were put forward:

1. Gas molecules exhibit physical adsorption on a solid surface in an infinite number of layers.
2. There is no interaction among each of the adsorption layers.
3. The Langmuir theory is applicable to each layer.

The resulted BET equation is as follows:

$$\frac{p}{V_{ads}(p^o-p)} = \frac{(C-1)}{V_m C}\frac{p}{p^o} + \frac{1}{V_m C}$$

where Vads represents the amount of gas adsorbed at the surface, Vm represents the amount of gas adsorbed at the monolayer level, p represents the equilibrium pressure of the adsorbates at the adsorption temperature, p° represents the saturation pressure of the adsorbates at the adsorption temperature and C represents the BET constant, which is proportional to the net adsorption energy.

The equation can be simplified by considering Vm and C as constants for a specific gas:

$$\frac{p}{V_{ads}(p^o-p)} = \alpha\frac{p}{p^o} + \beta$$

$$\alpha = \frac{(C-1)}{V_m C} \qquad \beta = \frac{1}{V_m C}$$

The equation of a line, $y=\alpha x+\beta$, is derived as a result, particularly within the relative pressure range of 0.05-0.30. After obtaining the values of α and β coefficients, the value of Vm can be calculated as $1/(\alpha+\beta)$.

The total surface area of the adsorbed gas, denoted as S, is calculated by the multiplication of Vm and S_0, where S_0 represents the surface area occupied by a single layer of adsorbed gas per unit volume of 1

cm^3. Therefore, the equation for S can be expressed as $S = Vm . S_0$. SSA can be calculated by the division of the sample size, S, by the sample weight, W.

The immersion of the sample holder in liquid nitrogen facilitates the adsorption process. After a short period of time, gas stabilization occurs and the process of adsorption is measured. Subsequently, the desorption mechanism is induced by replacing the liquid nitrogen with a water bath at ambient temperature, leading to the liberation of the previously adsorbed nitrogen. Ideally, the process of gas adsorption exhibits a completely reversible nature such that the subsequent desorption is equivalent in magnitude and direction to the initial adsorption.

Particle Size Distribution

The fluid dynamics phenomenon of a falling sphere in motion is characterized by the presence of three distinct forces. Hydrostatic force, also known as Archimedes principle, can be represented by the equation FA and FD refers to the drag force, which is the force of fluid friction [9]. In conditions of equilibrium, the sum of all forces acting on an object is equal to zero (FG + FA + FD = 0).

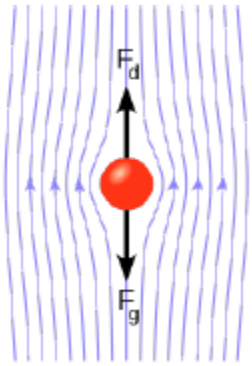

A more precise rigorous equation that characterizes the motion of the particle is:

$$mg - m^{o}g - F = m^{o}\frac{dv}{dt}$$

In this example, the variables denoted as "m," "m°," "g," "F," "v," and "t" represent the particle's mass, the mass of the liquid equivalent to the particle's volume, the force of gravity, the drag force, the velocity of the particle and the time, respectively.

Based on empirical evidence, it can be observed that particles have slower motion as the viscosity of the fluid increases. Conversely, smaller particles exhibit faster velocity variations, resulting in a rapid

decrease in dv/dt. The equation of motion for a sphere having a diameter D and density ρ, when it is in a fluid with density ρ°, can be expressed as follows:

$$F = \frac{\pi}{6} (\rho - \rho^{\circ}) g D^3$$

The Reynolds number (Re) and a frictional coefficient (C) are two dimensional quantities that describe the stabile motion of a sphere-shaped particle in a fluid.

$$Re = Dv\frac{\rho^{\circ}}{\eta} \qquad C = \frac{F}{(\pi D^2/4)(\rho^{\circ} V^2/2)}$$

The Stoke's law is derived based on the assumption of laminar flow (where $C \cdot Re \approx 24$).

$$D^2 = \frac{18\, v\, \eta}{(\rho - \rho^{\circ})\, g}$$

Sedimentation Theory

The study of sedimentation relates to the correlation between the velocity of a particle in a fluid and its size, according to Stoke's law, as larger particles exhibit higher velocities. The particle density, fluid density and viscosity are all variables that must be known in order to get an accurate estimate of the particle diameter from the falling velocity [10].

Analytical Technique

Theoretical evaluation of the falling velocity of particles of varying sizes is carried out by considering the characteristic parameters of the fluid using Stoke's law. Subsequently, the height of the sample cell is linked to a particle radius that is equal to or less than the value obtained by solving Stoke's law, based on real-time sedimentation analysis [11]. After the calibration of the instrument utilising sodium hexametaphosphate in an aqueous solution with a weight percentage of 0.05%, the particles of the specimen are subsequently dispersed in a comparable fluid. This fluid is then subjected to sonication to prevent the formation of aggregates before being pumped into the sample cell, as shown in Figure 11.

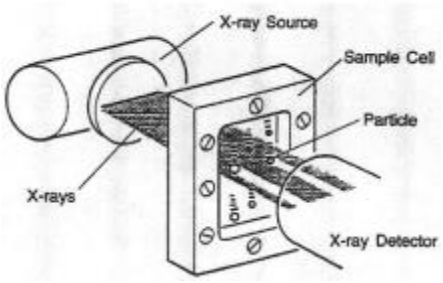

Figure 11: Sample cell detail during analysis.

The intensity of X-rays detected at various heights of the sample cell during gravitational sedimentation is utilised to monitor the size distribution of particles. In the end, a plot presenting the cumulative mass percentage as a function of particle diameter is derived.

Thermogravimetric analysis (TGA)

Thermogravimetric analysis is a useful technique for assessing changes in weight with respect to variations in temperature. The accuracy of the analysis is dependent upon a significant level of precision in three distinct measurements, namely weight, temperature and variation in temperature. Due to the similarity of weight loss curves, it may be required to apply a transformation to the curve in order to accurately interpret the results [12].

The weight loss curve enables the identification of the point at which weight loss is most apparent. In most cases, a high-precision balance with a pan carrying the sample is used as the analyser. The sample is positioned in a small electrically heated oven, which is equipped with a thermocouple to precisely determine the thermal conditions. To stop oxidation and other undesirable processes, it may be necessary to purge the environment with an inert gas. A computer controls the instrument's operation at all times. The process of analysis involves a gradual increase in temperature, followed by the plotting of weight against temperature. After collection of data, it may be necessary to perform curve smoothing and other associated operations to determine the precise points of inflection.

Rheology of suspensions

Rheology is an emerging field of science that investigates the behaviour of materials when subjected to external forces, specifically in terms of their flow and deformation properties. This is typically accomplished by a rheometer, which is a specialised instrument designed for measuring rheological characteristics. The rheological characteristics of ceramic suspensions are primarily influenced by the concentration of solid particles, the distribution of particle sizes and the extent of agglomeration [13]. At

extremely low shear, the fundamental solid particles exhibit a tendency to aggregate, potentially resulting in the formation of a three-dimensional network that involves all the suspension volume. The network structure confers elastic characteristics to the suspension and is responsible for the development of apparent yield stress. As the shear rate is increased, the network undergoes a breakdown process resulting in the formation of aggregates that show a continuous reduction in size. The size and configuration of aggregates are dependent upon the applied shear rate. The increase of shear rate can lead to microstructural variations that have the potential to alter the viscosity.

At higher rates of shear rate, the process of aggregate breakdown occurs through the breakdown of primary flocs. Since the rates of agglomeration and breakdown are not constant, the rheological characteristics vary with time, leading to thixotropic effects. The reported agglomeration phenomena are primarily associated with the interaction of Brownian, hydrodynamic and interparticle (attractive or repulsive) forces. Primary flocs are attracted to one another by Van der Waals forces, which are the main reason for flocculation. Steric stabilisation is frequently required to prevent agglomeration by introducing an appropriate quantity of effective dispersant (polymers) that are adsorbed onto the surfaces of the particles. The analysis of the rheological properties of suspensions containing calcium phosphate is a valuable technique for modifying the final performance of scaffolds.

Viscosity and Dynamic *Modulus*

Viscosity is a fundamental property of a fluid that characterises its ability to resist deformation and flow. When two plates are separated by a distance d and a force F is applied to a volume of material, a displacement or deformation takes place. The dynamic viscosity, denoted by η (Figure 12), is defined as the constant of proportionality between the shear stress (force per unit area parallel to the force) and the shear strain rate (displacement per unit time divided by the product of the plates' separation distance) [14].

$$\eta = \frac{shear\ stress}{shear\ rate} = \frac{\tau}{\dot{\gamma}}\ [Pa \cdot s]$$

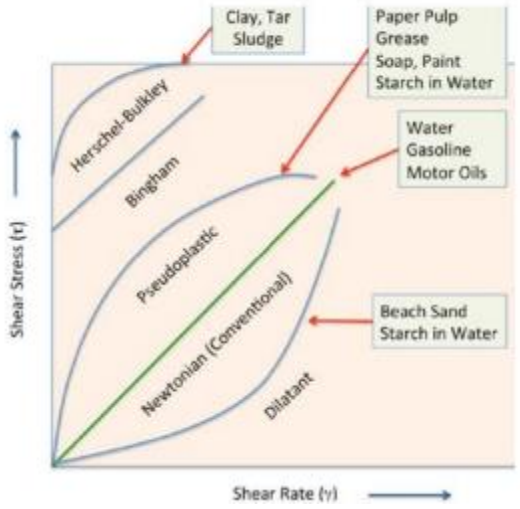

Figure 12: Shear Stress-Shear rate diagrams.

The rheological properties of ceramic formulations intended for 3D printing were assessed using the Discovery HR1 (Hybrid Rheometer, TA Instruments) in combination with a parallel Peltier plate system (with a plate diameter of 40mm and a gap of 1000μm). The study assessed the shear stress and viscosity of individual suspensions by gradually increasing the shear rate from 0.01 to 100. In addition, the material's dynamic mechanical characteristics (storage modulus, loss modulus and yield stress) have been evaluated by varying the shear stress from 1 to 100 Pa at a frequency of 1 Hz. The concept of storage modulus (G') relates to the capacity of a given material to store elastic energy, whereas the loss modulus (G'') is associated with the dissipation of energy. The yield stress refers to the critical stress level at which a substance with high viscosity exhibits liquid-like flow behaviour.

In order to evaluate the yield stress (Figure 13), the shear stress at zero shear rate was calculated using the Herschel-Bulkley model [15]. The viscosity was determined by exposing the substance to a constant shear rate that frequently occurs during the printing process ($\dot{\gamma} = 50s^{-1}$).

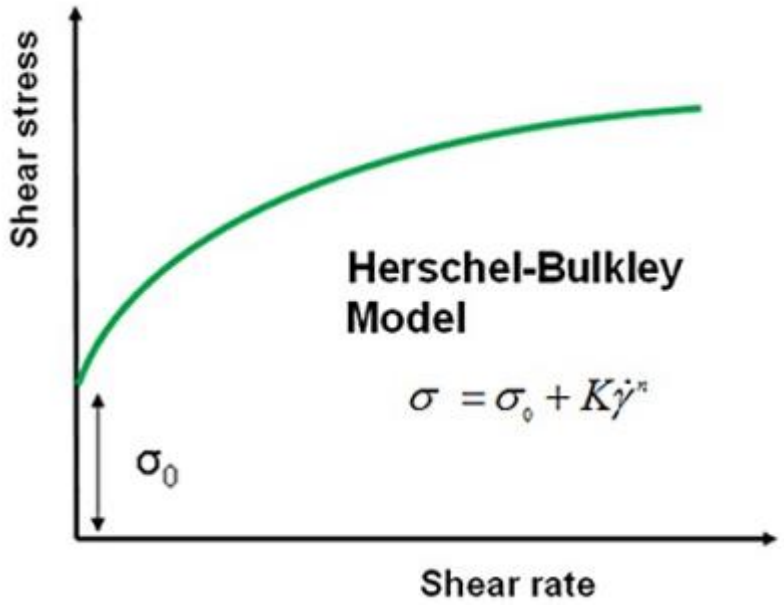

Figure 13: Schematic representation of the yield stress, σ0, according to the Herschel-Bulkely model.

Zeta Potential

The Zeta potential (ξ) is a physical characteristic that is displayed by any particle in suspension. It describes the factors that lead to particle dispersion, aggregation, or flocculation and evaluates the strength of electrostatic or charge repulsion/attraction between particles [16]. The shear plane, also known as the slipping plane, refers to the boundary of a region adjacent to the particle surface that is characterized by a strongly bound electrical double layer composed of ions and solvent molecules. The concept of the zeta potential relates to the difference in potential that exists between the surface of the shear plane of the particles and the electroneutral region of the solution, as shown in Figure 14.

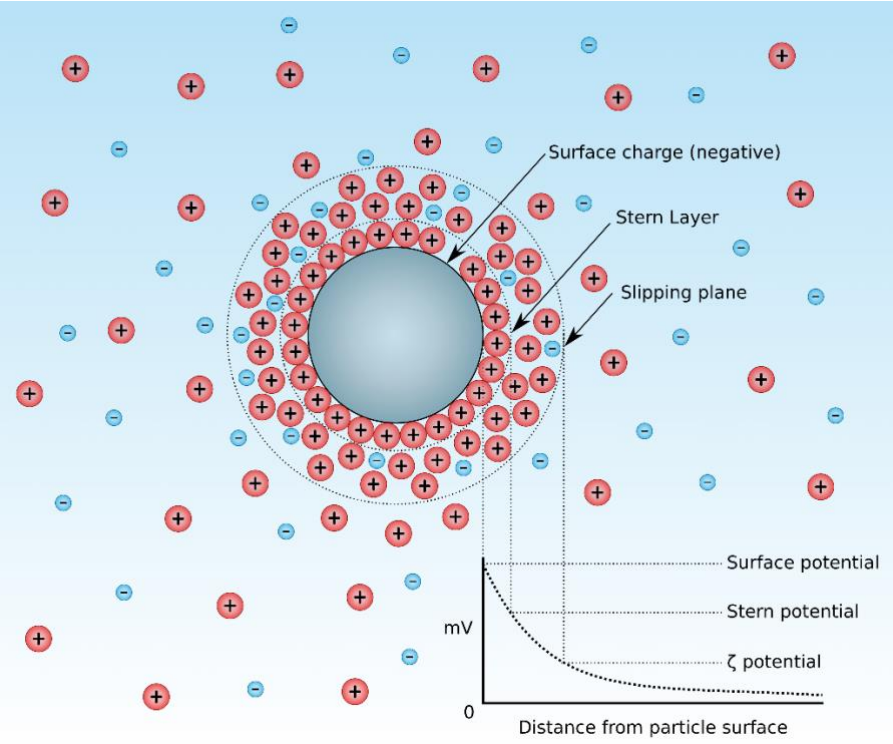

Figure 14: schematic view of Zeta potential.

Mechanical characterization

Compression

The compressive tests are primarily used to characterize the strength of ceramic materials due to the presence of inherent micron-scale defects that can be readily extended under tensile stress, thus affecting the measurement's accuracy [17]. Consequently, the compressive strength of ceramics is typically greater than their tensile strength. The compressive test of a specimen is a procedure that employs a system of converging forces that result in a reduction of its size. Therefore, force must be uniformly distributed across the entire surface of the specimen sections. This enables the calculation of the average value of the compressive stress, σ, by dividing the force, F, by the cross-sectional area, A. In axially loaded specimens, the normal stress is uniformly distributed, except for the regions where the loads are applied. The scheme of the compression test is shown in Figure 15.

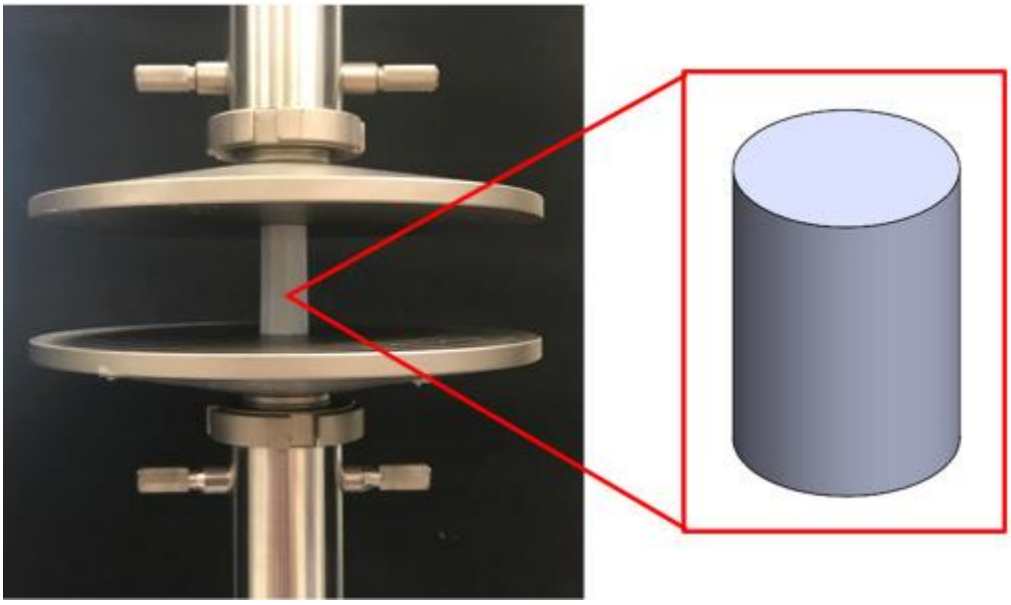

Figure 15: Scheme of the compression test.

The assessment of compressive strength was carried out after the achievement of endplate planarity, which was accomplished using an automatic surface grinder. The experiments were conducted under displacement control conditions at a rate of 1 mm/min and data was collected by Zwick Roell Z050 machine.

Flexural (4-point bending)

The flexural strength is a fundamental characteristic of a material that is determined by the stress at which it yields during a flexure test. In the case of a homogeneous material, the flexural strength would be equivalent to the tensile strength. However, it is common for materials to possess either small or large defects, which act as stress concentrators in localized regions, ultimately resulting in a localized weakness [18].

The flexural strength of a ceramic depends on its inherent toughness as well as the size and severity of any defects in the material. This test involved the computation of flexural strength through the utilization of 4-point bending tests. Specifically, a loading force was applied through the implementation of two loading pins, which were positioned at a distance equivalent to half of the distance between the supporting pins, as shown in Figure 16.

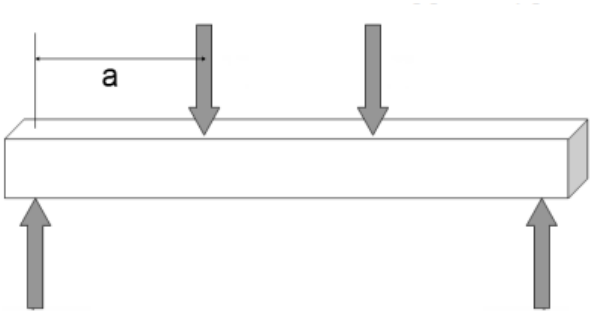

Figure 16: Scheme of the 4-point bending test.

It is important to highlight that there is a lack of established reference standards for conducting 4-point bending tests on macroporous ceramic material, so only certain indications were followed (ASTM C1341-00: Standard Test Method for Flexural Properties of Continuous Fiber Reinforced Advanced Ceramic Composites). The measurement of flexural strength was carried out through an analysis of parallelepiped specimens, measuring 45mm x 7mm x 7mm, for every given circumstance. The experiments were conducted under displacement control conditions at a rate of 1 mm/min. Figure 17 shows the stress state that was obtained as a result of the flexural testing.

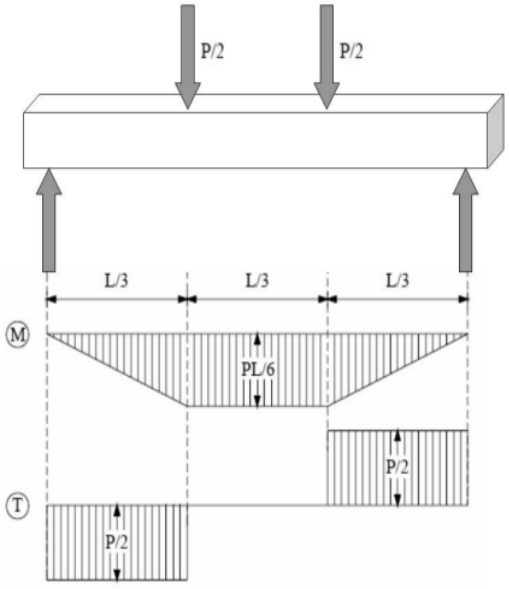

Figure 17: Shear force and bending moment distribution during a 4-point bending test.

Although it is supposed that a stress concentration exists locally at the loading points, the area of the specimen located between the upper pins exhibits a uniform bending moment and zero shear stress, resulting in pure bending loading (PL/6) in the central portion of the sample.

The flexural strength can be determined by utilizing the fracture load, P_N:

$$\sigma = \frac{3 \cdot P_N \cdot a}{b \cdot d^2}$$

The variables 'b' and 'd' denote the weight and height of the samples, respectively. The deformation ε was assessed for each test through displacement control.

References

1. Sharma, R., et al., *X-ray diffraction: a powerful method of characterizing nanomaterials.* 2012. **4**(8): p. 77-79.
2. Bunaciu, A.A., E.G. UdriŞTioiu, and H.Y.J.C.r.i.a.c. Aboul-Enein, *X-ray diffraction: instrumentation and applications.* 2015. **45**(4): p. 289-299.
3. Ul-Hamid, A., *A beginners' guide to scanning electron microscopy*. Vol. 1. 2018: Springer.
4. Ali, A.S.J.N. and t. Environment, *Application of nanomaterials in environmental improvement.* 2020.
5. Ghosh, S., et al., *Inductively coupled plasma–optical emission spectroscopy: a review.* 2013. **3**(1): p. 24-33.
6. Russ, J.C., *Fundamentals of energy dispersive X-ray analysis: Butterworths monographs in materials*. 2013: Butterworth-Heinemann.
7. Abd Mutalib, M., et al., *Scanning electron microscopy (SEM) and energy-dispersive X-ray (EDX) spectroscopy*, in *Membrane characterization*. 2017, Elsevier. p. 161-179.
8. Davis, B.H., *The BET Equation–Nominated for a Nobel Prize but Not Selected*, in *The Posthumous Nobel Prize in Chemistry. Volume 1. Correcting the Errors and Oversights of the Nobel Prize Committee*. 2017, ACS Publications. p. 165-206.
9. Crowe, C.T., et al., *Multiphase flows with droplets and particles*. 2011: CRC press.
10. Ferguson, R. and M.J.J.o.s.R. Church, *A simple universal equation for grain settling velocity*. 2004. **74**(6): p. 933-937.
11. Andre, C., et al., *Real-time analysis of the growth of granular media by an ultrasonic method: Application to the sedimentation of glass balls in water.* 2011. **208**(2): p. 301-307.
12. Coats, A. and J.J.A. Redfern, *Thermogravimetric analysis. A review.* 1963. **88**(1053): p. 906-924.
13. Mewis, J. and N.J. Wagner, *Colloidal suspension rheology*. 2012: Cambridge university press.
14. Eliades, T., et al., *Structure/property relationships in orthodontic polymers*, in *Orthodontic Applications of Biomaterials*. 2017, Elsevier. p. 39-59.
15. Saasen, A. and J.D.J.A.R. Ytrehus, *Rheological properties of drilling fluids: use of dimensionless shear rates in herschel-bulkley and power-law models.* 2018. **28**(5): p. 201854515.
16. Sjoblom, J., *Emulsions and emulsion stability: Surfactant science series/61*. Vol. 132. 2005: crc press.
17. Greer, J.R. and J.T.M.J.P.i.M.S. De Hosson, *Plasticity in small-sized metallic systems: Intrinsic versus extrinsic size effect.* 2011. **56**(6): p. 654-724.
18. Currey, J.D.J.J.o.E.B., *What determines the bending strength of compact bone?* 1999. **202**(18): p. 2495-2503.